

# Correlative electrochemical and spectroscopic Study of the Surface Reconstruction and the Oxygen Evolution Reaction on Structure- and Morphology-directed Nickel oxides

Korrelative elektrochemische und spektroskopische Untersuchung der Oberflächenrekonstruktion und der Sauerstoffentwicklungsreaktion von Struktur- und Morphologie-kontrollierten Nickeloxiden

Bei der Fakultät für Mathematik und Naturwissenschaften der Carl von Ossietzky Universität Oldenburg zur Erlangung des Grades und Titels eines

Doktors der Naturwissenschaften  
Dr. rer. nat.

## **Angenommene Dissertation**

von Herrn Konstantin Kimon Rücker  
geboren am 13.05.1998 in Wittmund

Erstgutachter:

Prof. Dr. Michael Wark, Institut für Chemie, Carl von Ossietzky Universität Oldenburg,  
Deutschland

Weitere Gutachter:

Prof. Dr. Michael Bron, Institut für Chemie, Martin-Luther-Universität Halle-  
Wittenberg, Deutschland

Prof. Dr. Dmitry Momotenko, Institut für Chemie, Carl von Ossietzky Universität  
Oldenburg, Deutschland

Eingereicht am: 08.10.2025

Tag der Disputation: 28.11.2025

This dissertation was prepared between February 2022 and October 2025 in the Department of Electrochemical Energy Technology of the DLR-Institute of Engineering Thermodynamics in the group of “Alkaline Membrane Electrochemistry” headed by Dr. Corinna Harms and in cooperation with the group of Prof. Dr. Michael Wark at the Carl von Ossietzky University Oldenburg. Within this PhD work, a research stay at the Colorado School of Mines Golden in the group of Prof. Dr. Ryan Richards was carried out. Additionally, the collaboration with Dr. Marcel Risch from the Helmholtz Zentrum Berlin enabled two one-week Synchrotron beamtime experiments at the BESSY II Light Source accompanied by extensive preparation and joint data evaluation. At last, *in-situ* Raman experiments in the group of Dr. Dulce Morales at the University of Groningen were conducted during a short-period research visit.

This work was funded within the bilateral NSF-DFG Echem project “SurFCat”. The German Research Foundation (DFG) is acknowledged for the financial support of this research which broadly aimed to elucidate the influence of facets, steps and kinks on oxygen electrocatalysis. The contributions of the project partners and collaborators is stated in the respective chapters and specified in the experimental part.



## Abstract

Transition metal oxides are promising electrocatalysts for the oxygen evolution reaction in alkaline media and are relevant for the emerging anion exchange membrane water electrolyzer technology. In this thesis, faceted rock salt nickel oxide with predominant exposure of the (111) plane is employed as a model system to investigate the correlation between surface reconstruction and catalytic activity during the oxygen evolution reaction.

For electrochemical characterization, fundamental rotating disc electrode experiments were performed in addition to an advanced half-cell configuration, designed to resemble conditions relevant for anion exchange membrane water electrolysis. Correlative spectroscopy techniques such as X-ray absorption, X-ray photoelectron, and (*in-situ*) Raman spectroscopy were used to investigate structural and compositional changes between the pristine catalyst material before electrochemical characterization (pre-catalyst) and the catalyst state after electrochemical OER characterization. The latter gives insight into reversible and irreversible changes of the catalyst material and allows estimation of catalytically relevant surface structures and active phases for the OER.

Pure nickel oxide (111) nanosheets synthesized via different routes were electrochemically evaluated for different applied annealing temperatures. Building on this model material, cobalt- and manganese-incorporated nickel oxide (111) samples were prepared to improve oxygen evolution performance. Although the activity enhancements were modest, distinct changes in redox behavior were observed. Both cobalt and manganese suppressed the formation of nickel oxyhydroxides, as evidenced by rotating disc electrode and X-ray photoelectron spectroscopy, and manganese was proven to leach during electrochemical testing.

Incorporation of iron enabled the synthesis of phase-pure materials up to iron contents of five mole-percent and below. Yet, the iron incorporation has led to drastic improvements of the oxygen evolution performance, far exceeding the performance of pure nickel oxide (111) and the cobalt- and manganese-incorporated samples. Comparing synthetically obtained iron-nickel (hydr)oxides with pure nickel (hydr)oxides, incorporating iron through spiking of the electrolyte revealed that only trace levels of iron incorporation are sufficient to achieve high oxygen evolution performances. The systems tested in iron-containing electrolytes even outperformed the synthetically compounded materials. The suppression of nickel oxyhydroxide formation in the presence of iron

challenges the assumption that pronounced reconstruction is required for high performances and instead highlights the high intrinsic activity of iron-containing nickel (hydr)oxides.

Finally, recommendations for reliable electrochemical testing and *ex-situ* spectroscopic characterization of oxygen evolution catalysts in alkaline solutions are provided based on insights from nickel oxide systems, with applicability to other catalyst families.

Overall, this work contributes to the knowledge of Ni-based OER electrocatalysts in alkaline media by studying the role of transition-metal doping on the oxygen evolution activity and the surface reconstruction of nickel oxide. High oxygen evolution reaction performances can be achieved without extensive surface reconstruction into NiOOH.

## Zusammenfassung

Übergangsmetalloxide sind vielversprechende Elektrokatalysatoren für die Sauerstoffentwicklungsreaktion im alkalischen Milieu und sind von Bedeutung für die aufkommende Technologie der Anionenaustauschmembran-Wasserelektrolyse. In dieser Dissertation wird facettierte Nickeloxid in Steinsalzstruktur mit überwiegender Exposition der (111)-Ebene als Modellsystem untersucht, um die Korrelation zwischen der Oberflächenrekonstruktion des Vorkatalysators und der katalytischen Aktivität während der Sauerstoffentwicklungsreaktion zu untersuchen. Für die elektrochemische Charakterisierung wurde die grundlegende Technik der rotierenden Scheibenelektrode verwendet und später um einen fortgeschrittenen Halbzellenaufbau erweitert, die den Bedingungen eines Anionenaustauschmembran-Wasserelektrolyseurs ähnelt.

Korrelative Spektroskopie-Techniken wie Röntgenabsorptionsspektroskopie, Röntgenphotoelektronenspektroskopie und (*in-situ*) Raman-Spektroskopie wurden eingesetzt, um strukturelle Veränderungen zwischen dem ursprünglichen Katalysatormaterial vor der elektrochemischen Charakterisierung (Vorkatalysator) und dem Katalysatorzustand nach elektrochemischen OER-Tests zu untersuchen. Letzteres gibt Aufschluss über reversible und irreversible Veränderungen des Katalysatormaterials und ermöglicht es, katalytisch relevante Oberflächenstrukturen und aktive Phasen für die OER aufzuklären.

Zunächst wurden reine, über verschiedene Syntheserouten hergestellte Nickeloxid-(111)-Nanoplättchen bei variierenden Kalzinierungstemperaturen elektrochemisch untersucht. Aufbauend auf diesem Modellmaterial wurden kobalt- und manganhaltige Nickeloxid-(111)-Nanoplättchen hergestellt, mit dem Ziel die Sauerstoffentwicklungsreaktion zu verbessern. Obwohl die Aktivitätsverbesserungen geringfügig waren, konnten deutliche Veränderungen im Redoxverhalten beobachtet werden. Sowohl Kobalt als auch Mangan unterdrückten die Bildung von Nickel-Oxyhydroxiden, was durch die rotierende Scheibenelektrode und Röntgenphotoelektronenspektroskopie nachgewiesen wurde. Bei Mangan konnte weiterhin ein Herauslösen aus der Elektrode während elektrochemischen Tests nachgewiesen werden.

Weiterhin wurde die Zugabe von Eisen in die verschiedenen Nickel-Materialien untersucht. Sowohl in die Nickelhydroxide, als auch in die Nickeloxid-(111)-Nanoplättchen konnte bis zu fünf Molprozent Eisen hinzugegeben werden. Darüber hinaus bildeten sich Eisenfremdphasen. Die Sauerstoffentwicklungsaktivität übertraf

jedoch bei weitem die von reinem Nickeloxid (111) und den kobalt- und manganhaltigen Proben. Der Vergleich von synthetisch hergestellten Eisen-Nickelhydroxiden und -oxiden mit analogen Materialien, bei denen Eisen ausschließlich über den Elektrolyten zugegeben wurde, zeigte, dass bereits geringe Eisenmengen genügen, um eine hohe Sauerstoffentwicklungsaktivität zu erzielen. Die in eisenhaltigem Elektrolyten getesteten Systeme übertrafen sogar die synthetisch gemischten Eisen-Nickelmaterialien. Die Unterdrückung der Nickeloxidbildung in Anwesenheit von Eisen stellt die Annahme in Frage, dass eine ausgeprägte Oberflächenrekonstruktion zu Nickeloxyhydroxid erforderlich ist, und lässt stattdessen die hohe intrinsische Aktivität eisenhaltiger Nickeloxyhydroxide vermuten.

Schließlich werden Empfehlungen für zuverlässige elektrochemische Tests und für die *ex-situ* spektroskopische Charakterisierung von Sauerstoffentwicklungskatalysatoren in alkalischer Lösung gegeben, die auf den Erkenntnissen auf den Nickeloxidsystemen basieren und auf andere Katalysatorfamilien übertragbar sind. Insgesamt wurde in dieser Arbeit die Rolle der Dotierung mit Übergangsmetallen auf die Sauerstoffentwicklungsaktivität und die Oberflächenrekonstruktion von Nickeloxid untersucht.

## Danksagung

An dieser Stelle möchte ich mich bei allen bedanken, die zum Erfolg dieser Arbeit beigetragen haben.

Zunächst danke ich Prof. Dr. Michael Wark, der es ermöglicht hat, meine Doktorarbeit am Deutschen Zentrum für Luft- und Raumfahrt (DLR) unter seiner Obhut zu verfassen. Ich danke ihm außerdem für den regelmäßigen Austausch und die wertvollen fachlichen Diskussionen.

Des Weiteren möchte ich Prof. Dr. Michael Bron danken für die Übernahme des Zweitgutachtens und die interessanten Gespräche auf den Konferenzen.

Dr. Corinna Harms möchte ich dafür danken, dass ich meine Doktorarbeit in ihrem Team im DLR in Oldenburg durchführen konnte. Dadurch wurden mir ausgezeichnete Rahmenbedingungen für meine Arbeit geboten.

Insbesondere möchte ich mich bei Dr. Julian Lorenz für seine wertvolle Expertise, den engen fachlichen Austausch sowie für das stetige Korrekturlesen bedanken, durch das er maßgeblich zur Entstehung dieser Arbeit beigetragen hat.

Ein besonderer Dank geht an meine Projektpartner, für die großartigen Diskussionen und die Bereitstellung der Katalysatormaterial. Insbesondere danke ich Dr. Dereje Hailu Taffa, dessen Erfahrung mir wesentlich dabei geholfen hat, mich in das Thema einzuarbeiten. Des Weiteren danke ich Prof. Dr. Ryan M. Richards, Dr. Darius Hayes und Dr. Elliot Brim für die enge Zusammenarbeit im Projekt und den warmen Empfang zu meinem Aufenthalt in Golden, Colorado.

Vielen herzlichen Dank für die fachlichen Diskussionen, den Austausch und diverse Messungen an Dr. Marcel Risch und Dr. Omeshwari Bisen für die maßgebliche Unterstützung bei der Beantragung, der Durchführung und der Auswertung der Synchrotron-Experimente.

Weiterhin bedanke ich mich bei Dr. Dulce Morales und Floris van Lieshout für die Ermöglichung von *in-situ* Raman-Experimenten in Groningen und bei der Unterstützung der Dateninterpretation.

Ich danke den Mitgliedern der Elektronen- und Lichtmikroskopie-Serviceeinheit sowie Jana Ewert für ICP-MS-Messungen.

Ich möchte mich bei allen Studierenden bedanken, darunter Jasmin Schmeling, Tom Eek und Nils Harder, für ihre großartige Unterstützung. Ein besonderer Dank gilt meinem

Masterstudierenden Nikhil Kadimi für seinen großartigen Beitrag zu den PTE-Halbzellmessungen.

Ein besonderes Dankeschön geht an mein wunderbares Kollegium. Ihr habt mich stets unterstützt und wertgeschätzt. Zunächst möchte ich meinen Bürokollegen Sebastian, Marek und Arne danken, für den regen Austausch und die gute Verpflegung. Weiterhin danke ich Claudia, Julia, Julia, Michael, Jana, Nadine und Imke.

Ich möchte mich bei Tanja für die gemeinsame Zeit bedanken, in der wir an unseren Doktorarbeiten gearbeitet haben, und die mir besonders Motivation geschenkt hat.

Schließlich gilt mein tiefster Dank für die Unterstützung in jeder Hinsicht während meines Studiums und meiner Promotion meinen wunderbaren Freunden, meiner Familie, meiner Partnerin Julia, ihrer Familie, und meinem Großvater Günther, dem ich diese Arbeit widme.

---

## List of Contents

<b>Abstract</b>	<b>1</b>
<b>Zusammenfassung</b>	<b>3</b>
<b>Danksagung</b>	<b>5</b>
<b>List of Contents</b>	<b>7</b>
<b>1 Introduction &amp; motivation</b>	<b>9</b>
<b>2 Fundamentals</b>	<b>12</b>
<b>2.1 Water electrolysis technologies</b>	<b>12</b>
<b>2.2 Electrocatalysis of the OER in alkaline media</b>	<b>18</b>
2.2.1 Electrocatalysts for the OER in alkaline media	20
2.2.2 Surface reconstruction of Ni-based OER catalysts	22
<b>2.3 Strategies to improve the OER performance of Ni-based pre-catalysts</b>	<b>25</b>
2.3.1 Faceted transition metal oxides as pre-catalysts	25
2.3.2 Mixed transition metal oxides to enhance Ni-based OER catalysts	26
2.3.3 <i>In-situ</i> incorporation of transition metals	27
<b>3 Key Techniques for electrocatalytic studies</b>	<b>30</b>
<b>3.1 Electrochemical characterization techniques to study the OER</b>	<b>30</b>
3.1.1 Rotating disc electrode as characterization platform for OER	30
3.1.2 Electrochemical impedance spectroscopy of OER electrocatalysts	32
3.1.3 Potentiodynamic and static electrochemical experiments for the OER characterization	34
3.1.4 Half-cell approaches towards application conditions	36
<b>3.2 Spectroscopic characterization of OER electrocatalysts</b>	<b>38</b>
3.2.1 XAS application for OER studies	38
3.2.2 Raman experiments for OER electrocatalytic studies	40
3.2.3 XPS for surface-sensitive investigations of OER catalysts	41
<b>4 Experimental details and tools</b>	<b>44</b>
<b>4.1 Catalyst synthesis</b>	<b>44</b>
4.1.1 Solvothermal synthesis of $\alpha$ -Ni(OH) <sub>2</sub>	44
4.1.2 Microwave-assisted synthesis of $\alpha$ -Ni(OH) <sub>2</sub>	44
4.1.3 Thermal annealing to receive faceted NiO	45
<b>4.2 Physical characterization of catalyst materials</b>	<b>45</b>
4.2.1 Supplementary structural characterization	45
4.2.2 Raman spectroscopy	46
4.2.3 Synchrotron based X-ray absorption spectroscopy	46
4.2.4 X-ray photoelectron spectroscopy	47
<b>4.3 Electrochemical characterization</b>	<b>48</b>
4.3.1 Preparation before rotating disc electrode testing	48
4.3.2 Electrochemical rotating disc electrode experiments	49
4.3.3 Porous transport electrode half-cell experiments	50
<b>4.4 Tools and software for data analysis</b>	<b>51</b>
<b>5 Results and discussion</b>	<b>52</b>
<b>5.1 OER performance of NiO(111) nanosheets from varied synthesis conditions</b>	<b>52</b>

5.1.1	<u>Structural characterisation of the NiO(111) nanosheets</u>	53
5.1.2	<u>Electrochemical trends as a function of the synthesis conditions</u>	56
5.1.3	<u>Summary of the variation of NiO(111) synthesis conditions</u>	59
<b>5.2</b>	<b><u>The influences of Co/Mn doping on NiO(111) nanosheets</u></b>	<b>60</b>
5.2.1	<u>Electrochemical trends as a function of the Co and Mn content</u>	60
5.2.2	<u>Spectroscopic analysis after electrochemical treatment</u>	69
5.2.3	<u>Summary of the effects of Co and Mn doping</u>	76
<b>5.3</b>	<b><u>Studying the introduction of Fe into Ni hydroxide and Oxide</u></b>	<b>78</b>
5.3.1	<u>Spectroscopic study of the Fe incorporation</u>	79
5.3.2	<u>Electrochemical trends after Fe incorporation</u>	86
5.3.3	<u><i>In-situ</i> and <i>ex-situ</i> characterisation of compounded Fe-incorporation</u>	92
5.3.4	<u>Summary of the Fe incorporation of Ni(OH)<sub>2</sub> and NiO(111)</u>	99
<b>5.4</b>	<b><u><i>In-situ</i> doping of Ni hydroxide and oxide electrocatalysts with Fe<sup>3+</sup></u></b>	<b>100</b>
5.4.1	<u>Electrochemical observations from Fe<sup>3+</sup> <i>in-situ</i> doping</u>	101
5.4.2	<u>Spectroscopic observations after <i>in-situ</i> Fe<sup>3+</sup> doping</u>	102
5.4.3	<u>Summary of the effect of Fe<sup>3+</sup> <i>in-situ</i> doping</u>	106
<b>5.5</b>	<b><u>Characterization of catalysts at application relevant conditions</u></b>	<b>107</b>
5.5.1	<u>Setup optimization by the example of the temperature variation</u>	107
5.5.2	<u>Electrochemical testing of Fe-containing Ni(OH)<sub>2</sub> and NiO(111)</u>	111
5.5.3	<u>Summary and limitations of the PTE setup</u>	113
<b>5.6</b>	<b><u>Considerations for reproducible electrochemical characterization</u></b>	<b>115</b>
5.6.1	<u>Reproducibility, repeatability and how they are affected by the catalyst processing</u>	115
5.6.2	<u>Influence of different electrochemical treatments on the catalysts</u>	120
5.6.3	<u>Importance of the sample storage for <i>ex-situ</i> experiments</u>	123
5.6.4	<u>Key learnings for future studies of OER electrocatalysts</u>	125
<b>6</b>	<b><u>Conclusion</u></b>	<b>129</b>
<b>7</b>	<b><u>Outlook</u></b>	<b>133</b>
<b>8</b>	<b><u>References</u></b>	<b>135</b>
	<b><u>Publications and contributions of the Author</u></b>	<b>151</b>
	<b><u>Publications in peer-reviewed journals</u></b>	<b>151</b>
	<b><u>Oral and poster presentations</u></b>	<b>152</b>
	<b><u>Appendix</u></b>	<b>153</b>
	<b><u>Supplementary material</u></b>	<b>153</b>
	<b><u>Synthesis and physical characterisation of NiO(111) nanosheets</u></b>	<b>154</b>
	<b><u>Synthesis and characterisation of Co and Mn doped catalysts</u></b>	<b>160</b>
	<b><u>Supplementary data of the characterisation of Fe doped hydroxides and oxides</u></b>	<b>165</b>
	<b><u>Supplementary data for the <i>in-situ</i> Fe incorporation</u></b>	<b>171</b>
	<b><u>Supplementary data of the implementation of the PTE setup</u></b>	<b>171</b>
	<b><u>List of abbreviations</u></b>	<b>174</b>
	<b><u>List of symbols</u></b>	<b>176</b>
	<b><u>Erklärung des bewerbers</u></b>	<b>177</b>
	<b><u>Curriculum vitae</u></b>	<b>178</b>

## 1 Introduction & motivation

H<sub>2</sub> produced by renewable energy has the potential to play an important role in the energy transition from mostly fossil energy sources towards renewable energies. As of 2025, the majority of H<sub>2</sub> is still produced through steam reforming of fossil natural gas, which should be substituted by water electrolysis (WE) to decarbonize the H<sub>2</sub> production.<sup>1</sup> Thereby, H<sub>2</sub> can be applied in multiple energy demanding sectors. Firstly, H<sub>2</sub> can be used to displace fossil fuels as energy carriers in transportation and residential applications.<sup>1,2</sup> This sector can be also decarbonized by electrification in many cases, unlike the following sectors. Secondly, H<sub>2</sub> can be a feedstock in industry e.g. for the direct reduced iron process, in oil refining, and in glass, ammonia and methanol production.<sup>2</sup> Thirdly, H<sub>2</sub> can be used for the long-term or seasonal storage.<sup>2,3</sup> During periods of high renewable energy production or when demand of electrical energy is low H<sub>2</sub> could be produced in a flexible operation by WE with fluctuating renewable energy. This concept is visualized for a duration of three days based on real data in Figure 1. Furthermore, the WE can be regulated down or off, when electrical energy production is low.

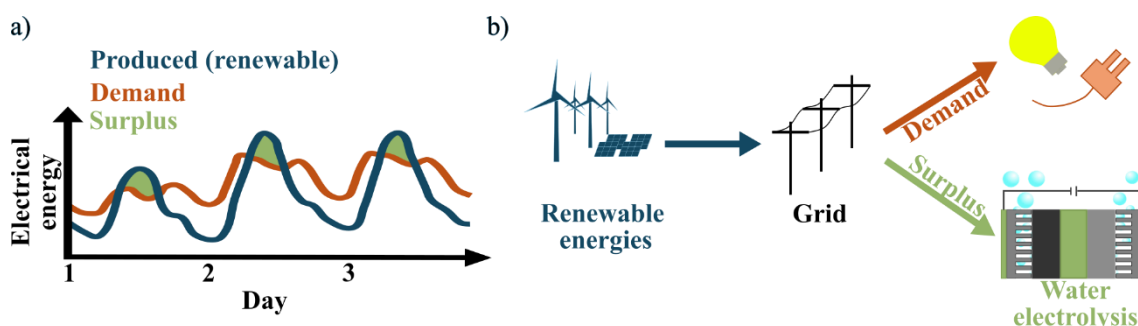


Figure 1: a) Simplified overlay of the electrical energy produced over three days from renewable energies, the total energy demand and the resulting surplus. Based on data from the Bundesnetzagentur.<sup>4</sup> b) Schematic of the energy usage from renewable energies.

To reduce carbon emissions in sectors that are otherwise challenging to decarbonize, it was proposed that a H<sub>2</sub> production up to 2.3 Gt per year is necessary.<sup>2</sup> This amount of H<sub>2</sub> production needs large amounts of production capabilities. The implementation of those large scale H<sub>2</sub> production capabilities could be limited by the availability of critical raw materials. Especially the proton exchange membrane water electrolysis (PEMWE) technology requires raw materials such as Iridium and Platinum.<sup>5</sup>

Consequently, suitable WE technologies should allow an operation at flexible loads over extended periods while using abundant raw materials. Anion exchange membrane water electrolysis (AEMWE) is a promising technology that meets these requirements.<sup>6</sup> However, the AEMWE technology needs further improvements in the aspects of the cell

---

performance, the durability of the membranes and the implementation of stable non-critical catalyst materials.<sup>6</sup>

For the AEMWE, the anode encompassing the oxygen evolution reaction (OER) is the primary source of overpotentials.<sup>6</sup> There are several challenges accompanied to the OER. One challenge is the highly oxidative conditions at the electrode during OER, which leads to dissolution of catalyst materials.<sup>7</sup> This dissolution processes make it difficult to balance activity and stability of the catalysts. Furthermore, OER catalysts have dynamic surface structures which make the design of the active catalysts challenging.<sup>7</sup> Because of the reconstruction occurring at OER conditions, the applied OER catalysts materials are called pre-catalysts before they transform into the active catalyst phase.

This thesis addresses the challenges of correlating the surface reconstruction of the pre-catalyst and to the OER activity. This will be done by applying a combination of rotating disc electrode (RDE) experiments and spectroscopic techniques. The characterization is focused on faceted rock salt NiO, specifically NiO(111), synthesized as a model pre-catalyst using a novel microwave (MW)-assisted route that significantly reduces the synthesis time. The well-defined structure of the faceted pre-catalyst enables detailed insights into the surface reconstruction by characterization before and after electrochemistry.

State of the art OER electrocatalysts often combine multiple metal oxides to obtain active OER electrocatalysts.<sup>8</sup> Therefore, the effect of Co, Mn and Fe incorporated into the NiO(111) host was studied. The surface reconstruction and the activity of the compounded materials was aligned. Furthermore, a comparison between the incorporation strategies of the compounded doping through synthesis and the Fe<sup>3+</sup> *in-situ* doping from the electrolyte.

RDE enabled fundamental electrochemical testing in this thesis. However, the RDE is not designed to resemble application-relevant conditions. To study catalyst performances closer to the application conditions, a customized half-cell setup will be established.

Furthermore, this thesis addresses the concerns of reproducibility in electrocatalytic studies. Important factors for the reproducibility of electrocatalytic experiments are discussed to be the catalyst coating,<sup>9</sup> electrolyte impurities<sup>10</sup> and the electrochemical conditioning of the catalyst.<sup>11</sup> Therefore, some factors influencing the reproducibility of OER studies are discussed for the NiO system. The effects are rated qualitatively, and practical recommendations are made for obtaining reproducible OER characterization by mitigating inconsistencies in reported data.

Overall, this thesis features multiple insights into how Ni-based catalysts transform during OER conditions and how the reconstruction is influenced by the addition of further transition metals. Furthermore, the study examines the widely held assumption that extensive reconstruction toward NiOOH is a prerequisite for achieving high OER activity.

## 2 Fundamentals

The following chapter introduces the background of AEMWE and thus the motivation for researching earth abundant catalysts for electrochemical water splitting in alkaline media. The chapter then narrows to the OER in alkaline media and nickel-based catalysts, which are central to this thesis. Finally, the rationale for investigating faceted NiO precursors and the consecutive surface reconstruction under OER conditions is presented.

### 2.1 Water electrolysis technologies

Electrolysis is a galvanic process that drives the non-spontaneous reaction of H<sub>2</sub>O into H<sub>2</sub> and O<sub>2</sub> by applying an electric current. The overall reaction of WE is given in Equation 1.



The WE consists of two spatially separate half-reactions. At the cathode, the **hydrogen evolution reaction (HER)** occurs. In alkaline media the HER consumes 4 e<sup>-</sup> and 4 H<sub>2</sub>O molecules to produce 2 H<sub>2</sub> Molecules and 4 OH<sup>-</sup> ions, as shown in Equation 2. The generated OH<sup>-</sup> ions migrate through the electrolyte and the e<sup>-</sup> are conducted through the electrical circuit from the anode. At the anode, the **OER** takes place, where 4 OH<sup>-</sup> ions are oxidized to form one equivalent of an O<sub>2</sub> Molecule, 2 H<sub>2</sub>O and to provide 4e<sup>-</sup> (Equation 3). In both half-reactions, H<sub>2</sub>O is participating, but it is ultimately consumed in the HER.



The standard electrode potentials  $E^0$  for the HER and the OER are 0 V vs. reversible hydrogen electrode (RHE) and 1.23 V vs. RHE under standard conditions, respectively. From these values, the equilibrium voltage for overall water splitting  $U_0$  can be calculated (Equation 4), which equals 1.23 V.

$$U^0 = \Delta E^0 = |E_{\text{Cathode}}^0 - E_{\text{Anode}}^0| = 1.23 \text{ V} \quad 4$$

In practice, a potential greater than  $U^0$  must be applied to drive the electrochemical conversion at measurable rates. Kinetic barriers and electrical resistances add to the thermodynamic required  $U_0$ , which results in the observation of an overpotential  $\eta$ . Only when sufficient  $\eta$  is applied, the electrochemical process can occur. The  $\eta$  is defined as

the difference between the applied electrode potential  $E(j)$  at a given current density  $j$  [ $\text{mA cm}^{-2}$ ], and the standard electrode potential  $E^0$  (Equation 5).

$$\eta = E(j) - E^0 \quad 5$$

For electrochemical water splitting, the total overpotential  $\eta_{WE}$  is the absolute difference between the overpotential at the cathode and the anode (equation 6). Figure 2 illustrates the overpotentials for HER and OER and the counter reactions of the ORR and the HOR. The large share of the  $\eta_{OER}$  to the  $\eta_{WE}$  is emphasized. In practice, the performance of a WE cell is evaluated at single-cell level, encompassing membrane resistances, the OER and the HER.<sup>6</sup> Details on the OER are discussed in Chapter 2.2.

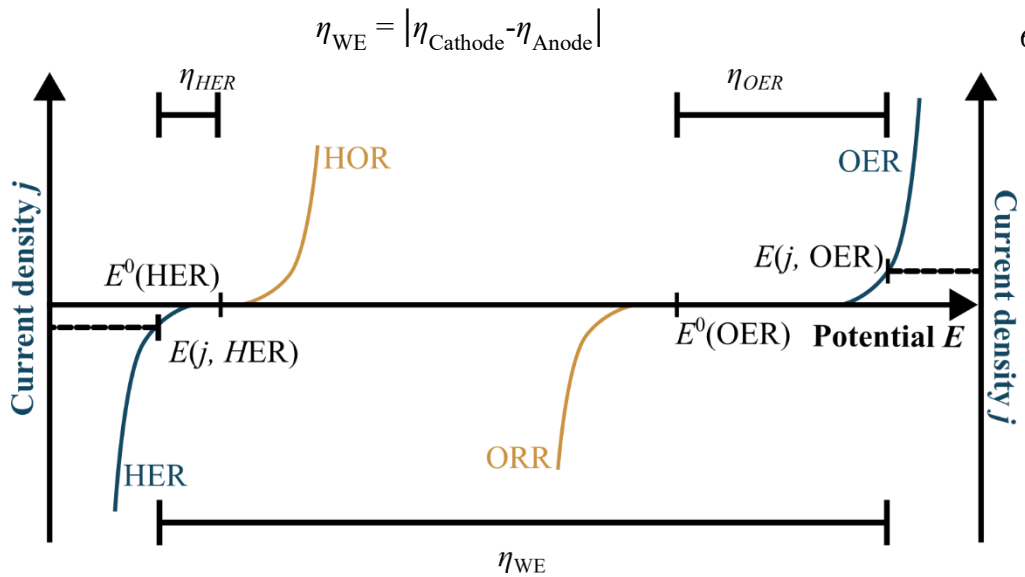


Figure 2: Representation of the overpotential for water electrolysis  $\eta(WE)$  including the OER(OER) and the Hydrogen evolution reaction (HER) as a plot of the Potential versus the current density. Furthermore, the counter reactions of the Oxygen reduction reaction (ORR) and the Hydrogen oxidation reaction (HOR), are shown.

Electrolysis can be viewed at several scales: at the plant level, an electrolysis system contains one or multiple electrolysis stacks together with the balance-of-plant components. Each stack contains several single cells connected by bipolar plates and sharing common inlets and outlets for reactants and product.

To compare the activity, stability and efficiency of electrolysis cells, different electrochemical metrics are employed.<sup>12</sup> The **activity** of an electrolysis cell is typically expressed as the geometric current density  $j_{geo}$ , and the overpotential  $\eta$ , required to reach a defined  $j_{geo}$ . Both values,  $j_{geo}$  and  $\eta$ , can be extracted from the polarization curves of the electrolyzer which are acquired by applying stepwise current densities and measuring the corresponding cell potential.<sup>12</sup> Conversely, the potential steps can be applied to measure the resulting current density.

The **stability** of an WE cell is characterized by monitoring either the  $\eta$  (chronopotentiometry) or the current density (chronoamperometry) over time. The stability is evaluated through long term testing (>1000h) or accelerated stress protocols, where reduced durations are used.<sup>13</sup>

The **efficiency** is usually measured as the faradaic efficiency, which describes the ratio between the experimentally measured amount of product (O<sub>2</sub> or H<sub>2</sub>) and the theoretical amount, derived from the integration of the chronoamperometric or chronopotentiometric data using Faraday's laws.<sup>12</sup> The efficiency can be reduced by side reactions at the electrolysis conditions like corrosion or by cross over of mostly H<sub>2</sub> gas through the separator.<sup>14</sup>

The metrics introduced above can be used to compare the different WE technologies, each of which has distinct characteristics, as summarized in Table 1. The most significant differences arise from the operation conditions, such as temperature and the type of electrolyte, which dictate the choice of anode and the cathode catalysts. These technologies also differ in the technology readiness level (TRL), which ranges from the proof of concept at TRL 1 to full-scale operational plants at TRL 9. In addition, the specific challenges associated with each technology are highlighted.

**Solid oxide electrolysis (SOE)** operates at high temperatures, which lowers the  $\eta$  for water splitting but increase requirements on the materials and hinder the load flexibility.<sup>15</sup> As a result, the SOE systems adapt only slowly to load changes.<sup>15</sup> Advantages of SOE are the relatively high efficiency and its bifunctional character as a solid oxide fuel cell or as an electrolyzer, and the electrolysis mode can process diverse feeds (e.g. steam and CO<sub>2</sub>).<sup>15</sup>

The **PEMWE** technology employs proton exchange membranes, typically made of perfluorinated alkyl polymers with sulfonic acid side chains.<sup>5</sup> These ionomers enable proton and water transport and create an acidic environment at up to 90°C and allowing operation at high current densities over a wide load range.<sup>5</sup> However, PEMWE technology requires scarce noble-metal catalysts and faces stability issues of parts in contact with the acidic environment.

Table 1: Overview of different WE technologies by comparison of several characteristics, such as the setup, operation conditions, the catalyst materials and some further application relevant metrics.

System	SOE	PEMWE	AWE
--------	-----	-------	-----

Set-up			
Electrolyte 1	O <sup>2-</sup> conducting Yttrium stabilized Zirconia and Gadolinium doped Ceria <sup>15</sup>	H <sup>+</sup> exchange membrane, perfluorinated alkyl polymers with sulfonic acid side chains, <sup>5</sup>	20–40 wt% NaOH and KOH electrolyte, diaphragm or anion exchange membrane separator between electrodes, <sup>14,16</sup>
Temperature	600-900°C	70-90°C	65-100°C
Anode 2	Anode (O <sub>2</sub> electrode) La <sub>1-x</sub> Sr <sub>x</sub> Co <sub>1-y</sub> Fe <sub>y</sub> O <sub>3</sub> and La <sub>1-x</sub> Sr <sub>x</sub> CoO <sub>3</sub> <sup>15</sup>	IrO <sub>x</sub> , ionomer binder, <sup>5</sup>	Ni, Fe-Ni alloys, Ni-Co alloys <sup>16</sup>
Cathode 3	Cathode (fuel electrode) Ni on Yttrium stabilized Zirconia and Gadolinium doped Ceria <sup>15</sup>	Platinum supported on Carbon, ionomer binder, <sup>5</sup>	Ni, Ni alloys, Ni-Mo alloys, <sup>16</sup>
Current density	0.26-0.9 A cm <sup>-2</sup> <sup>14,15</sup>	0.8-2 A cm <sup>-2</sup> <sup>5,14</sup>	0.2-0.6 A cm <sup>-2</sup> <sup>14,17</sup>
H <sub>2</sub> output pressure	<1 bar <sup>14</sup>	<80 bar <sup>5,14</sup>	<60 bar <sup>14</sup>
Flexibility	60 min cold start, 15 min warm start, cathode gas flexible (e.g. H <sub>2</sub> O and CO <sub>2</sub> ) <sup>14</sup> , bifunctional, <sup>15</sup>	15 min cold start, load adaptation in seconds, temporary operation at 160% load, <sup>14</sup> >2.5A cm <sup>2</sup> available, <sup>5,14</sup>	5-15 min cold start, min. load of > 20%, <sup>14,18</sup> designed for fixed load, <sup>16</sup>
TRL	TRL 4-6, <sup>14</sup> commercially available at kW scale, <sup>19,20</sup>	TRL 6-8, <sup>14</sup> commercially available at MW scale, <sup>21,22</sup>	TRL 9, <sup>14</sup> commercially available at MW scale, <sup>23,24</sup>
Research approaches	Sr segregation in anode, Ni migration in cathode, <sup>25</sup> proton conducting ceramics <sup>15</sup>	Fluorine free hydrocarbon ionomers and membranes, <sup>5,26</sup> Ir reduction at anode <sup>27-29</sup>	Gas crossover prevention, increased current densities, load flexibility <sup>16,17</sup>

**Alkaline water electrolysis (AWE)** is a mature technology, which uses liquid alkaline electrolyte in combination with a diaphragm or membrane to separate the reaction compartments.<sup>16</sup> AWE is easily scalable and relies on relatively low-cost. Its high TRL of 9 reflects decades of reliable operation under steady loads, dating back to the 1900s.<sup>16</sup> Nevertheless, conventional AWE designs are optimized for constant-load operation and are limited by low current densities and a poor tolerance to fluctuating load operation or even shutdown cycles.<sup>17</sup> The modern demands of a flexible operation with electricity from

renewable energies is not captured by the TRL classification. Thus, the flexible load operation of AWE systems is an open research question.

**AEMWE** combines the operational flexibility of PEMWE with the ability to employ abundant catalyst typical for AWE. This emerging technology will be further discussed in the following section and represents the target application of this thesis.

The configuration of an AEMWE is depicted in Figure 3a and closely resembles that of a PEMWE. A key difference is that the two reaction compartments of an AEMWE are separated by an anion exchange membrane (AEM). AEMs are typically polymers consisting of cationic groups along a polymer chain.<sup>6</sup> These groups enable the conductivity of  $\text{OH}^-$  ions through the membrane and within the catalyst layers.<sup>6</sup> Such ion-conducting polymers are generally referred to as ionomers. When casted as a membrane foil between the anode and the cathode, the AEM also acts as barrier against gas crossover.<sup>6</sup>

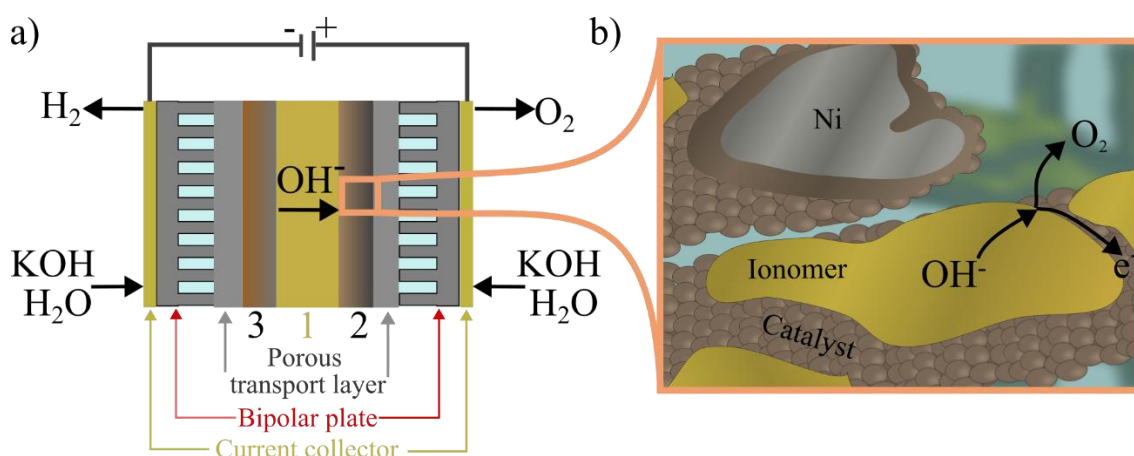


Figure 3: Schematic representation of an anion exchange membrane water electrolysis including the anion exchange membrane (1), the anode (2) and the cathode (3) with b) an enlarged view into the catalyst layer of the anode. The Ni-substrate is colored grey, the catalyst is colored in brown and the ionomer is colored in yellow. The simplified OER is depicted at an interface between ionomer, the catalyst and the liquid phase.

Ideally, AEMWE systems are fed with pure water, and ion conductivity is provided only by cationic groups of the ionomer both in the membrane and in the catalyst layers. In practice, however, dilute support electrolytes (e.g. 0.1-1 M KOH or  $\text{K}_2\text{CO}_3$ ) are often used to reduce ohmic losses.<sup>30-32</sup> Unlike in AWE, where ion transport is provided by concentrated alkaline solution.<sup>33</sup>

AEMWE is typically operated at temperatures between 50 and 80 °C<sup>14</sup> and at current densities of about 2 A cm<sup>-2</sup>.<sup>33</sup> It has also been reported to perform well under fluctuating load operation.<sup>34</sup> Another advantage over AWE, is that the membrane allows the production of pressurized  $\text{H}_2$ , with pressures expected to reach up to 70 bar.<sup>33</sup> Compared

to PEMWE, the main benefit of AEMWE is the possibility of operation without using scarce electrocatalysts materials.

Some AEMWE designs employ Pt/C as the cathode catalyst and self-supported IrO<sub>2</sub> as the anode catalyst, both materials coated on Ti foam substrates.<sup>14</sup> A recent study by Klingenhof et al.<sup>32</sup> demonstrated that the IrO<sub>2</sub> at the anode can be replaced by non-precious materials, such as Ni-Fe mixed hydroxides, while still achieving competitive current densities of >5 A cm<sup>-2</sup>. This performance was achieved by optimizing the Ni-Fe mixed hydroxide loading to 1 mg cm<sup>-2</sup>, avoiding limitations from poorly conductive hydroxide layers, and by employing catalyst coated membranes. For the cathode, Pt/C can be substituted with Ni-Mo alloys, which have been proven to be effective HER catalysts in alkaline media.<sup>6</sup>

However, his work focuses on the OER under alkaline conditions, as illustrated by the enlarged view of the anode catalyst layer in Figure 3b. This schematic is based on a scanning electron microscopy image of a catalyst coated Ni felt (Figure A1). The OER occurs at a three-phase boundary where (I) OH<sup>-</sup> ions are supplied by the ionically conductive electrolyte or ionomer binder, (II) electrons are transferred through the catalyst layer and (III) the oxygen is evolving. By this multistep, four-electron process with sluggish kinetics, the OER represents the principal source of  $\eta$  in AEMWE. Furthermore, the interface between the electrocatalyst and the ionomer binder is critical for AEMWE stability, because the combination of high pH and oxidative potential promotes oxidation of the ionomer at these interfaces, a degradation effect that is even more pronounced at neutral pH.<sup>30</sup>

To conclude, the AEMWE is a promising technology to meet the modern requirements of WE under fluctuating loads from renewable energy. Nevertheless, key challenges remain, including ionomer stability and the development of reliable electrocatalysts. This thesis addresses these challenges by advancing the understanding of Ni-based OER electrocatalysts in alkaline media.

## 2.2 Electrocatalysis of the OER in alkaline media

The OER was already described as a critical factor in the deployment of AEMWE above. Its significance for the AEMWE results from the high overpotentials of the OER and from the opportunity to replace scarce, precious-metal catalysts with earth-abundant transition metal catalysts. There is consensus in the literature, that the OER in alkaline media proceeds via a four-electron-four-proton electrocatalytic pathway.<sup>35-38</sup> According

to the Sabatier principle, the catalyst must bind the reaction intermediates neither too strongly nor too weakly, to achieve optimal catalytic activity.<sup>38</sup>

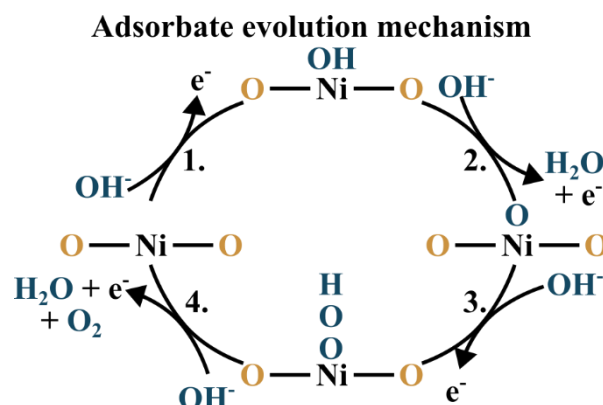


Figure 4: Schematic of the adsorbate evolution mechanism for the example of a NiO catalyst. Electrolyte oxygen is highlighted in blue whereas lattice oxygen is highlighted in yellow. Adapted from Grimaud et al.<sup>37</sup>

Two mechanisms have been proposed to describe the OER on transition-metal oxides. In the adsorbate evolution mechanism (Figure 4), oxygen atoms are introduced through adsorption of  $\text{OH}^-$  onto the metal active sites. Subsequent deprotonation produces an oxo species, followed by O-O bond formation due to reaction with an additional  $\text{OH}^-$  from the electrolyte. Finally,  $\text{O}_2$  is released through another deprotonation, and the active site is regenerated.<sup>37</sup>

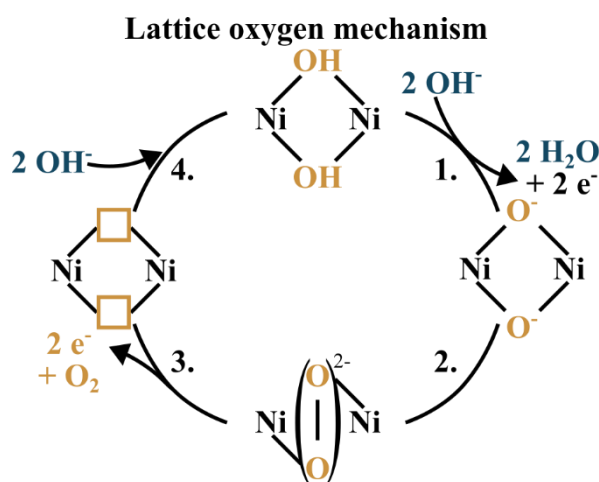


Figure 5: Schematic of the lattice oxygen mechanism for the example of a NiO catalyst. Electrolyte oxygen is highlighted in blue whereas lattice oxygen is highlighted in brown. Adapted from Grimaud et al.<sup>37</sup>

The second proposed pathway is the lattice oxygen mechanism (Figure 5), which involves the direct participation of oxygen atoms from the catalyst lattice.<sup>37</sup> In this mechanism, two neighboring lattice hydroxide groups are initially deprotonated, after which an O-O bond forms between the lattice oxygen species. These oxygens are then released as  $\text{O}_2$  accompanied by charge transfer from the catalyst. The resulting vacancies

in the lattice undergo follow up adsorption of OH<sup>-</sup> ions, thereby restarting the catalytic cycle.<sup>37</sup>

A recent study of electrodeposited NiFeO<sub>x</sub>H<sub>y</sub> reported a modified lattice oxygen mechanism, providing spectroscopic evidence that lattice oxygen participates in the reaction, an aspect not accounted for in the classical adsorbate evolution mechanism.<sup>35</sup> Thus, a partial lattice oxygen mechanism was suggested, indicating that lattice oxygen is not inert but actively involved in redox processes during the OER.<sup>35</sup> However, the detailed reaction pathway remains difficult to resolve and may vary depending on the nature of the active catalytic site.

Identifying the active catalytic sites in OER is a key challenge electrocatalysis, as the surface structure of catalyst materials strongly depends on reaction conditions such as temperature, pH and the applied potential. Consequently, the materials employed in AEMWE electrodes prior to electrochemical treatment are often referred to as **pre-catalysts**, reflecting surface transformation that will occur under OER conditions.<sup>39</sup> The following sections first introduce various pre-catalysts materials that are considered for OER applications. Building on this, the surface reconstruction of pre-catalysts under OER conditions is discussed.

### 2.2.1 Electrocatalysts for the OER in alkaline media

Over the past decades, a wide range of materials has been investigated for water electrolysis and particularly for the OER. Already in 1947, Hickling and Hill studied variety of electrodeposited electrode materials including Ag, Pt, Pd, Pb, Cd, Fe, Co, Ni, and Cu films for the OER.<sup>40</sup> They reported substantial differences in the overpotential required to reach a current density of 1 A cm<sup>-2</sup>, with the lowest overpotential value of 0.61 V observed for Co.<sup>40</sup> Today, studies on catalyst thin films or powders are typically complimented by structural characterization, enabling the derivation of structure-property relationships.<sup>39</sup>

The first material class considered here is the family of **rock salt** metal oxides, among which CoO and NiO are frequently investigated for OER applications. The compounds are present in a face-centered cubic structure, with metal cations alternating with anions in the lattice. In NiO, O<sup>2-</sup> anions alternated with Ni<sup>2+</sup> cations (Figure 6a). NiO is notable for its morphological flexibility, that allows the synthesis of materials with well-defined crystallographic facets.<sup>41-43</sup> In this work, the tuneability of NiO is exploited to prepare NiO(111), rock salt NiO with predominant exposure of the (111) via wet chemical

synthesis of nanosheets.<sup>41,42</sup> Rock salt oxides also enable mixing different transition metal oxides to enhance the OER activity.<sup>8,44</sup> However, mixing of transition metal oxides will be discussed in chapter 2.3.2 more detailed. In this thesis, the well-defined surface of NiO(111) is used as a model system for fundamental studies, combining spectroscopic and electrochemical techniques to investigate the effects of transition-metal doping and surface reconstruction on the OER activity.

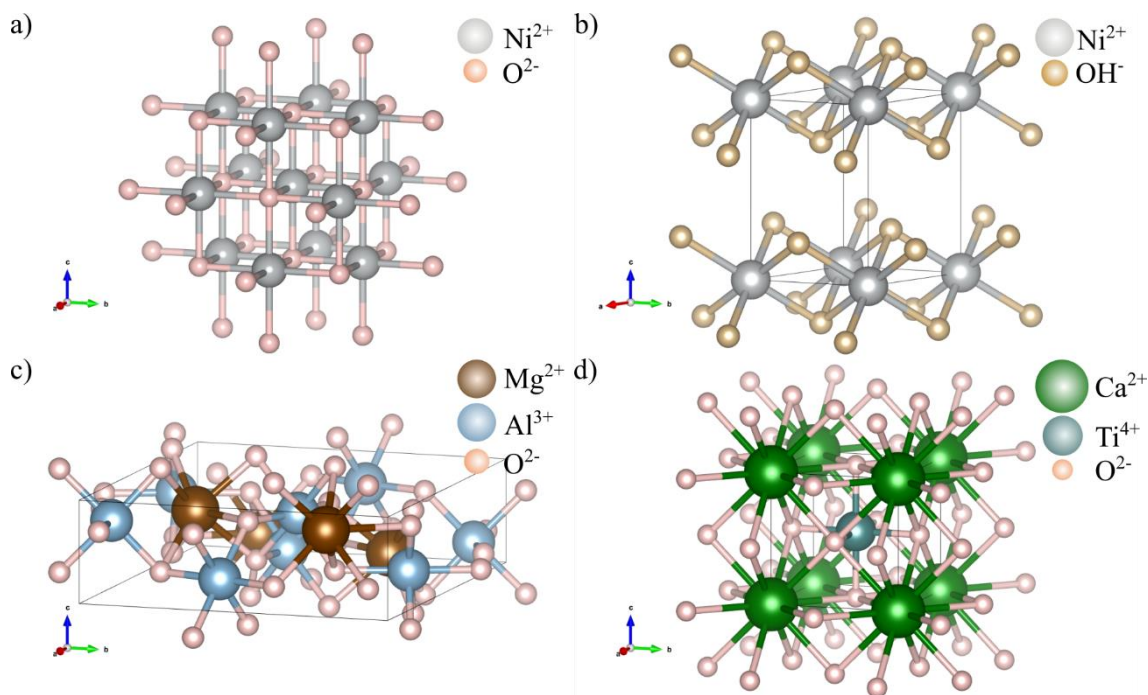


Figure 6: Crystal structures important for OER catalysis. a) Rock salt NiO, b) layered double hydroxide  $\beta$ -Ni(OH)<sub>2</sub> c) Spinel MgAl<sub>2</sub>O<sub>4</sub> and d) Perovskite CaTiO<sub>3</sub> are drawn with Vesta.<sup>45</sup> The structures were drawn from crystallography open data base entries 1010093, 1011134, 9010260 and 1567490.<sup>46</sup>

The next material class discussed is **the layered double hydroxide (LDH)** structure. The LDH are considered thermodynamically stable phases of Ni in alkaline electrolyte, and often form spontaneously on the surface after immersion of the pre-catalysts.<sup>47,48</sup> For Ni-based systems, the LDH phase can occur as  $\beta$ -Ni(OH)<sub>2</sub> (Figure 6a), a stacked structure adopting the brucite-type lattice of Mg(OH)<sub>2</sub>.<sup>48,49</sup> In this structure, edge-sharing MO<sub>6</sub> octahedra form two-dimensional layers with the composition Ni<sup>2+</sup>(OH)<sub>2</sub>, partially substituted by Ni<sup>3+</sup> cations introducing positive charges. The  $\alpha$ -Ni(OH)<sub>2</sub> has similar layer arrangement but contains intercalated water molecules between the sheets.<sup>48</sup> Upon oxidation,  $\beta$ -Ni(OH)<sub>2</sub> and  $\alpha$ -Ni(OH)<sub>2</sub> yield  $\beta$ -NiOOH and  $\gamma$ -NiOOH, respectively. The Ni<sup>3+</sup>OOH also adopts a brucite-like structure but contain one fewer proton per Ni and a

higher oxidation state ( $\text{Ni}^{3+}$ ).<sup>50</sup> Depending on the electrochemical treatment or synthetic route, mixtures of hydroxide and oxyhydroxide phases are typically obtained.<sup>49,51</sup>

**Spinel oxides** represent another important class of OER catalysts. The general formula of spinel oxides is  $\text{AB}_2\text{O}_4$ , derived from the  $\text{MgAl}_2\text{O}_4$  structure, in which  $\text{A}^{2+}$  cations occupy the tetrahedral sites and  $\text{B}^{3+}$  cations occupy octahedral sites (Figure 6c).<sup>39</sup> The spinel lattice readily incorporates different cations in either site, allowing tuning of redox properties, consequently enhancing activity and stability toward the OER.<sup>39</sup> Among spinel oxides,  $\text{Co}_3\text{O}_4$  and the  $\text{NiFe}_2\text{O}_4$  are extensively investigated for oxygen evolution catalysis.<sup>39,52,53</sup>

Another material class studied for OER applications are **Perovskites**, which adopt the general the formula  $\text{ABO}_3$ , derived from the  $\text{CaTiO}_3$  structure, in which alkaline-earth metals occupy the A-site and transition metals occupy the B-site (Figure 6d).<sup>54</sup> Former studies aimed to optimize the catalyst by tuning the occupancy of  $e_g$  molecular orbitals and increasing the oxygen stoichiometry at the B-site, to enhance the OER activity of the catalysts. Using this approach,  $\text{Ba}_{0.5}\text{Sr}_{0.5}\text{Co}_{0.8}\text{Fe}_{0.2}\text{O}_{3-\delta}$  was reported to exhibit intrinsic OER activities exceeding those of benchmark  $\text{IrO}_x$  catalysts.<sup>55</sup> However, subsequent investigations revealed that such perovskites undergo surface transformation under OER conditions, forming  $\text{Co}(\text{Fe})\text{O}_x\text{H}_y$  species that serve as the actual active phase.<sup>56</sup>

Beyond the crystalline phases discussed above, amorphous transition metal oxides have also been reported to exhibit promising OER activities.<sup>57</sup> However, their structural disorder complicated understanding of the surface phenomena. Furthermore, precious-metal oxides such as  $\text{IrO}_x$  and  $\text{RuO}_x$  are among the most efficient OER catalysts,<sup>8</sup> but the present work focuses primarily on non-precious transition-metal systems.

Unifying all the aspects of the material classes discussed is the surface reconstruction those pre-catalysts undergo once immersed in electrolyte and applied to anodic potentials. These transformations strongly influence the formation of the catalytically active phase.

### 2.2.2 Surface reconstruction of Ni-based OER catalysts

The following section presents the surface phenomena occurring on Ni-based electrodes after immersing in alkaline electrolyte and throughout the OER electrocatalysis. The discussion is based on the duplex layer proposed by Burke and O'Sullivan<sup>47</sup>, which describes metal/oxide/electrolyte interfaces on metals. Originally developed for Ir electrodes in acidic media, the model consists of three layers: the metallic

bulk, a anhydrous (compact) oxide layer and a hydrous oxide layer.<sup>47</sup> Key processes transferred to the *in-situ* reconstruction of NiO are illustrated in Figure 7.

The first process is the **Ni(OH)<sub>2</sub> formation** on the catalyst surface. This hydroxide may already be partially formed due to adventitious humidity or because of dispersion during the preparation. Ni(OH)<sub>2</sub> is also the thermodynamically stable form of Ni at open-circuit potential and at pH values above 9.<sup>58</sup> Considering the Pourbaix diagram of Ni, at a pH of 14 and potential below the OER, Ni(OH)<sub>2</sub> and Ni(OH)<sub>3</sub><sup>-</sup> are thermodynamically favored.<sup>58</sup> For this reason it is suggested to allow the electrode to equilibrate in the electrolyte before the starting electrochemical measurements.<sup>59</sup>

When the potential is raised above ~1.6 V vs. RHE, OER conditions are reached. For Ni-based catalyst, the **redox transition** from Ni<sup>II</sup>(OH)<sub>2</sub> towards Ni<sup>III</sup>OOH begins at 1.35 V vs. RHE.<sup>60–62</sup> This oxidation occurs at surface sites that are electronically accessible. Thus, the oxidation state may differ from anticipated Ni<sup>II</sup> and Ni<sup>III</sup> states of the redox transition and can depend on oxygen stoichiometry and treatment of the pre-catalyst.<sup>63</sup> Consequently, operando techniques are essential to study the oxidation state of Ni-based catalysts during electrochemical operation.<sup>3</sup>

Studies using X-ray absorption spectroscopy (XAS) and surface enhanced Raman spectroscopy studies have shown some Ni centers can exceed the +III state reaching average oxidation states of +3.7 and identifying Ni<sup>IV</sup> species (Ni<sup>IV</sup>OO<sup>-</sup>).<sup>63,64</sup> The extent and rate of surface reconstruction also depend on the nature of pre-catalyst and activation protocols (e.g. Ni(OH)<sub>2</sub>, NiS > NiO > Ni).<sup>65</sup>

Similar surface reconstruction has also been observed for other oxides, such as Co<sub>3</sub>O<sub>4</sub>, where the reversibility of the surface reconstruction under OER conditions exceptional.<sup>52,66</sup>

Another process rigorously investigated for Ni-based catalysts is the **dissolution** with subsequent **redeposition** of cations during the OER, forming a dynamically stable surface layer.<sup>7</sup> This phenomenon is discussed in detail in Chapter 2.3.3.

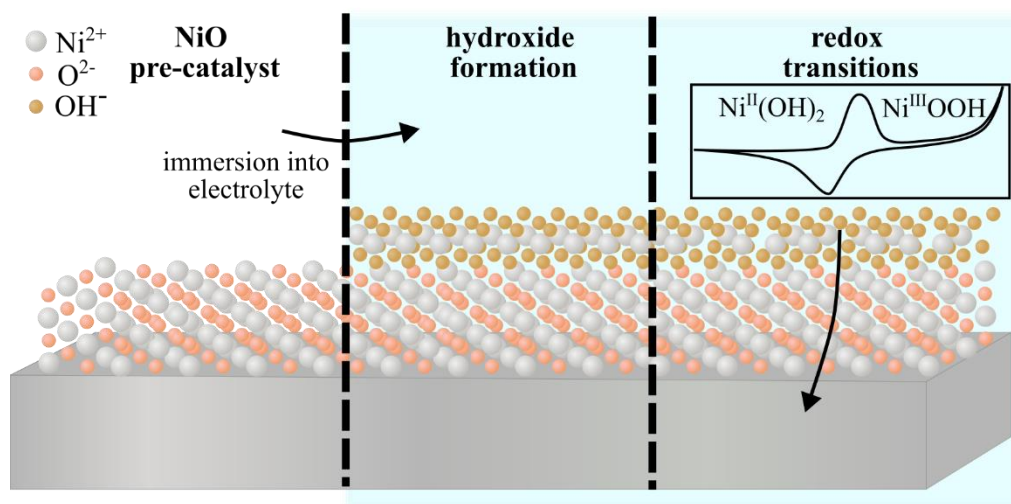


Figure 7: Schematic representation of reconstruction processes for the example of a NiO pre-catalyst at anodic conditions. Modified from He et al.<sup>39</sup>

Finally, the surface reconstruction may also depend on the electrolyte composition, including parameters such as pH and the containing cations (e.g.  $\text{K}^+$ ,  $\text{Na}^+$ ,  $\text{Li}^+$ ).<sup>39,67,68</sup> However, reported trends remain inconsistent, as different studies describe contrasting effects of alkali-metal cations on the apparent OER activity.<sup>39</sup> This variability indicates that electrolyte composition is not a crucial factor. Rather, parameters such as the choice of pre-catalyst and deposition of Fe from the electrolyte, likely play a more dominant role on the surface reconstruction and the effect on the OER activity.

To conclude, this chapter outlined the main reconstruction phenomena using NiO-based pre-catalysts as an example. In particular, the link between surface transformations and catalyst activity is central.<sup>39</sup> Equally important are insights into how the formation of electrocatalytically active phase can be promoted.<sup>39</sup> For advancing this understanding of the surface reconstruction, *operando*, *in-situ* and *ex-situ* techniques are essential.<sup>39</sup> Building on these insights, the next section will focus on current strategies for improving Ni-based electrocatalysts for the OER.

### 2.3 Strategies to improve the OER performance of Ni-based pre-catalysts

Building on the preceding discussion of OER electrocatalysis, the following chapter introduces strategies to enhance the activity of Ni-based pre-catalysts in alkaline media. In experiments, the apparent activity refers to the measured current (typically geometric current density ( $j_{\text{geo}}$ ) at a given  $\eta$ ) and reflects both the number of accessible active sites and the intrinsic activity of the accessible sites.<sup>69,70</sup> One route to higher apparent activity is to increase the population of accessible sites, by raising the catalyst loading or maximizing the specific surface area.<sup>70</sup> A complementary route is to improve the intrinsic activity of individual sites through controlled faceting, compositional tuning, or electronic modification.<sup>70</sup> Moreover, strategies that primarily increase the number of active sites may be limited by mass- or charge-transport constraints.<sup>70</sup>

Thus, the next sections examine the influence of faceting, the implementation of transition-metal mixing, and the *in-situ* incorporation of transition-metal cations from the electrolyte. Strategies primarily for improving the intrinsic activity of OER catalysts.

#### 2.3.1 Faceted transition metal oxides as pre-catalysts

The first approach to improve understanding of Ni-based OER electrocatalysts is through surface faceting. Faceted surfaces can be obtained either by preferential thin-film growth, for example by pulsed laser deposition,<sup>71</sup> or by wet-chemical routes employing structure-directing agents.<sup>41</sup> Because the chemical and electronic properties of transition-metal oxides depend strongly on surface atom arrangements, facet control offers a promising tool to tune activity.

For instance, Fungerling *et al.*<sup>71</sup> investigated pulsed-laser-deposited LaNiO<sub>3</sub> films with (001), (110), and (111) orientations and demonstrated that the observed activity trends correlate with the compatibility of the initial facet with the reconstructed NiOOH formed under OER conditions.

The study by Poulain *et al.*<sup>72</sup> demonstrated that the OER activity of reactively sputtered NiO thin films as pre-catalysts strongly depends on the preferential crystal facet. The OER activity trend was NiO(110) > NiO(111) > NiO(100), which was explained by a more favorable formation of  $\beta$ -NiOOH phase whereas the other orientations favor  $\gamma$ -NiOOH.

It thus demonstrates that facet-dependent surface transformation critically influences the activity of faceted transition metal oxides as pre-catalysts.

For NiO, powdered material with the predominant (111) plane is available by solvothermal (ST) synthesis.<sup>41</sup> Scanning electrochemical microscopy revealed that the edges of NiO(111) nanosheets exhibit multifold higher OER activity than basal planes.<sup>73</sup>

In NiO, the three most frequently studied facets are (100), (110), and (111).<sup>73–75</sup> The (100) plane is nonpolar, exposing equal numbers of Ni<sup>2+</sup> and O<sup>2-</sup>,<sup>74</sup> while the (110) surface is also nonpolar but features alternating cation and anion rows.<sup>75</sup> By contrast, the (111) plane is polar, composed of alternating single-ion layers, and in NiO it is typically oxygen-terminated, creating an electron-rich surface.<sup>73,76</sup> Kim et al.<sup>77</sup> showed that both morphology and faceting impact OER activity of NiO, attributing higher performance of (110) planes to greater surface concentrations of Ni<sup>III</sup>. Their work further highlighted that morphology and faceting can outweigh surface area, with hexagonal shaped particles displaying enhanced activity due to increased Ni<sup>III</sup> density.

Beyond ST synthesis, molten-salt routes have been employed to obtain NiO particles with various predominant facets, including (100) and (111).<sup>43,78</sup> However, NiO(100) prepared in this way exhibited lower OER activity compared to (111)-oriented nanosheets obtained via wet-chemical synthesis.<sup>78</sup> These results indicate that synthetic method and morphology interact with complex surface processes such as reconstruction, making it difficult to attribute activity solely to pre-catalyst faceting. Despite the challenges in producing directly comparable faceted NiO materials, NiO(111) nanosheets provide a well-defined model system for fundamental investigations in this thesis.

### 2.3.2 Mixed transition metal oxides to enhance Ni-based OER catalysts

The incorporation of different transition metals into a single pre-catalyst represents a widely employed strategy to improve OER performance. Such mixing can optimize catalyst characteristics, including adsorption energies, electrical conductivity, and stability.<sup>8</sup> These improvements could originate from changes in the electronic structure of the catalyst due to mixing, which is strongly influenced by the oxidation states of the metals and oxygen.

Two primary effects are typically considered to result from mixing of different catalyst materials.<sup>8</sup> One is the ligand effect, arising from charge transfer between neighboring metal cations via shared oxygen anions, alter the surface electronic structure by adjusting the electron-donating ability of the active sites.<sup>8</sup> The other is the strain effect, introduced when the lattice parameters of the host and the dopant differ, influence orbital overlap and thereby modify the electronic structure.<sup>8</sup> Since these effects are difficult to isolate in

practice, especially at low dopant levels, empirical screening of mixed-metal systems remains the dominant approach.

Among the possible dopants, Fe has emerged as the most influential in Ni- and Co-based host structures.<sup>44,58,79</sup> Bucci et al.<sup>44</sup> demonstrated that solution-combustion-synthesized NiO-based catalysts exhibited optimal activity at 40% Fe incorporation, whereas Co and Mn dopants provided only minor improvements. Their findings suggested that the primary role of dopants is to enhance the conversion affinity toward the catalytically active NiOOH phase.<sup>44</sup> Similarly, ST synthesis in tert-butanol has enabled unusually high Fe incorporation (up to 20%) into bimetallic NiO nanoparticles, again yielding marked activity improvements.<sup>80,81</sup>

Further approaches are the integration of multiple metals into one catalyst material.<sup>8</sup> Zhai et al.<sup>82</sup> reported a multi-metal perovskite  $\text{Sr}_{0.1}\text{La}_{0.9}\text{Co}_{0.5}\text{Ni}_{0.5}\text{O}_3$ , that was designed for pure water fed AEMWE.

Beyond intrinsic activity, electrical conductivity is a decisive factor for scaling electrocatalysts from thin-film tests to device-level AEMWE applications.<sup>83</sup> While  $\text{NiFeO}_x\text{H}_y$  materials consistently achieve high performance in three-electrode measurements, their relatively poor conductivity limits their competitiveness compared to more conductive oxides in membrane-electrode assemblies.<sup>83</sup> A way to mitigate the poor conductivity of  $\text{NiFeO}_x\text{H}_y$  is to incorporate Fe only on the active catalyst surface by Fe from the electrolyte. This concept will be discussed in the following section.

### 2.3.3 *In-situ* incorporation of transition metals

One of the most established concepts in Ni-based OER catalysis is the beneficial effect of Fe incorporation from the electrolyte. Numerous studies have shown that even trace Fe impurities in alkaline media dramatically enhance the apparent OER activity of Ni-based electrodes.<sup>10,84,85</sup> The conception of *in-situ* incorporation is visualized for the example of  $\text{Fe}^{3+}$  *in-situ* doping compared to the mixed synthesis in Figure 8.

This concept has been extended beyond NiO and  $\text{Ni}(\text{OH})_2$  to more complex materials, such as Ni-based perovskites. For example, spiking  $\text{Fe}^{3+}$  into the electrolyte during OER on  $\text{LaNiO}_3$  and  $\text{La}_2\text{NiO}_4$  pre-catalysts led to strong activity enhancements accompanied by the formation of surface  $\text{NiFeO}_x\text{H}_y$  phases.<sup>86</sup> The combination of a metallicly conductive  $\text{LaNiO}_3$  bulk with a reconstructed  $\text{NiFeO}_x\text{H}_y$  surface could be a promising approach for large-scale electrolysis. In a related strategy, perovskites were designed to combine both high intrinsic conductivity and beneficial surface reconstruction, as

demonstrated for  $\text{Sr}_{0.1}\text{La}_{0.9}\text{Co}_{0.5}\text{Ni}_{0.5}\text{O}_3$ , which delivered competitive performance in pure-water-fed AEMWE cells.<sup>82</sup> The effect was attributed to Sr leaching, which triggered reconstruction, and Co substitution, which stabilized the conductive bulk structure.<sup>82</sup>

A broader study by Mattinen and Schröder et al.<sup>65</sup> showed that a wide range of Ni-based precursors, when exposed to Fe-containing KOH and electrochemical conditioning, transform into  $\text{NiFeO}_x\text{H}_y$ . The transformation rate, however, depends strongly on the choice of pre-catalyst. Consistently, Fe from electrolyte impurities deposits onto  $\text{NiO}_x\text{H}_y$  and drives the high OER activity observed in these systems.<sup>10,84</sup> At the same time, Fe is known to dissolve from electrodes at OER potentials, and in many cases redeposition occurs, establishing a dynamic equilibrium between **dissolution and redeposition**. Under controlled conditions, this results in dynamically stabilized active sites.<sup>7</sup> This concept is visualized in Figure 8, which visualizes a NiO from the mixed synthesis, in which Fe is part of the bulk material, with the dissolution/redeposition mechanism.

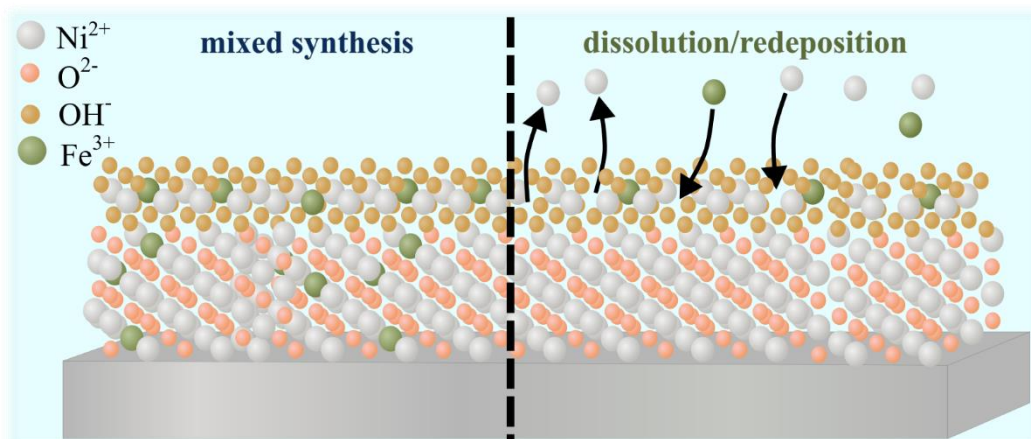


Figure 8: Schematic of the mixed synthesis and the dissolution/redeposition mechanism after *in-situ*  $\text{Fe}^{3+}$  doping.

The extent of Fe uptake depends not only on the pre-catalyst composition but also on experimental parameters such as Fe concentration in the electrolyte and the applied current density.<sup>7</sup> Interestingly, Fe incorporation also affects the kinetics of surface reconstruction. Incorporation of Fe into materials such as  $\text{Ni}(\text{OH})_2$ ,  $\text{NiS}_x$ , Ni, and NiO slows down the transformation into  $\text{NiOOH}$  but still enhances apparent OER activity.<sup>65</sup>

Furthermore, the reconstruction and Fe uptake are highly sensitive to the electrochemical protocol. Son et al.<sup>87</sup> showed that cyclic voltammetry (CV) induces a greater degree of surface reconstruction and Fe incorporation compared to chronopotentiometry for Ni, NiSe/FTO, and NiSe/Ni electrodes.

To elucidate the influence of Fe to the  $\text{NiFeO}_x\text{H}_y$ , *in-situ* XAS studies have demonstrated that Fe plays a direct role in OER catalysis.<sup>88</sup> At OER potentials, Fe centers undergo a change in coordination that may stabilize critical O–O bond formation steps. This observation is consistent with earlier reports that Fe remains in the +III oxidation state during OER,<sup>62,64</sup> yet provides a mechanistic explanation for how Fe contributes to the catalytic process without further oxidation.

Current research directions aim to integrate *in-situ* Fe incorporation with other improvement strategies. Key factors include the selection of the pre-catalyst, controlled electrolyte spiking, optimization of surface reconstruction, and ensuring sufficient electrical conductivity, all while maintaining system stability.

In this study, the  $\text{Fe}^{3+}$  *in-situ* doping is analyzed specially on its effect on the surface reconstruction and the resulting OER activity of the well-defined NiO(111) model system.

### 3 Key techniques for electrocatalytic studies

Electrocatalysts can be investigated from multiple complementary perspectives. This chapter will introduce key techniques to characterize electrocatalysts electrochemically and physically. Electrochemical methods are applied not only to determine catalytic activity metrics but also to provide indirect insights into structural changes and dynamic processes under reaction conditions.

Physical characterization, on the other hand, can be carried out at different stages of testing: on pristine materials to establish the structural and morphological features of the pre-catalyst, *operando* during OER operation, *in-situ* under controlled conditions comparable to OER testing, and *ex-situ* outside the electrochemical environment. The *ex-situ* characterization covers both pristine analysis and analyses after tested.

The presented techniques will provide the foundation for investigating the surface reconstruction and aligning it with the activity of Ni-based electrocatalysts at alkaline OER conditions.

#### 3.1 Electrochemical characterization techniques to study the OER

In the following, the electrochemical characterization techniques applied in this work are introduced. The chapter begins with fundamental methods for probing catalytic activity and mechanistic features, followed by techniques designed to more closely mimic application-relevant operating conditions.

##### 3.1.1 Rotating disc electrode as characterization platform for OER

The RDE setup consists of a flat disc electrode embedded in an insulating shroud, typically made of hydrophobic poly tetrafluoroethylene (Figure 9a). When the electrode is rotated, a well-defined hydrodynamic flow is generated, leading to uniform and quantifiable mass transport under diffusion-limited conditions. As a result, voltammograms with temporally stable diffusion layers can be recorded.<sup>89</sup> Historically, the first reports using the RDE technique focused on the oxygen reduction reaction (ORR).<sup>90</sup> The RDE concept was later extended by introducing a concentric ring-shaped electrode surrounding the disc, enabling the detection of reaction products or intermediates generated at the disc electrode. This configuration, known as the rotating ring–disc electrode (RRDE), allows product analysis at the ring with a geometry-dependent collection efficiency.<sup>90,91</sup>

For OER studies, electrocatalysts are typically drop-cast or otherwise deposited onto the disc electrode (Figure 9a). Reported catalyst loadings range from 0.005 to 0.8 mg cm<sup>-2</sup>, with ~0.1 mg cm<sup>-2</sup> being most common for RDE experiments.<sup>53,69,92</sup> OER catalysts are usually characterized in RDE mode by recording only the disc current, a practice widely accepted given their high selectivity toward oxygen evolution. In contrast, for reactions such as the ORR, Faradaic efficiencies can fall below 90%.<sup>69</sup> However, certain catalysts have been shown to undergo dissolution under oxidative potentials.<sup>93</sup> In such cases, RRDE collector experiments provide valuable insight by distinguishing between dissolved catalyst species from O<sub>2</sub>. For instance, in studies of LiMn<sub>2</sub>O<sub>4</sub>, dissolved Mn species were detected at the ring by reduction at ~1.2 V vs. RHE, while O<sub>2</sub> reduction occurred at ~0.4 V vs. RHE.<sup>93</sup>

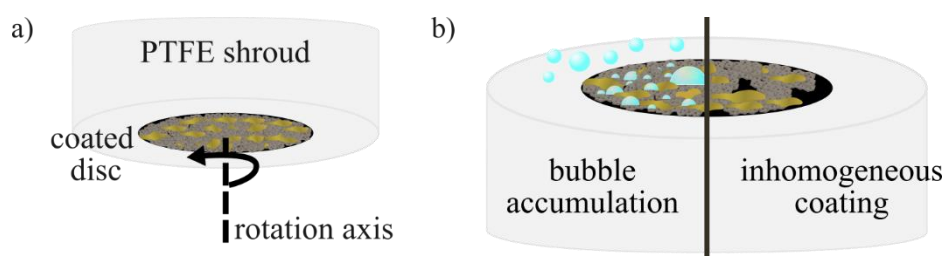


Figure 9: Schematic representations of a) a rotating disc electrode (RDE) with a coating consisting of catalyst particles and ionomer. b) Visualization of common limitations for RDE measurements of OER with the examples of bubble accumulation and inhomogeneous coatings.

For reliable OER studies with the RDE setup, thin and uniform catalyst layers are essential to ensure well-defined mass transport.<sup>69</sup> Conductive carbon supports are sometimes employed to improve conductivity during activity measurements, but their susceptibility to corrosion introduces uncertainty. Consequently, OER characterization is usually performed without carbon supports.<sup>69</sup> Despite its utility, the RDE technique has several limitations. The most critical are reproducibility issues and bubble formation during OER (Figure 9b).<sup>9,94</sup> Poor reproducibility is often linked to experimental errors, particularly non-uniform catalyst coatings on the disc electrode.<sup>9</sup> Both, the bubble accumulation and an inhomogeneous coating are represented in Figure 9b.

Bubble accumulation is especially problematic at high current densities and during static testing. Oxygen bubbles tend to adhere to the catalyst surface, leading to increased ohmic resistance and a loss of electrochemically active surface area.<sup>94</sup> Both micro- and nanobubbles may remain attached to the electrode surface, unaffected by electrode rotation.<sup>95</sup> Their removal is hindered by buoyancy in conventional RDE geometries and by the hydrophobicity of many catalyst materials.<sup>96</sup> Consequently, gas bubble coverage

introduces additional resistances during measurements.<sup>95</sup> Strategies to mitigate bubble accumulation include horn sonication of the electrolyte<sup>94</sup> or inverted RDE configurations that exploit bubble buoyancy,<sup>96</sup> though both approaches can be challenging in practice. A further limitation for long-term stability testing is the corrosion of the glassy carbon (GC) substrate, which passivates under OER conditions.<sup>96</sup>

These challenges can be partially addressed by optimizing catalyst coatings and referencing results against commercial benchmark catalysts to ensure reproducibility across laboratories. Despite its limitations, the RDE remains an indispensable tool due to its well-defined mass transport, low material requirements, and modest demands on instrumentation. It is therefore widely used for initial catalyst screening and benchmarking.

A typical RDE experiment combines several electrochemical techniques. First, the ohmic resistance of the electrolyte is determined, usually by electrochemical impedance spectroscopy (EIS). The electrode is then conditioned by CV or by holding a defined potential/current density to activate the catalyst. Finally, catalytic activity is evaluated using potentiodynamic, potentiostatic, or galvanostatic methods, as discussed in the following sections.

In this thesis, the RDE was employed as a primary screening tool to compare the activity of Ni-based catalysts under well-defined mass-transport conditions, while requiring only small amounts of material. The controlled hydrodynamics and reproducibility of RDE data provided a reliable basis for evaluating trends in catalyst activity before advancing to more application-relevant testing methods.

### **3.1.2 Electrochemical impedance spectroscopy of OER electrocatalysts**

Electrochemical impedance spectroscopy (EIS) probes the frequency-dependent response of an electrochemical system to a sinusoidal excitation.<sup>97</sup> Depending on the application, either a sinusoidal potential or current is applied under steady-state conditions such as open-circuit potential (OCP) or at a fixed bias.<sup>97</sup> The frequency is swept over several orders of magnitude (mHz to MHz) to differentiate processes with varying time constants.<sup>97</sup> The resulting impedance spectrum is commonly analyzed using electrical equivalent circuit models consisting of resistors, capacitors, and inductors, or more complex elements when required.<sup>97</sup> Thereby, the choice of the equivalent circuit model should always be physically justified. EIS data are often presented in Nyquist plots, with the real component  $Z'$  (resistance) plotted against the imaginary component  $Z''$

(reactance), or in Bode magnitude and phase plots, where  $\log(|Z|)$  and the phase angle are plotted versus  $\log(\text{frequency})$ . Examples of both are shown in Figure 10a.

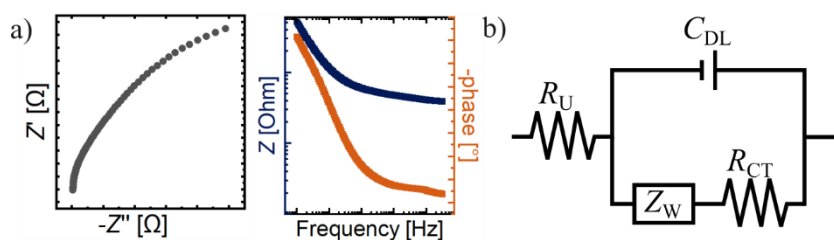


Figure 10: a) Representative EIS data in Nyquist (left) and Bode (right) formats. b) Equivalent circuit of the Randles cell.

In electrocatalysis, EIS is commonly measured at OCP to extract the high-frequency resistance. This uncompensated resistance ( $R_u$ ) arises from the electrolyte, electrical connections, and internal electrode resistances.<sup>97</sup>  $R_u$  is typically determined from the x-axis intercept ( $Z'$ , where  $Z'' = 0$ ) of the Nyquist plot, or from  $|Z|$  at the lowest measured phase angle in the Bode plot.<sup>69</sup> More accurate determination can be achieved by fitting the data with an equivalent circuit model that reflects the specific electrochemical configuration.<sup>69</sup> The most widely used model is the Randles cell (Figure 10b), in which  $R_u$  is represented by a resistor, the double-layer capacitance ( $C_{DL}$ ) by a capacitor, and the charge-transfer resistance ( $R_{CT}$ ) by a second resistor.<sup>69,97</sup> In addition, the Warburg impedance ( $Z_W$ ) accounts for mass transport of redox species to the electrode surface.<sup>97</sup>

Beyond such fundamental characterization, advanced EIS studies have been used to probe catalyst behavior under OER conditions. For example, Watzele et al.<sup>98</sup> proposed the estimation of the electrochemically active surface area (ECSA) at OER potentials by attributing EIS-derived pseudo capacitance to surface adsorbates. The ECSA is an important measure to convert the apparent electrode activity to an intrinsic catalyst activity. Therefore, the measurement of the ECSA is of interest in electrocatalysis research.

In particular, Watzele et al.<sup>98</sup> proposed an equivalent circuit that includes  $R_u$ ,  $C_{DL}$ ,  $R_{CT}$ , adsorption capacitance ( $C_{Ads}$ ), and adsorption resistance ( $R_{ads}$ ). In contrast, Farhoosh et al.<sup>99</sup> showed that, for  $\text{CoO}_x$ , the dominant capacitance at OER bias comes from bulk redox pseudo capacitance instead, enabling analysis of characteristic time constants such as the potential-dependent OER turnover frequency.<sup>99</sup> Additionally, transmission line models have been employed to describe porous electrodes.<sup>100</sup>

Together, these examples highlight the versatility of EIS as a diagnostic tool, extending its role from simple resistance determination to mechanistic evaluation of OER catalysts.

At the same time, the complexity of EIS data makes it prone to overinterpretation when models lack a clear physical basis. In this thesis, EIS was employed primarily to determine the  $R_u$  for reliable correction with the product of current and  $R_u$  ( $iR$ ) of activity data.

### 3.1.3 Potentiodynamic and static electrochemical experiments for the OER characterization

**Potentiodynamic** techniques such as CV and linear sweep voltammetry (LSV) are widely used to both condition electrocatalysts and determine their OER activity. In both techniques, the electrode potential is swept at a defined scan rate ( $v$ ). LSV applies to a unidirectional sweep, whereas CV alternates between forward and reverse scans, thereby probing both oxidation and reduction processes. CV is particularly valuable for assessing the reversibility of redox transitions and for tracking changes across successive cycles.<sup>101</sup> An example of a CV of a NiO electrode with the signal for the characteristic Ni<sup>II</sup>/Ni<sup>III</sup> redox couple and the OER onset is shown in Figure 11a.

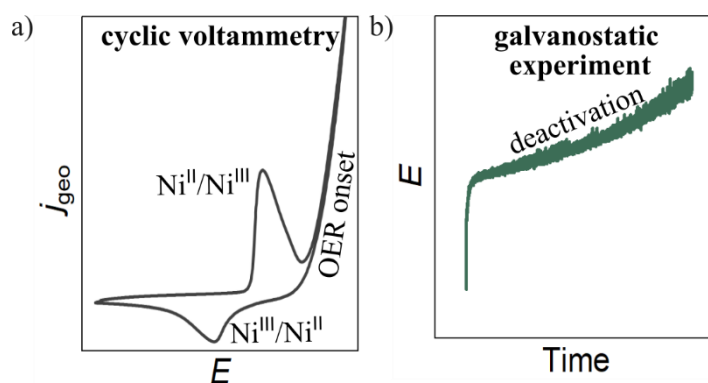


Figure 11: Examples of RDE experiments conducted with a glassy carbon electrode coated with NiO. a) Represents a CV with the characteristic Ni<sup>II</sup>/Ni<sup>III</sup> redox signal. b) Representation of a galvanostatic experiment at OER conditions, showing deactivation likely induced from bubble accumulation.

Activation of Ni-based catalysts is typically achieved by conditioning in a potential window around the Ni<sup>II</sup>(OH)<sub>2</sub>/Ni<sup>III</sup>OOH transition. Positive-going sweeps were reported to promote the growth of active NiO<sub>x</sub>H<sub>y</sub> species, while negative-going sweeps support the reorganization of oxy-cation species.<sup>11,87,102</sup> This reconstruction increases the number of oxidized sites and facilitates ion incorporation into the hydrous oxide layer, as discussed in Chapter 2.2.2.<sup>11</sup>

Conditioning protocols were reported to strongly influence the results for OER activity characterization. A comparative study has shown that scan rate, potential window, number of cycles, electrolyte concentration, and temperature are critical parameters

influencing the OER activity.<sup>11</sup> Fast CV scans ( $>100 \text{ mV s}^{-1}$ ) over wide potential windows accelerate activation within short times ( $\sim 30 \text{ min}$ ), whereas slow scans ( $10 \text{ mV s}^{-1}$ ) are more effective when the number of cycles is fixed.<sup>11</sup> Overall, CV conditioning generally induces stronger reconstruction than potentiostatic or galvanostatic protocols.<sup>11,85,87</sup> Still, the optimal method depends on the pre-catalyst: for instance,  $\text{Ni}_{70}\text{Fe}_{30}$  alloys benefit from CV activation, while NiSe films have shown higher OER activity after chronopotentiometry.

The OER activity is typically reported as an  $\eta$  to reach a defined current density (e.g.,  $10 \text{ mA cm}^{-2}$ ) or as the current density  $j$  obtained at a fixed potential (e.g.,  $1.55 \text{ V vs. RHE}$ ), with iR-correction applied.<sup>69</sup> In this thesis, usually the  $\eta$  will be reported as OER metric, acquired at a  $j_{\text{geo}} = 10 \text{ mA cm}^{-2}$  if not otherwise stated.

For flat, low-porosity RDE films, normalization of current density to the geometric electrode area is acceptable. In contrast, for high-surface-area oxides, neither physisorption nor ECSA methods provide fully reliable values because surface reconstruction during operation alters the accessible surface area.<sup>103</sup> A common approach to approximate the ECSA is to determine the  $C_{\text{DL}}$ . This can be done either by EIS or by CV, exploiting the linear relationship between the capacitive charging current ( $i_{\text{C}}$ ) and the  $\nu$  (Equation 8).<sup>104</sup>

$$i_{\text{C}} = \nu C_{\text{DL}} \quad 7$$

In practice, multiple CVs are recorded at varying  $\nu$  in a narrow potential window (typically  $\pm 50 \text{ mV}$  around the open-circuit potential, OCP),<sup>104</sup> where faradaic processes are negligible and the current is assumed to arise solely from double-layer charging.  $C_{\text{DL}}$  is then obtained from the slope of  $i_{\text{C}}$  versus  $\nu$ .<sup>104</sup> Due to the non-ideal behavior of catalyst materials, allometric fit of  $i_{\text{C}}$  vs.  $\nu$  with the Equation 9 can be applied, where the exponent  $\alpha$  describes the deviation from ideality ( $\alpha = 1$  corresponds to an ideal capacitor).<sup>105</sup>

$$i_{\text{C}} = \nu C_{\text{DL}}^{\alpha} \quad 8$$

Another metric for the ECSA is the integral of characteristic redox peaks.<sup>103</sup> The integral of the  $\text{Ni}^{\text{II}}(\text{OH})_2 / \text{Ni}^{\text{III}}\text{OOH}$  redox peak charge can be interpreted as an indication of the presence of electrochemically accessible Ni centers and is thus a parameter related to the surface area.<sup>103</sup> While ECSA-normalized metrics can provide useful comparative insights, best-practice guidelines emphasize the need to report multiple activity metrics with appropriate statistical deviations, and to benchmark the catalysts against commercial reference catalysts for transparent evaluation.<sup>69,106,107</sup>

**Static** methods such as galvanostatic and potentiostatic measurements are advantageous for activity determination because they minimize capacitive contributions that complicate the interpretation CV as an activity measure. However, in RDE setups, galvanostatic OER testing is hampered by bubble accumulation, which was already discussed more detailed in Chapter 3.1.1. For the example in Figure 11b bubble accumulation might explain the characteristic potential drift and the experimental noise observed.<sup>94,95</sup> Some strategies, such as electrolyte sonication, can improve bubble detachment and heat/mass transport,<sup>108</sup> but are rarely applicable for catalyst screening.

In summary, potentiodynamic and static techniques provide complementary means of conditioning and evaluating OER catalyst activities. The conditioning strategy should be chosen according to the research objective, and activity should be reported using multiple, transparent metrics referenced against commercial benchmarks. At the same time, limitations such as bubble accumulation, surface reconstruction, and normalization challenges highlight the need to complement them with more application-relevant methods. For this reason, these RDE based CV and galvanostatic holds were employed in this thesis as a first step to assess the activity of Ni-based catalysts. Later, an advanced half-cell setup was implemented.

### 3.1.4 Half-cell approaches towards application conditions

Single-cell experiments provide a closer approximation to AEMWE stacks than RDE testing, even though they lack certain complexities present at the stack level, such as heat management, current distribution, and mass transport effects.<sup>6</sup> The half-cell approach presented in this Chapter is designed to meet the conditions of an AEMWE, presented in Chapter 2.1. These conditions are temperatures up to ~80 °C, current densities exceeding 1 A cm<sup>-2</sup>, and membrane-separated reaction compartments. While operation with pure water feed is the ideal, state-of-the-art systems still commonly employ diluted KOH as supporting electrolyte.<sup>31</sup>

To study electrocatalysts under conditions approaching those of single-cell AEMWE, modified half-cell setups have been developed. In fuel-cell research, gas diffusion electrodes are commonly used for half-cell testing.<sup>109</sup> More recently, this strategy has been extended to electrolysis by mimicking the porous transport electrodes (PTE) of electrolysis cells.<sup>110</sup> For PEMWE applications, temperatures of 60 °C, current densities of 1.4 A cm<sup>-2</sup> and realistic catalyst layer architectures were realized. This respective PTE half-cell approach by Geuß et al.<sup>110</sup> is represented in Figure 12a. The PTE half-cell

approach combines some advantages of RDE and single-cell testing. For instance, half-cell setups enable more precise potential control by decoupling the working electrode from the counter electrode, while reducing the number of parameters that affect performance compared to single-cell testing.<sup>109</sup> They also require less complex and less costly equipment than single-cell experiments, which facilitates inter-laboratory comparability.<sup>109</sup>

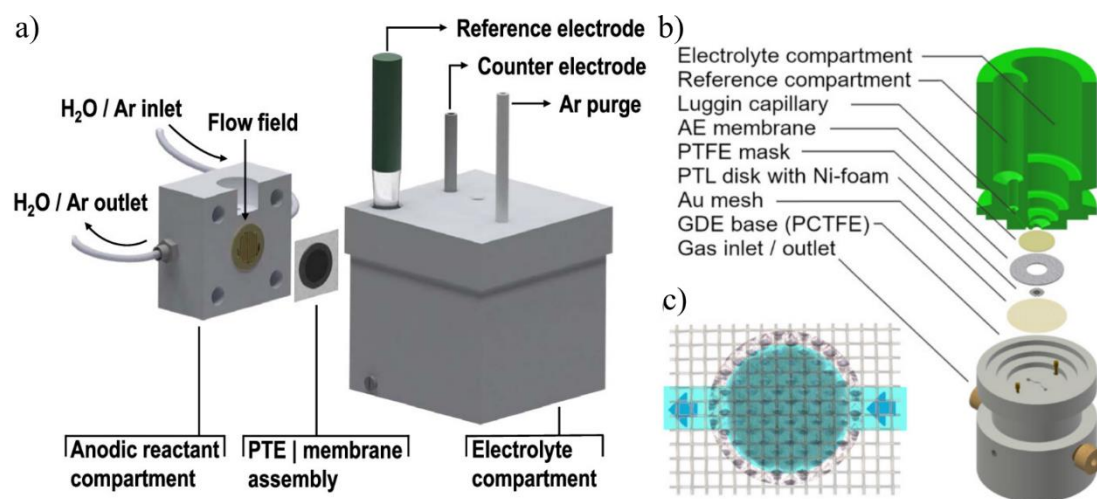


Figure 12: Half-cell approaches that were reported in the literature. a) Represents a medium area cell Reproduced from Geuß et al.<sup>110</sup> b) Represents the small geometric area flow cell and c) a closeup of the electrode geometry. Reproduced from Berner et al.<sup>111</sup>

Another advantage is the compatibility of half-cell setups with online product characterization and with operando or *in-situ* methods, as reported for studying  $\text{NiFeO}_x\text{H}_y$  OER catalysts.<sup>88</sup> Importantly, they also allow reproduction of critical AEMWE operating conditions. For these reasons, half-cell methods represent a promising intermediate step for characterizing catalysts under conditions relevant to device operation.

Recent studies have already demonstrated the use of PTE-type half-cells for OER in acidic electrolytes and, more recently, in alkaline media.<sup>110–112</sup> An example of a setup for tests in alkaline media is depicted in Figure 12b. These works highlight the suitability of half-cell approaches to bridge laboratory catalyst screening with device-relevant testing. In this thesis, a PTE-based half-cell setup was employed to approximate AEMWE operating conditions. This enabled characterization of the investigated materials at high current densities and elevated temperatures under realistic mass transport conditions, particularly in the absence of a dedicated single-cell test bench.

## 3.2 Spectroscopic characterization of OER electrocatalysts

This chapter introduces the spectroscopic techniques applied to complement the electrochemical experiments. XAS is first discussed as a bulk-sensitive method to probe oxidation states and local coordination environments. Raman spectroscopy, employed as the only *in-situ* technique available in this work, provides vibrational signals of surface phases, also under electrochemical conditions. Finally, X-ray photoelectron spectroscopy (XPS) is presented as a surface-sensitive tool to analyze chemical composition and electronic states. For XAS and XPS, insights are drawn primarily from *ex-situ* experiments, enabling structural and electronic characterization of the pre- and post-catalyst materials. Together, these spectroscopic methods provide complementary perspectives that, when combined with electrochemical data, enable understanding of how transition-metal doping, and Fe-surface incorporation influence the reconstruction and activity of the model Ni-based OER catalysts.

### 3.2.1 XAS application for OER studies

In X-ray absorption spectroscopy (XAS), the absorption of high-energy photons excites core-level electrons (e.g., from K or L shells), leaving a hole.<sup>113</sup> The principle mechanisms happening during XAS are depicted in Figure 13a. The resulting relaxation processes generate secondary electrons, which can be detected either through transmitted intensity, electron yield, or fluorescence yield.<sup>114</sup> The incident photon energy is tuned using a monochromator, typically at a synchrotron source that provides high photon flux across a wide energy range.<sup>113</sup> Because of the high attenuation length of X-rays, XAS is considered a bulk-sensitive technique, though for high-surface-area materials a large fraction of the signal can originate from surface sites.<sup>115</sup>

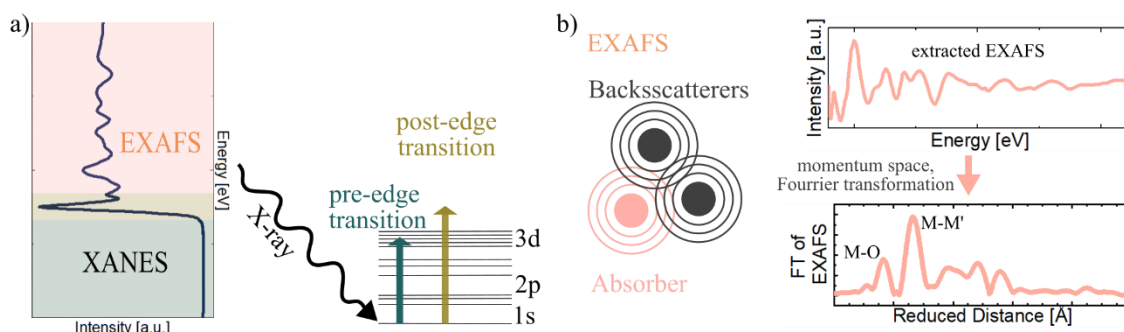


Figure 13: a) Schematic representation of the X-ray absorption process and the resulting pre-edge and post-edge signals. For visualization, the energy scale is aligned with the diagram. b) Visualization of the EXAFS process, spectra extraction and signal representation.

XAS spectra are divided into two main regions: the X-ray absorption near-edge structure (XANES) and the extended X-ray absorption fine structure (EXAFS).<sup>114</sup> The XANES region includes the pre-edge and edge features, which are sensitive to oxidation state and coordination environment. The absorption edge typically shifts to higher energies with increasing oxidation state, though bond lengths and local coordination also influence the edge position, requiring comparison to suitable reference compounds.<sup>113</sup> The EXAFS region arises from the interference of the ejected photoelectrons with backscattered waves from neighboring atoms (Figure 13b). Fourier transformation of the EXAFS oscillations yields radial distribution information, from which interatomic distances and coordination numbers can be extracted by fitting against structural models.<sup>113</sup> In transition-metal oxides, strong EXAFS peaks are typically observed at the metal–oxygen (M–O) and nearest-neighbor metal–metal (M–M') distances.<sup>113</sup>

In this work, XAS is used to complement macroscopic electrochemical studies with atomistic information on oxidation states and local coordination. *Ex-situ* measurements enable comparison of pristine and post-electrocatalysis samples, revealing irreversible changes induced by electrochemical treatment, storage, or electrode preparation.<sup>114</sup> Importantly, XAS is also applicable to amorphous phases, where conventional diffraction methods fail, provided that the surface transformation is sufficiently thick or the surface area is high.

*In-situ* and *operando* XAS have greatly advanced the mechanistic understanding of OER electrocatalysts by tracking dynamic oxidation state and coordination changes under reaction conditions.<sup>114</sup> For instance, Mefford and Akbashev et al.<sup>116</sup> employed scanning transmission X-ray microscopy at the Co L-edge to follow the oxidation of individual  $\beta$ -Co(OH)<sub>2</sub> particles from Co<sup>II</sup> to Co<sup>III</sup>. Similarly, *in-situ* XAS has also been applied to NiFeO<sub>x</sub>H<sub>y</sub>, where changes in Fe coordination at OER potentials were detected.<sup>62,64,88</sup> These studies demonstrate how XAS can resolve oxidation states and local geometries under realistic catalytic conditions, highlighting its value for probing the active state of mixed-metal catalysts.

In this thesis, *ex-situ* measurements at the Ni K-edge are emphasized, with additional Co, Mn, and Fe K-edge studies. While pre-edge features were generally weak, the post-edge and EXAFS regions provided characteristic fingerprints of the materials, allowing the interpretation of irreversible structural changes after electrochemical operation.

### 3.2.2 Raman experiments for OER electrocatalytic studies

Raman spectroscopy has become an important tool in electrocatalyst research, aided by the development of versatile laser sources, highly sensitive detectors, and dedicated *in-situ* and *operando* cells.<sup>117</sup> These advances have partially mitigated inherent limitations of the technique, including the risk of sample damage under intense laser irradiation, interference from fluorescence, and the intrinsically weak Raman scattering cross section.<sup>117</sup>

The Raman effect arises from inelastic scattering of visible light, in which incident photons excite an electronic state that relaxes into a higher (Stokes scattering) or lower (anti-Stokes scattering) vibrational state (Figure 14).<sup>117</sup> The far more intense elastic Rayleigh scattering is typically suppressed using a notch filter tuned to the excitation wavelength.<sup>117</sup>

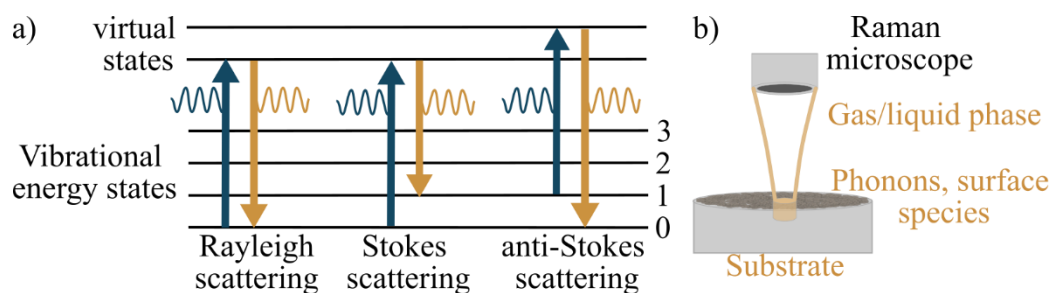


Figure 14: a) Raman scattering processes induced by incident light (blue), emitting Raman scattering (yellow). b) Example of a heterogenous sample of which multiple contents are probed.

The effective penetration depth depends strongly on the excitation wavelength, the optical absorption of the material, and the instrumental configuration.<sup>117</sup> Because Raman intensities depend on multiple experimental factors such as temperature, pressure, electrolyte composition, and excitation wavelength, quantitative analysis is challenging.<sup>117</sup>

Nevertheless, the technique is highly valuable for qualitative insights. The surface sensitivity can be dramatically enhanced using surface-enhanced Raman spectroscopy,<sup>118</sup> whereas conventional Raman spectroscopy probes contributions from the surrounding gas or liquid phase, the substrate, the catalyst surface, and the catalyst bulk. A representative sample for this study is visualized in Figure 14b. Conventional Raman experiments allow qualitative comparison of samples under the same conditions and possibly comparisons of pristine samples to electrochemically treated samples *ex-situ*.

For catalyst characterization, Raman spectroscopy is frequently applied to compare pristine and electrochemically treated samples *ex-situ*, offering information on

crystallinity and structural transformations. For example,  $\alpha$ - and  $\beta$ -Ni(OH)<sub>2</sub> phases can be distinguished by their characteristic bands,<sup>49,51</sup> while two-magnon peaks in NiO intensify with increasing annealing temperature, reflecting changes in crystallinity.<sup>119</sup>

Beyond *ex-situ* studies, *in-situ* and operando Raman spectroscopy provide dynamic insights into catalytic processes. For instance, *in-situ* Raman has enabled direct observation of  $\gamma$ -NiOOH formation during OER in Ni–Fe mixed catalysts, with Fe content influencing the relative  $\gamma$ -NiOOH peak intensities.<sup>120</sup> More advanced *in-situ* SERS studies on well-defined NiO thin films have even provided evidence for transient high-valent species such as Ni<sup>IV</sup>OO<sup>-</sup> as potential active intermediates.<sup>63</sup>

In this thesis, Raman spectroscopy was primarily applied *ex-situ* to pristine samples to assess the crystallinity of Ni-based catalysts. In selected cases, *in-situ* Raman was used to monitor the formation of oxyhydroxide species under OER conditions, providing complementary insights into the surface reconstruction of the catalysts.

#### 3.2.3 XPS for surface-sensitive investigations of OER catalysts

XPS is a surface-sensitive technique that probes material depths of up to ~10 nm.<sup>121</sup> This makes it highly valuable in electrocatalysis, as catalytic reactions are confined to the interfaces between catalyst and reactant.<sup>122</sup> The fundamental process of XPS is depicted in Figure 15a. XPS is based on the photoelectric effect, which describes that X-ray photons excite electrons from atomic core levels, ejecting them with kinetic energy  $E_K$ .<sup>121</sup> The measured kinetic energy relates to the binding energy  $E_B$  according to Equation 9 including the Plank's constant  $h$ , the photon wavelength  $V$  and the spectrometer constant  $\phi$ .<sup>121</sup>

$$E_B = hV - E_K - \phi \quad 9$$

Lab-based XPS typically uses X-ray tubes with Mg or Al K $\alpha$  sources due to their sharp emission lines. Synchrotron radiation, on the other hand, provides higher intensity, tunable photon energies, and superior resolution. Spin-orbit coupling further splits p, d, and f orbitals into doublets, producing a characteristic spectral fine structure. The resulting peak intensities depend on atomic sensitivity factors and the inelastic mean free path of electrons, allowing quantitative determination of surface composition.

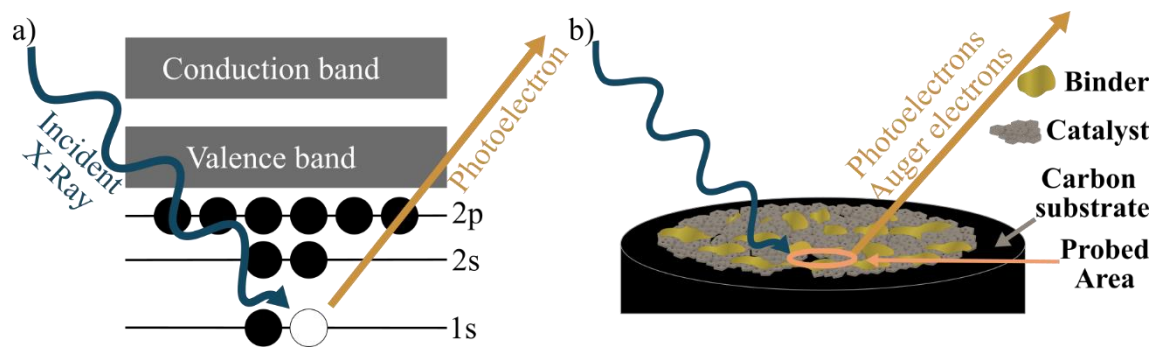


Figure 15: a) Illustration of the principle of XPS with emission of a photoelectron by X-ray radiation. b) Schematic of a heterogeneous sample representative of a coated Rotating Disc Electrode.

A practical challenge in XPS is surface charging because positive charge accumulates when electrons are emitted leading to peak shifts. Charge compensation (e.g. by electron flood gun) is usually applied, but energy calibration is still required.<sup>122</sup> The most common reference is the adventitious C 1s peak at 284.8 eV, though this assignment is debated.<sup>122,123</sup> Figure 15b illustrates a heterogeneous sample, which is representative for coated RDE discs tested in this thesis. In heterogeneous samples containing catalyst, substrate, and ionomer binder, differential charging can complicate charge referencing and thus the interpretation of binding energy shifts.

For electrocatalysts, the O 1s and transition-metal 2p regions are particularly informative. Therefore, Biesinger et al.<sup>124,125</sup> provided several reference studies for the interpretation of transition-metal XPS spectra. For Ni-based systems, the following binding energies are of interest.

For the O 1s spectra, lattice oxygen is expected at ~529 eV, while higher binding energy components (~531 eV) are attributed to hydroxyl species, oxygen near defects, or adsorbed water.<sup>123</sup> The ratio between oxide- and hydroxide-related signals can reveal irreversible transformations, such as conversion of oxides into hydroxides during electrochemical operation.<sup>63</sup> Moreover, higher valent oxyhydroxides can be observed after electrochemical oxidation of Ni(OH)<sub>2</sub> films by additional O 1s signals, but undergo partial decomposition into hydroxides after storage.<sup>61</sup>

For the Ni 2p<sub>3/2</sub> spectra, additional signals at ~854–856 eV in the region distinguish between NiO, Ni(OH)<sub>2</sub>, and oxidized NiOOH phases.<sup>124,125</sup> Multiplet splitting and satellite structures further support species identification, though quantitative deconvolution requires careful fitting.

Similar challenges arise for XPS spectra of Co, Mn, and Fe materials, where interpretation is complicated by multiple oxidation states and overlapping spectral

features. Among them, Mn exhibits one of the most complex 2p spectra due to its many stable oxidation states. Reliable deconvolution therefore requires sufficient signal quality. Surface Mn oxidation states can be estimated from the binding energy of the most dominant peak ranging from metallic Mn at 638.6 eV to  $\text{KMnO}_4$  at 645.5 eV.<sup>125</sup> Furthermore, the MnO can be identified by a characteristic shake-up satellite at 645.9 eV.<sup>125</sup>

For Co, partial decomposition of CoO into  $\text{Co}_3\text{O}_4$  was reported.<sup>125</sup> While the  $2p_{3/2}$  peaks often overlap, the distinct satellite structures can be considered for differentiating  $\text{Co}^{\text{III}}$  and  $\text{Co}^{\text{II}}$  species.<sup>125</sup> Accurate interpretation therefore benefits from combining XPS with complementary techniques such as XAS and Raman spectroscopy.

The situation is even more demanding for Fe, where numerous high-spin  $\text{Fe}^{\text{II}}$  and  $\text{Fe}^{\text{III}}$  (e.g. FeO,  $\text{Fe}_2\text{O}_3$ , FeOOH,  $\text{Fe}_3\text{O}_4$ ) species produce strongly overlapping 2p spectra, making precise assignments from XPS alone difficult.<sup>125</sup>

In this thesis, XPS was applied *ex-situ* to investigate the surface chemistry of Ni-, Co-, Mn-, and Fe-based OER catalysts. The analysis focused primarily on the Ni 2p and O 1s regions to trace irreversible changes after electrochemical operation, such as hydroxide formation and oxidation. By correlating these surface insights with bulk-sensitive methods, this thesis elucidates how surface chemistry and oxidation-state evolution relate to the activity of Ni-based electrocatalysts under OER conditions.

## 4 Experimental details and tools

### 4.1 Catalyst synthesis

#### 4.1.1 Solvothermal synthesis of $\alpha$ -Ni(OH)<sub>2</sub>

The ST synthesis was conducted by Dr. Elliot Brim at the Colorado School of Mines, Golden, Colorado and by Konstantin Rücker during a research stay at the Colorado School of Mines.

$\alpha$ -Ni(OH)<sub>2</sub> nanosheets were prepared via a ST process followed by pseudo-supercritical solvent removal, as previously reported.<sup>41</sup> Briefly, Ni(NO<sub>3</sub>)<sub>2</sub>·6H<sub>2</sub>O, urea, and benzyl alcohol (molar ratio 2:1:4) were dissolved in 50 mL methanol and stirred for 1 h before transfer to a 600 mL autoclave (Parr Instrument Company, USA). After a 1 min Ar purge, the vessel was pressurized to 9 bar, heated to 265 °C (equals the pseudo-supercritical point of methanol), and held for 90 min. Subsequent release of methanol vapor yielded the green  $\alpha$ -Ni(OH)<sub>2</sub> precursor powder.

#### 4.1.2 Microwave-assisted synthesis of $\alpha$ -Ni(OH)<sub>2</sub>

The MW-assisted synthesis was conducted by Dr. Dereje Hailu Taffa at the Carl-von-Ossietzky University of Oldenburg.

$\alpha$ -Ni(OH)<sub>2</sub> nanosheets were synthesized using a modified MW-assisted ST method.<sup>41</sup> First, 0.30 mmol Ni(NO<sub>3</sub>)<sub>2</sub>·6H<sub>2</sub>O (1.75 g) was dissolved in 20 mL methanol to form a light-green solution. Urea (0.15 mmol, 0.18 g) was added and stirred for 10 min, followed by benzyl alcohol (0.60 mmol, 1.23 g). The mixture was transferred to a 35 mL MW glass vial and heated to 140 °C for 30 min under stirring in a Discover SP MW synthesizer (CEM Corp., USA), reaching a pressure of 10–12 bar. After air cooling to room temperature, the product was washed repeatedly with methanol and was dried overnight at 60 °C under 250 mbar vacuum.

For the preparation of doped transition metal hydroxides, Mn- and Co-doped samples were prepared by adding the desired molar ratios of Mn or Co nitrates to the Ni nitrate precursor, keeping the total metal ion concentration at 0.3 mol. For the Fe-doping, the pH needed to be adjusted between 3.5-4.0 by adding 0.1 M methanolic solution of NaOH. This approach resulted in higher purity of  $\alpha$ -Ni(OH)<sub>2</sub>. Furthermore, longer MW synthesis time (180 min instead of 30 min) was used to allow the hydrolysis of more Ni ions to the hydroxide structure. Dopant levels are reported as mol % throughout this study.

### 4.1.3 Thermal annealing to receive faceted NiO

The thermal annealing was conducted by Dr. Dereje Hailu Taffa at the Carl-von-Ossietzky University of Oldenburg.

$\alpha$ -Ni(OH)<sub>2</sub> was then calcined in a box furnace (Linn High Therm, Germany) for 3 h with a heating/cooling rate of  $\sim 3$  °C min<sup>-1</sup> to receive NiO(111) nanosheets. During the calcination the color changed from black (low temperature) to dark gray (400–500 °C) and light gray (>600 °C). For the study of the synthesis conditions, annealing temperatures between 300 and 600 °C were used for studying the synthesis conditions. For the follow-up studies on transition metal doping, the calcination was conducted at 400 °C for 3 h.

## 4.2 Physical characterization of catalyst materials

### 4.2.1 Supplementary structural characterization

The supplementary structural characterization was conducted by Dr. Dereje Hailu Taffa and for the transmission electron microscopy (TEM) by Alexander Simon at the Carl-von-Ossietzky University of Oldenburg.

**Powder X-ray diffraction (PXRD)** was used to evaluate crystallinity and phase purity, employing an Empyrean Series 2 diffractometer (PANalytical, Netherlands) with Cu K $\alpha$  radiation ( $\lambda = 0.154$  nm). Data were collected in  $\theta$ – $2\theta$  geometry over a  $2\theta$  range of 5–80°.

**Nitrogen adsorption–desorption** isotherms were measured on a Tristar II (Micromeritics, USA) after degassing at 150 °C for 4 h (as-prepared nanosheets were degassed at 90 °C overnight to avoid calcination), with relative pressures ( $P/P_0$ ) from 0.005 to 0.95. Brunauer-Emmett-Teller (BET) surface areas were calculated from the isotherms.

**Transmission electron microscopy (TEM)** was performed on a JEOL 2100FS operating at 200 kV; samples were ultrasonically dispersed in ethanol and drop-cast onto copper grids. Elemental mapping of dopants was obtained by energy-dispersive X-ray spectroscopy (EDS) using an Oxford AZTEC system with an X-Max80 silicon drift detector.

The bulk composition was analyzed by **inductively coupled plasma mass spectrometry (ICP-MS)** by Jana Ewert (DLR). About 2 mg of metal oxide was dissolved overnight in 2 mL of concentrated HNO<sub>3</sub> (Suprapur, Carl Roth), then filtered and diluted with 2 wt % HNO<sub>3</sub> to a final volume of 50 mL. A scandium internal standard (1 mg L<sup>-1</sup>;

1000 mg L<sup>-1</sup> stock in 2 % HNO<sub>3</sub>, Carl Roth) was added. Calibration standards were prepared from Co, Mn, and Ni ICP solutions (1000 mg L<sup>-1</sup> in 2 % HNO<sub>3</sub>) to yield 20–750 µg L<sup>-1</sup> for Co and Mn and 2.0–5.0 mg L<sup>-1</sup> for Ni. Measurements were performed on an X-Series 2 ICP-MS (Thermo Fisher Scientific GmbH), ensuring a calibration correlation factor of  $\geq 0.999$ . Metal concentrations were determined using the <sup>55</sup>Mn, <sup>58</sup>Ni, <sup>60</sup>Ni, <sup>59</sup>Co, <sup>56</sup>Fe and <sup>57</sup>Fe isotopes.

#### 4.2.2 Raman spectroscopy

Raman spectra of the pristine NiO powder samples from chapter 5.1 were recorded on a Senterra Raman microscope (Bruker) equipped with a 488 nm laser source at the DLR Institute of Networked Energy Systems. The power was set to 10 mW with a spot size of 1 µm, except the  $\alpha$ -Ni(OH)<sub>2</sub>, which was measured at 5 mW avoid laser-induced calcination. The integration time was set to 20 s, and two coadditions were measured between 0 and 2600 cm<sup>-1</sup>.

Raman spectra were recorded using an RM5 Raman Microscope (Edinburgh Instruments) with a 532 nm Nd:YAG laser at the University of Groningen. The hydroxide samples were measured at 0.05 mW, whereas oxide samples were measured at 0.5 mW. All measurements were performed with a 1 s integration time. The number of scans was adjusted to achieve an adequate signal-to-noise ratio. The pristine powder samples were recorded as a compressed powder on a microscopic glass slide.

For *in-situ* experiments, the powder materials were dispersed in an dispersion consisting of 4 mg of catalyst powder, and 995 µL of Isopropanol and 10 µL of Nafion D-520 Dispersion (5 wt%). The dispersion was drop casted onto a carbon gas diffusion layer to receive complete coverage. The coated gas diffusion layer was mounted into a flow cell (GDE Raman ECFC, redoxme AB, Sweden) and electrochemically treated as the RDE experiments (Table A8). After the standard RDE protocol, potential hold experiments from 1.2 – 1.6 V vs. RHE were performed, to measure the polarized state of the catalyst material. For Fe<sup>III</sup> in situ spiking of the electrolyte, the flow cell was completely rinsed three times with 0.1 ppm Fe<sup>III</sup> containing 0.1 M KOH electrolyte.

#### 4.2.3 Synchrotron based X-ray absorption spectroscopy

XAS was performed at the KMC-2 beamline of the BESSY II synchrotron (Helmholtz-Zentrum Berlin für Materialien and Energie GmbH, Germany). Powder samples were spread on Kapton tape to an effective absorption length of 1.6 and folded to a 1 cm<sup>2</sup> area. Thin-film specimens were analyzed directly on their GC electrodes (see Electrochemical

Measurements). Representative powders were examined as powder samples, as as-prepared thin-films and after electrochemical treatment.

Calibration experiments of reference samples and some other powder materials were carried out in transmission mode (Figure A2a), utilizing an ionization chamber detector. The reference metal foil of the particular edge (Ni, Co, Fe and Mn) was measured as a reference in a second subsequent ionization chamber detector.

The thin film measurements were carried out in fluorescence mode with the sample set at 45° to a silicon photodiode (Figure A2b). For this, the reference metal foils were placed in front of an ionization chamber for simultaneous transmission detection. Energy calibration used the first inflection points of the metal foils (8333 eV for Ni-K, 7112 eV for Fe-K, 7709 for Co-K, and 6539 eV for Mn-K edge). Spectra were normalized by subtracting a linear pre-edge and dividing by a post-edge polynomial fit for XANES analysis. Edge positions were determined by the half-height method to monitor oxidation-state changes from doping and electrochemical conditioning.<sup>126,127</sup>

EXAFS data were Fourier transformed over 35–360 eV (3.03–9.72 Å<sup>-1</sup>) using a cosine window. *Ex-situ* samples were received by stopping the corresponding electrochemical experiment after the electrochemical conditioning and storing the GC discs under Argon.

#### 4.2.4 X-ray photoelectron spectroscopy

XPS was used to determine surface composition and oxidation states with an ESCALAB 250 Xi spectrometer (Thermo Fisher Scientific, UK) equipped with a Mg K $\alpha$  source ( $h\nu = 1253.6$  eV). High-resolution spectra of the Ni 2p, Fe 2p, O 1s, and C 1s regions were recorded at a pass energy of 10 eV and 20 meV step size. The C 1s signal from adventitious carbon at 284.8 eV served as the charge-correction reference. Data processing and peak deconvolution, including O 1s and C 1s, were performed in Avantage 4.97 using an iterative Shirley (smart) background.<sup>128</sup> *Ex-situ* samples were received by stopping the corresponding electrochemical experiment after the electrochemical conditioning and storing the GC discs under Argon.

### 4.3 Electrochemical characterization

#### 4.3.1 Preparation before rotating disc electrode testing

The RDE tips were polished with 1  $\mu\text{m}$  and 0.05  $\mu\text{m}$  alumina (MicroPolish, Buehler), rinsed for 3 min with ultrapure water, and sonicated for 2 min each in isopropanol and deionized water to remove residues, then dried under N<sub>2</sub>.

The catalyst dispersions (also known as inks) were optimized for the needs of the materials tested throughout the different studies. For studying the **synthesis of pure NiO(111)**, NiO(111) dispersions were prepared by mixing 4 mg of NiO(111) powder in 1.8 mL water, 0.2 mL 2-propanol, and 9  $\mu\text{L}$  of 5 % Nafion solution (Nafion D520CS, Ion Power). The mixture was sonicated for 5 min with a titanium horn (Q500, QSONICA, USA). The GC working electrodes (3 mm diameter, Metrohm) were coated with 4  $\mu\text{L}$  of dispersion was drop-cast on each electrode and spin-coated at 750 rpm for 30 min to yield  $\sim 0.1 \text{ mg cm}^{-2}$  catalyst loading, then air-dried.

For characterization of **Co and Mn doping** Catalyst dispersions were prepared by dispersing 4 mg of metal oxide in 1.59 mL water, 0.40 mL isopropanol, and 9  $\mu\text{L}$  of 5 wt % Nafion D-520 (Sigma-Aldrich). The suspension was horn-sonicated (Digital Sonifier 250, Branson) for 10 min at 25 W (10 s on / 5 s off) in an ice bath. A 9.8  $\mu\text{L}$  aliquot was drop-cast onto the rotating RDE (100 rpm) and dried while spinning at 700 rpm, yielding  $\sim 0.1 \text{ mg cm}^{-2}$  catalyst loading. Exchangeable GC RDE (5 mm diameter, Pine Research AFE6R1PTPK) fitted with SIGRADUR G discs (HTW,  $5 \pm 0.05 \text{ mm}$ ) served as substrate.

For **studying the Fe doping**, Catalyst dispersions were prepared by dispersing 4 mg of NiO powder in 995  $\mu\text{L}$  isopropanol, horn-sonicated for 10 min at 25 W (10 s on / 5 s off) in an ice bath, then mixed with 10  $\mu\text{L}$  of 5 wt % Nafion (D-520). The suspension was bath-sonicated for another 10 min, drop-cast onto the rotating RDE GC (5.61 mm diameter, Pine Research E7R9) at 100 rpm, and dried at 500 rpm to achieve  $\sim 0.1 \text{ mg cm}^{-2}$  catalyst loading.

All Electrochemical tests were performed in a custom single-compartment poly tetrafluoroethylene cell with a graphite counter electrode and a Hg/HgO reference (ALS, Japan) separated by polypropylene-frits, using 0.1 M KOH as electrolyte. The electrolyte was purged with  $\text{N}_2$  for 30 min before the experiment. The comparison of **synthesis of pure NiO(111)**, was done with KOH in analysis grade (85%, Sigma Aldrich), the characterization of **Co and Mn doping** with KOH (suprapur 99.995% (metal basis), Sigma Aldrich) and the study of **the Fe doping** with purified KOH (EMSURE 85%, MERCK). The purification was done according to Marquez et al.<sup>129</sup> by precipitating  $\text{Ni}(\text{OH})_2$  from  $\text{Ni}(\text{NO}_3)_2 \cdot 6\text{H}_2\text{O}$  and resting the 1 M KOH stock solution with the  $\text{Ni}(\text{OH})_2$ . Between experiments, cross contamination was counteracted with sonicating the cell and parts with 1 M  $\text{H}_2\text{SO}_4$ , followed by three times sonication in Millipore water. The reference was calibrated against a reversible hydrogen electrode (RHE) consisting of a Pt disk (AFE7R8PTPT, Pine Research) in  $\text{H}_2$ -saturated 0.1 M KOH.

### 4.3.2 Electrochemical rotating disc electrode experiments

For studying the **synthesis of pure NiO(111)** EIS from 1 Hz to 100 kHz (10 mV AC) provided the electrolyte resistance ( $R_u$ ) for post compensation was recorded in N<sub>2</sub> saturated electrolyte. This was followed by  $C_{DL}$  measurements.  $C_{DL}$  was obtained from CV in a non-faradaic window (0.90–1.15 V vs. RHE) at scan rates of 5–500 mV s<sup>-1</sup>. For OER measurements, the solution was saturated with O<sub>2</sub> for 10 min and maintained under O<sub>2</sub>. Initial OER activity was recorded by RDE voltammetry (2500 rpm) from 1.14 to 1.94 V vs. RHE at 10 mV s<sup>-1</sup>. Electrodes were then activated by 50 CV cycles between 1.04 and 1.64 V vs. RHE at 100 mV s<sup>-1</sup>, followed by three final CV scans, again with (2500 rpm) from 1.14 to 1.94 V vs. RHE at 10 mV s<sup>-1</sup>. All measurements were conducted with an Autolab PGSTAT12 potentiostat controlled by NOVA 2.1 software.

For characterization of **Co and Mn doping** Electrochemical measurements the electrolyte was purged with N<sub>2</sub> for 30 min and the electrode equilibrated at open-circuit potential. The  $C_{DL}$  was measured in N<sub>2</sub>-purged electrolyte by CV (5–500 mV s<sup>-1</sup>) between 0.9 and 1.1 V vs. RHE. The current at 0.93 V from the negative sweep was plotted versus scan rate ( $v$ ) and fitted to  $i = C_{DL} v^\alpha$ , where  $\alpha$  accounts for non-ideal capacitive behavior ( $\alpha = 1$  for an ideal capacitor). For OER activity, the electrolyte was purged with O<sub>2</sub> for 15 min. Electrolyte resistance ( $R_u$ ) was determined by EIS and used for full  $iR$  correction. CVs were recorded at 2500 rpm from 1.0 to 2.2 V vs. RHE at 10 mV s<sup>-1</sup> before and after conditioning. Conditioning consisted of 350 CV cycles at 100 mV s<sup>-1</sup>. Each material was tested in triplicate with freshly prepared electrodes.

For the characterization of **the Fe doping** initial CVs were recorded from 1.0 to 2.2 V vs. RHE at 10 mV s<sup>-1</sup> to measure OER activity, reported as the  $\eta$  at 10 mA cm<sup>-2</sup>. This was followed by electrochemical conditioning between 1.0 and 1.7 V vs. RHE for 50 CVs at 100 mA cm<sup>-2</sup>. Activities were assessed before conditioning, after conditioning, and following a 1 h galvanostatic hold. For durability testing, one electrode of each material underwent an additional 10 h galvanostatic hold prior to final characterization.

### 4.3.3 Porous transport electrode half-cell experiments

The PTE setup was a modified commercial half-cell (Flexcell, Gaskatel, Germany). The optimization of the PTE setup was realized in a master thesis by Nikhil Kadimi.<sup>130</sup> Also the practical lab work regarding the PTE preparation and electrochemical experiments were performed by Nikhil Kadimi

The dispersion for the spray coating was prepared by weighing 84 mg of respective catalyst and dispersing it in 998 mg of deionized water. This was followed by horn-sonication for 10 min (10 seconds pulse on, 5 seconds pulse off, 10% amplitude) with a Digital Sonifier 250 (Branson) and ice cooling. After horn-sonication, 184 mg of FAA-3 ionomer solution (Fumion) was added to the dispersion with simultaneous bath sonication. This was followed by another horn-sonication for 10 min. After addition of 780 mg isopropanol, a last horn-sonication step for 30 min was used. The dispersion was freshly used. The PTE were obtained by spray coating the dispersion onto a Ni porous transport layer (~0,2 mm thickness, ~80% porosity, Bekaert, Belgium). A spray gun (SRi Pro spray gun, DeVilbiss) was used to coat the area underneath a 3D-printed polypropylene mask. The hand spraying process was done by scanning the substrate in each preferential direction and with dry spraying in between. The dispersion was prepared with a safety factor of 3 to consider over-spraying and catalyst precipitation to receive a target loading of 3 mg cm<sup>-2</sup>.

The electrochemical experiments were conducted in a modified commercial half-cell (Flexcell, Gaskatel, Germany). The setup is depicted in Figure 49. Details on the optimization of the setup can be found in the related masterthesis.<sup>130</sup> If not otherwise stated, the cell was operated with 1 M KOH at 60 °C and with a pump flow rate of 60 mL min<sup>-1</sup>. First, EIS was recorded at open-circuit potential OCP to determine the  $R_u$ . Measurements were performed for 5 min with a 10 mV amplitude over a frequency range of 100 kHz–10 Hz. This baseline value was used for all subsequent iR corrections of CV. The potentials of all CVs were compensated for the ohmic resistance with 95 % of  $R_u$  during the experiment and the remaining 5 % were corrected in the data processing. The working electrode was electrochemically cycled by 50 CV between 1.0 and 1.6 V vs. RHE at 100 mV s<sup>-1</sup>. After conditioning, a linear sweep voltammogram from 1.0 to 1.59 V vs. RHE was recorded, and a second EIS spectrum was collected at 1.59 V vs. RHE (10 mV amplitude, 100 kHz–10 Hz). This potential lies within the oxygen evolution region and after the Ni<sup>II</sup>/Ni<sup>III</sup> oxidation. Catalytic activity was evaluated by CV between 1.0 and 1.7 V vs. RHE at 10 mV s<sup>-1</sup> for two cycles. An 1 h chronopotentiometry at a current density of 50 mA cm<sup>-2</sup>. This should reflect the short time durability and condition the catalyst at a static condition. Following the durability test, galvanostatic EIS (GEIS) was carried out at 50 mA cm<sup>-2</sup> with a 20 % current perturbation over 100 kHz–100 Hz. A second EIS spectrum at 1.59 V vs. RHE was then acquired, followed by a repeat of the CV activity test (10 mV s<sup>-1</sup>, two cycles) to gauge changes in catalytic performance. To

obtain a polarization curve, stepwise chronopotentiometry was performed at current densities of 1, 5, and 10 mA cm<sup>-2</sup> (60 s each); 25, 50, 75, 100, and 250 mA cm<sup>-2</sup> (30 s each); and 500, 750, and 1000 mA cm<sup>-2</sup> (5 s each). At each step, GEIS was recorded (20 % current amplitude, 100 kHz–100 Hz). All potentials were subsequently corrected for 100 % iR drop. The acquisition time was balanced between minimizing the cell heat-up during high current densities and reaching a stable potential response. A final EIS measurement at 1.59 V vs. RHE and a third CV scan (10 mV s<sup>-1</sup>, two cycles) completed the testing sequence, enabling assessment of cumulative effects of prolonged electrochemical stress on catalyst activity and interfacial stability.

#### 4.4 Tools and software for data analysis

XAS experiments were analyzed with the BESSY 4.0 (workgroup Dau, Freie Universität Berlin) software suite. XPS data were acquired and analyzed by aid of Thermo Advantage (version 5.9925, Thermo Fisher Scientific). The Raman data were measured and exported from Ramacle (Edinburgh Instruments Ltd.)

The electrochemical experiments and the protocol preparation was conducted with Nova (version 2.1.6.-2.1.8, Metrohm). The electrochemical data was iR corrected and the overpotentials were extracted with a python script running on a Django framework (Django Software Foundation) implemented by Marius Gollasch (ece-easyanalysis).

The large language model Meta Llama 3.3 70 B Instruct was run on Chat AI (version v0.9.0, Gesellschaft für wissenschaftliche Datenverarbeitung mbH Göttingen) and used to improve python codes and text syntax. Data representation and deconvolution of Raman spectra was done with Origin (version 2025, OriginLab Corporation). Schematics were drawn with Inkscape (version 1.4.2.).

Crystallographic structures were drawn with Vesta (Version 3).<sup>45</sup>

## 5 Results and discussion

The central focus of this thesis is the electrochemical characterization of NiO(111) nanosheets, employed as a model system to investigate electrocatalytic activity and surface reconstruction after electrochemical treatment. Chapter 5.1 first addresses the synthesis of NiO(111) nanosheets under different conditions and their impact on material properties. Building on this, the influence of transition-metal incorporation (Co, Mn, and Fe) into the Ni-based host material is explored. Particular attention is given to Fe, which was studied both as a bulk dopant and via *in-situ* incorporation from the electrolyte. In addition, selected Fe-based catalysts were evaluated in a PTE half-cell setup, enabling characterization under conditions closely resembling those of the AEMWE. Finally, challenges in reproducibility encountered during electrochemical testing are compiled, and recommendations are provided to guide future experiments.

### 5.1 OER performance of NiO(111) nanosheets from varied synthesis conditions

*The Materials studied in this chapter were prepared in collaboration between the DLR, the Colorado School of Mines (MINES) and the University of Oldenburg in the labs of MINES by Dr. Elliot Brim and in the UOL by Dr. Dereje Hailu Taffa. The content of this chapter was published in ACS Appl. Mater. Interfaces.<sup>42</sup> Dr. Dereje Hailu Taffa performed the MW synthesis, the thermal annealing, the PXRD, the XPS and the electrochemical testing in this study. Konstantin Rücker performed Raman spectroscopy, AFM imaging, the XAS analysis and assisted with the electrochemical testing. Dr. Elliot Brim performed the ST synthesis and the HR-TEM imaging.*

For nickel oxides, performance is strongly facet-dependent; thin-film studies indicate that (111) and especially (110) surfaces favor formation of catalytically active oxyhydroxides and lower overpotentials.<sup>71,72</sup> However, most facet-activity insights come from thin films on oriented substrates, which are not readily scalable.<sup>72,131</sup> Scalable, solution-based syntheses are therefore crucial for fundamental studies and practical deployment of facet-controlled NiO.<sup>41,132</sup>

In this work, NiO(111) nanosheets were synthesized via a fast MW-assisted route and compared to ST prepared analogues, followed by controlled annealing to tune structure and morphology. The materials are then evaluated for OER, enabling assessment of how synthesis route and annealing govern morphology, electrochemically active surface area, and catalytic performance.

### 5.1.1 Structural characterization of the NiO(111) nanosheets

During synthesis,  $\alpha$ -Ni(OH)<sub>2</sub> formation was favored below pH 8, where urea decomposition maintained alkalinity by releasing NH<sub>3</sub>, which hydrolyzed to OH<sup>-</sup> ions that reacted with Ni<sup>2+</sup>.<sup>133</sup> PXRD patterns of MW-synthesized samples at 140 °C (Figure 16a) confirm the formation of highly crystalline  $\alpha$ -Ni(OH)<sub>2</sub> (P $\bar{3}$ 1m, PDF 00-038-0715), with both crystallinity and yield increasing with synthesis time.<sup>50</sup> A synthesis time of 30 min at 140 °C was therefore optimized and selected as standard conditions. Upon annealing at 300–600 °C for 3 h,  $\alpha$ -Ni(OH)<sub>2</sub> converted into pure rock-salt NiO (Fm $\bar{3}$ m, PDF 98-018-4918), with higher temperatures yielding sharper peaks indicative of increased crystallinity and lattice contraction. For both synthesis methods, the relative intensity of the (111) reflection increased after annealing, suggesting the preferential growth of the (111) plane (Figure 16b).

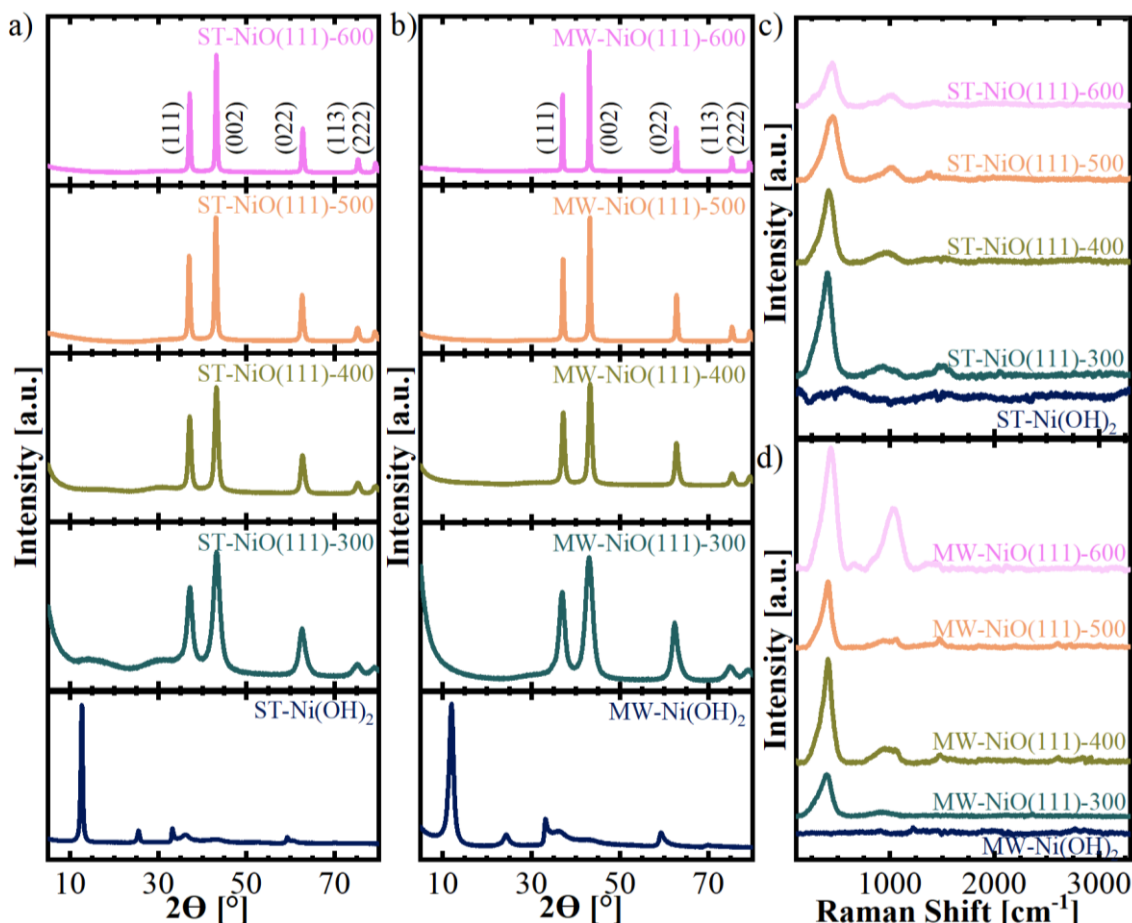


Figure 16: PXRD patterns of NiO(111) nanosheets heat treated at different temperatures: a) ST prepared and b) MW prepared. Assignments correspond to PDF 98-018-4918. Raman spectra of the Ni(OH)<sub>2</sub> samples and the annealed NiO(111) samples from c) ST synthesis and d) MW synthesis. Reproduced from Taffa et al.<sup>42</sup>

Average crystallite sizes were calculated via the Scherrer equation from the (111) reflection.<sup>134</sup> The MW samples exhibit sizes ranging from 4 to 49 nm, whereas ST

samples range from 6 to 25 nm ranged from 4–49 nm for MW samples and 6–25 nm for ST samples (Table A1). Across the investigated temperature range, ST samples consistently displayed smaller crystallites than MW samples.

Raman spectroscopy provided complementary insights (Figure 16c and d). As-prepared  $\alpha$ -Ni(OH)<sub>2</sub> showed only weak bands, consistent with its limited long-range order. Upon conversion to NiO, spectra displayed the dominant one-phonon transverse-optical (TO) mode at 200–500 cm<sup>-1</sup> and a two-phonon feature at 700–1200 cm<sup>-1</sup>, with the latter increasing in intensity at higher calcination temperatures.<sup>63,135</sup> The two-phonon feature was also correlated to a two magnon mode, which has been attributed to lattice vibrations and correlated with crystallite growth.<sup>119,136</sup> The growth of this band therefore corroborates the PXRD results, confirming the increased crystallinity of heat-treated samples.

Furthermore, nitrogen adsorption–desorption isotherms (Figure A3) revealed that NiO(111) nanosheets showed high surface areas at 300 °C (165 m<sup>2</sup>/g for MW, 149 m<sup>2</sup>/g for ST), which decreased sharply at 600 °C due to coarsening. Pores were ~3 nm below 500 °C, with additional 7–8 nm mesopores at 400 °C. ST samples retained microporosity up to 600 °C, while MW lost area faster.

The PXRD and Raman findings were further correlated with morphological trends using HR-TEM (Figure 17). At 300 °C, MW samples showed small, irregular pores (1.7–3.1 nm). Annealing at 400 °C produced well-defined hexagonal pores (10–15 nm wide, 20–30 nm long) alongside smaller hexagonal holes (5–6 nm). With further heating to 500 °C, pores enlarged (15–20 nm wide, 25–30 nm long) and began merging, while at 600 °C the nanosheet structure collapsed into plate-like crystals. In contrast, ST samples developed hexagonal pores from 400 °C onward, which remained stable at higher temperatures. TEM also confirmed highly crystalline NiO nanosheets oriented along (111), with lattice fringes of 0.243 nm (MW) and 0.240 nm (ST). These morphological features, particularly the edges and corners of hexagonal pores with (001) orientation, are expected to strongly influence OER activity.<sup>73</sup>

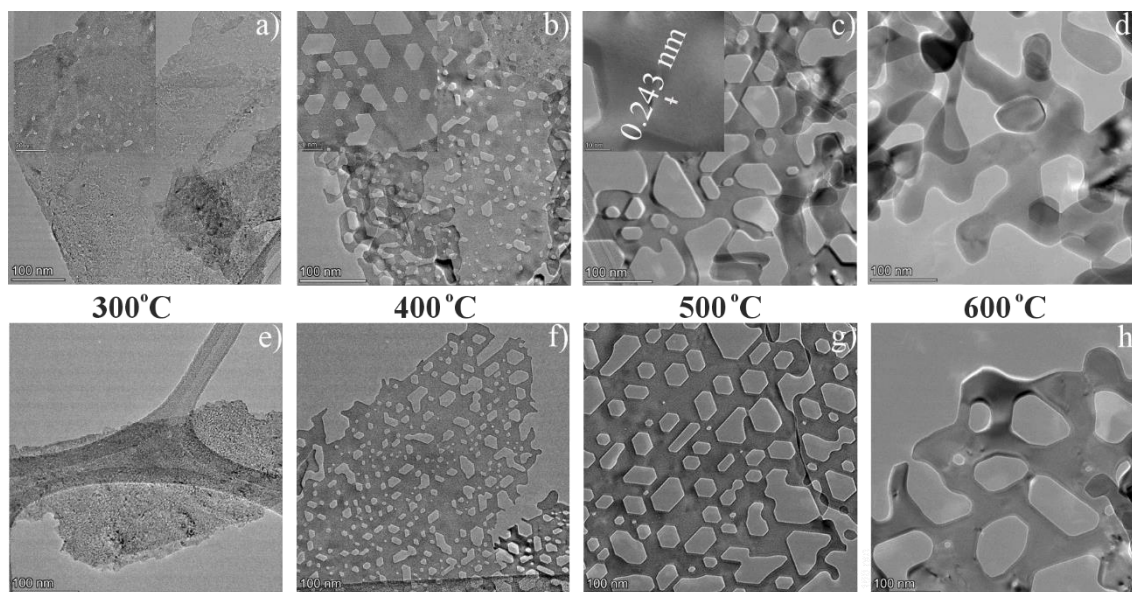


Figure 17: HR-TEM images (a–d) for MW samples and (e–h) for ST samples showing the formation of hexagonal pores on annealing of the samples. The measured lattice spacing suggests the NiO(111)-oriented nanosheets. Reproduced from Taffa et al.<sup>42</sup>

To gain height information of singular nanosheet materials, non-contact atomic force microscopy was used (Figure A4). Samples annealed at 400 °C exhibited comparable thicknesses of 12 nm (ST) and 14 nm (MW), confirming a similar nanosheet thickness.

XPS was used to investigate the surface composition and oxidation states of Ni-based samples. Survey spectra showed Ni, O, and C as the dominant elements (Figure A5). Residual nitrogen species from urea or nitrate precursors were present in the as-prepared hydroxides and at 300 °C but were largely removed in MW samples due to extensive washing, while ST samples retained more N after supercritical drying.

The O 1s spectra of annealed samples revealed two main features (Figure A6b, d). The lattice oxygen peak at 528.9–529.6 eV, was slightly shifting to lower binding energies with increasing annealing temperature. A second peak at ~531.0–531.4 eV attributed to Ni–OH groups or oxygen defects was observed.<sup>124</sup> A higher-energy component at ~532.2 eV in as-prepared samples indicated adsorbed water or C–O species.

The Ni 2p<sub>3/2</sub> binding energy (Figure A6a,c) shifted from 854.2 eV in hydroxides to ~853.3 eV after annealing at 600 °C, confirming the conversion from Ni(OH)<sub>2</sub> to NiO with surface Ni<sup>2+</sup> as the dominant species.<sup>128</sup> The surface Ni:O ratio decreased with annealing (MW: 0.97→0.85; ST: 0.95→0.81), pointing to oxygen-rich surfaces in line with OH-terminated NiO(111) planes.<sup>137</sup> Such oxygen enrichment may promote non-stoichiometry at the surface and partial Ni<sup>III</sup> formation, though precise quantification of Ni<sup>III</sup> is difficult due to strong satellite contributions.<sup>138</sup>

XAS was employed to probe bulk oxidation state and coordination. The Ni K-edge XANES of MW- and ST-NiO(111)-500 placed the edge between NiO and LiNiO<sub>2</sub> references, indicating an average Ni oxidation state of  $\sim +2.5$  (Figure A7a) EXAFS analysis showed overlapping Ni–O and Ni–Ni peaks for both samples (Figure A7b), confirming the absence of structural differences, consistent with PXRD results. There is no indication of structural differences in EXAFS, correlating with the PXRD results.

To conclude the structural analysis of the MW and the ST samples, both exhibits nearly identical electronic structures, differing mainly in morphology and a decreasing crystal size with increasing annealing temperature. The following section will continue with a comparative analysis of the OER activity of the various materials.

### 5.1.2 Electrochemical trends as a function of the synthesis conditions

OER activity was evaluated in alkaline media using a three-electrode RDE setup under hydrodynamic conditions. The applied protocol is depicted in Table A2. The electrochemical protocol was designed for screening of the electrode activities of the catalyst materials.

The analysis of the  $C_{DL}$  revealed a decrease after conditioning of the electrocatalysts; among activated samples, MW-NiO(111)-500 and ST-NiO(111)-500 showed the highest  $C_{DL}$  values, though these values should be treated cautiously for low-conductivity NiO at low annealing temperatures, where ohmic distortions can occur.<sup>105</sup>

During activation, CVs exhibited the characteristic Ni<sup>II</sup>/Ni<sup>III</sup> redox peaks near 1.40 V vs. RHE followed by a steep current rise of the OER onset (Figure A8). The electrochemical conditioning was observed to stabilize after about 40 scans, consistent with conversion of dense rock salt NiO to more permeable, conductive Ni oxy/hydroxides.<sup>63,79</sup> In contrast,  $\alpha$ -Ni(OH)<sub>2</sub> showed relatively stable CVs during activation (Figure A9). MW-NiO(111) displayed a narrower, more symmetric redox peak than ST-NiO(111), likely reflecting differences in coating/contact or intrinsic conductivity. The first scan was anodically shifted relative to subsequent scans for both material types, and activation increased the redox peak current and lowered the OER onset. Potential Fe-impurity effects were considered, but ICP–MS of the electrolyte showed an absence of Fe or a content below the 0.105  $\mu\text{g L}^{-1}$  detection limit. Yet, influences of Fe of the activity of Ni based systems are likely, but assumed to be constant.<sup>10,84,129</sup>

## 5.1 OER performance of NiO(111) nanosheets from varied synthesis conditions

Figure 18a and b show the third CV after electrochemical conditioning. For all activated samples, the Ni<sup>II</sup>/Ni<sup>III</sup> redox transition is observed. A shift of the Ni<sup>II</sup>/Ni<sup>III</sup> redox signal of the hydroxide samples towards positive potentials is observed. It was reported, that both NiO(111) and  $\alpha$ -Ni(OH)<sub>2</sub> form  $\gamma$ -NiOOH on their surfaces during the OER.<sup>72</sup> Thus, the electrochemically formed surface hydroxides on the NiO(111) nanosheets and  $\alpha$ -Ni(OH)<sub>2</sub> are similar, and the difference in the CV behavior most probably relies on different accessibility of formed Ni(OH)<sub>2</sub> to the Ni<sup>II</sup>/Ni<sup>III</sup> redox transition and the electronic structure.

The integrated Ni<sup>II</sup>/Ni<sup>III</sup> anodic charge decreased with annealing temperature, Ni(OH)<sub>2</sub> > 300 °C > 400 °C > 500 °C > 600 °C for both MW and ST, matching BET area (Figure A3, Table A1). The integral of the redox peak charge can be interpreted as an indication of the presence of more electrochemically accessible Ni centers and is thus a parameter related to the surface area.

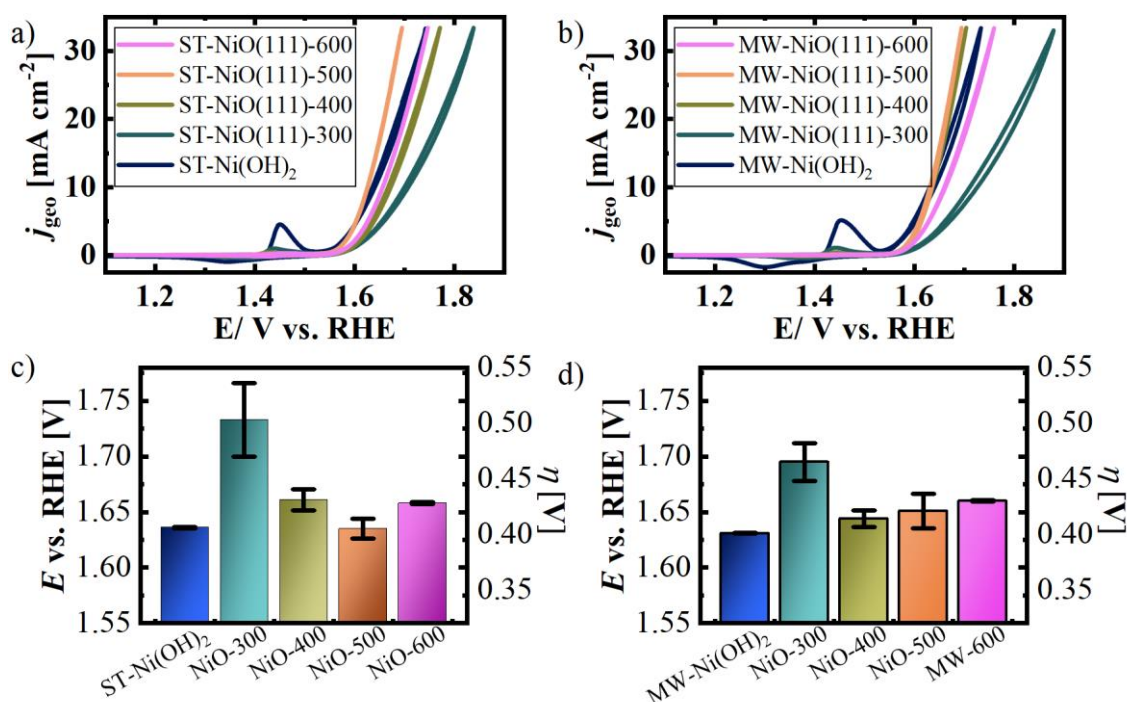


Figure 18: iR-corrected cyclic voltammograms of a) ST-NiO(111) nanosheets and b) MW-NiO(111) nanosheets, annealed at different temperatures and measured at 10 mV s<sup>-1</sup> in 0.1 M KOH solution. Corresponding  $\eta$  comparison at 10 mA cm<sup>-2</sup> and 25 mA cm<sup>-2</sup> for the of c) ST-NiO(111) nanosheets and d) MW-NiO(111) nanosheets and deviations from the repetition experiments. Adapted from Taffa et al.<sup>42</sup>

To compare the OER performance of the NiO(111) nanosheet electrodes, the  $\eta$  at 10 mA cm<sup>-2</sup> (normalized to the GC disc area) for a catalyst loading of  $\sim$ 0.1 mg cm<sup>-2</sup> (Figure 18c, d) was plotted. The best-performing samples were obtained at 400 °C for MW-NiO(111) and 500 °C for ST-NiO(111). At these conditions, MW-NiO(111)

required an  $\eta$  of 414 mV and ST-NiO(111) 405 mV to reach  $10 \text{ mA cm}^{-2}$ . These values are comparable to or slightly better than nanoparticulate NiO catalysts reported elsewhere.<sup>53,92</sup> However, lower overpotentials were reported for NiO thin films.<sup>63</sup> Notably, the OER trend does not follow the BET surface areas: low-temperature samples with high BET areas show poor activity, likely due to low crystallinity and residual organics blocking active sites. Instead, optimal activity arises between 400–500 °C, where crystallinity and porosity are balanced. In this range, well-defined hexagonal cavities introduce additional edge sites, which have been shown to expose more active (100) facets than the basal plane.<sup>73</sup>

To connect the similar OER trends of MW- and ST-NiO(111) with their intrinsic properties, we compared current densities at 1.6 V vs. RHE normalized by both geometric area ( $j_{\text{geo}}$ ) and BET area ( $j_{\text{BET}}$ ) (Figure 19). The  $j_{\text{geo}}$  values increased with annealing temperature and peaked at 400 °C (MW) and 500 °C (ST), then declined at higher temperatures. Overall, ST-NiO(111) exhibited higher  $j_{\text{geo}}$  than MW-NiO(111). The  $j_{\text{BET}}$  values of ST samples followed the same trend as  $j_{\text{geo}}$ , whereas MW samples continued to increase above 400 °C, even as BET areas decreased. Since BET measures the total surface area rather than the number of catalytically active sites, this suggests that higher annealing temperatures can increase the exposure or intrinsic activity of active sites despite reduced surface area. Above 500 °C, coarsening and sintering in ST-NiO(111) likely caused loss of active sites, while MW-NiO(111) retained improved intrinsic activity up to >600 °C. Another explanation is that the intrinsic activity per site increases with crystallinity, as previously reported for  $\text{Co}_3\text{O}_4$ ,<sup>139</sup> consistent with the observed rise in BET-normalized currents with increasing crystallite size.

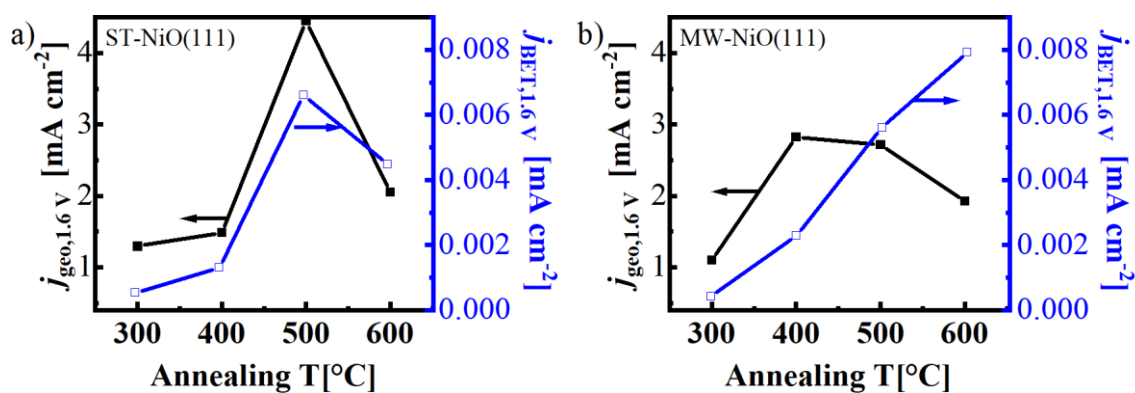


Figure 19: Comparison of geometric current density  $j_{\text{geo}}$  and BET area normalized current densities against temperature: (c) MW-NiO(111) and (d) ST-NiO(111) samples. Adapted from Taffa et al.<sup>42</sup>

Furthermore, EIS experiments were performed at 1.6 V vs. RHE to gain a more comparative insight into charge transfer phenomena (Figure A11). At 1.6 V vs. RHE OER onset occurs. The data were fitted with the equivalent circuit model of Watzele et al.<sup>98</sup>, including  $R_u$ ,  $C_{DL}$ ,  $R_{ct}$ ,  $C_{Ads}$ , and  $R_{ads}$ . Due to the concerns of the interpretation of values like the  $C_{Ads}$  stated in Chapter 3.1.2, the emphasis is put on the analysis of the  $R_{ct}$ .<sup>98</sup> The most active electrodes, MW-NiO(111)-400 and ST-NiO(111)-500, showed the lowest  $R_{ct}$  values (Figure A11c), suggesting that their enhanced OER activity could arise from more efficient interfacial charge transfer.

### 5.1.3 Summary of the variation of NiO(111) synthesis conditions

To summarize the electrochemical characterization, it revealed that both MW- and ST-derived NiO(111) nanosheets exhibit competitive OER activity, with performance strongly governed by annealing temperature. Optimal activity was achieved for MW-NiO(111) annealed at 400 °C ( $\eta = 414$  mV) and ST-NiO(111) annealed at 500 °C ( $\eta = 405$  mV). These electrodes combine high  $C_{DL}$  and low  $R_{ct}$ , suggesting efficient interfacial kinetics. While low-temperature samples with large BET areas showed poor activity, higher annealing temperatures improved crystallinity and intrinsic activity per site, despite a reduced BET surface area. The MW approach of MW-NiO(111) showed potential for further intrinsic activity enhancement at >600 °C, albeit with loss of geometric current density. The higher density of pores and exposed (001) edges in MW samples may also contribute to activity. Overall, MW synthesis offers a rapid and versatile route to faceted NiO(111) nanosheets, with opportunities for further optimization through doping or structural modification to lower OER overpotentials.

Accordingly, the synthesis conditions for the NiO(111) nanosheets in the subsequent work were selected based on the findings of this chapter. The following chapters examine how the incorporation of additional transition metals into the NiO(111) host influences both the OER activity and the associated surface reconstruction.

## 5.2 The influences of Co/Mn doping on NiO(111) nanosheets

*The Materials studied in this chapter were prepared in collaboration between the DLR and the UOL in the labs of the UOL by Dr. Dereje Hailu Taffa. Most of the content of this chapter was previously published in the Journal of Physical Chemistry C.<sup>140</sup> Konstantin Rücker performed the XPS analysis, the XAS analysis and the electrochemical characterization. Dr. Dereje Hailu Taffa performed the MW synthesis, the PXRD, the BET analysis and the HR-TEM analysis.*

The synthesis was adapted from the previous chapter, but with addition of dopant transition metal precursor nitrate salts. Herein, doping is defined as a phase pure solid solution of the dopant into the host material. Different dopant transition metals were tested such as Co, Mn and Fe. However, the Fe dopant formed separate phases at low doping levels and deviated drastically from the aimed doping levels. The Fe-doped materials are further discussed from Chapter 5.3 onwards.

The initial physical characterization was according to chapter 5.1. In the following, the outcomes are briefly covered. PXRD (Figure A12a, b) suggested that the addition of transition metals in the given doping levels lead to phase pure NiO nanosheets in the rock salt structure. For the case of the Mn doping the hexagonal holes appear to be slightly affected by the Mn-doping (Figure A12c-e) which results in the increased apparent BET surface area (Table A5 1). For the case of the Co-doping no effect on the morphology was evident because the TEM images and the specific surface area were close to the pure NiO(111) sample. In contrast, the higher Co doping results in lower BET surface areas and decreasing crystallite sizes. For electrochemistry it is expected that surface areas improve the electrocatalytic performance of metal oxide based OER electrocatalysts. The OER activity and electrochemical responses are studied in the following section.

### 5.2.1 Electrochemical trends as a function of the Co and Mn content

For the electrochemical analysis the cyclic voltammetry for conditioning of the materials is compared in representative experiments in Figure 20a. The conditioning is expected to change the surface structure of the different NiO(111) pre-catalyst into an OH/OOH functionalities as active phase for the OER. Representative CV from the scan 1 to 350 are shown for the different materials which represent the evolving Ni<sup>II</sup>/Ni<sup>III</sup> redox peaks. The consecutive development of the Ni<sup>II</sup>/Ni<sup>III</sup> oxidation and reduction peaks represent the growth of the OH/OOH layer on the catalyst surface. The peak position of

the NiO(111) sample remains stable throughout the consecutive scans. This indicates a steady hydroxide formation throughout the conditioning.

The shape and peak position of the Ni<sup>II</sup>/Ni<sup>III</sup> redox peaks for the 5% and 10% Co doped sample behaves similar to the pure NiO(111) material. This was also observed for Co-spiked NiO<sub>x</sub>H<sub>y</sub> and of Ni-spiked CoO<sub>x</sub>H<sub>y</sub> films by Ou, Twight and Samanta et al.<sup>85</sup> The absence of the Co<sup>II</sup>/Co<sup>III</sup> oxidation peak at about 1.1 V vs. RHE implies an incorporation of the Co ions into the NiO lattice and with this a formation of a mixed hydroxide/oxyhydroxide layer. Furthermore, no the Ni<sup>II</sup>/Ni<sup>III</sup> redox peak shift was observed for Co-doped NiO<sub>x</sub>H<sub>y</sub>.

On the other hand, the Mn-doped materials exhibit drastic shifts of the Ni<sup>II</sup>/Ni<sup>III</sup> redox peak positions. Specifically, the first CV of the electrochemical conditioning was shifted from 1.43 V vs. RHE of the pure NiO(111) to 1.6 V vs. RHE of the NiO(111)+5% Mn sample. This was previously observed for the incorporation of Fe into NiO<sub>x</sub>H<sub>y</sub> host material and was explained by electronic influences of the dopant onto the bulk of the catalyst material.<sup>10,85</sup> However, the fundamental origin of the peak shift remains under debate.<sup>85</sup> This Ni<sup>II</sup>/Ni<sup>III</sup> oxidation peak shift is only reported for the bulk incorporation (e.g. via CV) of dopants into the material and not for surface restricted transition metal incorporation.<sup>85</sup> Therefore, the shift of the Ni<sup>II</sup>/Ni<sup>III</sup> oxidation peak is evidence for the Mn to be incorporated into the NiO host structure initially.

However, after the first 100 cycles a splitting into two separate oxidation peaks at 1.43 and 1.52 V vs. RHE is observed. There was no additional reduction peak observed. The absence of the second reduction peak indicates an irreversible reaction. This oxidation peak splitting was previously observed and attributed to octahedral and tetrahedral metal species in spinel type transition metals.<sup>141,142</sup> In this case we have an octahedral rock salt NiO host structure, which makes it more likely that the additional signals arise from additional redox changes of the Mn species on the surface. It was observed that the Mn oxidation towards MnO<sub>4</sub><sup>-</sup> leads to leaching from LiMnO<sub>4</sub> electrodes.<sup>93,143</sup> This possible leaching process will be further analyzed, after studying the difference in peak charges of the samples after 350 CVs from Figure 20a.

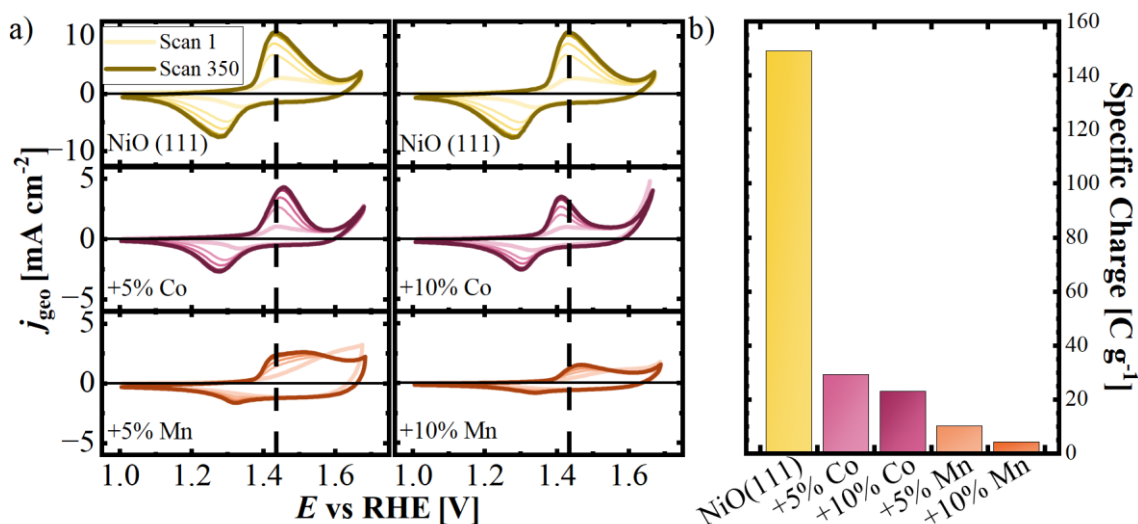


Figure 20: a) Representative CV of the electrochemical conditioning with 350 CVs of 5% doped samples and 10% doped samples. b) Bar chart of the mass specific  $\text{Ni}^{\text{II}}/\text{Ni}^{\text{III}}$  oxidation charges for representative samples of the 350th scans with  $100 \text{ mV s}^{-1}$  and subtracting the OER background currents. Adapted from R ucker et al.<sup>140</sup>

The  $\text{Ni}^{\text{II}}/\text{Ni}^{\text{III}}$  oxidation charges are plotted in Figure 20b. The pure NiO(111) material has a oxidation charge of about  $149 \text{ C g}^{-1}$ . After doping the NiO(111) with the transition metals with 5% and 10%, the oxidation and reduction currents decrease drastically. The oxidation charge of the NiO(111)+5% Co is with  $29 \text{ C g}^{-1}$  unproportionally smaller than the charge of the NiO(111) sample. A charge of about 95% of the pure NiO(111) sample was expected, calculated from the composition of the NiO(111)+5% Co sample. Instead, an oxidation charge of about 19% to the pristine NiO(111) sample was observed. These observations are qualitatively transferable to the 10% Co-doped sample. For the case of the Mn-doping, the oxidation charge is reduced to  $23 \text{ C g}^{-1}$  which is 15 % of the NiO(111) sample.

The lower oxidation charge could be explained by suppressed oxidation towards NiOOH. However, the reason for the suppression of the  $\text{Ni}^{\text{II}}/\text{Ni}^{\text{III}}$  oxidation could be electronically or structurally.<sup>79</sup> Electronic suppression could stem from a lower conductivity of the mixed oxide bulk material.<sup>144</sup> This was observed for the in-plane conductivity of Mn-based oxy-hydroxides films in a previous study.<sup>145</sup> Another factor for suppression of the  $\text{Ni}^{\text{II}}/\text{Ni}^{\text{III}}$  oxidation process could be structural incompatibility of the dopant to form a NiOOH structure, formed after  $\text{Ni}^{\text{II}}/\text{Ni}^{\text{III}}$  oxidation.

For further analysis of the additional peaks of the Mn-samples, the leaching of Mn in the form of  $\text{MnO}_4^-$  was studied by the aid of RRDE generation-collection experiments and ICP-MS measurements of the electrolyte after the experiments. The RRDE generation-collection experiments were previously described for a  $\text{LiMn}_2\text{O}_4$  catalysts in

the potential window for the OER.<sup>93</sup> Such generation-collection experiments were performed with the corresponding protocol of the previous experiments and the NiO(111)+10% Mn material in N<sub>2</sub> saturated electrolyte.

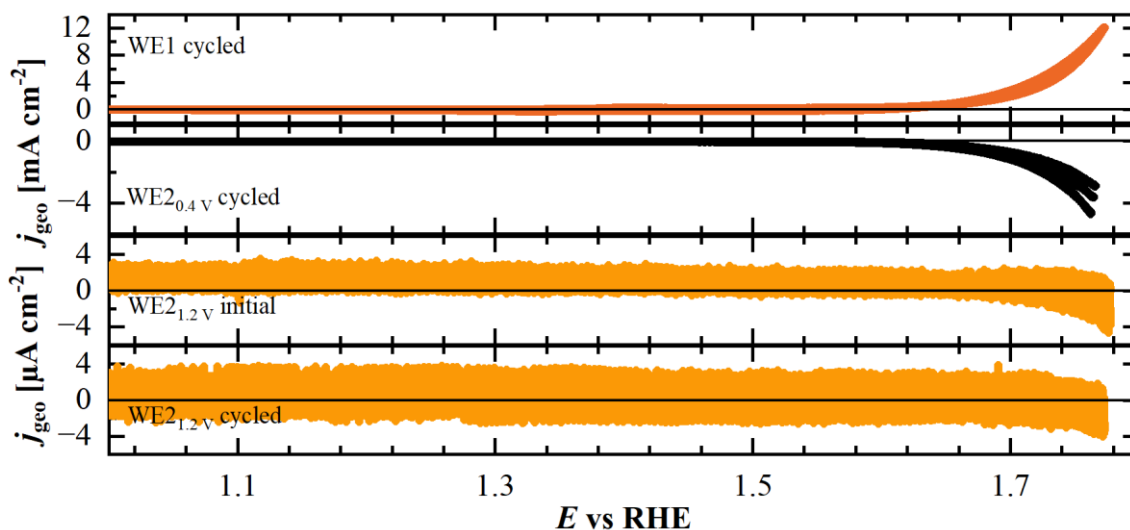


Figure 21: CVs of the WE1 disc current and the corresponding WE2 collector currents of the Platinum ring with a ring potential at 0.4 (WE2<sub>0.4V</sub>) and 1.2 V vs. RHE (WE2<sub>1.2V</sub>) for the detection of O<sub>2</sub> and Mn leaching, respectively. The ring currents of the initial CVs as well as the ring currents after 350 CV (cycled) are shown. Adapted from R ucker et al.<sup>140</sup>

In Figure 21 one experiment depicts the collection of O<sub>2</sub> by applying 0.4 V vs. RHE at the ring electrode (WE2<sub>0.4V</sub>) and the other experiments detect the Mn-reduction by applying 1.2 V vs. RHE to the Pt ring electrode (WE2<sub>1.2V</sub>). First, the OER onset is observed at the WE2<sub>0.4V</sub> above disc potentials of 1.6 V vs. RHE. Furthermore, the results of the WE2<sub>1.2V</sub> suggest low currents for the Mn reduction in which the initial collector experiments show an obvious reduction current of -4  $\mu\text{A cm}^{-2}$  above 1.7 V vs. RHE disc potential. This is first evidence of some reductive species that are generated at the disc electrode. On the other hand, the collector experiments of the cycled catalyst layer (WE2<sub>1.2V</sub> cycled) show noise in the  $\pm 3 \mu\text{A cm}^{-2}$  range with slight reduction currents of about -4  $\mu\text{A cm}^{-2}$ . The electrochemical data provides a potential dependent first evidence of the Mn leaching.

Further analytical proof for evidence of Mn leaching is provided by ICP-MS measurements of the electrolyte after the respective collector experiments with the NiO(111)+10% Mn sample and are noted in Table 2. First, the pristine electrolyte was analyzed to have the baseline of the transition metals contents in solution. The contents of Ni and Mn were close to the detection limits of about 0.007 and 0.012  $\mu\text{g L}^{-1}$  respectively but still suggest minor impurities. The detection of 1.54  $\mu\text{g L}^{-1}$  Fe is also worth mentioning, because of its effect on electrocatalysis of Ni and Co based materials

for OER.<sup>10</sup> A concentration of  $0.902 \mu\text{g L}^{-1}$  of Mn was detected in the electrolyte after the experiment with the 10% Mn sample. Under consideration of the material concentration in the pristine electrolyte, this implies a leaching of about 6 wt% of Mn out of the catalyst layer, compared to 0.5 wt% of the Ni. This proves that there is a measurable leaching of Mn from the electrode, which is stronger than the leaching of the Ni. The leaching product is assumed to be  $\text{MnO}_4^-$  but could not be further identified.

Table 2: ICP-MS results of a) the pristine 0.1 M KOH electrolyte before electrochemical experiments and b) the results of ICP-MS experiments after generation-collection experiments and the calculation of the approximate mass fraction  $\omega$  of dissolved catalyst from the RDE catalyst layer of NiO(111)+10% Mn assuming the stoichiometry  $\text{Ni}_9\text{Mn}_1\text{O}_{10}$ .

a) Pristine electrolyte			b) Electrolyte after generation-collection experiments	
	Average concentration [ $\mu\text{g/L}$ ]	Standard deviation [ $\mu\text{g/L}$ ]		
Mn	0.05	0.00	c(Mn, electrolyte) – pristine	$0.85 \mu\text{g L}^{-1}$
Fe	1.54	0.30	c(Ni, electrolyte) – pristine	$0.66 \mu\text{g L}^{-1}$
Ni	0.06	0.01	V(electrolyte)	0.11 L
Co	0.05	0.01	m(Mn, electrolyte)	93 ng
			m(Ni, electrolyte)	73 ng
			m(NiO(111)+10% Mn, electrode)	$19.6 \mu\text{g}$
			m(Mn, electrode, assuming $\text{Ni}_9\text{Mn}_1\text{O}_{10}$ )	$1.5 \mu\text{g}$
			m(Ni, electrode, assuming $\text{Ni}_9\text{Mn}_1\text{O}_{10}$ )	$14 \mu\text{g}$
			$\omega$ (Mn, from electrode in electrolyte)	6 wt%
			$\omega$ (Ni, from electrode in electrolyte)	0.5 wt%

From the structural insights of the CV and complementary methods above, the OER activity of the electrodes is now considered. The electrocatalytic activity of the materials was compared with CVs at  $10 \text{ mV s}^{-1}$  after electrochemical conditioning. Representative CVs of each sample are plotted in Figure 22a and b. All Co- and Mn-doped samples are compared to the NiO(111) material. The Co-doped samples in Figure 22a have an  $\eta$  similar to the pure NiO(111) sample. More obvious differences for the materials are changes in the oxidation and reduction peak height, which agree to the observations from the conditioning in Figure 21b). The NiO(111)+2% Co sample has a similar curvature of

the CV as the pure NiO(111) sample, whereas the 5% and 10% Co-doped samples have much lower oxidation charges but similar  $\eta$  than the NiO(111) and the +2% Co sample. In the comparison of NiO(111) and the Mn-doped samples in Figure 24b the differences are more obvious. First, the position of the redox peak is slightly shifted towards higher potentials. Second, the oxidation peak shape is changed, which was already discussed for the Figure 20a and b above. Third, the  $\eta$  increases with increasing Mn-doping content.

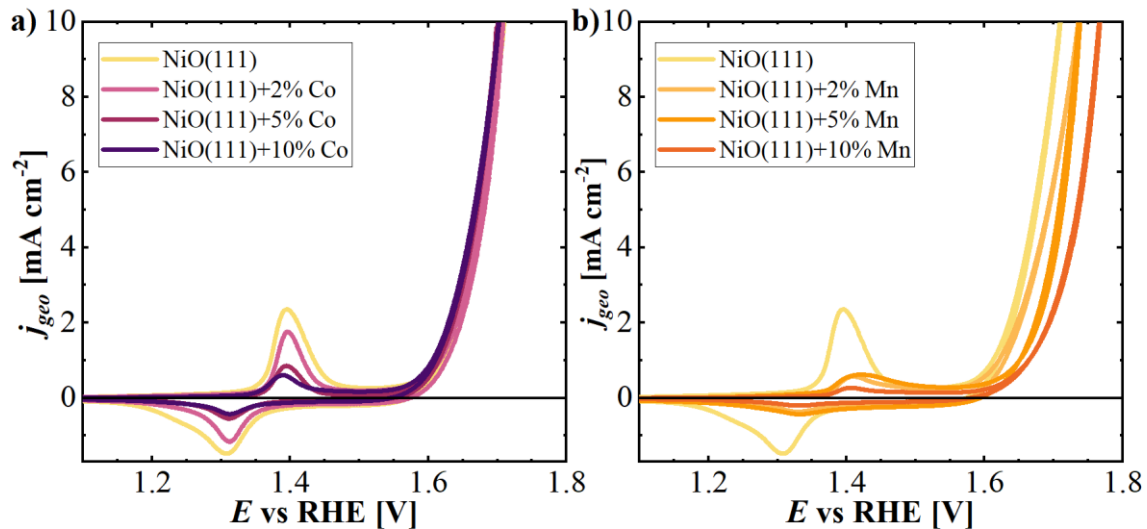


Figure 22: Representative CVs of the a) Co and b) Mn doped samples in comparison to the pure NiO(111) sample. Adapted from R ucker et al.<sup>140</sup>

As metric for the OER activity of each catalyst, the average overpotentials at  $10 \text{ mA cm}^{-2}$  were determined of each independent repetition experiment and are compiled in Figure 23. As Benchmark material, a commercial  $\text{NiO}_{\text{USNano}}$  was added to the comparison, which resembled slightly lower overpotentials than the NiO(111) but a larger standard deviation.

Overall, the NiO(111)+5% Co has the lowest  $\eta$  and the NiO(111)+10% Mn has the highest  $\eta$  with  $447 \pm 16 \text{ mV}$  and  $537 \pm 3 \text{ mV}$ , respectively. Thereby, the Co-doped samples also have a large standard deviation which could be explained by a worse dispersion stability connected to a less homogenous coating of the disc electrodes of the  $\text{NiO}_{\text{USNano}}$  and the Co-doped samples.<sup>9</sup> However, no macroscopic differences were observed regarding the dispersion stability and homogeneity of the catalyst films.

The standard deviation of the pure NiO(111) and the Mn doped materials was acceptable and in the range 1-5 mV. The optimization of the dispersion for each material was out of scope in this study but should be done for future analysis of these materials. The overpotentials of the Mn-doped materials are increased drastically in comparison to the NiO(111) materials.

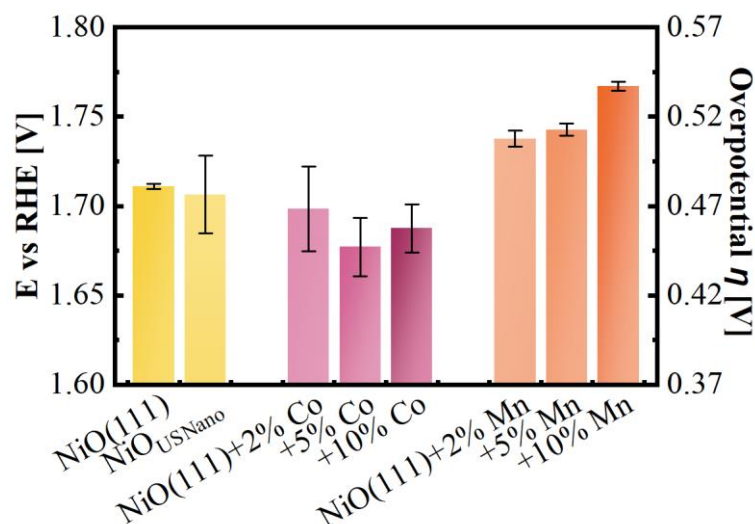


Figure 23: Average of the  $\eta$  at  $10 \text{ mA cm}^{-2}$  of each sample after electrochemical conditioning with an error bar indicating the standard deviation. Adapted from Rucker et al.<sup>140</sup>

The positive effect of Co on Ni-based OER catalysts that is also shown here, was already reported in the literature.<sup>44,58</sup> In studies conducted with comparable catalyst loading and measurement conditions of similar Co-Ni-based OER catalysts,  $\eta$  of about 360 and 470 mV were found, respectively.<sup>146,147</sup> This is well in the range of the observed  $\eta$  for herein studied materials, but showcases the high deviations between literature reports. More detailed discussion of the reproducibility of electrochemical data is done in chapter 5.6.

In contrast, for the Mn containing Ni-based OER catalysts a range of observations were reported, with some increasing<sup>44,148</sup> and others decreasing the OER activity of the host material.<sup>147,149,150</sup> For example, in the study of Dionigi et al.<sup>147</sup> the observed effect of Mn increasing the OER  $\eta$  at  $10 \text{ mA cm}^{-2}$  from 570 mV for pure Ni(OH)<sub>2</sub> to 620 mV for NiMn LDH was explained with theoretical density functional theory calculations of single phased  $\gamma$ -NiMn LDH showing an increase of the reaction free energy of the OER intermediates due to Mn compared to  $\gamma$ -Ni LDH. This contrasts with reports of the positive effect of Mn-doping onto the OER activity.<sup>44,148</sup> The observations of why Mn lead to  $\eta$  decrease for OER was usually not further investigated

However, the differences in the apparent activities could possibly be explained by the variety in synthetic approaches of each study, ranging from wet-chemical approaches to solution combustion methods, which could affect the purity of the catalyst and the chemical state of the Mn incorporated products.<sup>44,147,150</sup> Another consideration is the influence of reproducibility of independent electrochemical repetition experiments. Not every study has reported measures for reproducibility.

The observation of the lower OER electrode activities and the low Ni<sup>II</sup>/Ni<sup>III</sup> oxidation charges of the Mn doped materials contrast with the high physical surface area of the doped metal oxides, that were observed with BET. In the following, the ECSA was probed with  $C_{DL}$  data, that was recorded for this study. The  $C_{DL}$  in Figure 24a, b suggests similar trends to the oxidation charges depicted Figure 21b. The Mn-doped materials exhibit a drastic decreased in  $C_{DL}$ , whereas the Co-doping leads to slightly lower  $C_{DL}$  values. The relative difference between the  $C_{DL}$  of the pure NiO(111) and the doped materials is lower than the difference in the Ni<sup>II</sup>/Ni<sup>III</sup> oxidation charges. However, the analysis of  $C_{DL}$  indicates that small amounts of dopant of just 2% show a large influence onto the  $C_{DL}$ . Overall, the  $C_{DL}$  data gives further evidence that the thin catalyst layers of the different materials are not contributing equally to the charge of the electrode.

The contradiction of the  $C_{DL}$  data to the BET surface areas of the Mn-doped sample, strengthens the argument that most of the physical surface area of the sample observed from physisorption experiments is not accessible for non-faradaic ( $C_{DL}$ ) or faradaic charge (Ni<sup>II</sup>/Ni<sup>III</sup> redox peak). Because Ni<sup>2+</sup> species are insulating and Ni<sup>3+</sup> species are conductive, the electrochemical potential, which controls the oxidation state, directly determines the conductivity of Ni-based oxide and hydroxide catalysts and thus their ECSA.<sup>144</sup> Low conductivity of a catalyst layer can lead to an underestimation of the material's ECSA. In contrast, a previous study on NiO<sub>x</sub>-based transition metal oxides found that introducing cobalt into binary (NiCoO<sub>x</sub>) and ternary (NiCoFeO<sub>x</sub>) materials resulted in enhanced conductivity.<sup>83</sup> Another study in which electrodeposited hydroxide films has suggested that MnO<sub>x</sub>H<sub>y</sub> films are poor electrical conductors.<sup>144</sup> The low conductivity of MnO<sub>x</sub>H<sub>y</sub> films might explain the observations of the low  $C_{DL}$  and Ni<sup>II</sup>/Ni<sup>III</sup> oxidation peak charge in the present study.<sup>144</sup> Keeping in mind the low catalyst loading that was used in this study, the conductivity of the materials should play a minor role.

The CV traces of each material within the considered potential window, as shown in Figure 24a), deviated from ideal box-shaped behavior of the experiments. This narrow window of 200 mV might be insufficient for full charge/discharge cycles of some materials, leading to reduced apparent capacitance values and potentially introducing faradaic metal redox reactions to the detected currents.<sup>105,151</sup> As additional metric for the ideality of the fits, the  $\alpha$ -value was received from the allometric fit of the LSV at different scan rates. The  $\alpha$ -value resembles the deviation of the regression from a linear fit and thus from the ideal behavior of a capacitor and is shown in (Figure A13) for the respective materials.<sup>105</sup> The pure NiO samples have a similar high  $\alpha$ -value close to 0.9, which is

expected, because of the chosen potential window for the experiment being optimized for this material. However, the doped materials exhibit lower  $\alpha$ -values with increasing doping level. This implies that the addition of further transition metals decreases the ideal capacitive behavior of the metal oxides in the respective potential window.

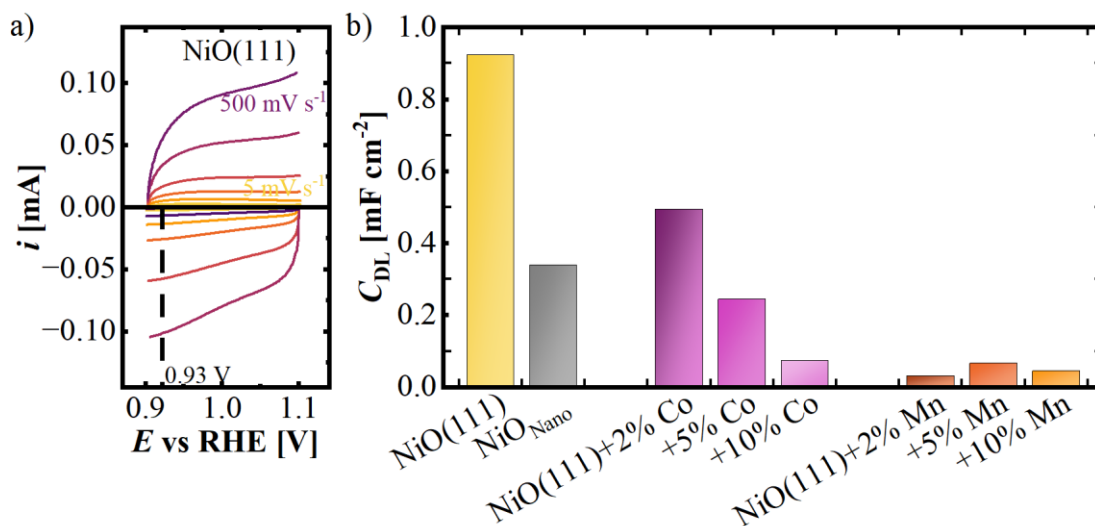


Figure 24: a) Subsequent and negative going LSV at scan rates from 5 to 500  $\text{mV s}^{-1}$  for the example of NiO(111) and the value of 0.93 V vs. RHE at which the current was red of. b) Estimated Double layer capacitance values  $C_{DL}$  from plotting the currents from the LSVs versus the scan rate. Adapted from R cker et al.<sup>140</sup>

Summarizing the electrochemical results, the activity metrics of the NiO(111) and the Co- and Mn-doped materials were found to be comparable to literature. Moreover, the electrochemical behavior upon electrochemical conditioning was interesting and suggested that the Co remains well incorporated, whereas the Mn was found to leach out into the electrolyte. Compiling the observed leaching of the Mn from the conditioning of the Mn-doped materials and with the low activity towards the OER, the Mn-doped material is not suitable for application as OER electrocatalyst in alkaline media. Both dopants indicate a much lower surface reconstruction, apparent by lower  $\text{Ni}^{\text{II}}/\text{Ni}^{\text{III}}$  oxidation peak charge. The changes of the material will be further studied by spectroscopic analysis before and after electrochemistry in the following section.

### 5.2.2 Spectroscopic analysis after electrochemical treatment

In the following, the spectroscopic techniques of XAS and XPS were used to study the bulk and surface structure of representative materials for pure NiO and its Co and Mn-doped counterparts. The techniques were applied to study pristine materials (before, bf) as well as electrochemically treated (after electrochemistry, aEC) samples.

XAS studies before and after electrochemical treatment were conducted to elucidate the impact of Co and Mn doping on the bulk oxidation state and crystal structure, thereby correlating these aspects with the electrocatalytic activity of the samples. Notably, bf-samples were derived from as-received powder samples, whereas aEC-samples were obtained from processed films on GC disc electrodes following the application of an electrochemical protocol (Table A4). The oxidation state trends were qualitatively assessed through edge position analysis, where the centroid of normalized XANES spectra (Figure A14) was used to determine the edge energy.<sup>93,126</sup> The local coordination environment of the materials were determined by comparing the EXAFS of the samples with suitable references. Insights from the Ni-K, Co-K and Mn-K edges are compared below.

In the following sections, the relationship between the edge energy  $E$  subtracted by the corresponding metal edge energy  $E_0$  will be discussed. Initially, the effects of doping on the as-prepared powders (bf samples) were studied. The initial Ni-K edge position of undoped NiO(111) fell between the edge energies of the reference materials NiO<sub>Roth</sub> and LiNiO<sub>2</sub> with nominal oxidation states of Ni<sup>II</sup> and Ni<sup>III</sup>. This indicates that the initial oxidation state of Ni was between II and III. An initial oxidation state of 2.5+ is estimated for the NiO(111), which is highlighted as a guideline in Figure 25. No changes in the edge position or corresponding Ni oxidation state were observed for samples doped with either Co or Mn at concentrations of 5% and 10%.

At the Co K-edge of the Co-doped NiO(111) materials, no significant variation between the samples was observed, and the edge position matched with that of the CoO reference material, assuming an oxidation state of approximately II. In contrast, at the Mn-K edge of Mn-doped NiO(111), the samples displayed distinct edge positions between those of Mn<sup>III</sup> and Mn<sup>IV</sup> references, with 10% doping resulting in a higher edge position than 5% doping. Notably, the edge position at the Mn K-edge depended on the level of doping, whereas the corresponding Ni-K edge position remained unchanged. This observation can be rationalized by suggesting that changes in oxygen stoichiometry occurred, rather than alterations to the metal coordination environment. Qualitatively, the

Fourier Transform of EXAFS data (Figure 26) supports higher oxygen coordination with 10% Mn doping compared to 5% Mn doping, which is consistent with the expected changes in metal oxidation state.

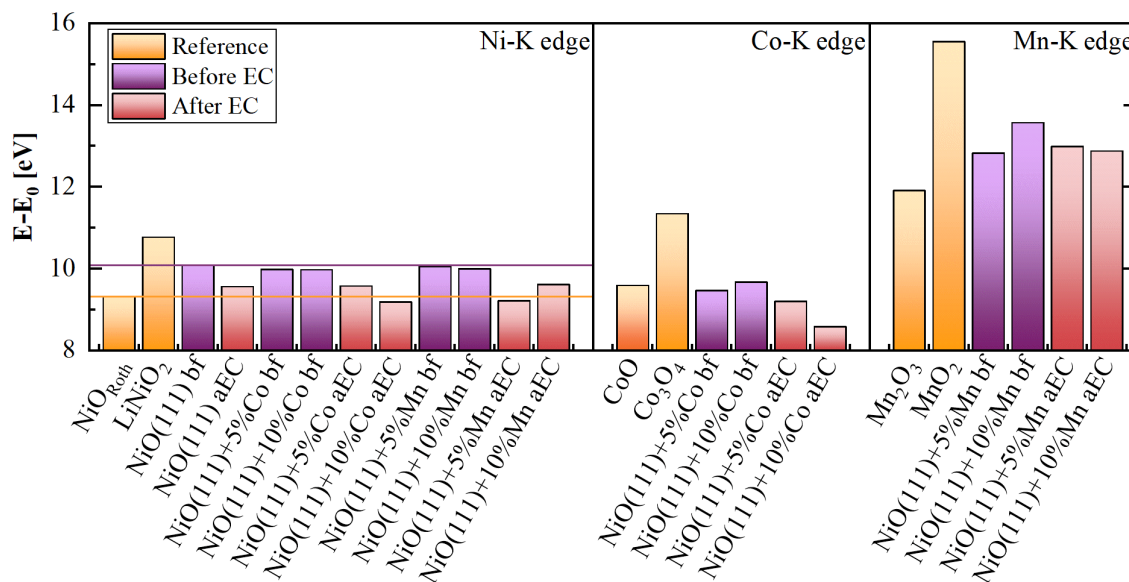


Figure 25: Normalized edge energies  $E-E_0$  from XANES, subtracted by the respective edge energies of the Ni-, Co- and Mn-K metal edge energies  $E_0$ . Materials of different doping levels before (bf) and after EC (aEC) were tested. Guide lines for the  $E-E_0$  of  $\text{Ni}^{\text{II}}\text{O}_{\text{ROTH}}$  and  $\text{NiO}(111)$  were drawn in yellow and violet, respectively.

Next, it was studied how electrochemical treatment affects the observed edge positions relative to the as-prepared powder samples. This *ex-situ* analysis was done according to the description in chapter 3.2.1. Briefly, the aEC samples are a closer approximation of the active state during electrocatalysis than the as-prepared samples, resembling the irreversible changes from EC treatment.<sup>114</sup> Following the EC treatment, both the undoped and doped  $\text{NiO}(111)$  samples exhibited a reduced edge positions at the Ni-K edge, indicating decreased oxidation state relative to their as-prepared powder samples. The edge positions of these samples were consistent, varying by less than 0.3 eV from that of the  $\text{Ni}^{\text{II}}$  reference material depicted in Figure 25. At the Co-K edge of the Co-doped samples, no significant shift was observed for 5% Co doping, whereas the 10% Co doping sample displayed an edge position lower than that of its corresponding as-prepared powder and lower than the  $\text{Co}^{\text{II}}\text{O}$  reference material.

Similarly, at the Mn-K edge of the Mn-doped samples, the trends in edge position were comparable to those observed at the Co-K edge, with no significant change for 5% doping and a decrease in edge position for 10% doping. In contrast, the Mn-K edge position remained above that of the  $\text{Mn}^{\text{III}}$  reference material. The equalization of the oxygen stoichiometry among the differently doped samples is hypothesized to occur due to the

formation of the active OER state. Furthermore, the presence of the  $\text{Mn}^{\text{IV}}$  species in the Mn-doped material suggests introducing strain and electronic distortion into the coordination environment, contributing to the observed instability of the Mn materials.<sup>58</sup> This observation suggests that Mn-doping leads to the oxidation of  $\text{Mn}^{\text{III}}$  to  $\text{Mn}^{\text{IV}}$  and subsequently to the reduction of  $\text{Ni}^{\text{III}}$  to  $\text{Ni}^{\text{II}}$ . This was evident by the lower aEC sample edge energies compared to their bf counterparts. However, it is essential to note that a decrease in edge position does not necessarily imply a change in oxidation state. The edge position can be significantly influenced by the coordination environment.<sup>114</sup> Therefore, the EXAFS data was analyzed to qualitatively assess whether the observed low edge positions are indeed indicative of an unusual coordination environment due to the different dopant species.

The EXAFS analysis in Figure 26 depicts the Ni-K, Co-K and Mn-K edge of the 10% samples, because they are representative for each dopant. The EXAFS revealed that the peak positions and relative intensities were found to be consistent with the respective metal-oxide references for Ni and Co, confirming that the bulk structure is consistent with a rock salt metal-oxide framework, as supported by previous PXRD analysis. However, the presence of surface hydroxides could not be resolved in our EXAFS experiments. The portion of the reconstructed surface might be too low in relation to the bulk state. Consequently, the surface structure is elucidated by XPS at later point.

The Co-doped samples, the NiO(111)+10% Co sample had Co-O and Co-M' peaks aligning with the Ni-O and Ni-M' peaks at the same sample's Ni K-edge, which implies a similarity in the coordination environment of the Co and the Ni.

Moving on to the Mn-doped samples, the Mn-M' peak position was found to align with the Ni-M' peak position at the same sample's Ni K-edge than with the Mn-Mn peak position of MnO and the other Mn reference materials. The Mn-O peak has distinct reduced distances, being close to the  $\text{Mn}^{\text{III}}$  and  $\text{Mn}^{\text{IV}}$  references. This indicates a similar oxygen coordination as the  $\text{Mn}_3\text{O}_4$  and  $\text{MnO}_2$  reference samples. Notably, there is no evidence of separate phase formation of  $\text{Mn}_3\text{O}_4$  and  $\text{MnO}_2$ , because the Mn-M' distances rather align with the Ni-M' distances. Moreover, it is hypothesized that also the Mn is incorporated into the host structure but exhibiting a high valent coordination of oxygen.

These observations support that both Co and Mn could be incorporated into the NiO matrix. Furthermore, the unusually low edge position of the 10% Co doped sample may be attributed to an untypical coordination environment of the Co in the doped materials, compared to the cubic Cobalt (II) oxide. However, further experiments would be required

to rigorously elucidate this point. Additionally, the shifts in the Mn-K edge may not be quantitatively converted into a change in Mn oxidation state, as Mn also experienced a similar bonding environment to that of Ni. Nevertheless, the magnitude of the edge position is higher than that of Co, indicating possible oxidation above  $\text{Mn}^{\text{III}}$ .

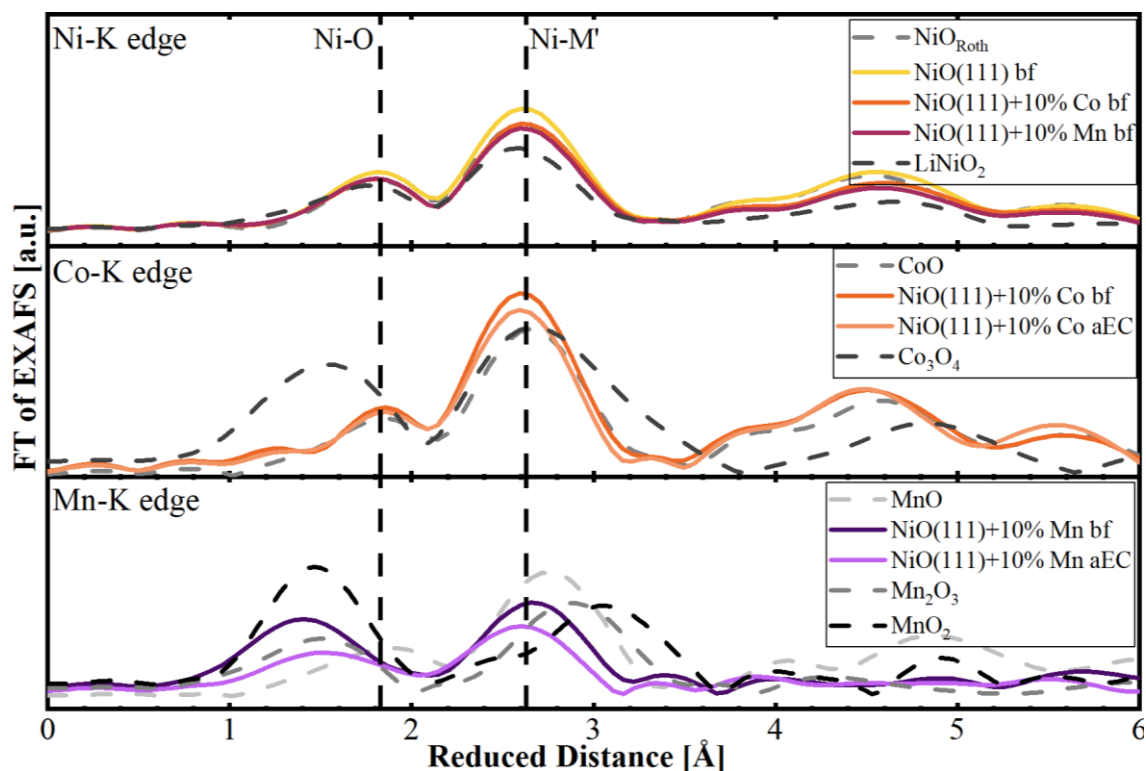


Figure 26: Fourier transformation of the Ni-, Co- and the Mn-K EXAFS for the prepared samples and reference materials. The reduced distance between Ni-M' as well as the Ni-O from the Ni-K edge are marked as a guide to the eye.

Moreover, metal sites forced to untypical bonding environments can lead to catalytic enhancements. This was suggested for a prominent OER candidate system with octahedral Fe sites with shortened Fe-O distances in an  $\text{Ni}_{1-x}\text{Fe}_x\text{OOH}$  system.<sup>62</sup> This may explain the slight decrease in  $\eta$  observed in Figure 24 upon Co doping. On the other hand, the high edge position of  $\text{Mn}^{\text{IV}}$  is correlated with increased OER  $\eta$ .<sup>93,152</sup> As was denoted in the RDE section above, high valent metal cations may be lost to the electrolyte, particularly for the Mn-doped materials.<sup>93</sup> Finally, neither  $\text{Ni}^{\text{II}}$  nor  $\text{Co}^{\text{II}}$  are known to be high-performance active sites,<sup>153–155</sup> but they might be oxidized on the surface, which will be probed by XPS in the following section.

XPS was performed to gain insights into the irreversible surface changes that occurred because of electrochemical treatments. The XPS data were collected from both the before-electrochemistry (bf) samples and the after-electrochemistry (aEC) samples by removing

the coated GC disc substrate electrode at a stop potential of 1.7 V vs. RHE from the electrochemical cell.

The survey spectra of the aEC experiments are depicted in Figure A15. The spectra revealed the expected presence of elements on the surface of the samples. Notably, the NiO(111) bf-sample exhibited peak positions for O, Ni, C, F, and S, as well as X-ray satellite peaks around the dominant signals like Ni 2p and F 1s from the non-monochromatized Mg K $\alpha$  source. Furthermore, the survey spectra of Co- and Mn-doped samples also revealed the presence of their respective dopant elements.

Due to the complexity of transition metal 2p spectra, peak deconvolution was limited to high-resolution O 1s spectra. Figure 27a) displays the Ni 2p<sub>3/2</sub> spectra for NiO(111) and its corresponding 5% Co- and Mn-doped bf-samples. Notably, the Ni 2p<sub>3/2</sub> spectra of all three samples exhibit similarities, suggesting a similar surface composition and chemical state of Ni atoms that align with the XANES analysis results obtained from the Ni-K edge. As a result, even at low doping levels, there is a relatively minimal impact on the surface-sensitive XPS signal. In addition, the Ni 2p spectra reveal characteristic multiplet splitting consistent with NiO, featuring a dominant peak at a binding energy of 854.2 eV and a less intense satellite peak at 855.9 eV.<sup>156</sup> The first signal at 854.2 eV is neither found for Ni(OH)<sub>2</sub> samples nor for NiOOH.<sup>156</sup> The signal at 855.9 eV corresponds to surface hydroxide and is typical for Ni 2p spectra of NiO.<sup>125,156</sup>

Following electrochemistry, the survey spectra depicted in Figure A15b reveals an unexpected presence of K signals at the sample surface, which can be attributed to residual KOH electrolyte that was not fully removed by rinsing the GC disc with ultrapure water after the electrochemical experiment. Figure 27b shows the Ni 2p<sub>3/2</sub> spectra for the aEC-samples. For all samples, the peak at 855.9 eV increased in intensity, but the magnitude of this change varied significantly between the samples. The NiO(111) aEC sample exhibited the largest increase in peak intensity, followed by the 5% Co aEC sample, and then the 5% Mn aEC sample. This enhancement is attributed to the partial formation of NiOOH and Ni(OH)<sub>2</sub>, with the remaining NiO surface characterized by a corresponding decrease in intensity at 854.2 eV.<sup>156</sup> This formation of NiOOH and Ni(OH)<sub>2</sub> from NiO after electrochemical treatment was reported previously for chemical vapor deposited NiO<sub>x</sub> films as well as for thin film catalysts from hydrothermal synthesis.<sup>79,157,158</sup> It's worth noting that the decomposition of NiOOH to Ni(OH)<sub>2</sub> may have occurred during the *ex-situ* experiment, as has been observed in recent studies.

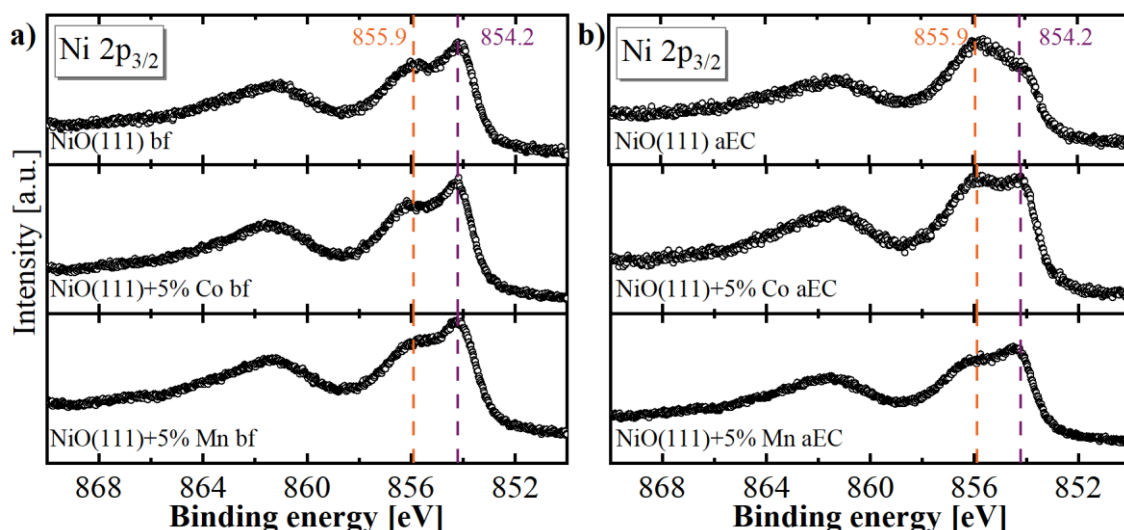


Figure 27: XP-spectra of the Ni  $2p_{3/2}$  of the of the NiO(111) samples without dopants, as well as with 5% Mn and Co doping a) before electrochemistry (bf) and b) after electrochemistry (aEC). All samples were measured as coated films on a GC substrate.

Figure A16 displays the Co 2p and Mn 2p spectra, which exhibit relatively low intensities due to the limited amount of dopant present in the materials. The Co  $2p_{3/2}$  spectra show a satellite peak at 786 eV, indicating the presence of a  $\text{Co}^{\text{II}}$  species. In contrast, the Mn 2p spectra does not display a satellite peak at 647 eV, suggesting that no  $\text{Mn}^{\text{II}}$  species are present.<sup>125</sup> This finding suggests that the Co surface species in the bf material contain  $\text{Co}^{\text{II}}$  species, while the Mn surface species are predominantly  $\text{Mn}^{\text{III}}$  or higher oxidation states. Both observations align with the XAS results and support the notion of a similar surface composition to the bulk. Notably, the Mn 3s spectra doublets could not be fully resolved in this study, which suggests an correlation between the spacing of the doublets and the Mn oxidation state.<sup>159</sup>

Figure 28a shows the O 1s spectra of the bf samples. The features of the O 1s spectra were attributed to three species of different chemical shifts. The feature A at 529.8 eV was attributed to lattice oxide oxygen in  $\text{NiO}$ <sup>125</sup>, was expected for the oxide-based materials and is the dominant signal in the bf-samples. The feature B is attributed to hydroxide oxygen as a native hydroxide layer or as non-stoichiometric oxygen<sup>125</sup>. The feature C is attributed to oxygen from adsorbed water and organic species.<sup>125</sup> Latter can be explained by contribution of the sulfonic acid and fluorinated ether groups due to the Nafion content in the thin films.<sup>160,161</sup> Comparing the fitting results of O 1s of the different bf-samples, is suggesting that the materials are similar. The peak area ratios of the A/B/C in the O 1s spectra differs for the 5% Mn bf sample with 1/0.22/0.1 compared to the bf-NiO(111) and the 5% Co bf-samples with 1/0.27/0.1 and 1/0.26/0.1, respectively. The

higher ratio of feature A in 5% Mn bf-sample can be explained by a contribution of higher valent Mn species in the material (e.g. Mn<sup>III</sup>) as supported by XAS.<sup>125</sup>

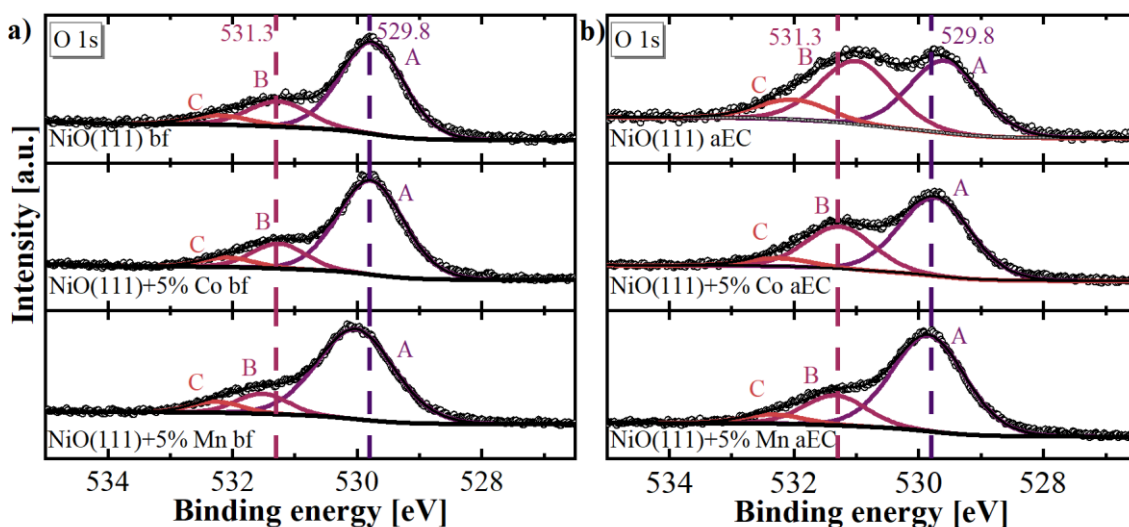


Figure 28: XPS O 1s spectra of the of the NiO(111) samples without dopants, as well as with 5% Mn and Co doping a) before electrochemistry (bf) and b) after electrochemistry (aEC) with a stop potential of 1.7 vs. RHE. All samples were measured as thin films on a GC substrate.

Figure 28b shows the corresponding O 1s of the aEC-samples. For all aEC-samples feature B became more dominant, together with the lower relative amount of feature A. This could result from the formation of NiOOH and Ni(OH)<sub>2</sub> on the surface of the materials after electrochemistry.<sup>158</sup> It is also likely that residual KOH contributes to the feature B. The Contribution of KOH to feature B is considered negligible due to the relatively low amounts of observed K in the survey spectra. As for the Ni 2p<sub>3/2</sub> spectra, the O 1s spectra of the aEC samples differ in the change of surface reconstruction depending on the dopant. The simple peak structure of O 1s allows the relative quantification of surface change. The 5% Mn doped sample resembles the least change in the relative peak area. In fact, the relative ratio of feature B changes from 0.22 to 0.3 for the 5 % Mn comparing the bf- to aEC-sample. The relative ratio of feature B of the 5% Co aEC sample changes from 0.26 to 0.54, in which the feature B will also include minor contributions of the Co(OH)<sub>2</sub> species. The feature B of the pure NiO(111) on the other hand has the largest change of the feature B from 0.27 to 0.88. These observations indicate that the surface of pure NiO(111) transforms the most to a NiOOH/Ni(OH)<sub>2</sub> rich surface layer.

The observation from XPS is consistent with the oxidation changes observed in XANES analysis and the CV data, which were described earlier. In contrast, doping with Co and Mn hindered the transformation of the NiO host structure to a NiOOH/Ni(OH)<sub>2</sub>,

with Mn being the most inhibitive dopant. This is supported by minor changes observed in XANES data. Interestingly, the relative contributions and changes of the discussed XPS features also correlate with CV analysis, which revealed a strong redox peak for pure NiO(111), indicating significant surface reconstruction with (oxy)hydroxide formation. However, lower redox charges were observed for the doped samples. The modest transformation of Co- and Mn-doped samples to the catalytically active NiOOH terminated surface might explain the observed low activity increase upon electrochemical activation in OER evaluation. However, it's worth noting that adding Co and Mn is expected to improve OER electrode activity, so we interpret our findings as follows: the decreased NiOOH formation and, for Mn doping, also parasitic currents from leaching of Mn, likely minimize the effect of activity improvement. Notably, the case of Mn doping even resulted in a decrease in OER electrode activity.

### 5.2.3 Summary of the effects of Co and Mn doping

In summary, the effect of Co and Mn doping on the OER electrode activity was observed to be modest for the studied faceted NiO(111) system, compared to generally reported activity enhancement of bimetallic transition metal oxides. The influence of Co and Mn dopants on the physical surface area was found to be partial contrary to the electrochemical activity trends. The effect of different doping levels on the OER electrode activity was observed to be influenced by the extent of surface reconstruction of the rock salt pre-catalyst to a Ni(OH)<sub>2</sub> terminated surface. The hypothesis of the differences in surface reconstruction was analyzed with XPS of the catalysts before and after electrochemical tests. XPS revealed a modest change in Mn-doped samples relating to the lesser degree of hydroxide formation may hinder the formation of a more active NiOOH surface during OER, leading to limited activity. The Co-doped samples exhibited moderate surface reconstruction and decreasing the OER  $\eta$  for lower doping levels. The increase in OER  $\eta$  at higher doping levels (< 10 mol%) was attributed to hindered reconstruction by Co<sub>3</sub>O<sub>4</sub> impurities, indicating that electrochemical conditioning may not be an effective strategy for provoking surface reconstruction of higher Co-doped materials. The XAS analysis was found to be in accordance with the electrochemical results, indicating a lack of changes in the bulk Ni oxidation state with doping, and modest changes in activity with doping. The absolute oxidation states of Ni are close to II, suggesting that it may not be among the most active pre-catalyst for OER. The generation-collection experiments of Mn dissolution by RRDE and supporting ICP-MS results

suggest corrosion of Mn from the film, which can partially explain the low OER electrode activity and minor degree of hydroxide formation. The instability of the Mn material is suggested as a focus for future studies. The main driver for activity is suggested to be various factors, including dopant metal sites in an untypical bonding environment, surface hydroxides, and changes in electrochemically accessible surface area. Overall, the results showed that the combination of facet-control and transition metal doping for Ni oxide-based catalysts as a promising strategy to study the effect of Co and Mn doping on the OER activity. However, further material optimization by tuning synthesis parameters is necessary to develop more active catalysts, such as a successful incorporation of Fe into faceted NiO(111).

### 5.3 Studying the introduction of Fe into Ni hydroxide and oxide

*The materials studied in this chapter were prepared in collaboration between the DLR and the UOL in the UOL labs by Dr. Dereje Hailu Taffa. Most of the content of this chapter is prepared for publication in a peer reviewed paper. Konstantin Rücker performed the XPS analysis, the XAS analysis, the Raman spectroscopy analysis and the electrochemical characterization. Dr. Dereje Hailu Taffa performed the MW synthesis, the PXRD experiments, the BET analysis and the HR-TEM analysis. Floris van Lieshout has supported the Raman spectroscopy. Dr. Elliot Brim performed TEM experiments.*

The synthesis of the materials in this chapter is a MW approach based on the synthesis in chapter 5.2 with special emphasis on producing a phase pure Fe-doping. Briefly, to synthesize the materials, precursor nitrate salts were dissolved in dry methanol. During addition of iron, the control of the pH was crucial due to the acidity of the  $\text{Fe}(\text{NO}_3)_3 \cdot 9\text{H}_2\text{O}$  precursor salt. This was mitigated by the addition of KOH dissolved in methanol to adjust the pH value. A longer MW synthesis time of 180 minutes at  $140^\circ\text{C}$  compared to the Co/Mn-doping approaches above was chosen,<sup>140</sup> to mitigate too high molar ratios of Fe in the product. The tendency of Fe to be overproportioned in the product was explained by higher hydrolysis rates of  $\text{Fe}^{\text{III}}$  compared to the  $\text{Ni}^{\text{II}}$ .<sup>162</sup>

On one hand, the Fe-doped  $\alpha$ -Ni(OH)<sub>2</sub> received after washing the product of the MW synthesis was characterized. On the other hand the  $\alpha$ -Ni(OH)<sub>2</sub> was calcined at  $400^\circ\text{C}$  to obtain Fe-doped NiO(111). However, ICP-MS analysis of the optimized synthesis route for Fe incorporation still resulted in an apparent molar ratio of Fe that deviated significantly from the intended Fe content (Table A6). Therefore, all doping levels reported in this study are expressed as mol% based on the apparent Fe content determined by ICP-MS. The powder X-ray diffraction (Figure A17) patterns indicate that the hydroxide material remains phase-pure across all doping levels. Nevertheless, the addition of iron leads to peak broadening, which is consistent with a decrease in crystallite size, as calculated using the Scherrer equation (Table A7). In contrast, the oxide materials obtained minor peaks of  $\text{Fe}_2\text{O}_3$  alongside the characteristic NiO reflexes for molar ratios of 24% Fe and higher, after calcination, respectively. Nitrogen physisorption experiments reveal a notable change in the pore structure of the material upon Fe addition, with a notable increase in pore volume at approximately 5 nm, starting from the 5% sample and increasing up to the 31% sample. The specific surface area, as determined by BET analysis, is also strongly affected by doping, with a pronounced increase in surface area

observed at 13% Fe content. The drastic change observed by the BET surface area suggests a significant impact of Fe doping on the materials in morphology.

The TEM images suggest nanosheet morphology of Ni(OH)<sub>2</sub> was preserved after Fe incorporation, though with reduced lateral dimensions (Figure A18). Upon annealing at 400 °C, pristine NiO(111) developed hexagonal pores, while Fe-doped samples exhibited pore merging into larger, irregular voids, indicating that Fe modifies the stability of the pore framework during crystallization. While lattice spacings in Fe-doped samples revealed additional crystal planes beyond the (111) orientation, PXRD intensity ratios confirmed that Fe did not significantly alter the global crystal orientation. These observations further underline that Fe incorporation affects nanoscale morphology and local crystallinity rather than the overall orientation.

Overall, the addition of Fe was found to have a profound impact on the physisorption results. The data for the oxide materials suggest that Fe additions of 24% and higher are not fully incorporated into the rock salt host structure. To confirm the successful incorporation of Fe into the hydroxide host structure and the lower-doped oxide host structures, further spectroscopic characterization such as XAS, Raman, and XPS is necessary. Furthermore, the effect of Fe addition on electrochemical behavior and OER electrocatalysis will be investigated in detail in the following section.

#### 5.3.1 Spectroscopic study of the Fe incorporation

The spectroscopic analysis aims to provide evidence on whether the Fe is successfully doped into the Ni hydroxide and oxide host structures or if separate Fe phases are formed, even at low Fe contents. The Ni K-edge XANES spectra, shown in Figure 29a, reveal that the edge energy of the Ni(OH)<sub>2</sub> samples are slightly higher than the oxide samples, for both the pure and the Fe containing samples. However, the XANES spectra after Fe-incorporation induces a slide shift towards lower edge energies. Notably, all the edge positions are found to be between those of the Ni<sup>II</sup>O and LiNi<sup>III</sup>O<sub>3</sub> reference samples, indicating an oxidation state of about +2.5 for the oxides and +2.7 for the hydroxides. In the literature,  $\alpha$ - Ni(OH)<sub>2</sub> from MW synthesis was reported to have oxidation state of +2.<sup>64</sup> Therefore, the materials produced in this study initially have a relatively high oxidation state.

The Fe K-edge XANES spectra, presented in Figure 29b, display a similar trend. The hydroxide and oxide materials exhibiting similar edge shapes. Nevertheless, the edge positions of the materials appear to be slightly above those of the Fe<sup>III</sup><sub>2</sub>O<sub>3</sub> reference

sample, suggesting an oxidation state of approximately III or higher. Similar oxidation states were found for MW based Ni-Fe mixed hydroxides in the literature.<sup>64</sup> However, it is essential to consider that the edge energies can also be influenced by the coordination environment.<sup>163</sup>

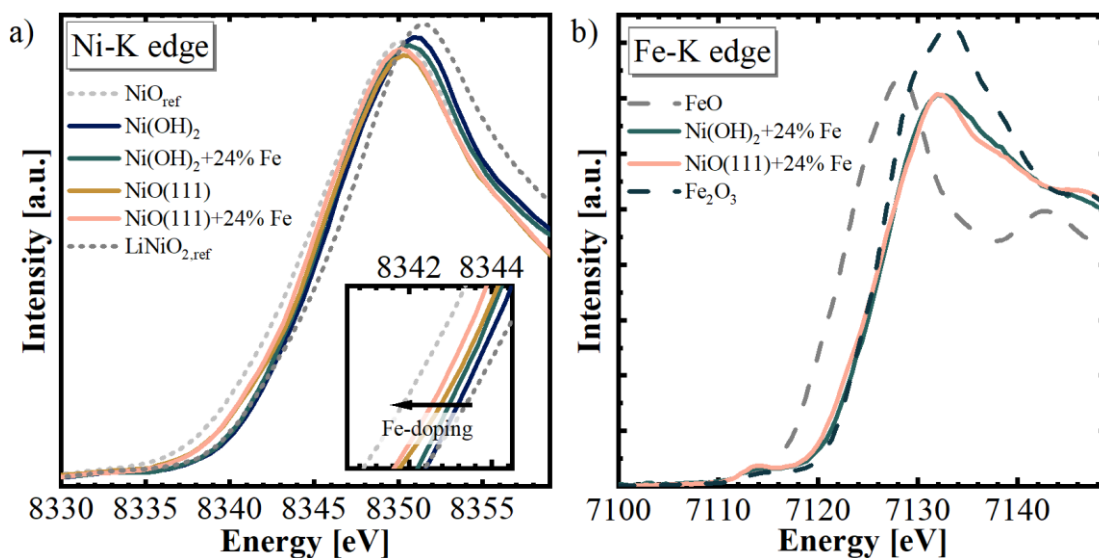


Figure 29: XANES of a) Ni-k edge and b) of Fe-k edge including some reference material. All experiments have been performed on thin films coated on GC discs.

To further elucidate the coordination environment of the materials, the EXAFS was analyzed. The EXAFS of the doped hydroxide samples is represented in Figure 30a. The comparison of the reduced distances of the Ni-M' distances to the Fe-M' distances in one graph was chosen for better comparability. No changes of the Ni-coordination are observed after Fe addition, highlighted with the  $\text{Ni}_{\text{Ni(OH)}_2}\text{-M}'$  reference line of the pure sample. The hydroxide materials display a similar Ni-O distance, but with a different Ni-O/Ni-M' relative ratio and a higher Ni-M' distance of about 2.9 Å. The reported  $\text{Ni}_{\text{Ni(OH)}_2}\text{-M}'$  distance is higher than reported for comparable  $\alpha\text{-Ni(OH)}_2$  materials,<sup>64</sup> but can be explained by the higher oxidate state of the hydroxide material.

The observation, that the Fe content does not influence the distances in the Ni-k edge EXAFS suggests a lack of interaction between the Fe and the Ni, even at Fe-contents of 24%. was used for interpreting the nature of the interaction between Ni and Fe. The Fe K-edge EXAFS spectra of the hydroxide materials reveal an overlap with the reduced Ni-M' distance of the hydroxide at the 5% Fe doping level.

However, at 24% doping, the peak splits into two distinct features, indicating the presence of two different coordination environments for the Fe atoms in the  $\text{Ni(OH)}_2+24\% \text{ Fe}$ . The difference in distance between the Fe-M' peak and the reference

hydroxide  $\text{Ni}_{\text{Ni}(\text{OH})_2}\text{-M}'$  distance suggests that a separate phase exists, in which Ni and Fe do not share the same local environment.

In the case of the oxide materials, depicted in Figure 30b, the Fe-M' peak is shifted to higher distances compared to the oxide  $\text{Ni}_{\text{NiO}}\text{-M}'$  reference, and a larger Ni-O peak is observed. Furthermore, the coordination environment of the Fe in both oxide materials appears to differ from that of the Ni, implying that the Fe is present in a distinct phase. This suggests that the Fe is not fully incorporated into the  $\text{NiO}(111)$  host structure, but rather forms a separate phase, even at low doping levels. Unfortunately, no complete dataset for all samples could be acquired for both samples. Still, the trends suggest a phase separation also occurring at 5% Fe contents.

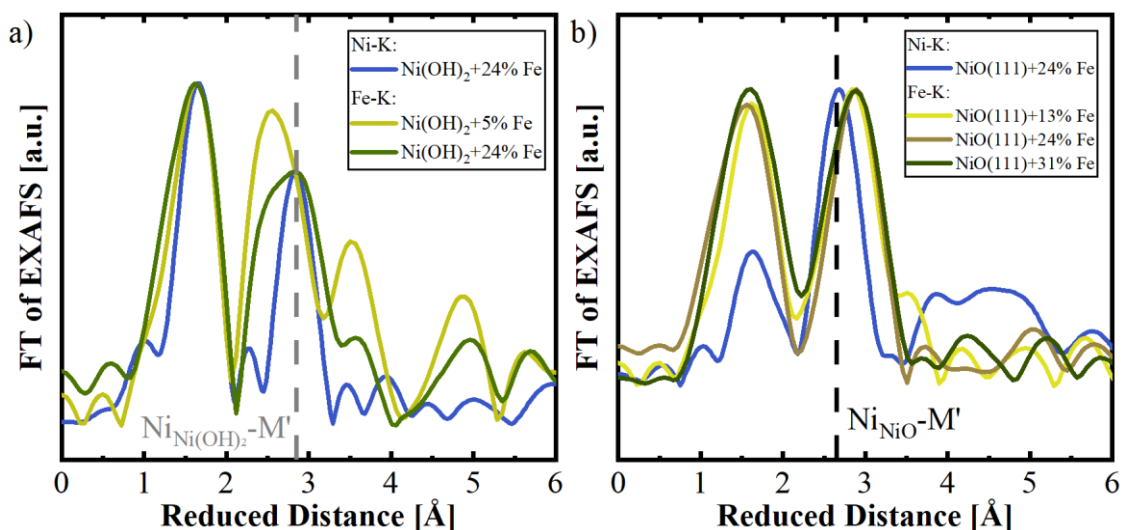


Figure 30: EXAFS of a) the doped hydroxide materials and d) the oxide materials, both including the respective reference distance of Ni-M' pure  $\text{Ni}(\text{OH})_2$  ( $\text{Ni}_{\text{Ni}(\text{OH})_2}\text{-M}'$ ) in gray and of pure  $\text{NiO}(111)$  ( $\text{Ni}_{\text{NiO}}\text{-M}'$ ) in black. All experiments have been performed on coated GC discs.

To gain a more complete understanding of the catalyst's properties Raman spectroscopy was used as a complementary technique following the XAS analysis. In general, the hydroxide samples have been prone to calcination by the laser. The vulnerability to calcination was increasing with Fe content, possibly due to the brown color after Fe addition accompanied with increased laser absorption. The calcination of the catalyst material was observed by slight change of the peaks but mostly by Fluorescence at higher wavenumbers and qualitatively by darkening of the powder observed in the Microscope. According to this, the number of scans needed to be decreased for the hydroxide materials.

Figure 31 represents the Raman experiments of hydroxide samples. The signal A is weak for the pure  $\text{Ni}(\text{OH})_2$  sample and can be attributed to the vibrational  $\text{Ni}^{\text{II}}\text{-OH}$  mode

( $A_{1g}$ ).<sup>58,119</sup> This peak is shifted to higher wavenumbers of  $510\text{ cm}^{-1}$  with increasing Fe doping level. The highest shift was observed at 5% of Fe content. This peak was already reported to be sensitive to structural changes in the lattice, e.g. by temperature or defects.<sup>63,164</sup> The peak B at  $680\text{ cm}^{-1}$  is increasing in intensity with Fe doping and is attributed to  $A_{1g}$  vibrational mode of Fe–O.<sup>58</sup> The peak position of the Fe–O vibrational mode is independent of the Fe content. The peaks C at  $\sim 1000$  to  $1300$  could arise from the precursor  $\text{Ni}(\text{NO}_3)_2$  and  $\text{Fe}(\text{NO}_3)_3$  residuals in the powder after washing. For  $\text{Ni}(\text{NO}_3)_2 \cdot 6\text{H}_2\text{O}$  signals at  $1042$ ,  $1337$  and about  $1456\text{ cm}^{-1}$  were reported.<sup>49,165</sup>

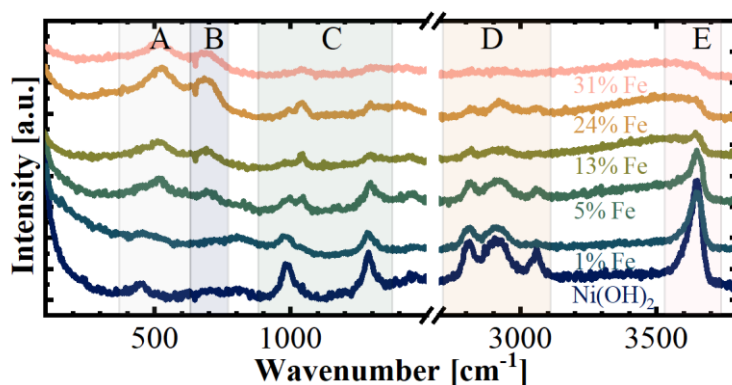


Figure 31: Raman Spectra of the Fe doped Hydroxide samples. The peaks are highlighted with annotations from A–E for the hydroxides.

In the higher wavelength regime of the hydroxide spectra in Figure 31, Signal D was assigned to characteristic C–H stretching vibrational modes of organic substances like precursor benzyl alcohol and possible impurities like fingerprints.<sup>166</sup> The fading of the peak D with increasing Fe content could not be fully resolved. The fading of D could be related to reduced number of readings with increased Fe content. However, the complete disappearance could be related to an easier removal of organic contaminants due to smaller crystallites, as stated above. The characteristic peak E at  $3650\text{ cm}^{-1}$ , which is attributed to a characteristic O–H stretching modes of  $\alpha\text{-Ni}(\text{OH})_2$ ,<sup>51</sup> is drastically broadening with increased Fe doping. It was suggested that this peak broadening can be due to disorder which is promoted by ions between the layered structures and changing hydration.<sup>49</sup> Similar broadening effects were found for oxide and hydroxide samples in PXRD. It is hypothesized that this peak broadening and diminishing is also attributed to the decreasing crystallite sizes.

Figure 32 represents the Raman spectra of the oxide samples. Signal A and B are minor but could be assigned to 1P Phonon modes  $160\text{ cm}^{-1}$  and transversal Optical lattice modes of NiO at  $390\text{ cm}^{-1}$ .<sup>63,167</sup> Peak C was assigned to the  $d(\text{O–Ni–O})$  bending ( $E_g$ ) mode of

the NiO, reported at  $480\text{ cm}^{-1}$ . The Signal D was also found in the hydroxide samples and is assigned to A1g vibrational mode of Fe–O at  $680\text{ cm}^{-1}$ . The peak intensity of Peak C is decreasing with the doping level, which is expected because of the lower Ni content. However, the degree of shrinkage is higher than expected due to the Fe content. The observed peak shrinking could be related to a reduced crystal order. Furthermore, the peak D is rising in the relative ratio to peak C. The broad signal at  $1000\text{ cm}^{-1}$  is attributed to the 2P Phonon Mode. The broadening or disappearing of this peak with increasing Fe content is attributed to the decreasing crystallite sizes.<sup>63</sup> The observed peak broadening agrees with observations from above, as well as with indications from the hydroxide samples.

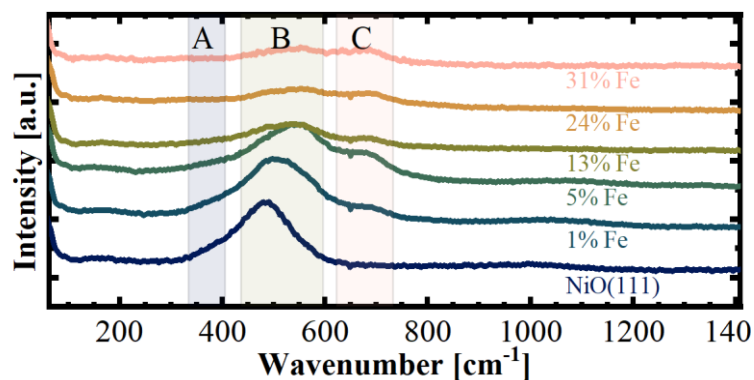


Figure 32: Raman Spectra of the Fe doped oxide samples. The peaks are highlighted with annotations from A-C for the oxides.

The surface of the materials was probed by XPS. The first observation from the survey spectra of the as-prepared powder samples, both hydroxide and oxide samples, is the absence of Fe in the survey spectra (Figure A19). The only sample with a Fe 2p signal was the 31% samples of hydroxide and oxide samples with 0.4% and 1.4%, respectively. However, the presence of Fe was confirmed by ICP-MS and other bulk techniques, such as Raman spectroscopy and XAS. This discrepancy suggests that the powder samples exhibit a layered structure, where the fast-precipitating  $\text{Fe}^{\text{III}}$  serves as a condensation nucleus for the Ni precipitate. This concept is known as self-regulated nucleation and growth, a common approach in colloidal synthesis where the sequential growth of two materials with different rates is applied to form core-shell materials in a single step synthesis.<sup>168</sup>

The peak deconvolution was not possible due to the low signal intensity of the Fe 2p spectra. Additionally, the interpretation of the satellite position to distinguish between  $\text{Fe}^{\text{II}}$  and  $\text{Fe}^{\text{III}}$  was not possible.<sup>125</sup> Similar observations were made with the C 1s signal, which was about 7% in the hydroxide and 5% in the oxide spectra. In these cases, peak

deconvolution of the adventitious carbon for charge reference was possible, but challenging. Furthermore, Nitrate species were found in the N1s signal, which overlaps with the Ni LM2 Auger line in the experiments conducted with the non-monochromatized Mg anode. In an experiment conducted with the monochromatized Al anode, the survey spectra revealed  $\text{NO}_3^-$  species at 407 eV.<sup>169</sup>

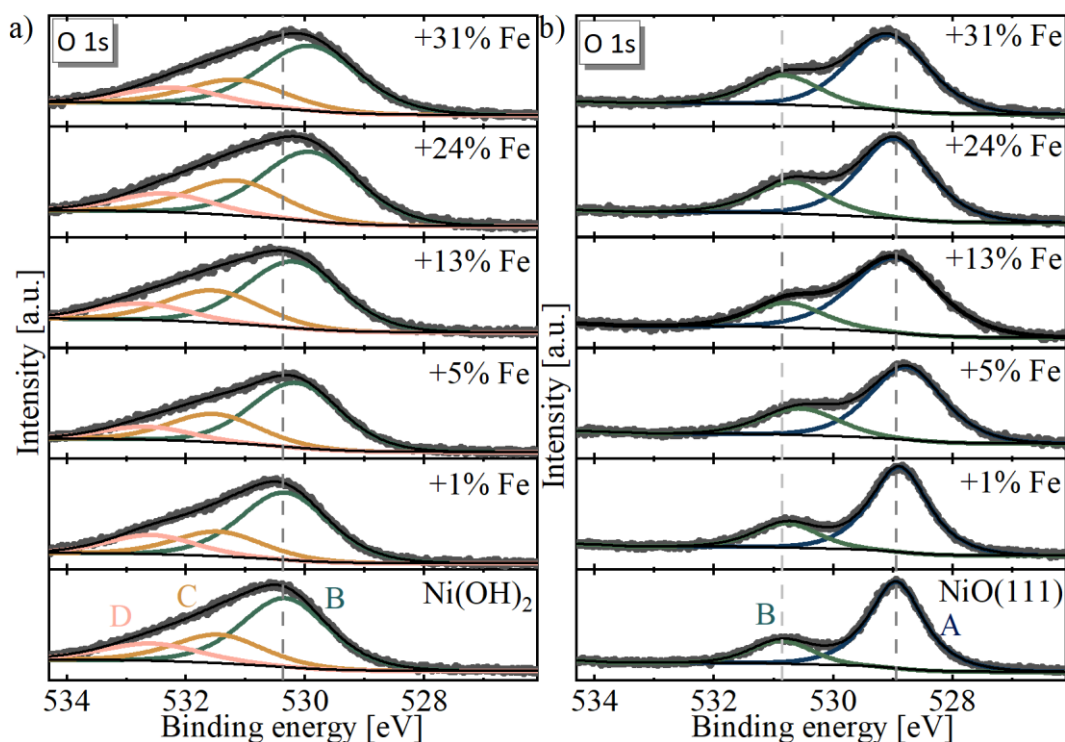


Figure 33: XPS spectra of the a) and b) O1s signal of the hydroxide and the oxide. The spectra include reference lines of characteristic peak position of the pure material and labeling of characteristic peaks.

The O 1s spectra of the hydroxide sample in Figure 33a was deconvoluted into three peaks. The pure  $\text{Ni}(\text{OH})_2$  peaks agree with the previously reported signals for Nickel hydroxide.<sup>42</sup> The main feature B at 530.4 eV is attributed to oxygen in hydroxide species. This peak is shifted to lower binding energies compared to the reference values reported by Biesinger et al.<sup>125</sup> Moreover, this feature broadens and shifts further with increasing Fe content, reaching 530.0 eV at 31% Fe. The observed broadening may be attributed to the above discussed crystallite size decrease. The contribution of iron hydroxides to the O 1s spectra is expected to be minor due to the low Fe signal intensity. The additional peaks C at 531.5 and D at 532.4 eV are attributed to C-O species and adsorbed water, respectively.<sup>42,125</sup> A minor contribution from residual nitrate precursor, observed in the survey spectra at 407 eV may be present but is expected to be low.<sup>169</sup>

The O1s spectra of the oxide samples in Figure 33a can be deconvoluted into two primary peaks A at 528.9 and B 530.9 eV, corresponding to lattice Ni–O and surface hydroxide species, respectively.<sup>42,125</sup> No clear trend in binding energy shift with Fe content was observed in the oxide samples. However, significant peak broadening, particularly for the lattice Ni–O component, was noted. As with the hydroxide samples, this broadening could result in reduced crystallite sizes with increasing Fe content.

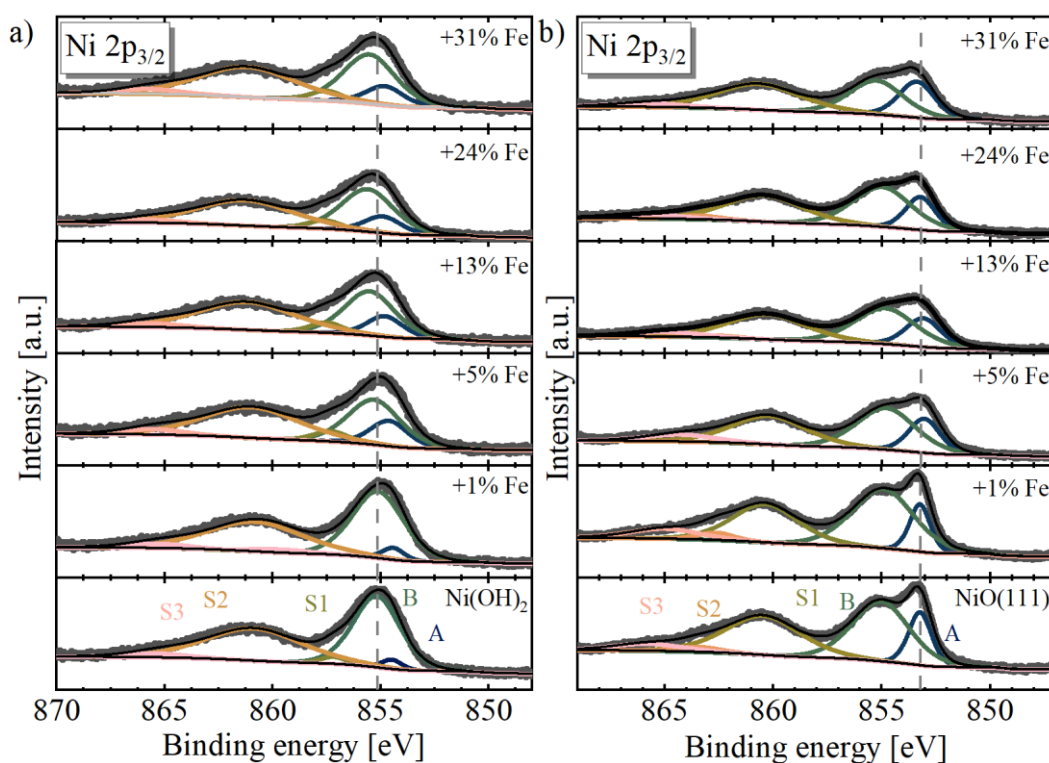


Figure 34: XPS Ni<sub>2p<sub>3/2</sub></sub> spectra of the a) hydroxide and b) oxide materials. The spectra include reference lines of characteristic peak position of the pure material and labeling of characteristic peaks.

The hydroxide Ni<sub>2p<sub>3/2</sub></sub> spectra in Figure 34a resemble the characteristic multiplet splitting including for Ni(OH)<sub>2</sub>, including the satellite structures.<sup>42,125</sup> Compared to the reference data from Biesinger et al. for Ni(OH)<sub>2</sub>,<sup>125</sup> the peaks are broader, primarily due to the use of a non-monochromatic Mg X-ray source, resulting in less pronounced features, such as the satellite at 860 eV (peak S1), and a slight overall shift to lower binding energies. With increasing Fe content, a slight shift (~0.4 eV) of the signals to higher binding energies is observed. Additionally, peaks A–B exhibit notable broadening, along with changes in the area ratio between peaks A and B, which shifts from 0.13:1 in the pure Ni(OH)<sub>2</sub> sample to 0.28:1 in the 31% Fe sample. The satellite structure remains unchanged across Fe concentrations. A Mg K $\beta$  satellite from the Ni 2p<sub>1/2</sub> signal may also

contribute to the peak near 856 eV (S2) but is expected to be consistent across all measurements.

The Ni 2p<sub>3/2</sub> spectrum of the oxide sample Figure 34b resembles the typical spectrum of NiO.<sup>42,125</sup> Comparing the pure NiO(111) sample to the NiO reference of Biesinger et al.<sup>125</sup>, a systematic shift to lower binding energies is observed, though the relative peak distribution remains consistent with the literature. Unlike in the hydroxide samples, the main NiO peak at 853.2 eV does not follow a clear trend with increasing Fe content. However, pronounced peak broadening occurs: the full width at half maximum of peak A increases from 1.3 to 2.0 eV upon addition of 31% Fe. Moreover, the A/B peak area ratio shifts significantly from 0.4:1 to 0.7:1.

Concluding the pristine characterization of the samples suggests, that the Fe might only be phase pure incorporated until doping levels of 5%. The samples with higher Fe-content have considerable indications of being a mixture of multiple phases. It is hypothesized that one of these phases could be Fe<sub>2</sub>O<sub>3</sub>. Furthermore, a lowered crystallinity is correlating with an increasing Fe-content. The increased surface area and the occurrence of the Fe<sub>2</sub>O<sub>3</sub>, which is known to be a sluggish OER catalyst,<sup>170</sup> are expected to counteract in the OER activity.

### 5.3.2 Electrochemical trends after Fe incorporation

The electrochemical characterization was conducted in an adapted procedure, depicted in Table A8, to measure activity metrics at multiple steps (3, 6, 7 and 9). First, the electrolyte resistance was determined from the EIS in step 2 at OCP. The number of scans in step 4 was minimized to 50 Scans, because of homologation to the broad literature and because the hydroxide material has reached an oxidation peak plateau faster than the tested oxides. The main metric that will be discussed is the  $\eta$  at 10 mA cm<sup>-2</sup> from step 6, because by consideration of the standard deviation of each activity metric, step 6 gave repeatable results. Step 5 included an EIS measurement at a constant potential to estimate the pseudo capacitance of the materials. However, the currents at this potential were too high for most of the Fe containing samples, leading to unreliable data. First observations of the measurement series before the electrochemical results, were the poor coating that was achieved for the hydroxide materials in comparison to the oxide material, also after optimization of the dispersion. The dispersion optimization will we further discussed in chapter 5.6.1.

Figure 35a and b show representative cyclic voltammograms of the hydroxide and the oxide materials, respectively. On first notice, the shift of the oxidation peak position of the hydroxide materials is apparent. This is not observed with oxide materials. The shift of the  $\text{Ni}^{\text{II}}/\text{Ni}^{\text{III}}$  redox peaks was previously reported for Ni-Fe-mixed hydroxides<sup>10,84</sup> and indicates electronic effects of the Fe onto the Ni sites by bulk incorporation into the material.<sup>87</sup> This is contradictory to our spectroscopic observation, where many results implicate that the Fe is not or to a little extent doped into the Ni-host material. This little extent of Fe-incorporation might be enough for electronic influences by the Fe. However, there was only a slight oxidation peak shift observed between different treatments of one electrode (Figure A20). The largest oxidation peak shift was observed between the pure  $\text{Ni}(\text{OH})_2$  and the 31% Fe sample. The shift in the  $\text{Ni}^{\text{II}}/\text{Ni}^{\text{III}}$  redox peak is again evidence for partial incorporation of Fe into the Ni bulk.

Interestingly, the  $\text{Ni}^{\text{II}}/\text{Ni}^{\text{III}}$  redox peaks have similar heights, decreasing towards higher Fe-content. The decrease in redox peak height is not steady, which can be explained by the inconsistent coating quality of the hydroxide materials. Additionally, to the novel catalyst materials, a commercial NiO ( $\text{NiO}_{\text{USNano}}$ ) was measured. The given conditions of further purified KOH electrolyte and the low numbers of cycles in step 3 result in a low  $\text{Ni}^{\text{II}}/\text{Ni}^{\text{III}}$  redox peak and in a high OER  $\eta$ .

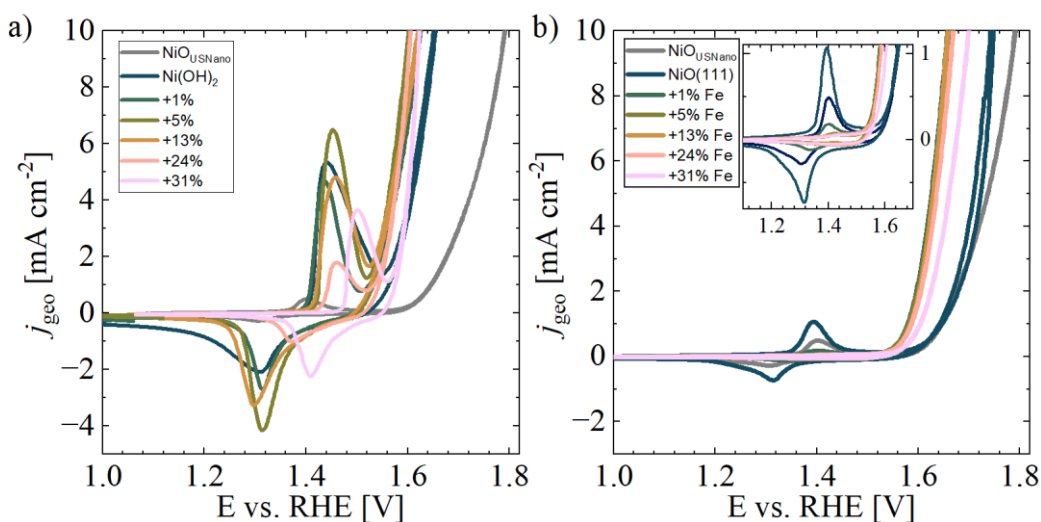


Figure 35: Representative CV of a) the hydroxide and b) the oxide materials from the second scan of the step 6.

Taking the  $\text{NiO}_{\text{USNano}}$  as a benchmark, the pure  $\text{NiO}(111)$  in Figure 35b has a slightly larger oxidation peak and a lower  $\eta$  with a similar onset potential as the benchmark material. In this regard, the insert of a zoom into the different peaks was analyzed and no dominant peak shift was observed for the oxide samples upon addition of Fe. The lower

magnitude of oxidation peaks of the oxide materials in general compared to the hydroxide materials suggest that most of the material sustains in the oxide structure after conditioning and only the surface is transformed into an  $\text{Ni}(\text{OH})_2$ . Furthermore, the observation agrees with the lower specific surface area of the oxide materials compared to the hydroxide materials from nitrogen adsorption experiments. In addition, the unproportional decay of the  $\text{Ni}^{\text{II}}/\text{Ni}^{\text{III}}$  redox peak heights with increased doping level was already observed for the Co and Mn doping in chapter 5.2 and was connected to a possible suppression of the oxidation towards  $\text{NiOOH}$  and a possibly lower conductivity of the mixed oxide bulk material.<sup>79,171</sup> The rationale behind the strong decrease of  $\text{Ni}^{\text{II}}/\text{Ni}^{\text{III}}$  redox-signals due to transition metal incorporation is still under debate.<sup>85</sup> For the 24% and the 31% sample, the  $\text{Ni}^{\text{II}}/\text{Ni}^{\text{III}}$  redox peaks are barely observed. The overpotentials are in general higher for the oxide materials, compared to the hydroxides.

For more detailed discussion of the overpotentials, the average values and the deviations across the experiments are depicted in Figure 36a and b. As already observed above, the hydroxide materials exhibit a high variation between the experiments. However, a trend can be estimated from the overpotentials. The pure  $\text{Ni}(\text{OH})_2$  itself already has an exceptionally low  $\eta$  of about 0.41 V, which indicates that there might be still residual Fe in the system. The commercial  $\text{NiO}_{\text{USNano}}$  on the other hand, has an exceedingly high  $\eta$ , which could either be a result of lower susceptibility of the  $\text{NiO}_{\text{USNano}}$  for uptake of impurities or due to intrinsic activity differences. Generally, the  $\eta$  difference between the hydroxide and its Fe containing counterparts was expected to be higher, because of reports from comparable studies.<sup>10,172</sup> It is suggested that the  $\text{Ni}(\text{OH})_2+24\%$  Fe with an average  $\eta$  of 0.37 V is an optimal Fe content. The optimal content of about 24% would agree with the broad literature of different pre-catalyst materials.<sup>10,62,173,174</sup> On the other hand, the large deviations in the average overpotentials between the independent experiments have to be mentioned, as well as the variety of optimal Fe loadings in Ni-Fe-based materials that were reported for OER applications.<sup>44,64</sup>

For the overpotentials of the oxide materials in Figure 36b a clear difference between the pure  $\text{NiO}(111)$  and the Fe-containing materials can be observed. Otherwise, no clear trend arises from the data. Interestingly the  $\eta$  of the  $\text{NiO}_{\text{USNano}}$  and the  $\text{NiO}(111)$  differ significantly from each other. Moreover, the 31% Fe sample exhibits a drastic increase in  $\eta$  in comparison to all other Fe-containing metal oxides.

In comparison to reports of comparable materials and experiments from the literature, the reported activity metrics herein are similar but not setting new benchmarks. Dionigi

et al.<sup>175</sup> managed to receive an  $\eta$  of  $\sim 350$  mV for a compounded NiFe-LDH material. Other less comparable RDE studies on NiFe-LDH materials reported  $\eta$  of less than 300 mV at  $10 \text{ mA cm}^{-2}$ .<sup>176,177</sup> The lower  $\eta$  in this study could be explained by the impurity phases observed for the materials in this study.

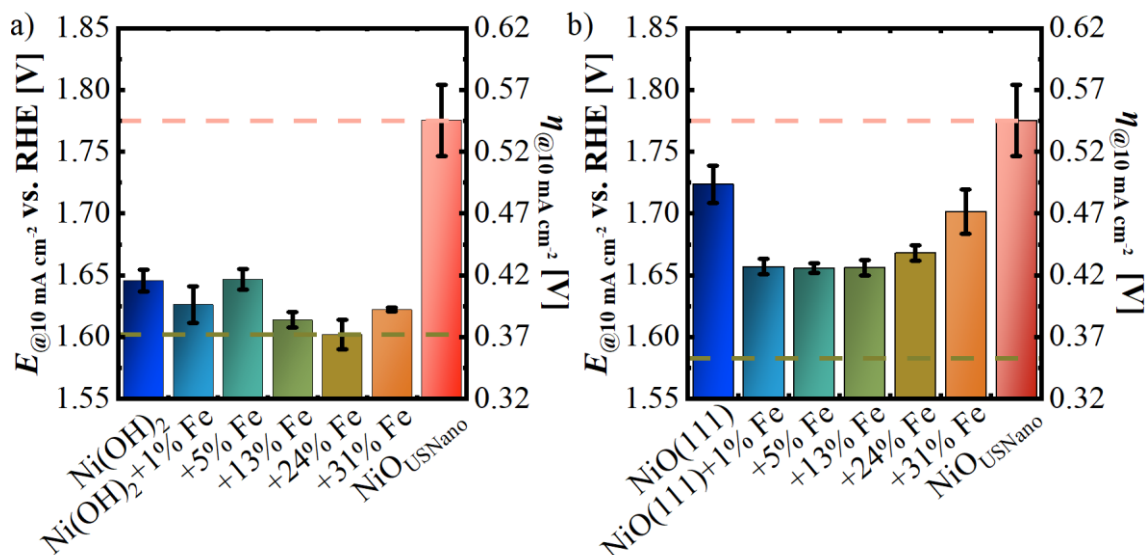


Figure 36: The average  $\eta$  at  $10 \text{ mA cm}^{-2}$  and standard deviations for the a) hydroxide and d) oxide materials from the second scan of the EC-protocol step 6.

For a more comparable investigation of the catalyst materials disregarding capacitive currents, galvanostatic experiments at  $10 \text{ mA cm}^{-2}$  were performed and represented in Figure 37. During the experiments of both the hydroxide materials and the oxide materials deactivation of most materials was observed. This deactivation of only 1 h of experiments can be attributed to  $\text{O}_2$  bubble detachment issues.<sup>96</sup> For example of the Ni(OH)<sub>2</sub> even the cut off at  $2.2 \text{ V vs. RHE}$  was reached. Other materials such as the NiO(111)+31% Fe exhibit major potential jumps, probably because of periodic bubble detachment. More insights and an alternative activity trend can be extracted from the average  $\eta$  at 150-250 s and 3500-3600 s for each material. The early  $\eta$  value should contain only minor influences of bubble induced deactivation, whereas the latter  $\eta$  value could not be extracted for every material.

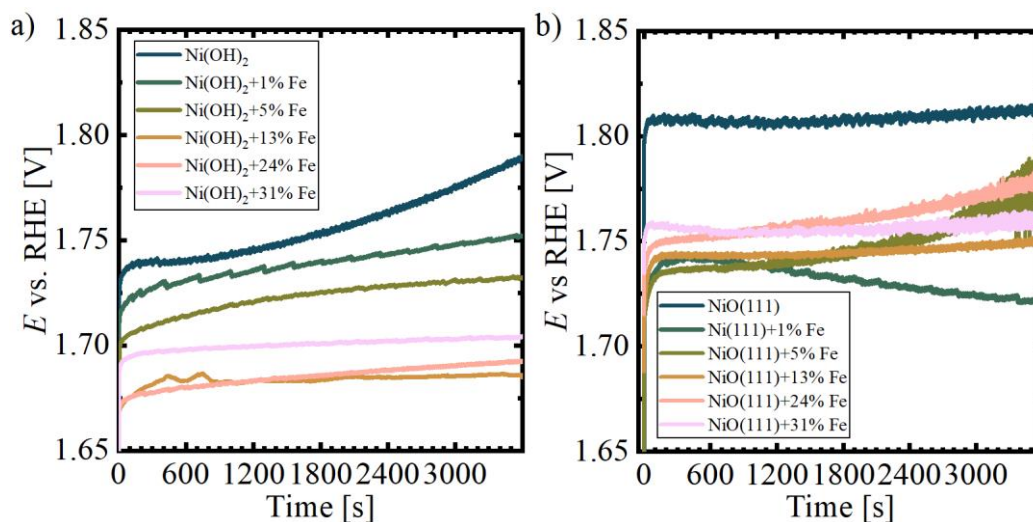


Figure 37: a) and b) show representative 1h galvanostatic hold experiments for each sample at 10 mA cm<sup>2</sup>.  $\eta$  of the galvanostatic experiments were extracted between 150-250 and 3500-3600 s and plotted for c) the hydroxide and d) the oxide samples.

For the hydroxide materials in Figure 38 the  $\eta$  values from the galvanostatic hold distinguish more than those of the CV. In general, the  $\eta$  were higher than those from potentiodynamic experiments, probably because of disregarding the capacitive currents. The material with the lowest  $\eta$  between 150-250 s in the comparison was the Ni(OH)<sub>2</sub>+13% Fe and closely followed by the 24% sample. An interesting addition is that the hydroxides with higher Fe content exhibit a lower  $\eta$  increase from 150-250 s to 3500-3600 s. This observation can either be explained by dissolution-redeposition of Fe from the catalyst<sup>7</sup> or by a more favorable oxygen detachment.<sup>94,95</sup> The NiO<sub>USNano</sub> is by far the material with the highest  $\eta$ . With the initial  $\eta$  being like the pure Ni(OH)<sub>2</sub> but the ending  $\eta$  being close to the cut off potential of 2.2 V vs. RHE.

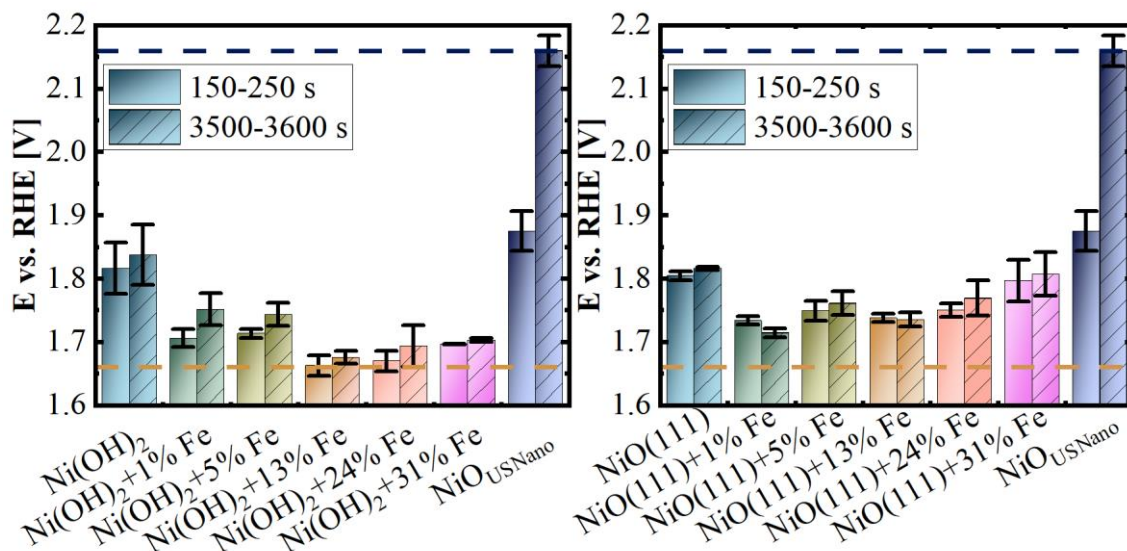


Figure 38:  $\eta$  of the galvanostatic experiments, extracted between 150-250 and 3500-3600 s to highlight the deactivation. a) contains the hydroxide and b) the oxide samples.

The oxide materials in Figure 38b have a lower standard deviation than the hydroxide materials. In this comparison the  $\eta$  of the pure  $\text{Ni}(\text{OH})_2$  and the  $\text{NiO}(111)$  are similar. For  $\text{NiO}(111)$  no strong deactivation was observed at the end of the experiment duration. Still a clear optimal loading could not be found, because the  $\eta$  of  $\text{NiO}(111)$  between 1% Fe and 13% Fe are similar. The 24% and 31% samples are characterized with a higher  $\eta$  approaching the pure  $\text{NiO}(111)$  sample. For all the oxide materials, the changes from the first to the second analyzed interval is small. However, the deviations between the experiments seem to increase with the Fe content of the oxide materials.

A comparison of the  $\eta$  from galvanostatic experiments with the literature is difficult because this metric is usually not reported for RDE experiments. However, in a study about the evaluation of RDE stability experiments with a Ir catalyst in acidic media, most of the experiments started at Potentials of about 1.7 V vs. RHE and ended at potentials of 2.2 V vs. RHE.

The trends of the OER activities reported here agree with expectations from the pristine physical characterization of the materials above. It was stated that the increased surface area and the occurrence of the Fe impurity phase could compensate each other, resulting in a modest OER activity, compared to literature. Still, the OER activity is much better than for pure  $\text{Ni}(\text{OH})_2$  and the  $\text{NiO}(111)$ . Another factor governing high OER activity is the formation of the active  $\text{NiOOH}$  and  $\text{Ni}_x\text{Fe}_{1-x}\text{OOH}$  phase. Therefore, the reconstructions of the catalyst materials are further studied in the following section.

### 5.3.3 *In-situ* and *ex-situ* characterization of compounded Fe-incorporation

The characterization of electrocatalysts in operando techniques is important to understand the electrocatalytically active species in the catalysts. The closest available approach in this study were *in-situ* experiments and *ex-situ* experiments after electrochemical treatment.

The *ex-situ* XAS experiments are covered in Figure 40. First, the XANES of the materials after aEC is analyzed. In this study, the EC-experiments were stopped at 1.7 V to sustain the oxidation state of the active catalyst. However, it needs to be considered that the active NiOOH species was observed to decay faster than this XAS experiments could be measured. Still, this *ex-situ* experiments are a close approximation of the active state. Most of the differences observed for the edge positions at the Ni-k edge (Figure 40a) were in the low 0.1 eV range for the aEC samples compared to the pristine samples. The pure Ni(OH)<sub>2</sub> and the NiO(111) samples have shown a slight reduction aEC. Yet, the differences are too small to speak of a trend. Interestingly, the Fe doped samples both exhibit oxidation after EC. For the oxide sample, this oxidation is about 0.5 eV. This implies that the Fe has an influence in the Nickels oxidation state during the electrochemical treatment and that this influence is larger than the electrochemical polarization of the catalyst material. However, this observation contradicts to *in-situ* and quasi *in-situ* XAS experiments, where the Ni-k edge position was changing drastically after applying OER potentials.<sup>62,64</sup> The measured sample might be just the irreversibly changed material after decay of the active state.

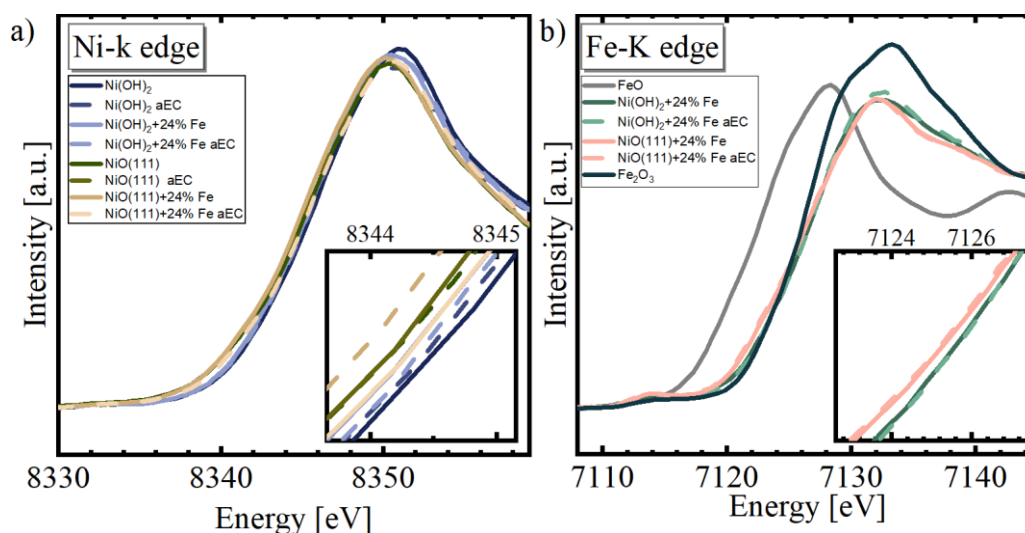


Figure 39: *Ex-situ* experiments of electrochemically treated samples (aEC) with XANES of a) Ni-k edge and b) of Fe-k edge including reference materials. All experiments have been performed on thin films coated on GC discs.

For the Fe-k edge (Figure 40b) no differences in the oxidation states were observed aEC. Both edge positions of the 24% Fe doped Ni(OH)<sub>2</sub> and the NiO(111) remain close to the Fe<sup>III</sup><sub>2</sub>O<sub>3</sub> reference material. This supports the hypothesis by Görlin et al. in which no oxidation state changes were observed for Fe during quasi *in-situ* XAS experiments of a Ni-Fe-mixed hydroxide.<sup>64</sup> This would explain why no changes are detected in these experiments. However, there are also studies that reported visible changes of the Fe-k edge during electrocatalysis.<sup>62</sup>

The EXAFS of the 24% Fe doped Ni(OH)<sub>2</sub> (Figure 40a) agrees with the XANES in the sense that no changes are observed for the Ni-K edge. The Fe-K edge, on the other hand, has slight changes of the oxygen stoichiometry, indicated by different peak ratios. Also, the EXAFS of the 24% Fe doped NiO(111) sample (Figure 40) reveals no visible changes upon electrochemical treatment. It was expected that Fe is mixed with the Ni phase during electrochemical conditioning, which would have increased the overlap of EXAFS at similar reduced distances. However, if there is mixing during electrochemical treatment, this might be surface confined.

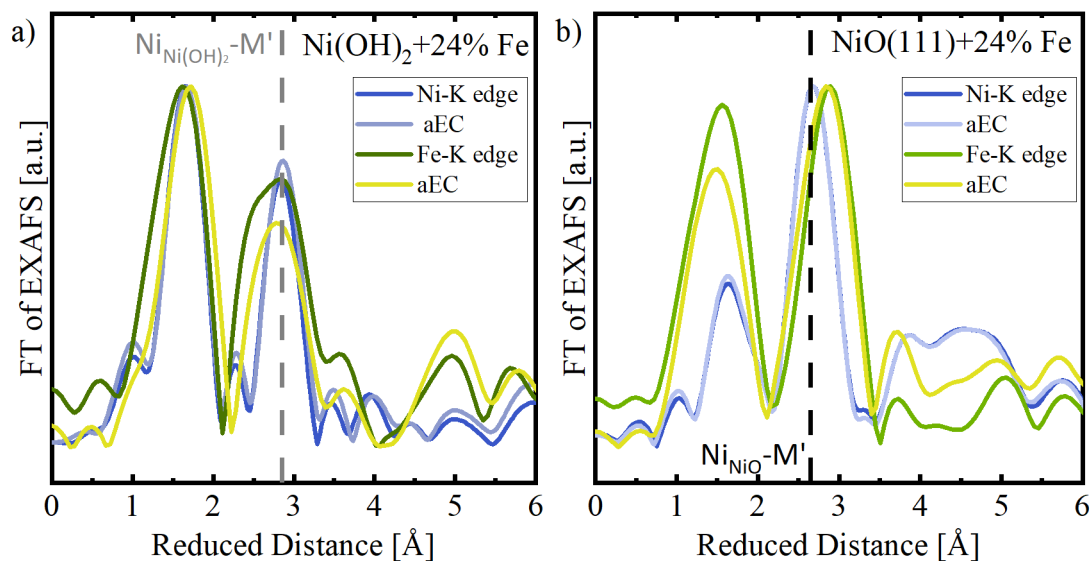


Figure 40: *Ex-situ* experiments of electrochemically treated samples (aEC) with EXAFS of a) the hydroxide and d) the oxide samples both including the reference distance of Ni-M' from NiO(111) in black and Ni(OH)<sub>2</sub> in gray. All experiments have been performed on thin films coated on GC discs.

The *in-situ* Raman measurements of Ni(OH)<sub>2</sub> materials are depicted in Figure 41a and b. During electrochemical treatment the weak signals A-C, that were already observed for the powder materials above, at about 450 cm<sup>-1</sup> transform into the NiOOH signals F and G at 490 and 560 cm<sup>-1</sup>.<sup>63</sup> That implies, that the oxyhydroxide is readily formed and has very dominant bands. The characteristic peaks of Fe-O and of the  $\alpha$ - or  $\beta$ -Ni(OH)<sub>2</sub> could not be resolved clearly in the spectra of the Fe containing hydroxide. However, there is a broad signal between Peak A and B in both hydroxide samples, which could be related to the Fe-O vibration. This signal disappears after the potential hold. The peaks C and D are interpreted to result from Carbon of the substrate.<sup>178</sup> Furthermore, vibrations from residuals of organic precursor are visible in E.<sup>166</sup>

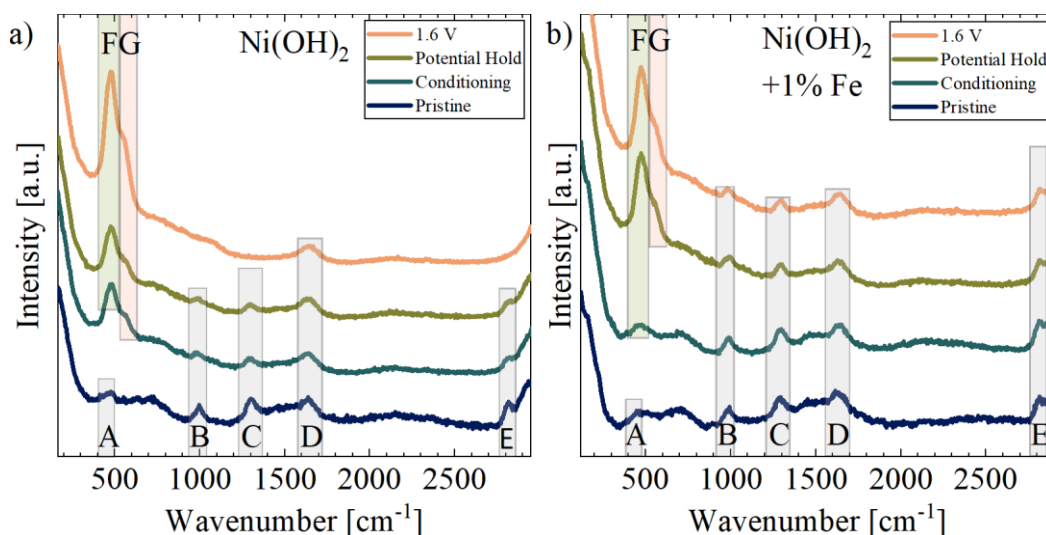


Figure 41: *In-situ* Raman experiments after different electrochemical treatments of representative  $\text{Ni}(\text{OH})_2$  and  $\text{Ni}(\text{OH})_2+1\% \text{Fe}$  samples after background correction. The experiments were acquired with a potential hold at the end of the individual steps V vs. RHE.

The oxide materials in Figure 42c) and d) have strong peaks. The oxide modes in A and B seem to sustain throughout the electrochemical treatment. However, the shoulder C of the formed  $\text{NiOOH}$  becomes visible after conditioning and grows with further electrochemical treatment. The Peak B is a composed of the initial Ni mode from  $\text{NiO}$  and the formed  $\text{NiOOH}$ . Also, for the oxide materials the Fe-O modes were not visible. The peaks C and D correspond to  $\text{NiO}$  2P Phonon signals and bands from the Carbon substrate.

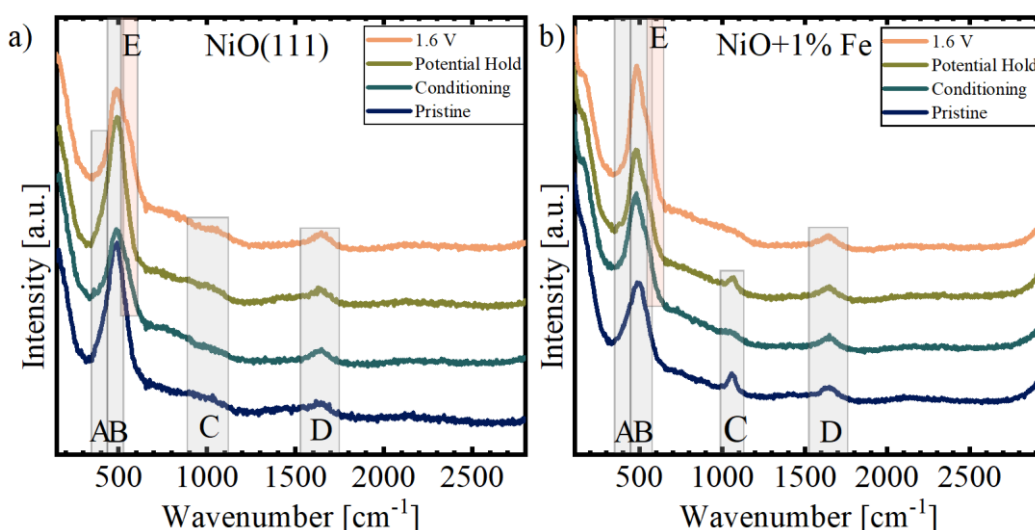


Figure 42: *In-situ* Raman experiments after different electrochemical treatments of representative  $\text{NiO}(111)$  and  $\text{NiO}(111)+1\% \text{Fe}$  samples after background correction. The experiments were acquired with a potential hold at the end of the individual steps V vs. RHE.

For further insights, the characteristic Ni Peak between  $350$  and  $750 \text{ cm}^{-1}$  was deconvoluted to study differences in the composition of the material after electrochemical

treatment at a hold potential at 1.6 V (Figure 43). The measurement at a potential of 1.6 V could be measured for all samples and lead to a strong NiOOH signal. On the other hand, measurements at 1.8 V were not possible for the Ni(OH)<sub>2</sub> samples, because of considerable oxygen evolution, which hampered Raman measurements.

The deconvolution of the peaks at 1.6 V of the Ni(OH)<sub>2</sub> materials revealed the contribution of mostly two peaks (F and G). Also, the peak ratio of both peaks was similar with 2.6 for the Ni(OH)<sub>2</sub> and 2.8 for Ni(OH)<sub>2</sub>+1% Fe (Table A9). Looking at the NiO(111) samples, peak A sustained throughout the electrochemical treatment. The peak A resulted in a third peak to be deconvoluted at ~405 cm<sup>-1</sup>. The peak ratio between the Peak B and E is smaller for both samples with 1.4, having a more intense peak E compared to the peak G of the Ni(OH)<sub>2</sub> samples. To be noted, the peak positions remain similar between the hydroxide and the oxide samples and are in agreement with the peak positions of previously reported *in-situ* experiments at 486 cm<sup>-1</sup> and 563 cm<sup>-1</sup>.<sup>63</sup> After Fe introduction, the peaks shift towards lower wavenumbers. The peak shifts are low for the hydroxides (~2 cm<sup>-1</sup>) and higher for the oxides (~6 cm<sup>-1</sup>). This peak is known to be sensitive to structural changes, however the differences between the pure and Fe containing samples are considered as negligible.

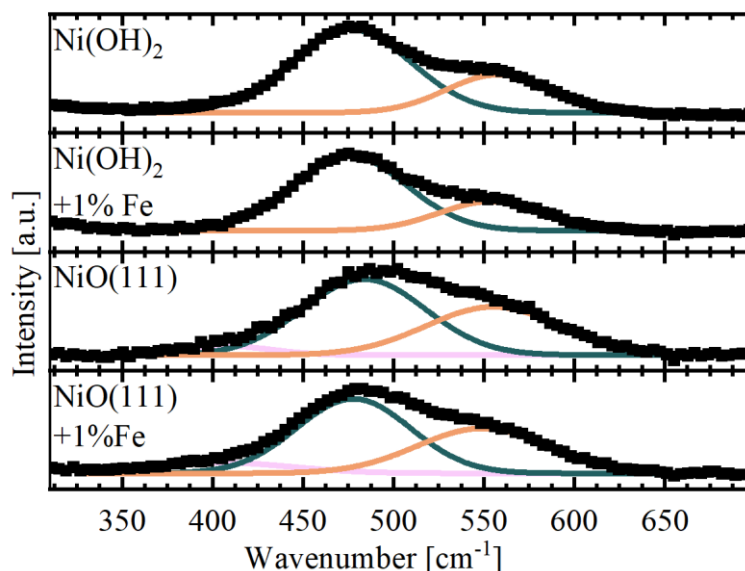


Figure 43: Deconvolution of the characteristic Raman Bands of *in-situ* Raman experiments at 1.6 V vs. RHE. This Potential was chosen because this potential was reached with every sample and the NiOOH band at ~550 cm<sup>-1</sup> was dominant at this measurement.

For the comparison between the Ni(OH)<sub>2</sub> samples and the NiO samples, the better electrochemical performances would suggest, that the Ni(OH)<sub>2</sub> is forming more of the active species characterized by the peak at ~475 and ~555 cm<sup>-1</sup>. However, the NiO has the initial peak at ~480 cm<sup>-1</sup> making the deconvolution between the characteristic peaks

of the active NiOOH and the initial NiO difficult. Yet, the lower ratio between the peaks indicates that the oxide material forms more of the active Ni<sup>III</sup>-OOH species. It must be stated that an additional 1LO peak was observed for NiO samples at  $\sim 600\text{ cm}^{-1}$  which could further affect the peak ratios of the *in-situ* sample.<sup>63</sup>

To conclude the *in-situ* Raman experiments, it was revealed that the oxide structure of the NiO(111) and the +1% Fe sample are retained to some degree during electrochemical treatment. This agreed with other experiments above, such as XAS and the Co/Mn study in chapter 5.2. Interestingly, except for the characteristic NiO peak at  $\sim 405\text{ cm}^{-1}$ , the different materials exhibited similar spectra characteristic for NiOOH with similar peak positions and similar ratios after electrochemical treatment. The influence of Fe and differences between the NiO and the Ni(OH)<sub>2</sub> is limited. Further insights on the electrocatalytically active surface will be obtained from *ex-situ* XPS experiments.

To begin with the XPS analysis after electrochemical treatment, it was observed that all the aEC samples are slightly shifted to higher binding energies. The shift to higher binding energies is also observed for the Ni 2p<sub>3/2</sub> samples in Figure A21. This could be related to a differential charge accumulation of the GC film experiments. The samples have shown minor contributions of KOH from electrolyte residuals and signals of the Nafion in the F 1s, C 1s and the O 1s spectra. Again, the Fe-containing aEC samples only show minor signals of about 1% and 3% of Fe in the Ni(OH)<sub>2</sub> and the NiO(111) sample, respectively.

The O 1s spectra of the Ni(OH)<sub>2</sub> related samples in Figure 44a show a pronounced shoulder A at lower binding energies above 529 eV. This signal A could be related to lattice oxygen, which was reported at similar binding energies.<sup>61,63</sup> However, it would be expected that a lattice oxygen signal is also observed in pristine samples. More likely, the lower binding energy signal is attributed to oxygen from higher valent Ni<sup>III</sup>OOH oxygen. This signal was reported for Ni-based samples under OER conditions.<sup>61</sup> Yet, the Ni<sup>III</sup>OOH species were reported to degrade quickly after immersion. Decomposition of NiOOH needs to be considered. The other signal B-D corresponds to features that were also

assigned for the pristine samples, with B being attributed to oxygen in hydroxide species, C to C-O species and D to adsorbed water, respectively.<sup>42,125</sup>

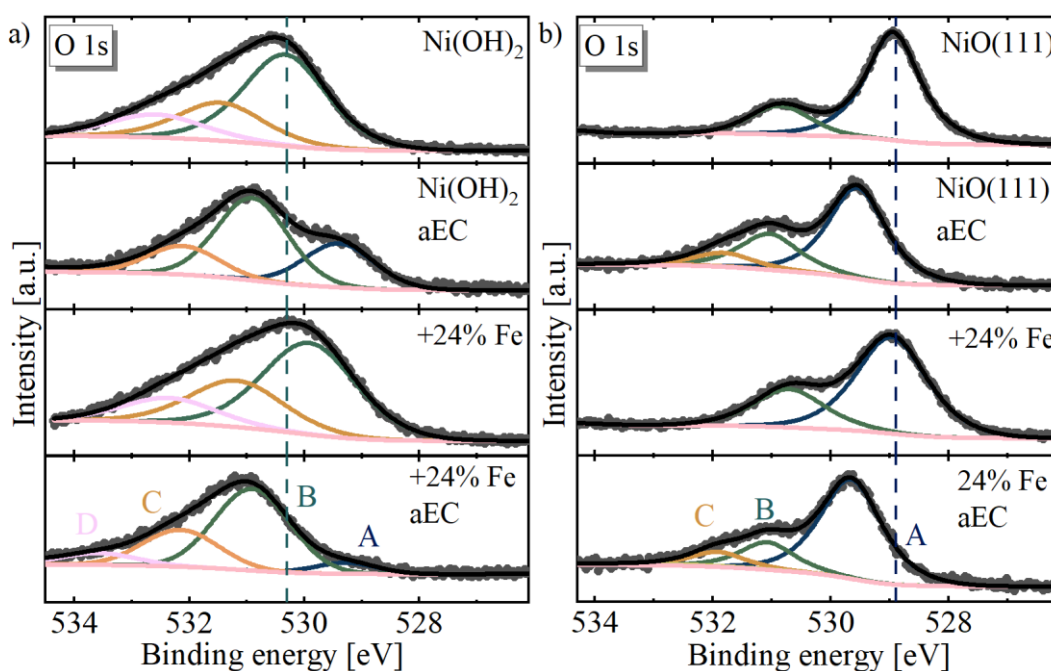


Figure 44: *Ex-situ* XPS O 1s spectra of the representative samples  $\text{Ni}(\text{OH})_2$  and  $\text{NiO}(111)$  and either 24% Fe containing samples. The samples after electrochemical treatment (aEC) GC discs are compared to pristine samples. Characteristic peaks for the  $\text{Ni}(\text{OH})_2$  and  $\text{NiO}(111)$  samples are each labeled.

The O 1s spectra of the  $\text{NiO}(111)$  materials in Figure 44b show less insights. The signals are shifted to higher wavelengths, and a higher binding energies signal occurs. This higher binding energies signal is attributed to C-O from the substrate and from the Nafion binder. The  $\text{Ni}^{\text{III}}\text{OOH}$  could not be resolved for the  $\text{NiO}(111)$  samples. Explanations are an overlap with the lattice oxygen signal of the  $\text{NiO}$  and the already mentioned degradation of  $\text{Ni}^{\text{III}}\text{OOH}$  into hydroxides. For the pure  $\text{NiO}(111)$  sample aEC, a slight growth of the hydroxide peak at 531 eV can be observed, relative to the lattice oxygen peak. This growth is not observed for the Fe containing sample, agreeing with the already reported hampering effect of Fe to reconstruct Ni-based systems into hydroxide systems.<sup>65</sup> The peaks are attributed to lattice Ni-O for A, to surface hydroxide species for B 530.9 eV and C to C-O species.<sup>42,125</sup>

In correlation with the other *ex-situ* and *in-situ* results of this chapter, the XPS could neither resolve an enrichment of Fe on the surface, nor could the catalytically active  $\text{NiOOH}$  phase be doubtlessly identified after electrochemical treatment. However, observations of smaller low binding energy signals of the  $\text{Ni}(\text{OH})_2+24\%$  Fe sample and lower hydroxide formation of the  $\text{NiO}(111)+24\%$  Fe samples agree with the

electrochemical observations above. Despite that the influence of the Fe on the apparent catalyst structure appears to be low, the intrinsic activity improvement of the Fe containing catalysts must be strong. It is stated, that the intrinsic OER activity of the  $\text{Ni}_x\text{Fe}_{1-x}\text{OOH}$  must be much stronger than those of the NiOOH phases, considering that more reconstruction was observed for the pure samples without Fe.

#### 5.3.4 Summary of the Fe incorporation of Ni(OH)<sub>2</sub> and NiO(111)

Overall, the compounded Fe-incorporated hydroxides and oxides materials were characterized using various techniques, including XAS, Raman spectroscopy, and XPS. The XAS results suggest that the Fe is not fully incorporated into the NiO(111) host structure but forms a separate phase from this MW synthesis approach. Furthermore, the electrochemical characterization of the OER points out that the hydroxide materials exhibit a high variation in  $\eta$  between experiments, while the oxide materials show a lower standard deviation. The  $\eta$  values were higher for the oxide materials compared to the hydroxide materials, pointing towards a lower OER activity of the oxide samples.

The *in-situ* and *ex-situ* characterization of the compounded Fe-doped samples was conducted using XAS, Raman spectroscopy, and XPS. The *ex-situ* XAS experiments showed that the Fe has a minor influence on the Ni oxidation state after electrochemical treatment, while the *in-situ* Raman experiments revealed that the oxide structure of the NiO(111) and the +1% Fe sample are retained to some degree after electrochemical treatment. Furthermore, the *ex-situ* XPS data show that Fe has a hindering effect on the surface reconstruction of Ni-based host materials. No clear surface enrichment of Fe or formation of NiOOH could be detected after electrochemical treatment. Therefore, the redeposition of Fe is not measurable in the conducted experiments. However, slight differences in the low binding energy features for the Ni(OH)<sub>2</sub>+24% Fe sample and a lower hydroxide formation in the NiO(111)+24% Fe sample are consistent with the electrochemical data. This suggests that Fe improves the catalytic activity whilst retaining the surface reconstruction. Overall, the study indicates that the Fe doping level has a significant impact on the surface reconstruction and electrochemical performance of the NiO(111) and Ni(OH)<sub>2</sub> materials. The optimal Fe loading for the hydroxide materials was found to be around 24%, while no clear trend was observed for the oxide materials. For both materials, the Ni(OH)<sub>2</sub> and the NiO(111) at least 31% Fe content the OER  $\eta$  increased, probably because phase separation dominates over the active mixed material.

The study also highlights the importance of *in-situ* and *ex-situ* characterization techniques to resemble the conditions during the catalytic process.

The results contradict with the significance of the amount of Fe content on the properties and electrochemical performance of the materials. Further studies are needed to fully understand the mechanisms underlying the electrochemical performance of these materials and to optimize their properties for specific applications. To support the fundamental insights of these materials, a focus should be to prepare homogeneously distributed Ni-Fe doped materials with the same surface faceting and with clear evidence of phase pure doping of Fe into the Ni(OH)<sub>2</sub> and NiO host structure. This and more detailed *in-situ* experiments could help to understand the effect of Fe on the OER of Ni-based materials. Furthermore, the characterization of the materials at application conditions would be an important next step. The following study will develop further the effect of Fe in the electrolyte, onto the different host materials, NiO(111) and Ni(OH)<sub>2</sub>.

## 5.4 *In-situ* doping of Ni hydroxide and oxide electrocatalysts with Fe<sup>3+</sup>

*The materials studied in this chapter were prepared in collaboration between the DLR and the UOL in the UOL labs by Dr. Dereje Hailu Taffa. Most of the content of this chapter is prepared for publication in a peer reviewed paper. Konstantin Rücker performed the XPS analysis, the XAS analysis, the Raman spectroscopy analysis, and the electrochemical characterization. Dr. Dereje Hailu Taffa performed the MW synthesis, the PXRD experiments, the BET analysis, and the HR-TEM analysis. Floris van Lieshout has supported the Raman spectroscopy.*

One of the research directions with the most attention in the field of alkaline OER with transition metal electrocatalysts is the study of the effect of electrolyte modification. Usually, this electrolyte is modified by intentional addition of transition metals such as Fe. As described above, the Fe<sup>III</sup> ions are known to have a drastic effect on electrocatalytic performance. The materials that were evaluated in this project have the novelty that we have two different Ni-based host structures, which are powder based and well defined. These well-defined Ni(OH)<sub>2</sub> and NiO(111) based materials were assessed for their response to intended Fe<sup>III</sup> impurities. It was hypothesized that the host material will influence the activity boosting effect of Fe<sup>III</sup> and that the structural changes differ.

### 5.4.1 Electrochemical observations from Fe<sup>3+</sup> *in-situ* doping

The effect of Fe<sup>3+</sup> on electrochemistry is visualized in CV after electrochemical conditioning in Figure 45a. The most drastic change in OER onset and  $\eta$  was observed for the NiO(111) sample. The height of the Ni<sup>II</sup>/Ni<sup>III</sup> redox peaks was similarly high with and without the *in-situ* Fe<sup>3+</sup> doping. Also, the peak position of the Ni(OH)<sub>2</sub> and NiO(111) did not change significantly after Fe incorporation. This suggests that the Fe incorporation into both catalysts is surface confined or in other words, confined to the surface oxyhydroxide layer. This agrees with literature observations in which the surface reconstruction of NiO is slowed by Fe saturated KOH and in which the Fe incorporation was surface confined for the NiO pre-catalyst.<sup>65</sup> In the study by Mattinen et al. it was also observed, that the dramatic Ni<sup>II</sup>/Ni<sup>III</sup> redox peak shifts most dramatically after increased numbers of CV cycles.<sup>65</sup> Furthermore, the Ni(OH)<sub>2</sub> sample has a less dramatic change in  $\eta$ . This implies that the measurement of Ni(OH)<sub>2</sub> in purified electrolyte still contains leftover Fe<sup>3+</sup> ions. Still, the addition of the 100 ppm Fe improves the  $\eta$  visibly.

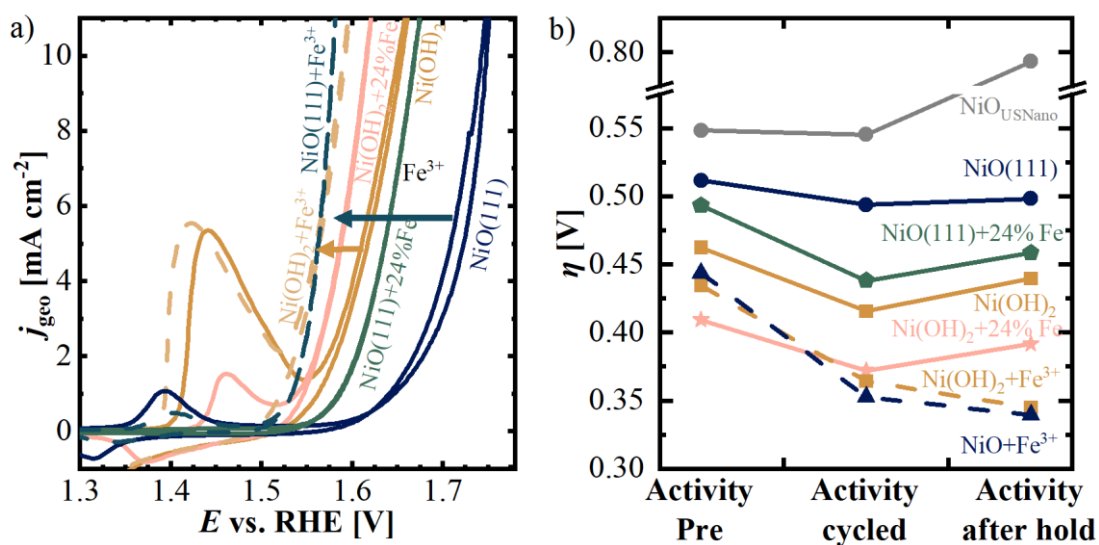


Figure 45: a) Representative CV of the of *in-situ* doped Fe samples from the second scan of the step 6. The effect of Fe on the pure NiO(111) sample is highlighted. b) From multiple independent experiments, the average  $\eta$  at  $10 \text{ mA cm}^{-2}$  and standard deviations were determined and plotted in as  $\eta$  of *in-situ* doped  $\text{Fe}^{3+}$  samples in comparison to compounded doped samples. The  $\eta$  for different subsequent characterization steps were followed. Activity Pre, cycled and after hold represent the  $\eta$  from step 3, 6 and 9, respectively.

Furthermore, the  $\eta$  measured at the different steps of the electrochemical protocol for representative samples are depicted in Figure 45b. This representation was chosen to follow the  $\eta$  pre and after cycling, and after the hold experiment measured from step 3, 6 and 9. The hydroxide materials exhibit a high variation at various stages of the protocol. The differences in the  $\eta$  of the  $\text{Ni(OH)}_2$ -based samples were low, which was already discussed above. For the NiO(111) materials on the other hand, it was observed that the difference in  $\eta$  of NiO(111) to the  $+\text{Fe}^{3+}$  equivalent is about 140 mV. The NiO(111)+ $\text{Fe}^{3+}$  sample has reached the lowest average  $\eta$  in comparison and in the whole thesis. This trend breaks with the clear trend of the previous experiments in which the NiO(111)-based samples always had higher  $\eta$ . The activity NiO(111)+ $\text{Fe}^{3+}$  has a competitive  $\eta$  of  $\sim 340$  mV, compared to reports of  $\sim 350$  mV for a compounded NiFe-LDH material.<sup>175</sup> All samples exhibit an activation after the electrochemical conditioning steps.

The trends across the different protocol steps are as follows. Most of the samples increase in  $\eta$  after the galvanostatic hold. This  $\eta$  increase might be explained by an interplay of catalyst deactivation, carbon corrosion, and irreversible bubble accumulation at the electrodes. Furthermore, Fe in the bulk of the compounded Fe-containing materials is not available for participating in electrocatalytic processes. Yet, the *in-situ*  $\text{Fe}^{3+}$  incorporation samples undergo a further  $\eta$  decrease throughout the different

electrochemical protocol steps. This could be correlated to a continuous and dynamic Fe<sup>3+</sup> deposition/ dissolution process throughout the hold experiment.

#### 5.4.2 Spectroscopic observations after *in-situ* Fe<sup>3+</sup> doping

Throughout the following chapter the nature of the *in-situ* doped materials will be studied to understand their interesting behavior. The drastic effect of the addition of Fe was proven by electrochemical experiments. However, to understand this effect on the different host materials several spectroscopy techniques were applied.

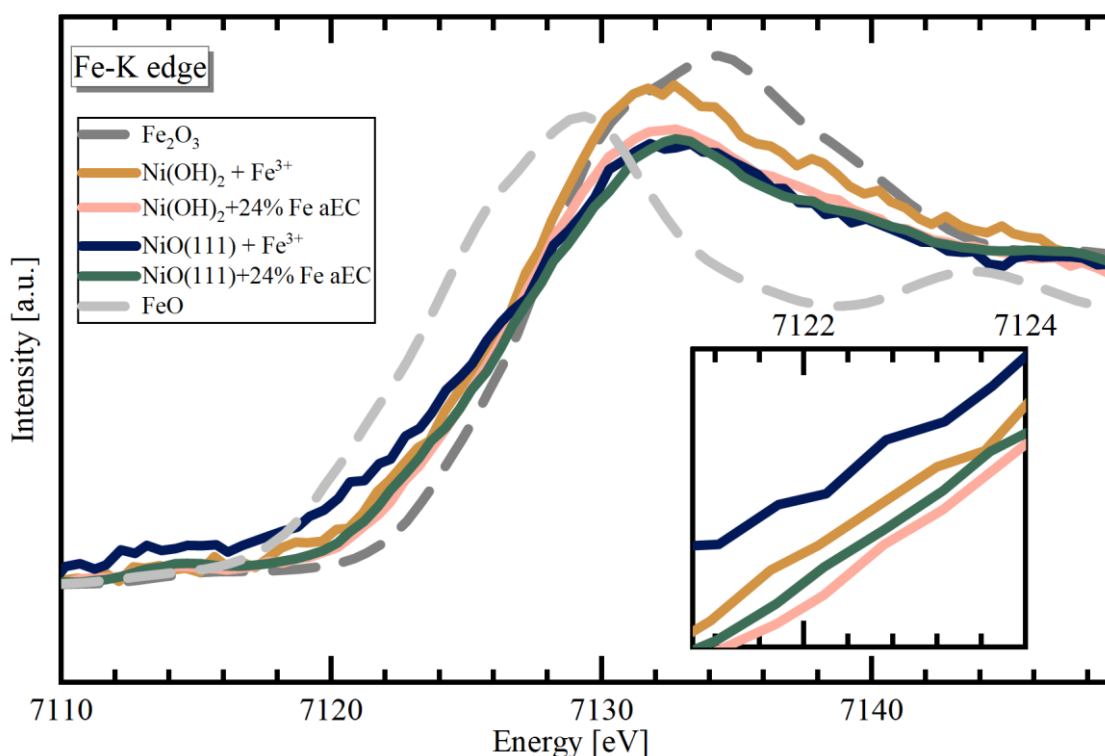


Figure 46: a) *Ex-situ* Fe k-edge XANES spectra of the *in-situ* Fe<sup>3+</sup> doped samples and compounded Fe containing samples with respective reference materials.

The XAS experiments in Figure 46 were conducted to gain structural insights into the oxidation state and the local coordination environment of the dopants after addition of the Fe to the electrolyte with the pristine catalyst material. The XANES gave insights into the oxidation state of the Fe dopant. For both samples, the Fe signal was very weak, which allowed only qualitative analysis of the spectra. The qualitative analysis allows the comparison to the reference material and suggests that the edge step read from the half height of the normalized edge step to be close to the compounded doped samples. This results in Fe oxidation states between 2.5 and 3 respectively. As already stated, detailed analysis of the EXAFS was not possible because of low signal intensity. However, these experiments have proven that Fe was readily incorporated into both host materials and

suggest that the chemical state is similar to the compounded Fe sites in *ex-situ* experiments.

*In-situ* insights of the active catalytic process are available from *in-situ* Raman experiments. The pure Ni(OH)<sub>2</sub> and NiO(111) materials were evaluated in purified electrolyte. The same experiments were performed with fresh electrodes but in 0.1 mM Fe<sup>3+</sup> containing electrolyte and are represented in Figure A22. The observations for the *in-situ* Raman experiments of the Ni(OH)<sub>2</sub>+Fe<sup>3+</sup> were similar to the pure Ni(OH)<sub>2</sub> samples in Chapter 5.3. In particular, the pristine material exhibits weak signals of the Ni(OH)<sub>2</sub> and included signals of the precursor and the substrate. With increasing electrochemical treatment, the characteristic NiOOH signals also grew. For the NiO(111)+Fe<sup>3+</sup> interestingly the signal intensity decreased in comparison to the pure NiO(111) sample in Chapter 5.3. Also, the rise of the NiOOH shoulder, which was observed for the pure sample without Fe<sup>3+</sup> introduction, could not be resolved.

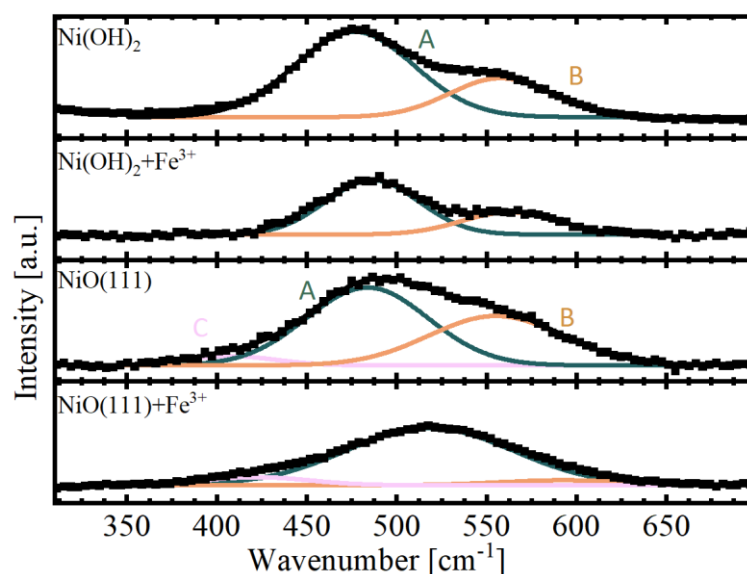


Figure 47: Deconvoluted *in-situ* Raman Spectra of the pure Ni(OH)<sub>2</sub> and NiO(111) samples, collected at 1.6 V in purified 0.1 M KOH and after Fe<sup>3+</sup> addition. Characteristic peaks are labeled.

The peaks at a 1.6V potential hold were compared more detailed and deconvoluted in Figure 47b. Throughout the peak deconvolution it was observed that the overall peak intensity is much lower for the Fe<sup>3+</sup> containing samples compared to the pure samples. The quantitative analysis of the peaks is difficult, because the loading of the samples and the surface area exposed to electrolyte is difficult to standardize. But because of the low depth of the focal field, the peak intensities might be comparable. However, it was already suggested in literature that the *in-situ* doped Fe delays the transition of Ni(OH)<sub>2</sub> to the

NiOOH whilst increasing the turn over frequency of the Nickel atoms.<sup>65</sup> This could explain why the weak Raman signal of the pristine Ni(OH)<sub>2</sub> forms less of the NiOOH.

Another observation was the slightly lower peak ratio between peak A and B of 2.4 of the Ni(OH)<sub>2</sub>+Fe<sup>3+</sup> compared to 2.6 for the pure Ni(OH)<sub>2</sub>. However, this slight difference of the peak ratios is less significant. More considerable is the behavior of the NiO(111)+Fe<sup>3+</sup> sample, in which no distinct shoulder of peak B was observed. The deconvolution suggests an insignificant contribution of the peak B to the shape. Interestingly, the peak shape of the sample NiO(111)+Fe<sup>3+</sup> is still similar to the pristine sample depicted in Figure A22. This suggests that the reconstruction of the NiO lattice might be surface constrained and that the bulk NiO is mostly unchanged during the experiments. The NiO(111) sample on the other hand clearly evolves the characteristic NiOOH signal (peak B). The electrocatalytic effect of the Fe<sup>3+</sup> on the NiO(111) host material was proven electrochemically. For the surface resolved insights, *ex-situ* XPS has to be considered.

The *ex-situ* XPS results after electrochemical treatment of the O 1s signals are depicted in Figure 48a. The lower binding energy component of the Ni(OH)<sub>2</sub> samples, which was discussed above (chapter 5.3.3), is interpreted to be a from the oxylic-O of NiOOH.<sup>61,124</sup> The in situ doped Ni(OH)<sub>2</sub>+Fe<sup>3+</sup> has a minimally lower feature. This might be related to a lower amount of NiOOH formation. However, the decomposition of NiOOH may restrict the significance of *ex-situ* NiOOH observation. For the oxide sample, again no additional peak at low binding energies gives evidence for the NiOOH formation. However, the relative height between the peak A and the peak B suggests a lower amount of hydroxide formation for the NiO(111)+Fe<sup>3+</sup> sample.

Further evidence for the NiOOH formation of the Ni(OH)<sub>2</sub> samples is given by consideration of the Ni 2p<sub>3/2</sub> signals in Figure 48b. The Ni 2p<sub>3/2</sub> spectra of Ni(OH)<sub>2</sub> samples show no evidence of the formation of anhydrous oxide, compared to the NiO(111) samples. Therefore, it is hypothesized that the peak A of the Ni(OH)<sub>2</sub> material is residual NiOOH and Fe lowers the NiOOH formation.

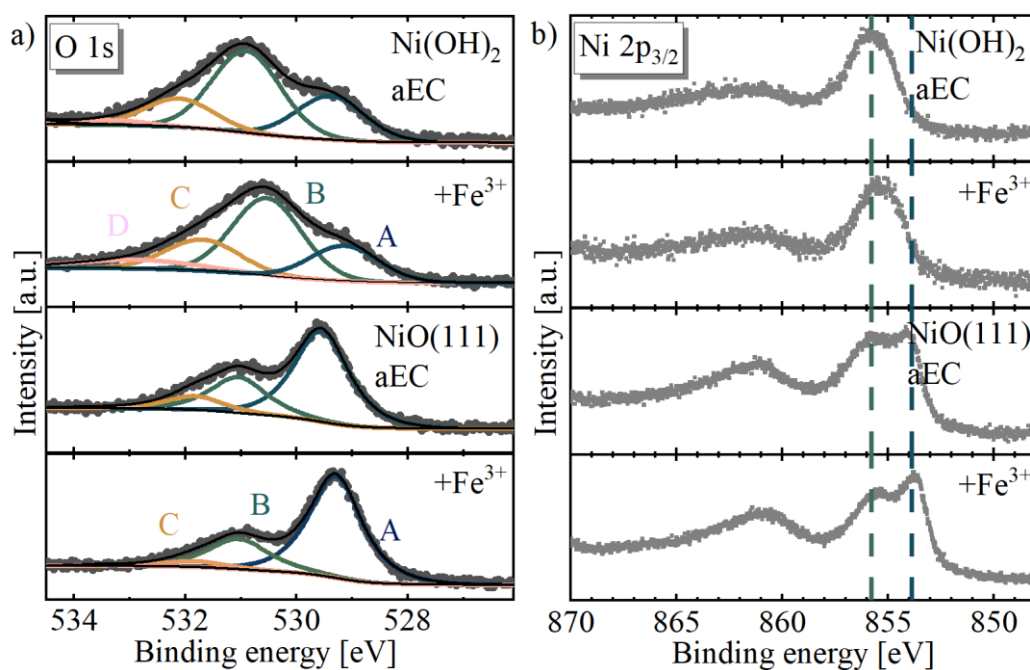


Figure 48: *Ex-situ* XPS a) O 1s and b) Ni 2p<sub>3/2</sub> spectra of the representative samples Ni(OH)<sub>2</sub> and NiO(111) samples. The samples after electrochemical treatment (aEC) are compared to samples measured after *in-situ* spiking with Fe(NO<sub>3</sub>)<sub>3</sub>. Characteristic peaks are labeled for NiO(111) and Ni(OH)<sub>2</sub> materials, respectively.

### 5.4.3 Summary of the effect of Fe<sup>3+</sup> *in-situ* doping

In summary, the addition of Fe<sup>3+</sup> to the electrolyte leads to a pronounced enhancement in the electrocatalytic performance of both Ni(OH)<sub>2</sub> and NiO(111) based materials, with the effect being especially significant for NiO(111). Electrochemical data revealed a reduction in OER  $\eta$  upon *in-situ* Fe doping, particularly for NiO(111), where a decrease of approximately 140 mV was observed. Despite similar Ni<sup>II</sup>/Ni<sup>III</sup> redox features with and without Fe<sup>3+</sup>, the data agrees with the literature findings about the surface confined Fe incorporation.

Spectroscopic investigations further support this surface-limited incorporation. XAS measurements confirmed the presence of Fe in both host structures, indicating an oxidation state close to that of pre-compounded Fe-doped references, despite low signal intensity. *In-situ* Raman spectroscopy offered insight into the catalytic transformations under operating conditions. For NiO(111)+Fe<sup>3+</sup>, the diminished signal intensity and lack of NiOOH shoulder formation suggest that the NiO oxidic bulk structure remains intact and the Fe-induced activity enhancement might stem from modified surface dynamics. Similarly, for Ni(OH)<sub>2</sub>, the Fe<sup>3+</sup> doping subtly alters the spectral features while still promoting OER performance. However, the amount of surface incorporated Fe was too low for XPS fitting of the Fe surface species. Yet, the Fe could be detected by XPS.

Overall, the data point toward a mechanism in which Fe<sup>3+</sup> incorporation enhances catalytic activity by modifying the surface oxyhydroxide layer without altering the bulk structure, by even decreasing the surface reconstruction. This is further supported by literature observations in which Fe<sup>3+</sup> *in-situ* incorporation improved the TOF of the catalyst and slowed down reconstruction. The lowered  $\eta$  support the usage of controlled *in-situ* Fe doping as a strategy for optimizing Ni-based OER electrocatalysts.

## 5.5 Characterization of catalysts at application-relevant conditions

*The materials studied in this chapter were prepared in collaboration between the DLR and the UOL in the UOL labs by Dr. Dereje Hailu Taffa. Nikhil Kadimi optimized the setup and performed the electrochemical characterization. Konstantin Rücker assisted with the electrochemical characterization and analyzed the data. Dr. Dereje Hailu Taffa performed the MW synthesis of the novel materials.*

The objective of this study was to investigate the performance of the novel Fe containing catalysts covered in Chapter 5.3 at conditions relevant to the AEMWE application to neglect the limitations of the RDE techniques. The limitations of the RDE technique are the bubble detachment issues as well as unrealistic mass transport and sample geometry. The hypothesis of this comparison is that the RDE experiments above do not resemble the performance of an electrocatalyst in a single cell electrolysis set-up, which operates at temperatures of up to 80°C and current densities of above 1 A cm<sup>-2</sup> are applied. Since there was no single cell setup available during preparation of this thesis, a half-cell setup was implemented. For further reading about the optimization of the setup, the reader is referred to the master thesis of Nikhil Kadimi.<sup>130</sup>

### 5.5.1 Setup optimization by the example of the temperature variation

This section will briefly cover the optimization of the setup and take an example of the comparison of different operating temperatures.

First, the PTE half-cell setup was optimized in regards of thermal management and the effective gas removal from the porous electrode. This resulted in the setup depicted in Figure 49.

Second, the flow rate of the pump was optimized in regards of effective bubble removal and stable electrochemical readings. The flow rate of 60 mL min<sup>-1</sup> was chosen for further experiments.

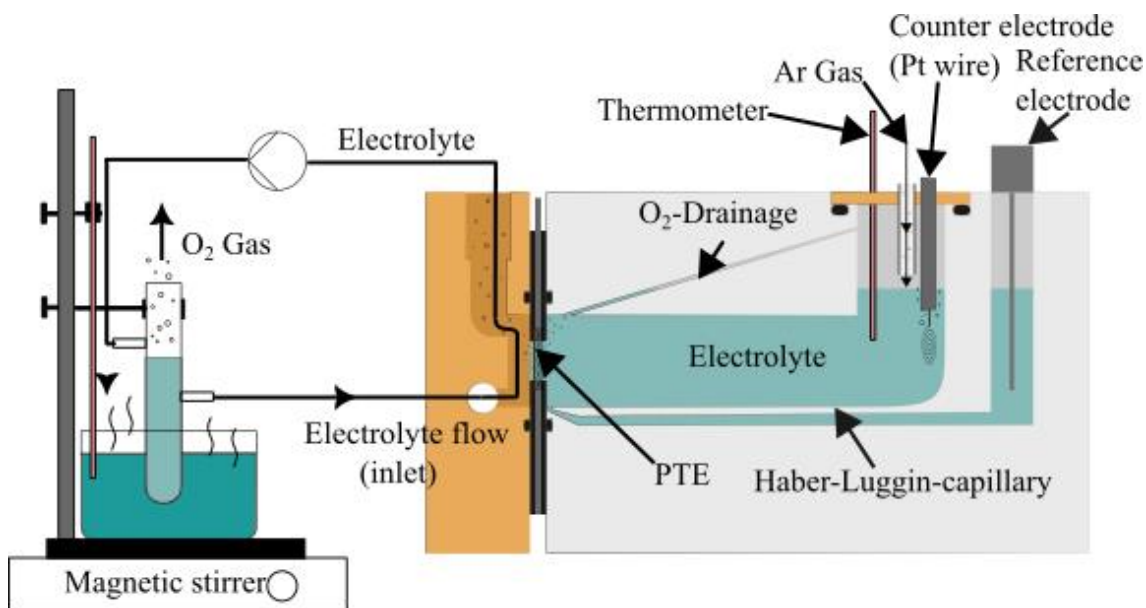


Figure 49: PTE half-cell setup based on the commercial FlexCell with an improved thermal loop and gas removal. Reproduced from Kadimi<sup>130</sup> and adapted from Schechterle.<sup>179</sup>

Third, the working electrode orientation varied with the outcome that an orientation towards the electrolyte flow instead of towards the counter electrode had a superior bubble removal.

Fourth, working electrodes with the diameters of  $\varnothing$  1 cm and  $\varnothing$  2 cm were evaluated. Letter one surpassed the compliance voltage of the potentiostat to reach the aimed  $1 \text{ A cm}^{-2}$ .

The following experiments were conducted with  $\varnothing$  1 cm working electrodes. The temperature optimization will be covered in the following section. The operation temperature is a fundamental parameter influencing reaction kinetics, ionic transport, thermodynamics of the reaction and the catalyst as well as the dynamics of gas evolution at the electrocatalyst surface.

To systematically assess the effects of temperature, all other experimental variables were optimized in previous tests and held constant. The temperature analysis experiments were conducted at four distinct temperatures: 25 °C, 40 °C, 60 °C, and 80 °C. 25°C was chosen to be close to the room temperature, at which RDE experiments were conducted. 60 °C and 80 °C were chosen as a typical temperature range at which AEMWE single cells are operated. The experimental approach included CV to evaluate catalytic activity, along with polarization measurements across the temperature range.

The parameter optimization of the temperature was started by comparing the CV data of the varied materials, as depicted in Figure 50a. The different temperatures exhibit a

progressive shift towards lower onset potentials with rising temperature. This is likely due to the increased mobility of ions at higher temperatures, which facilitates the OER reaction. The zoomed insert of the CV data shows peaks corresponding to the reversible transformation of  $\text{Ni}^{\text{II}}/\text{Ni}^{\text{III}}$ . These peaks shift to lower potentials as temperature increases, indicating enhanced surface redox kinetics and reduced activation energy for the  $\text{Ni}^{\text{II}}/\text{Ni}^{\text{III}}$  transition. Furthermore, the reduction peak of the 80°C sample is split into multiple peaks. With increasing temperature, the separation between the oxidation and reduction peaks in the cyclic voltammograms decreases. In addition, the onset of the OER is shifted towards lower potentials with increasing temperature. This behavior aligns with the Arrhenius relationship, where the OER current density increases with temperature, which was previously correlated to an improvement of the kinetics, the ionic conductivity and mass transport.<sup>110</sup>

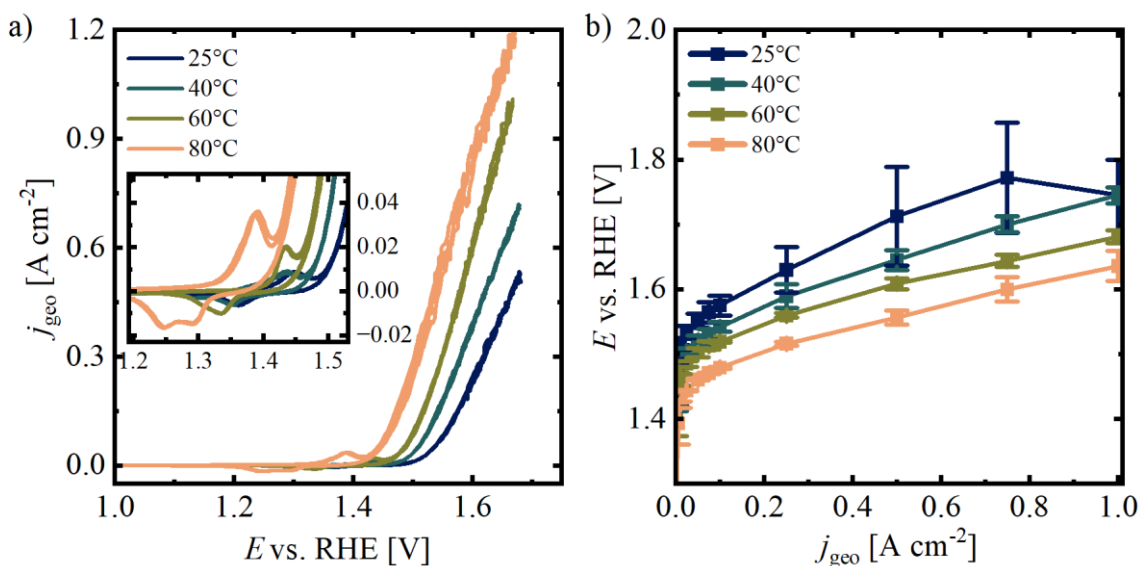


Figure 50: Electrochemical data of the commercial  $\text{NiFe}_2\text{O}_4$  material at temperature between 25 and 80 °C. a) represents CV with an insert of a zoom onto the  $\text{Ni}^{\text{II}}/\text{Ni}^{\text{III}}$  redox signal at 10 mV/s from step 10 of the PTE procedure. The CV results are 95% compensated and 5% post-corrected for the HFR. b) Polarization curves of the material from step 8 of the PTE procedure in the PTE half-cell set up in 1 M KOH, at a flow rate of 60  $\text{mL min}^{-1}$ , with a working electrode area of 0.78  $\text{cm}^2$  ( $\varnothing$  1 cm). The polarization curve is post-corrected for the HFR.

The polarization curves, depicted in Figure 50b, provide further insight into the impact of temperature on OER performance under galvanostatic conditions. Notably, these curves show that increasing the temperature consistently results in a decrease in the potential required to achieve a specific current density. This reduction in potential is again attributed to the enhanced electron transfer rates that occur at higher operating temperatures, which in turn facilitate the OER reaction. Moreover, the repeatability

between the experiments should be discussed because it is a critical parameter for the evaluation of the suitability of this PTE half-cell set-up.

Interestingly, the 25 °C and the 80 °C experiments have the largest standard deviation between the repetition experiments. The high deviations of the 25 °C samples were explained by a drastic heat up of the electrochemical cell, especially at current densities of 0.2 A cm<sup>-2</sup> and above. In the present experiments, the temperature was monitored between the working electrode and the counter electrode. This allowed to follow the temperature progression as a function of the applied current density (Figure A23). It was found that conducting experiments at 25 °C set-temperature exceeded the measured temperature of 40 °C in some experiments. This also explains the high deviations at 1 A cm<sup>-2</sup>. In general, the 25 °C set temperature was too unsteady to be considered for further experiments. The critical heating up of low temperature experiments was also observed in a study by Geuß et al.<sup>110</sup> in which the OER was studied under acidic conditions for Ir-based catalysts at 20 and 60 °C. This heat up during the 25 °C experiments affect the EIS measurements drastically by shifting the HFR towards lower values (Figure A24a).

Even higher variations in the measured potentials during the UI-curve were observed for the 80 °C sample. This could not be explained by a local heat up, because the heat up during the galvanostatic experiments can be neglected at 80 °C. The EIS data acquisition was not possible for some 80 °C experiments and noise with jumps during the acquisition. The GEIS data suggests that bubbles might induce increased resistance with rising current density (Figure A24b). Furthermore, the 80 °C sample was observed to have visible catalyst detachment off the substrate after the electrochemical treatment (Figure A25). However, it was not possible to differentiate if the catalyst film was detached due to mechanical or thermodynamic instability.

With this observation, a tradeoff between elevated application relevant conditions and stable experiments was made by choosing 60 °C for the further experiments. Reaching higher current densities might be challenging at 1 M KOH concentration, because the potentials applied between the counter and the working electrode was already close to the compliance voltage of the potentiostat. This is also why experiments with lower KOH concentrations, which are desired in future AEMWE electrolysis systems, cannot be depicted in this set up.

### 5.5.2 Electrochemical testing of Fe-containing Ni(OH)<sub>2</sub> and NiO(111)

As stated above, the main objective of the PTE study was the application of the novel materials from this study at application relevant conditions. The amount of powder material was limited, resulting in measurements of pure Ni(OH)<sub>2</sub> and NiO(111) together with their 5% Fe containing counterparts. One electrode coating was possible for the novel materials. The comparison of the materials was done in the PTE setup with the optimized parameters.

In Figure 51a cyclic voltammetry of the material from the final CV (step 10) are compared. It was noticed that the OER onset potential of the Ni(OH)<sub>2</sub>+5% Fe underscores any other material. This is expected from the high surface area of the material observed from Nitrogen Physisorption experiments (chapter 5.3). The hydroxide material is a beneficial pre-catalyst because it can readily be oxidized into the electrocatalytically active Ni<sup>III</sup>OOH. The NiO(111) on the other hand resembles the highest OER onset potentials. The PTE procedure, including electrochemical conditioning, the galvanostatic hold and the polarization curve, might transform enough oxide materials, both rock salt NiO(111) and spinel NiFe<sub>2</sub>O<sub>4</sub> into hydroxide. Further evidence of the low surface reconstruction can be concluded from the size of the reduction peaks of each material.

The reduction peak should be less influenced by OER currents than the oxidation peak, which overlaps for most of the materials with the OER onset. The area underneath the reduction peaks is about 2 C cm<sup>-2</sup> for the largest peak of the Ni(OH)<sub>2</sub>+5% Fe ranging down to 50 mC cm<sup>-2</sup> for the NiFe<sub>2</sub>O<sub>4</sub>. The different charge of the Ni(OH)<sub>2</sub> materials as well as between the NiO(111) materials could be a result of slight variations in the catalyst loading. The lower charge for the Spinel NiFe<sub>2</sub>O<sub>4</sub> could be explained by reports on inhibited hydroxide formation observed for other nickel containing spinel oxides.<sup>79</sup> Another consideration is that the porous Ni felt substrate might add up to the charge of the Ni<sup>II</sup>/Ni<sup>III</sup> redox peaks. However, this influence is assumed to be consistent across all samples.

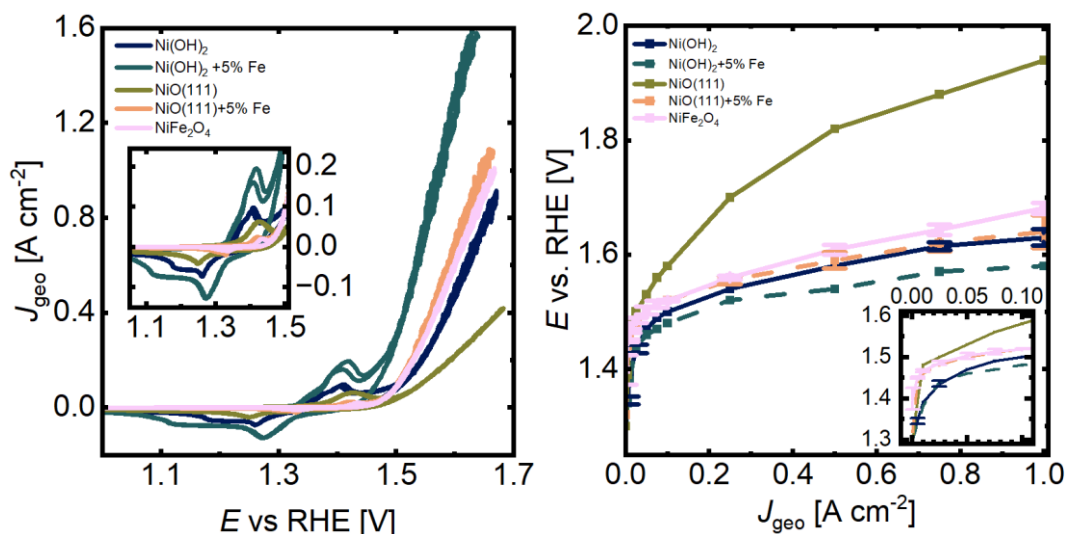


Figure 51: Electrochemical data of the pure  $\text{Ni}(\text{OH})_2$  and  $\text{NiO}(111)$  as well as the 5% Fe doped Materials and commercial  $\text{NiFe}_2\text{O}_4$  material. a) representative CV at 10 mV/s from step 10 of the PTE procedure. The insert shows a zoom on the characteristic  $\text{Ni}^{\text{II}}/\text{Ni}^{\text{III}}$  redox peaks b) average polarisation curves of the materials from step 8 of the PTE procedure. The insert shows a zoom at lower current ranges. Experiments were performed in the PTE half cell set up in 1 M KOH, at a flow rate of  $60 \text{ mL min}^{-1}$ , with a working electrode area of  $0.78 \text{ cm}^2$  ( $\varnothing 1 \text{ cm}$ ) and at  $60^\circ \text{C}$ , each of which had a loading of  $\sim 3 \text{ mg cm}^{-2}$ . Note, that only one electrode of the  $\text{NiO}(111)$  was measured successfully.

A more application-oriented comparison of the varied materials is obtained by considering the polarization curves of each material (Figure 51b). Looking at the higher current densities, the highest potential of more than 1.9 V is necessary with the pure  $\text{NiO}(111)$  to reach  $1 \text{ A cm}^{-2}$ . This was expected from the CV analysis. However, when comparing the results for the  $\text{Ni}(\text{OH})_2$  material, the material performs as second-best material in comparison with an potential of 1.63 V vs. RHE at  $1 \text{ A cm}^{-2}$ . This high activity can be explained using Fe-containing KOH electrolyte, for which  $\text{Ni}(\text{OH})_2$  is prone to absorb it and form a decent electrocatalyst. It suggests, that the  $\text{NiO}(111)$  material is less susceptible for Fe incorporation from trace level impurities, than the  $\text{Ni}(\text{OH})_2$ . The best material in the comparison was the  $\text{Ni}(\text{OH})_2 + 5\% \text{ Fe}$ , which reached the  $1 \text{ A cm}^{-2}$  at 1.58 V vs. RHE. The Fe containing oxides,  $\text{NiFe}_2\text{O}_4$  and  $\text{NiO}(111) + 5\% \text{ Fe}$ , performed similar in the polarization curves. The polarization curves of both materials even overlapped in the current densities up to  $100 \text{ mA cm}^{-2}$ . This suggests that the  $\text{NiFe}_2\text{O}_4$  and  $\text{NiO}(111) + 5\% \text{ Fe}$  of different Fe content and of different crystal structures have comparable OER kinetics. Differences in  $\eta$  occur at higher current densities, which is interpreted to be strongly dependent on bubble transport.

Overall, the trends that were observed in RDE (Chapter 5.3), in which the hydroxide materials were more active, could be reproduced. However, it was found that the PTE

experiments of the pure NiO(111) material allow a more prominent differentiation from the Fe-doped NiO(111) +5% Fe sample than the RDE results. Another emphasis is addressed towards the differences between the low current density regime and the high current density regime of the polarization curves. When materials had remarkably similar polarization curves below  $50 \text{ mA cm}^{-2}$ , the differences became more significant at higher current densities. This strengthens the need of the characterization of novel and promising catalysts at high current densities and application relevant conditions.

### 5.5.3 Summary and limitations of the PTE setup

As successful the objective of creating a setup for more application relevant conditions was, the here demonstrated PTE setup still revealed challenges that differentiate it from single cell applications. As already stated above, the minimum concentration of KOH to be used at such high current densities of  $1 \text{ A cm}^{-2}$  was 1 M. This originates from the cell geometry, in which the reference electrode and the counter electrode have both a fixed distance to the working electrode. These distances lead to increased ohmic resistances, especially between the reference and the counter electrode, and result in reaching the compliance voltage of the potentiostat/galvanostat during the experiments.

Another limitation is the open geometry of the system, which allows an effective gas separation from the electrolyte, but leads to evaporation of water and makes it difficult to run long-time experiments, especially at high current densities. Further optimization would be needed to run long-time experiments, such as humidification of inert purge gas and a condenser at the gas outlets.

Further challenges were identified by the usage of a membrane attached to the PTE, to separate the PTE from the counter electrode. For the membrane tests, a 3D printed flow field was tested, to improve the gas removal from the PTE. So far, the gas removal could not be improved, and further optimization would be needed to test thicker PTL and to use membranes in the PTE setup.

Further constraints for reliable experiments with the PTE setup were found in the current collectors. The Ti mesh that was used as current collector realized a good electrical contact between the PTE and the potentiostat. Unfortunately, it underwent corrosion during the experiment due to exposure to the alkaline electrolyte at elevated temperatures. This corrosion was apparent visibly (Figure A26) and by an additional ohmic resistance in the range of  $0.3\text{-}0.4 \Omega$ . This current collector should be replaced for

future experiments by a flat and thin substrate, which can be polished before each use (e.g. Ti foil or Ni foil).

In conclusion, the PTE half-cell approach effectively bridges the gap between RDE measurements and AEMWE single cell testing, revealing performance trends more accurately than the RDE setup. The study validates that hydroxide-based materials, especially  $\text{Ni(OH)}_2+5\% \text{ Fe}$ , are promising for the use in AEMWE anodes, and highlights the necessity of testing new catalysts under high current densities and elevated temperatures to assess their practical viability.

## 5.6 Considerations for reproducible electrochemical characterization

*The materials studied in this chapter were prepared in collaboration between the DLR and the UOL in the UOL labs by Dr. Dereje Hailu Taffa. Konstantin Rücker performed electrochemical characterization and analyzed the data. Dr. Dereje Hailu Taffa performed the MW synthesis of the NiO(111) materials.*

Reproducibility of electrochemical experiments are an already addressed issue in the electrocatalysis community.<sup>9,106</sup> Therefore, this chapter covers the efforts that were made throughout this work, to improve the reproducibility of the tested materials. The optimization started with the dispersion procession of the catalysts, the electrochemical treatment, the ionomer binder, and end with considerations for *ex-situ* experiments.

### 5.6.1 Reproducibility, repeatability and how they are affected by the catalyst processing

The first examined parameter was the dispersion procession. To understand the effect of the dispersion procession first, the pristine powder was compared to the film samples on GC discs. Therefore, the oxidation state of the samples was compared in XANES in Figure 52a. The Ni-K edge of both samples proceeds similar, but the NiO(111) film sample is slightly shifted to higher edge energies. The difference between the edge positions is low but should be considered. The shift between the powder and the film sample is larger than some shifts that were observed for comparisons in chapters above.

The FT of the EXAFS on the other hand (Figure 52b) shows no significant changes after drop casting. The bulk coordination environment seems to maintain the rock salt NiO structure. The minor changes observed in the edge positions might be surface confined. To study the changes of the surface structure, XPS of the powder and the thin-film samples were performed.

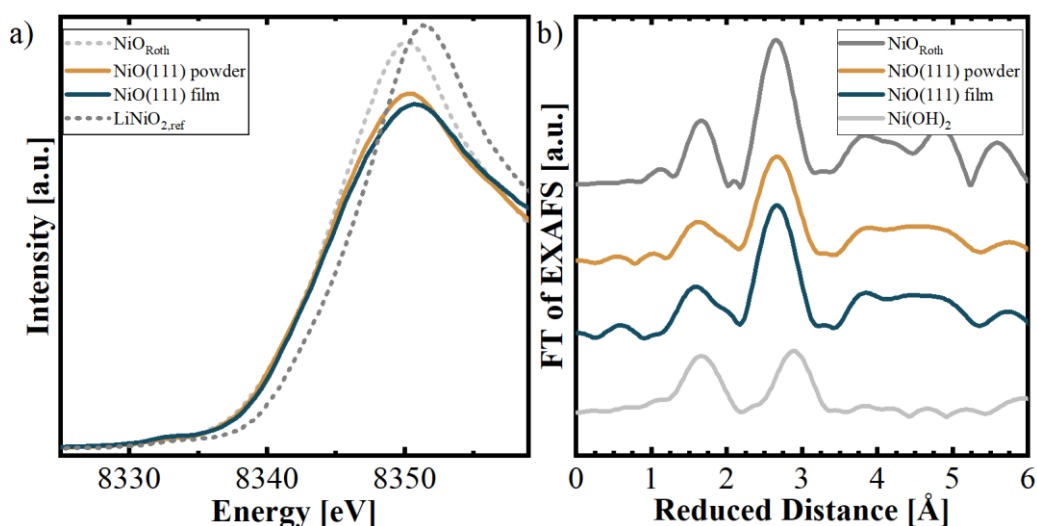


Figure 52: a) Ni-K edge XANES of NiO(111) powder and film samples (ink on GC disc) in comparison to commercial reference samples. b) Ni-K edge EXAFS of the respective NiO(111) powder and film samples with representative reference samples.

The survey spectra of the film sample (Figure 53) reveal additional features to the powder samples. Both samples contain Ni, O from the catalyst, arbitrary C and Na, probably from contaminations. The film sample adds F from the Nafion binder, which also influences the C 1s and the O 1s spectra by adding signals from the Nafion backbone and side chain. S, which is expected from the sulfonic acid groups, is only present in traces. The GC substrate is also expected to contribute to the C 1s spectra of the film sample.

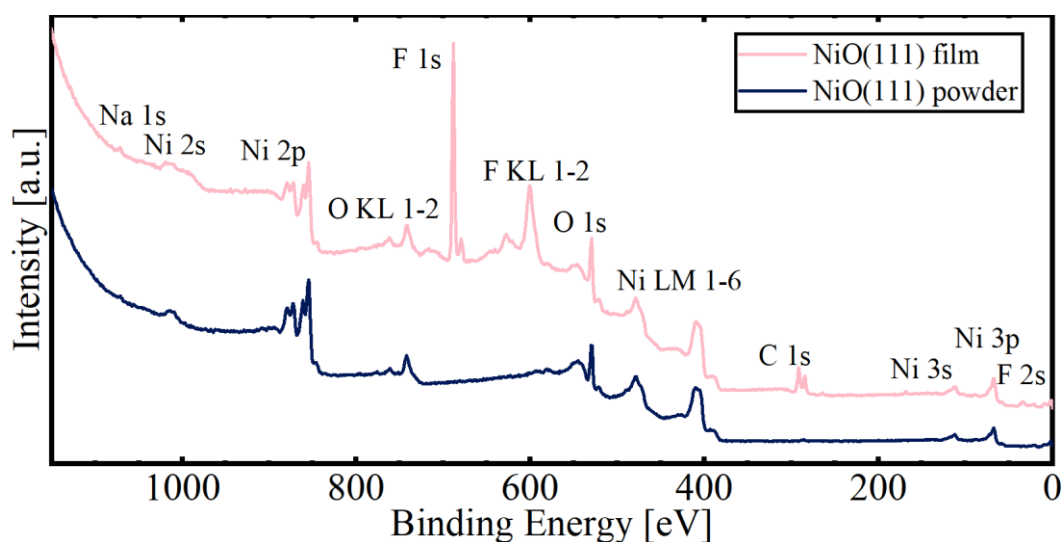


Figure 53: XPS survey spectra of the NiO(111) powder and film (ink on GC). Dominant signals are annotated.

The O1s signal of the powder sample in Figure 54a was already discussed in chapter 5.3 and the signals correspond to lattice Ni–O and surface hydroxide species, respectively.<sup>42,125</sup> For the film sample, an additional peak is observed at higher binding

energies and can be attributed to oxygen from adsorbed water and organic species.<sup>125</sup> Latter can be explained by contribution of the sulfonic acid and fluorinated ether groups due to the Nafion content in the thin films.<sup>160,161</sup> Also, contributions of oxidized GC should be considered to contribute to the higher-binding energy feature. These additional signals might overlay with changes of the NiO(111) sample surface. However, the peak intensity ration of peak A and B of the powder and the film sample are similar. Thus, only a limited contribution of the dispersion preparation onto the material is expected.

Furthermore, the qualitative observation between the powder and the film samples of the Ni  $2p_{3/2}$  signal is similar (Figure 54b). It represents the characteristic spectra of a NiO discussed above.

The comparability between the powder and the film is possible, but the differences in the C 1s spectra and O 1s spectra need to be considered for the analysis. It is recommended to compare an electrochemically treated sample with a pristine film sample without electrochemical treatment. This improves the comparability between before and after electrochemical treatment.

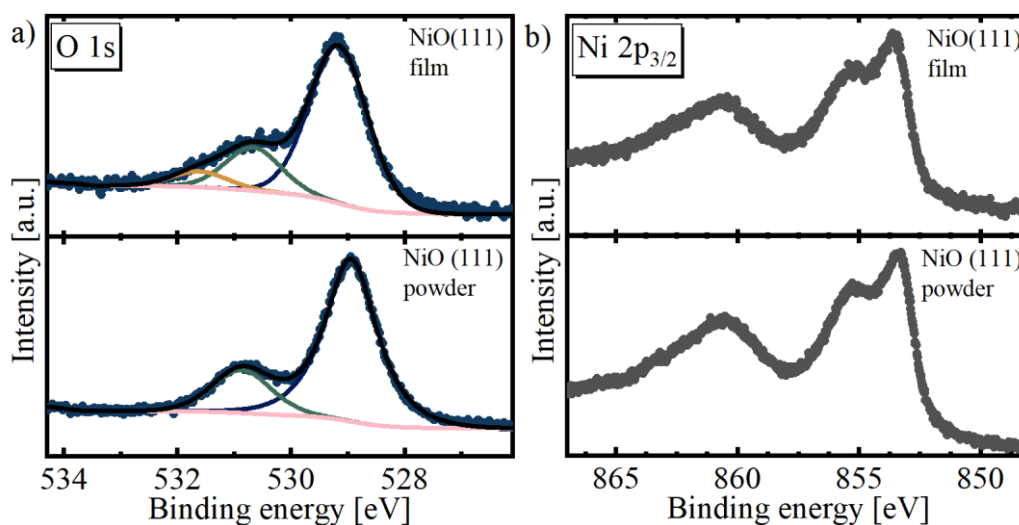


Figure 54: a) XPS O 1s and b) Ni  $2p_{3/2}$  spectra of the NiO(111) powder and film samples.

The main factor that is discussed in the regards of the reproducibility of independent RDE experiments is the quality of the catalyst film coating.<sup>9</sup> The catalyst film on the disc electrode needs to be thin to facilitate the unique mass transport of RDE experiments. This thin coating is prone to be inhomogeneous due to the low amounts of catalyst contained in the dispersion and depends on the stability of the dispersion. Thus, the dispersion coating is discussed in the following paragraph.

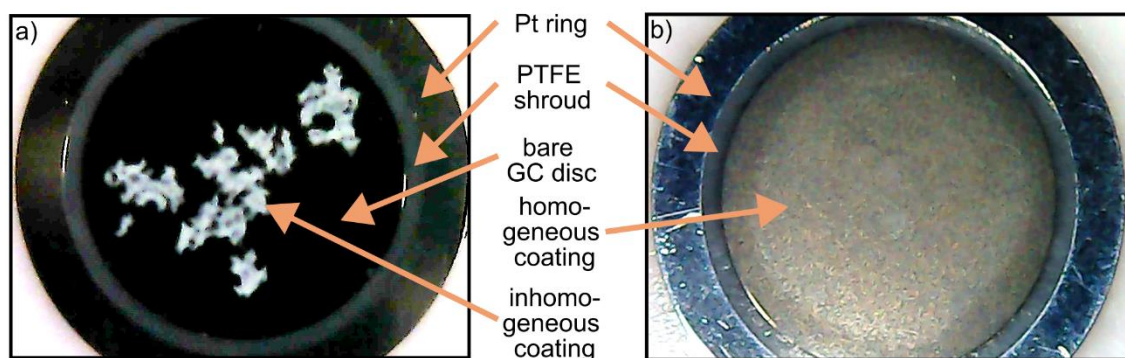


Figure 55: Photographs of RDE coatings of Ni(OH)<sub>2</sub> a) without cooling and b) with cooling of the sonication bath during the dispersion preparation.

Throughout the different chapters of this work, the dispersion needed to be adapted to the tested materials. First, dispersions with high water content and low isopropanol content were used because they were effective to disperse the tested oxide materials. After including hydroxide materials into the study, the dispersion needed to be adjusted, because the hydroxide materials tend to quickly precipitate in aqueous mixtures at the tested catalyst concentrations. The solvent was changed to purely isopropanol with a higher concentration of catalyst materials. After implementing additional cooling of the sonication bath and using only isopropanol as solvent, complete coating of the disc electrode was reached. Another improvement was made by cooling the dispersion in the last sonication step. This increased the viscosity of the dispersion and further delayed the precipitation of the catalyst material. Figure 55 illustrates the difference between cooling on the coating outcome. The coating in Figure 55b is complete, but the coating still exhibits a coffering effect at closer look, leaving room for improvements.

This observation suggests that the dispersion must be optimized individually, to reach optimal disc electrode coatings for every material. However, this approach would also be time-consuming and would limit the comparability of varied materials across each other. A suitable compromise would be to optimize the dispersion composition for each class of material (e.g. hydroxide, rock salt oxide, spinel) to reach comparably homogenous catalyst dispersions. Additionally, the pipetting of the catalyst dispersion onto the disc electrode brings in a source of error by and the accuracy is strongly dependent on the on the experimenter. The personal influence of the experimenter could be mitigated by increasing the catalyst mass weight in, using higher dispersion volumes for the coating and by using automated pipetting. The effect of the disc coating on the reproducibility is expected to be high.

The next section will cover the influence of the binder material on the OER activity measurements. Figure 56a) depicts a schematic of the coated disc electrode which contains the catalyst that is bound to the disc substrate by the binder material. Interestingly, Nafion is often used as a binder material, also in alkaline environment, even though it is known as a proton conducting ionomer. However, the binder in the RDE powder thin films is not meant to serve as an ion conductor, but it should mostly guarantee the mechanical stability of the films.

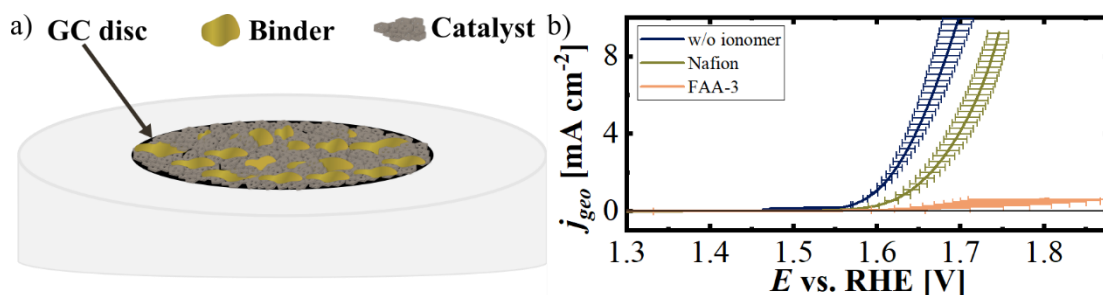


Figure 56: Schematic of the catalyst and ionomer distribution on a disc electrode. Observations for the RDE tests of  $\text{NiO}_{\text{USNano}}$  with different binder materials (Nafion and FAA-3) and without binder.

First observations of catalyst coatings without binder led to mechanically unstable catalyst films. Moreover, it was found (Figure 56b), that the Nafion even decreases the OER activity compared to the experiments of films without ionomer. It is expected that the Nafion attached to the catalyst material to the disc, also blocks some active sites. This active site blockage was more tremendous in the anion conducting ionomer FAA-3 that was evaluated for comparison. Using the equivalent ionomer loading of about 10%, the FAA-3 increased the  $\eta$  of the catalyst several hundreds of mV. This example suggests that the ion conductance is of less importance in RDE experiments and implies that the FAA-3 has a blocking effect, hindering the mass transport at the active sites.

Furthermore, the different density of the ionomer materials Nafion and FAA-3 plays a role, which could lead to the less dense FAA-3 covering a larger area. This could be evaluated by a variation of ionomer loading. However, the ionomer loading of the FAA-3 is not expected to make up the multifold higher activity that was observed for the Nafion containing samples or even the ionomer free samples. Experiments without ionomer were not continued, because a catalyst layer detachment was often observed, for higher current densities. Therefore, Nafion was chosen as suitable for RDE experiments. Other studies also suggested PTFE as a binder material.<sup>146</sup> PTFE could prevent ionomer induced changes of the catalyst, which was reported for Mn based catalysts.<sup>180</sup>

A comparably high influence is expected to be introduced by the electrochemical treatment of the samples, which is studied in the following paragraph.

### 5.6.2 Influence of different electrochemical treatments on the catalysts

The report of electrochemical data and of electrocatalytic metrics is not standardized across the electrocatalysis community. The lack of standardization limits the comparability between studies, producing incomparable electrochemical protocols. There are approaches to guideline the community and improve comparability in future studies.<sup>59,107</sup> An example on the effect of different conditioning methods is plotted in Figure 57, where a 1 hour galvanostatic hold at  $10 \text{ mA cm}^{-2}$  is compared to a rigorous electrochemical conditioning at  $100 \text{ mV s}^{-1}$  for 350 scans.

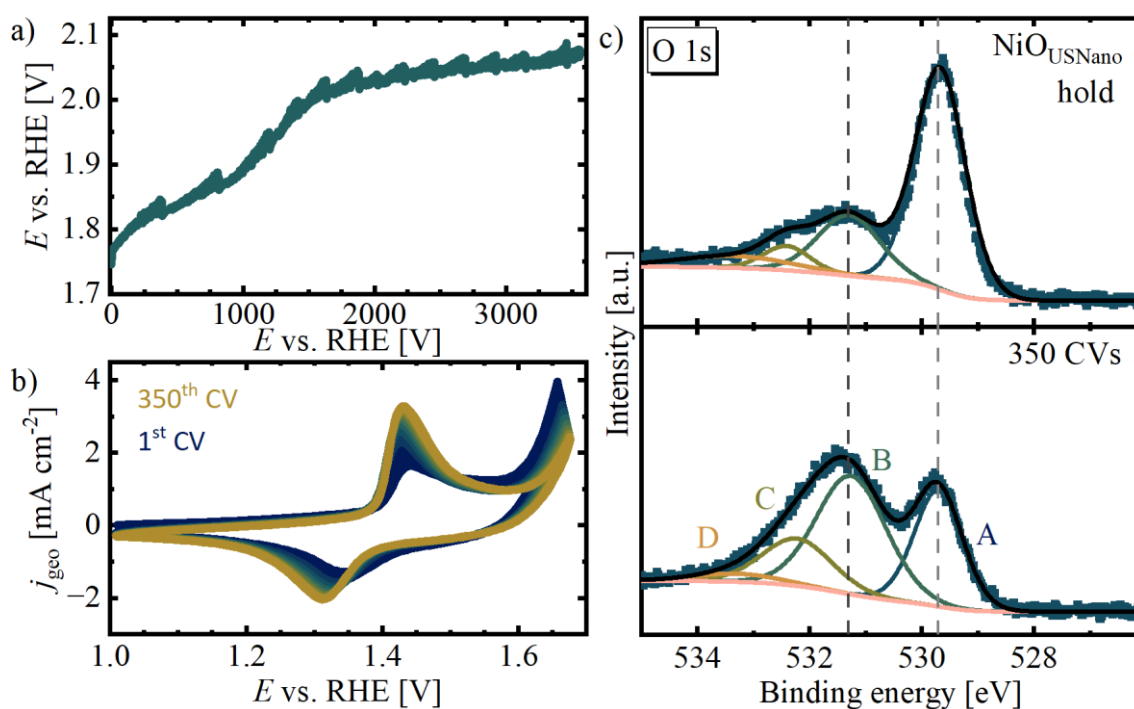


Figure 57: The figure depicts the comparison of electrochemical treatment on NiO<sub>USNano</sub> films. The corresponding hold experiments and CVs are plotted in a) and b), respectively. c) shows XPS O 1s spectra of NiO<sub>USNano</sub> samples after 1 h hold at  $10 \text{ mA cm}^{-2}$  and after 350 CVs. Characteristic peaks are denoted.

The effect of the conditioning on the sample surface was investigated by *ex-situ* XPS in Figure 57a and b. Both samples were prepared identically, which should enable a comparison of the effect of sample conditioning. The sample that underwent the galvanostatic hold is similar to the pristine NiO film samples as discussed Figure 54b. In particular, the dominant signal A is corresponding to lattice Ni–O and the less dominant signal B to surface hydroxide species, respectively.<sup>42,125</sup> The small intensity of signal B is suggesting, that most of the probed surface layer are still in the NiO rock salt structure,

with a thin surface hydroxide layer. Signals at higher binding energies C and D are attributed to organic compounds and adsorbed water.<sup>42,125</sup>

The cycled sample on the other hand depicts a much more intense peak B and C. This peak B and C was already assigned to the growth of surface hydroxide, which is the reduced form of the catalytically active  $\text{Ni}^{\text{III}}\text{OOH}$ . This observation suggests that the electrochemical conditioning is transforming the NiO more effectively to catalytically available  $\text{Ni}(\text{OH})_2$ . Only minor amounts of  $\text{Ni}(\text{OH})_2$  were found in the galvanostatic treated sample. This observations agrees with literature in which the electrochemical conditioning was found to make thicker hydroxide films than potentiostatic holds from a NiSe pre-catalyst.<sup>87</sup> Even if activity metrics were recorded for both samples after the respective treatments, their direct comparison would be misleading, as the surface structures are fundamentally different and therefore no longer represent comparable electrochemical interfaces. The following paragraph will cover different approaches for electrochemical conditioning on the example of the NiO(111) sample.

In Figure 58, the conditioning with 350 CV was done at different scan rates of 50 and 100  $\text{mV s}^{-1}$  and were compared to the use of different electrolyte concentrations. After the different potentiodynamic treatments, the samples were compared in CVs at scan rates from 1, 5 and 10  $\text{mV s}^{-1}$ , to account for differences of capacitive currents.  $iR$ -correction was done to compensate the different electrolyte resistances of 0.1 and 1 M KOH.

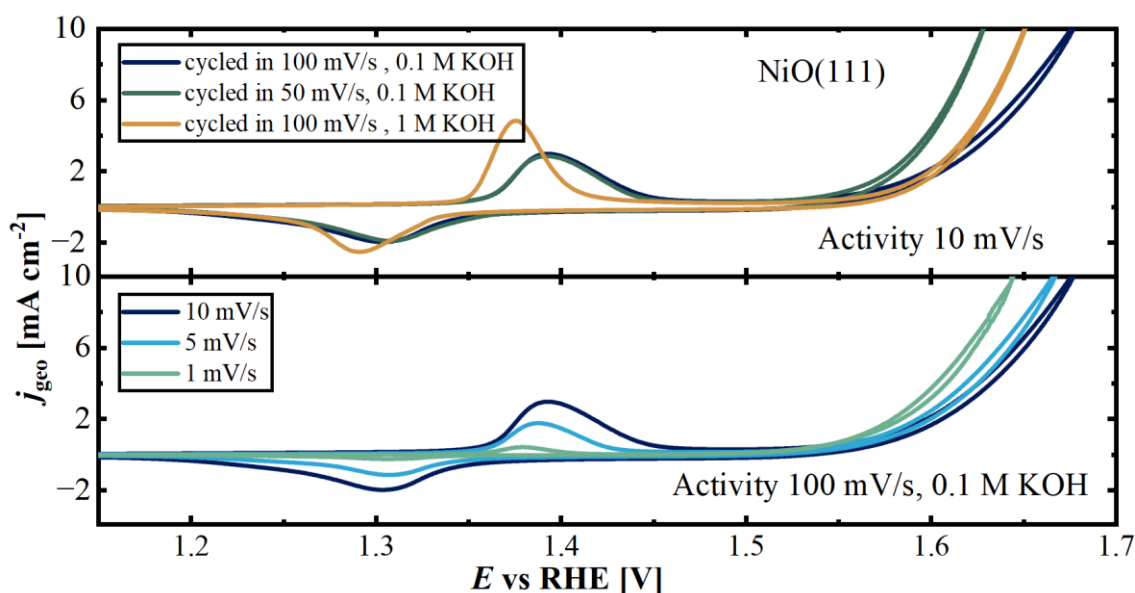


Figure 58: CV comparison of independent NiO(111) samples after 350 CVs at different scan rates (100 and 50  $\text{mV/s}$ ) and electrolyte concentration (0.1 and 1 M KOH). The CV above were recorded at 10  $\text{mV/s}$  respectively. Below, the CVs were recorded at the scan rate 1, 5 and 10  $\text{mV s}^{-1}$  after conditioning at 100  $\text{mV/s}$  in 0.1 M KOH.

All three scan rates gave the same trends of which the samples cycled at  $50 \text{ mV s}^{-1}$  in  $0.1 \text{ M KOH}$  gave the best results, followed by the sample conditioned in  $1 \text{ M KOH}$  and the sample condition in  $0.1 \text{ M KOH}$  at  $100 \text{ mV s}^{-1}$ . This could be explained by the  $50 \text{ mV s}^{-1}$  conditioning doubles the time of the conditioning, which could explain the positive effect by the fact that the electrode is longer polarized at oxidative potentials and was already reported in literature.<sup>11</sup> However, the  $\text{Ni}^{\text{II}}/\text{Ni}^{\text{III}}$  oxidation peak height of the  $50 \text{ mV s}^{-1}$  and the  $100 \text{ mV s}^{-1}$  sample indicates that the amount of formed hydroxide on the catalyst surface should be comparable between the different scan rates. Furthermore, the higher electrolyte concentration of  $1 \text{ M KOH}$  was found to improve the activity compared to the  $0.1 \text{ M KOH}$  electrolyte, even after  $iR$ -correction. The comparison was made in unpurified  $\text{KOH}$ , which leads to the two possible explanations of an tenfold higher amount of residual  $\text{Fe}$  in the electrolyte as well as positive effects of  $\text{Ni}(\text{OH})_2$  formation due to higher  $\text{KOH}$  concentrations.

Furthermore, the OER was evaluated with CV at three different scan rates. It was expected that the  $10 \text{ mV s}^{-1}$  sample has the lower  $\eta$  at  $10 \text{ mA cm}^{-2}$  because of capacitive currents that possibly add up to the intrinsic OER currents. However, the CV recorded at  $1 \text{ mV s}^{-1}$  was found to have the lower  $\eta$ . This could be explained by the same fact as the improving effect of the  $50 \text{ mV s}^{-1}$  conditioning of the sample above, which is the increased time of oxidative polarization of the  $\text{NiO}(111)$  electrode, which could improve the number of oxidized  $\text{Ni}^{\text{III}}\text{OOH}$  sites, thus leading to improved activities and lower  $\eta$ .

Often, the scan rate of  $1 \text{ mV s}^{-1}$  is discussed as quasi-equilibrium conditions of the material, e.g. for Tafel analysis of OER electrocatalysts.<sup>181</sup> The observations of the overestimation from  $1 \text{ mV s}^{-1}$  scans indicate the differently. The results agree with the comparative analysis of galvanostatic experiments and CV in chapter 5.3, where higher  $\eta$  were measured for the galvanostatic experiments in every sample tested. Instead, the results herein suggest that the slow scan rate CV rather increase the activity results than representing an equilibrium condition for the characterization.

The results of this section suggest that the electrochemical treatment of the samples has a tremendous influence on the surface structure and the apparent activity of the electrocatalyst. CV is effective to reconstruct the Ni-based catalyst surfaces into  $\text{Ni}(\text{OH})_2$ . The role of the scan rate onto the activity was found to be higher than the electrolyte concentration for the studied system. These results strengthen the efforts to implement a standardized protocol for the report of electrocatalytic activity metrics. Furthermore, each implemented electrochemical protocol should be classified by evaluating it with a

commercially available pre-catalyst material. This allows to transfer activity trends between else incomparable studies. The next chapter will continue from the electrochemical investigations to considerations for the *ex-situ* characterization.

### 5.6.3 Importance of the sample storage for *ex-situ* experiments

The sample storage is usually overseen aspect of catalyst research. However, since the surface of a catalyst is always exposed to air, moisture, light, or contaminants, it can potentially change over time. First, the exposure to ambient air can lead to adsorption of carbonates, water, or hydrocarbons, which may alter surface-sensitive measurements like XPS. Second, reaction intermediates or surface species may only be stable under specific electrochemical conditions and degrade upon exposure to air. With this, control of the sample storages reduces one variable that can influence the chemical state of the sample and ensures that *ex-situ* characterization reflects the condition after the electrochemical process.

The optimal storage condition could vary from material to material. E.g. materials that are prone towards dehydration might be unstable in vacuum, materials that are readily oxidized will degrade in air. To find proper sample storage conditions for the NiO materials before the XAS *ex-situ* experiments, in which several weeks passed from EC experiment to the beamtime, NiO<sub>USNano</sub> films have been prepared and tested electrochemically. Those samples were cycled electrochemically and stored for two weeks under vacuum, N<sub>2</sub>, Ar and were compared to a fresh sample at the XPS.

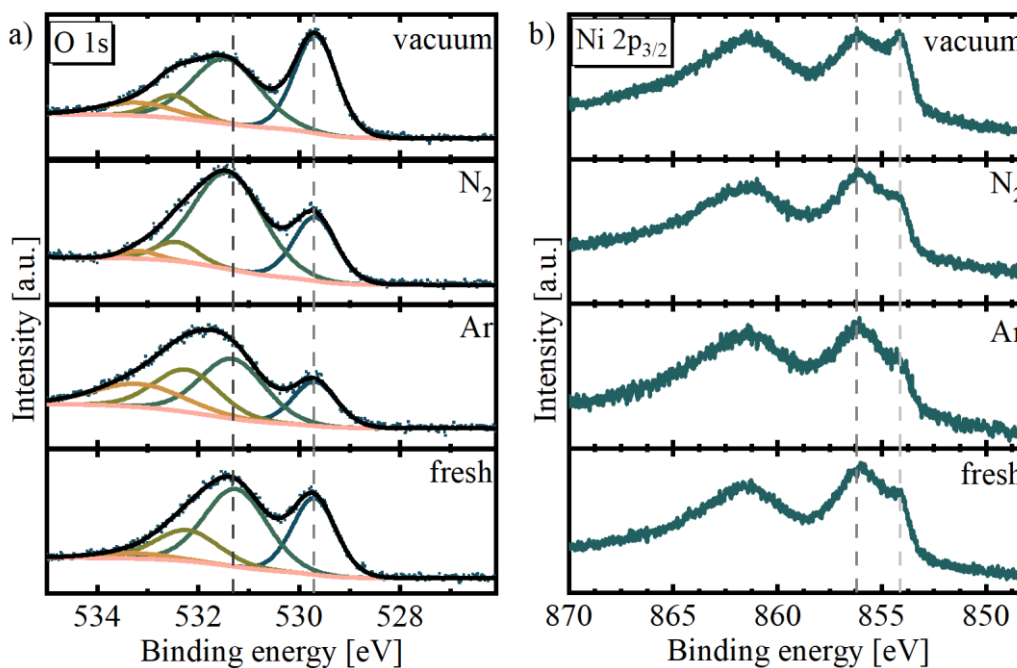


Figure 59: XPS results of a) O 1s and b) Ni 2p<sub>3/2</sub> for NiO<sub>USNano</sub> film samples on GC discs, freshly after electrochemical testing as well as after 2 weeks of storing under vacuum, N<sub>2</sub> and Ar atmosphere.

The Figure 59a represents O 1s spectra, which reveals slight differences between the experiments. The fresh sample shows the already reported lattice oxygen peak at lower binding energies, followed by the hydroxide peak, a third peak correlated to organic oxygen and adsorbed water<sup>125</sup> and a fourth peak, correlated to carbonate species of adsorbed CO<sub>2</sub> from the KOH electrolyte<sup>182</sup>. The position of the main peaks remains similar, but the relative ratio between the peaks strongly differs between the samples. The vacuum stored sample has the most dominant lattice oxygen peak, indicating a less hydroxide on the catalyst, also by desorption of water. This observation is supported by the qualitative comparison of the Ni 2p<sub>3/2</sub> spectra in Figure 59b, which resembles a distinct NiO character.<sup>125</sup> The inert gases N<sub>2</sub> and Ar have similar signals compared to the fresh samples, by which means pronounced hydroxide signals. The signals at higher binding energies differ a bit. However, the consideration of the Ni 2p<sub>3/2</sub> signal suggests that the surface composition of the Ni is consistent between the inert gases to the fresh sample.

This differences in the hydroxide coverage of the samples after different storage conditions highlights that false correlations could be observed, when the sample storage before *ex-situ* analysis is not comparable.

#### 5.6.4 Key learnings for future studies of OER electrocatalysts

In the following, the observations from previous paragraphs are extended into practical guidelines aimed at ensuring reliable and reproducible outcomes in EC experiments. One key consideration is that a single EC experiment cannot stand alone, and measurements must be repeated to ensure that the results are reliable. Throughout this work, multiple materials were presented that exhibit high standard deviations (e.g. Ni(OH)<sub>2</sub>+1% Fe, NiO(111)+2% Co) in which a single experiment might have implied a drastically higher or lower trend than the average value of the OER  $\eta$ , respectively. The minimum number of experiments to obtain trends is two. However, the more experiments conducted the trend of the data becomes more reliable and experimental outliers can be identified. In this study, usually three independent electrodes were assessed to report an average and a standard deviation.

Exemplary, the overall activity trends that were collected in this thesis are described by a collection of the  $\eta$  at a geometric current density of 10 mA cm<sup>-2</sup> and by the metric of the specific current density of the BET surface area normalized  $j_{\text{BET}}$  at a potential of 1.55V. The  $j_{\text{BET}}$  is used as an approach to measure the intrinsic activity of the catalyst materials. The potential at which  $j_{\text{BET}}$  was determined is a trade-off between the Ni<sup>II</sup>/Ni<sup>III</sup> oxidation peak position and the OER onset of each sample. It is stated that the  $\eta@10$  mA cm<sup>-2</sup> is a more valuable metric for a comparison of such different catalyst materials. The overlap of the Ni<sup>II</sup>/Ni<sup>III</sup> oxidation peak of some samples at the  $j_{\text{BET}, 1.55 \text{ V}}$  limits the validity of the activity metric. This collection is a valuable collection of the effect of the different electrochemical protocols with each other.

Interestingly, the  $\eta$  of the materials NiO<sub>USNano</sub> and the NiO(111), differ by 72 mV and 12 mV when comparing the conditioning with 350 and 50 CV, respectively. The lower activity of the samples after 50 CV in purified KOH are related to the absence of Fe in the purified electrolyte as well as the lower amounts of surface reconstruction due to lower number of CV scans in the latter case.

## 5.6 Considerations for reproducible electrochemical characterization

Table 3: Summary of metrics from representative materials after conditioning. Different MW-based materials were chosen that were tested throughout the different studies in this work. The subscript describes the conditioning procedure, either after 50 and 350 CV in unpurified electrolyte (50CV and 350CV), after 50 CV in purified electrolyte (50CV, purified KOH) or after 50 CV in 0.1 ppm Fe(NO<sub>3</sub>)<sub>3</sub> spiked electrolyte (50CV, 0.1 ppm Fe(NO<sub>3</sub>)<sub>3</sub>). The sample NiO(111)<sub>50CV</sub> equals the MW-NiO(111)-400.

MaterialConditioning	$\eta$ @10 mA cm <sup>-2</sup> [V]	$j_{\text{BET}, 1.55 \text{ V}}$ [mA m <sup>2</sup> ]
NiO(111) <sub>50CV</sub>	0.414 ± 0.019	24 ± 3
NiO <sub>USNano</sub> 350CV	0.476 ± 0.022	49 ± 4
NiO(111) 350CV	0.481 ± 0.001	41 ± 3
NiO(111)+5% Co 350CV	0.447 ± 0.016	25 ± 8
NiO(111)+5% Mn 350CV	0.513 ± 0.003	24 ± 1
NiO <sub>USNano</sub> 50CV, purified KOH	0.548 ± 0.029	29.5 ± 1.3
NiO(111) <sub>50CV</sub> , purified KOH	0.493 ± 0.015	20.9 ± 1.2
NiO(111)+5% Fe 50CV, purified KOH	0.426 ± 0.004	29.5 ± 2.7
NiO(111)+Fe <sup>3+</sup> 50CV, 100 ppb Fe(NO <sub>3</sub> ) <sub>3</sub>	0.353 ± 0.014	346 ± 173
Ni(OH) <sub>2</sub> 50CV, purified KOH	0.416 ± 0.009	302 ± 54
Ni(OH) <sub>2</sub> +5% Fe 50CV, purified KOH	0.417 ± 0.008	750 ± 137
Ni(OH) <sub>2</sub> +Fe <sup>3+</sup> 50CV, 100 ppb Fe(NO <sub>3</sub> ) <sub>3</sub>	0.364 ± 0.023	634 ± 297

The comparison of the pristine materials with the experiments after Fe<sup>3+</sup> spiking shows a decrease in  $\eta$  by 52 mV and 140 mV for the Ni(OH)<sub>2</sub> and NiO(111) samples, respectively. The highest  $j_{\text{BET}, 1.55 \text{ V}}$  values were obtained for the Fe doped hydroxides and the NiO(111)+Fe<sup>3+</sup>. This is explained by the relatively low BET surface area and the high OER activity.

The NiO<sub>USNano</sub> 50CV, purifiedKOH followed by the NiO(111)+5% Mn 350CV had the highest  $\eta$  in the comparison. The measured activity is broadly consistent with prior studies of analogous systems.<sup>9,53,175</sup> To recall, a comparative study has reported  $\eta$  for a compounded NiFe-LDH material of ~350 mV.<sup>175</sup> Other less comparable RDE studies have reported  $\eta$  of less than 300 mV at for compounded NiFe-LDH materials.<sup>176,177</sup>

A further concern is the deviations in between the RDE experiments. Some experiments exhibit standard deviations >20 mV which were explained by invisible unevenness in the catalyst coating. These deviations are still acceptable compared to other studies.<sup>9,146</sup> Tesch et al.<sup>9</sup> monitored in a Round Robins test, that some labs had deviations of >20 mV. However, for some materials such as the NiO(111) 350CV it was proven that

lower deviations are possible. This low standard deviation might be explained by the optimization of the catalyst ink for the NiO(111) material.

To minimize the variation between experiments, uncontrollable factors that could influence the experiments should be avoided. For example, dispersions should be used freshly and the time between the coating and the electrochemical experiment should remain comparable. In correlation with the comparison of sample storage conditions, the time at which *ex-situ* samples are stored should be similar in-between an *ex-situ* experiment series.

Additionally, the backside contact corrosion of exchangeable RDE electrodes used for *ex-situ* experiments should be considered. This corrosion can introduce high ohmic resistances and can be avoided by sanding the backside contacts of the disc inserts. Particularly for experiments at OER conditions, it is essential to freshly polish the GC discs prior to the coating, since the carbon is expected to corrode in alkaline and oxidative conditions.

Furthermore, the use of unsuitable binder materials should be avoided, since it was found that it can hamper the OER currents by an order of magnitude.

A factor that was well studied by the example of Fe are electrolyte impurities. Especially unknown electrolyte impurities can influence observed trends drastically. To mitigate these issues, either electrolyte purification or the saturation of the electrolyte with critical ions such as Fe can be performed to account for known impacts. However, the influences of electrolyte impurities on the OER activity were in the range of the same order of magnitude.

It is also essential to clean the electrochemical cell and its parts between experiments, with special attention to cleaning after each material change. A suitable cleaning procedure, such as acid treatment to remove transition metal impurities, should be used to ensure that the cell and its parts are thoroughly cleaned. By taking these precautions, researchers can minimize the impact of uncontrollable factors and obtain reliable and reproducible results from their EC experiments.

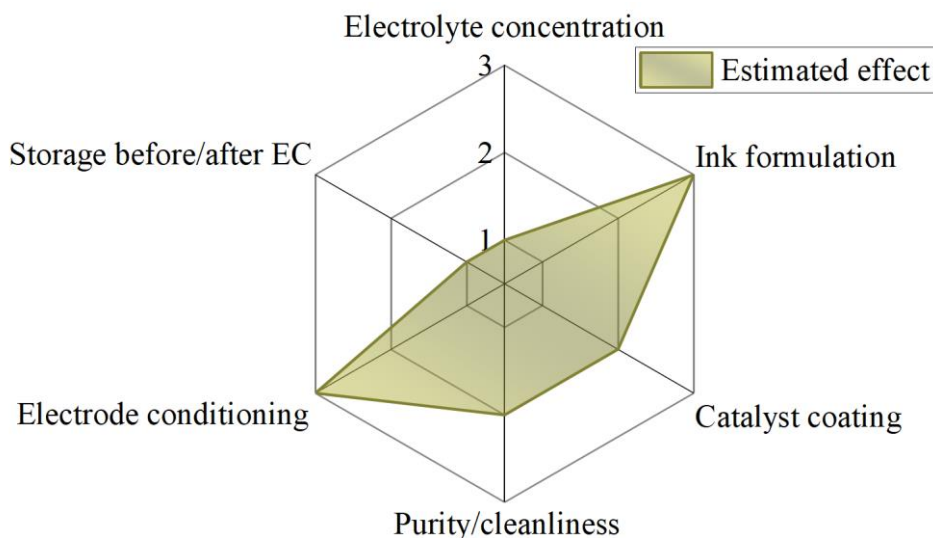


Figure 60: Summary of the estimated effect of different parameters that were tested in regards of the reproducibility of RDE measurements of the OER on NiO catalysts. The ranking is from 0 (no effect) to 3 (high).

The different effects that were considered to influence the reproducibility and the reliability of electrochemical data throughout this thesis are summarized in Figure 60. The highest influences are connected to the dispersion formulation and the electrode conditioning. The wrong choice of binder and insufficient conditioning were observed to obscure the OER activity of a catalyst completely.

Lower effects are attributed to the quality of the catalyst coating and the purity and cleanliness of the measurement. These factors can drastically influence the variations between experiments but are less likely to distort the observed trends.

The influences of the electrolyte concentration and the storage of the samples are expected to be less, but still accountable. It must be stated, that this collection may not be complete and was solely based on empirical observations for Ni-based catalysts. Yet, it is recommended to follow these guidelines in future experiments. Especially the parameters with the highest effect should be optimized beforehand each study.

---

## 6 Conclusion

This thesis sets out to study how NiO transforms during OER conditions and how the reconstruction is influenced by the addition of the transition metals Co, Mn and Fe. Thereby, the correlation between the surface reconstruction towards NiOOH and the electrode activity is explored.

In the first part of this work, the MW and the ST synthesis route were compared for preparing faceted, pure NiO(111) nanosheets, focusing particularly on how annealing temperature influences morphology and catalytic performance. It was found that the MW-derived nanostructures were more sensitive to annealing temperature: at 600 °C they were sintered into larger particles, whereas the ST-derived nanosheets retained their morphology for the same temperature range. This conclusion was supported by TEM imaging, crystallite sizes determined by PXRD and N<sub>2</sub> physisorption measurements. Furthermore, lower annealing temperatures were correlated to higher surface areas. Yet, the optimal OER activity was observed at 400 °C for the MW samples and 500 °C for the ST samples, indicating that intrinsic activity differs despite morphological similarities. Thus, the MW synthesis was combined with annealing at 400 °C for further studies, as a balance of surface area and activity.

The second study was focused on doped NiO(111) nanosheet from the MW synthesis route. Co- and Mn-doping were found to form phase pure materials, which was evaluated by PXRD and EXAFS. The focus of this study was to investigate the reconstruction of the NiO(111) pre-catalyst after 350 CV scans of conditioning. The Co-dopant seemed to remain in the NiO lattice. The Co-dopant has not led to a separate oxidation/reduction peak in the CV and no significant changes in its oxidation state. In contrast, the Mn-dopant had a strong influence on the Ni<sup>II</sup>/Ni<sup>III</sup> oxidation peak. The initial cyclic voltammograms exhibited a distinct shift of oxidation potentials followed by splitting into separated oxidation peaks. After electrochemical treatment, XAS revealed that Ni and Co remained predominantly in the II oxidation state, whereas Mn was present at oxidation states between III and IV, which are reported to be the less active for the OER. In addition, RRDE experiments and *ex-situ* ICP-MS analysis detected up to ~6 % of Mn based on initial catalyst loading in the electrolyte, indicating Mn-leaching. Furthermore, the charge of the oxidation peak of the electrodes was drastically lowered in both doped samples compared to pure NiO(111). This was a first indication of a hindered Ni<sup>II</sup>/Ni<sup>III</sup> oxidation and further confirmed with lower observation of surface reconstruction product in XPS.

Despite the lower surface reconstruction towards Ni(OH)<sub>2</sub> and NiOOH for both dopants, electrode activity was slightly increased by Co-doping. The observed activity enhancement of Co-doped NiO(111) was attributed to dopant sites in unusual coordination environments instead of the surface hydroxide formation. The well-defined pre-catalyst enabled tracking of irreversible material changes.

The incorporation of Fe was elucidated more carefully because it is known to be one of the most active dopants for Ni-based OER catalysts. However, the doping was challenging because the Fe<sup>3+</sup> precursor readily precipitated in the conventional synthesis route reported for Co and Mn incorporation, resulting in Fe impurity phases. Controlling the pH could decrease but not completely prevent this effect, leading to discrepancies between the intended and apparent Fe content. Fe incorporation into Ni(OH)<sub>2</sub> and NiO(111) host materials, was compared for two approaches: the compounded incorporation during the synthesis and *in-situ* Fe<sup>3+</sup>-doping due to Fe<sup>3+</sup>-spiking of the electrolyte.

Compounded doping enhanced the OER activity significantly. For the NiO(111)-materials, the lower doping levels exhibit the lowest  $\eta$ , without a distinct optimum. Instead, Ni(OH)<sub>2</sub>-materials did not exhibit a clear trend of an optimal composition. Likely owing by high deviations between the RDE experiments of the Ni(OH)<sub>2</sub> samples. The most pronounced  $\eta$  decrease was found with *in-situ* spiking of Fe<sup>3+</sup> through the electrolyte. This was explained by the surface confined *in-situ* doping, which might distribute the Fe more effectively on the surface.

The higher  $\eta$  of the compounded samples compared to the *in-situ* Fe<sup>3+</sup> doped samples are explained by observations of phase impurities in the compounded samples by EXAFS. The EXAFS suggested distinct local coordination environments for the Ni- and Fe-K edge of the compounded samples. This was confirmed by observations from Raman and PXRD. It was proposed that above of 5% Fe, separate phases next to the mixed Ni-Fe lattice were formed.

CV, *in-situ* Raman and *ex-situ* XPS revealed a similar effect of Fe on the surface reconstruction as the Co and Mn dopants. Through both doping strategies, compounded incorporation during the synthesis and *in-situ* Fe<sup>3+</sup>-doping, Fe doping suppresses the NiOOH formation. The enhanced activity of Fe-containing samples was attributed to the intrinsically higher catalytic activity of Ni<sub>x</sub>Fe<sub>1-x</sub>OOH compared with  $\beta$ -NiOOH, which is expected to form on the surface of pure Ni(OH)<sub>2</sub> and NiO(111).

---

More application oriented electrochemical testing was realized with the PTE half-cell setup. In this setup, the PTE resembles the anode of an AEMWE. The PTE half-cell setup was optimized to conditions that are reported for AEMWE single cell experiments. The targeted current density was  $1 \text{ A cm}^{-2}$ , which was achieved at KOH concentration down to 1 M and temperatures up to  $60 \text{ }^\circ\text{C}$ . The PTE half-cell setup revealed more pronounced activity trends than the RDE setup. The  $\eta$  at  $1 \text{ A cm}^{-2}$  differed more than 300 mV between the sample NiO(111) and the Ni(OH)<sub>2</sub>+5% Fe. The study validates that hydroxide-based materials, especially Ni(OH)<sub>2</sub>+5% Fe, are promising for the use in AEMWE anodes. The limitations identified for this setup were the restriction to relatively high KOH concentrations, to meet the compliance voltage of the tested potentiostat and the disregarding of the membrane between the working and the counter electrode and thus the complex catalyst/membrane interface. The results of the PTE half-cell setup highlight the critical need to evaluate new catalysts under high current densities and elevated temperatures to assess their practical viability.

In the last chapter, considerations for reliable RDE experiments and *ex-situ* studies were compiled. Herein, guidance for future studies, especially for RDE experiments of Ni-based OER electrocatalysts, was given. Several aspects were identified to be the most critical for reliable results. Less but still significant are the influences by the catalyst coating quality and the cleanliness of the cell, which can distort trends but not extinguish the OER activity. Additionally, factors such as the electrolyte concentration and the sample storage conditions should be constant throughout comparative study. The most critical aspects for the studied NiO catalysts have been the binder choice in the dispersion formulation and the electrode conditioning procedure were identified as critical aspects. Based on this findings, future studies should optimize the catalyst dispersion and should try to implement a unified electrochemical protocol that suits the respective research question.

Together, this work contributes to the knowledge of Ni-based OER electrocatalysts in alkaline media. In particular it was found that extensive surface reconstruction into NiOOH is a prerequisite for high activity. Instead, several doped systems, particularly those containing Fe, displayed enhanced performance despite showing only limited NiOOH formation. This suggests that intrinsic activity of Ni–Fe oxyhydroxide species, rather than the extent of surface transformation alone, governs catalytic activity. In contrast, Mn was identified as an unsuitable dopant for NiO-based pre-catalysts due to its leaching tendency and suppression of beneficial redox transitions. Fe, however, proved

consistently effective across both synthetic and electrolyte-derived incorporation strategies, reaffirming its role as the most impactful dopant for Ni-based (hydr)oxides.

By extending electrochemical testing from conventional RDE protocols to application-relevant half-cell measurements mimicking AEMWE relevant conditions, this work further demonstrates that catalyst evaluation should be performed at high current densities and elevated temperatures to yield meaningful conclusions for practical deployment.

Beyond scientific insight, the thesis also offers methodological guidance for catalyst testing based on results for NiO, contributing to more reliable and comparable OER characterization across the field.

---

## 7 Outlook

The results of this work suggest multiple directions for future investigation. The insights into the reconstruction of Fe-doped materials could be improved by a phase pure Fe-incorporation. Previous reports have demonstrated phase-pure Fe incorporation via compounded synthesis at Fe contents above 15%.<sup>62,64</sup> Achieving comparable phase-pure doping, in a faceted material with well-dispersed Fe–Ni active sites would provide valuable insights. This might be challenging, because reports of well dispersed Ni-Fe-LDH materials were realized in a surfactant-free approach under exclusion of water,<sup>64,183</sup> contrasting the surfactant-based (benzyl alcohol) synthesis used in this work. Further understanding of the  $\text{Ni}_x\text{Fe}_{1-x}\text{OOH}$  could be achieved under operando conditions.

Furthermore, the findings from this study, derived from *ex-situ* and *in-situ* characterization, could be further validated using *operando* techniques. This would require integrating the material into an operating device, such as an AEMWE single cell. Investigating *in-situ*  $\text{Fe}^{3+}$  incorporation into faceted materials under *operando* conditions would be particularly insightful. Suitable *operando* techniques include synchrotron-based X-ray absorption spectroscopy, *operando* Raman spectroscopy and operando X-ray computed tomography.

Moreover, the pronounced influence of Fe incorporation, whether unintentional through electrolyte impurities or intentionally through *in-situ* spiking, highlights the need for standardized protocols that rigorously control Fe content during catalyst synthesis, electrochemical conditioning, and testing. Only under such controlled conditions, intrinsic activities can be distinguished from impurity-based influences.

In this study, faceted NiO(111) materials were synthesized as well-defined pre-catalyst. Future investigations could expand this approach on other predominantly faceted materials. Although comparable electrocatalytic studies for Ni-based thin film catalysts or for powder materials produced by distinct synthetic routes have been reported,<sup>71,78</sup> exploring powder materials with different dominant facets would provide valuable insights into facet-dependent reconstruction processes. Further study of  $\text{Fe}^{3+}$  impurities and their facet-specific incorporation mechanisms could enhance understanding of the underlying surface phenomena.

Additionally, the *in-situ*  $\text{Fe}^{3+}$  incorporation could be investigated using larger sample amounts to enable detection of Fe by *ex-situ* characterization techniques. Higher Fe-uptake may be achieved by increasing the surface area of the  $\text{Ni}(\text{OH})_2$  or NiO host

materials or by increasing the  $\text{Fe}^{3+}$  concentration in the electrolyte. Such conditions would allow determination of the Fe-state, coordination environment, and total uptake of Fe by XPS, EXAFS and ICP-MS, respectively.

The usage of the PTE set-up was demonstrated for the characterization of some materials in this study. Accordingly, a comparative study of the PTE half-cell to an AEMWE single cell should follow, to evaluate the transferability of the PTE half-cell results. More comparability could require attaching a membrane to the PTE, for more realistic mass transport conditions. With some further optimizations, the PTE half-cell setup could be applied as an *in-situ* cell or for online analysis. Furthermore, the application for short-time stability testing could be realized.

Finally,  $\text{Ni}(\text{OH})_2$  and  $\text{NiO}$  serve as insightful pre-catalysts for understanding the behavior of Ni-based electrodes under AEMWE conditions. A key limitation of both materials is their low electrical conductivity. Future approaches could explore more conductive pre-catalysts that undergo surface-confined reconstruction to form core-shell-type active materials. Perovskites such as  $\text{LaNiO}_3$  are promising candidates, combining metallic conductivity with high activities in pure-water-fed AEMWE single cells.<sup>82</sup> Another challenge in pure-water-fed AEMWE operation is ionomer degradation at the anode. In this study, the ionomer was solely used as binder. However, operation in pure-water-fed systems requires stability of the ionomer. Protective layers between the ionomer and the catalytically active side were demonstrated for preventing corrosion while maintaining ion conductivity.<sup>184</sup>

---

## 8 References

- (1) Kovač, A.; Paranos, M.; Marcius, D. *Int. J. Hydrogen Energy* **2021**, *46* (16), 10016–10035, DOI: 10.1016/j.ijhydene.2020.11.256.
- (2) Oliveira, A. M.; Beswick, R. R.; Yan, Y. *Curr. Opin. Chem. Engineering* **2021**, *33*, 100701, DOI: 10.1016/j.coche.2021.100701.
- (3) Caglayan, D. G.; Weber, N.; Heinrichs, H. U.; Linßen, J.; Robinius, M.; Kukla, P. A.; Stolten, D. *Int. J. Hydrogen Energy* **2020**, *45* (11), 6793–6805, DOI: 10.1016/j.ijhydene.2019.12.161.
- (4) *SMARD Marktdatenvisualisierung: Stromerzeugung, Stromverbrauch (for the period: 17.-21.08.2024)*. [www.smard.de/home](http://www.smard.de/home) (accessed 03.09.25).
- (5) Wang, C. R.; Stansberry, J. M.; Mukundan, R.; Chang, H.-M. J.; Kulkarni, D.; Park, A. M.; Plymill, A. B.; Firas, N. M.; Liu, C. P.; Lang, J. T.; *et al.* *Chem. Rev.* **2025**, *125* (3), 1257–1302, DOI: 10.1021/acs.chemrev.3c00904.
- (6) Du, N.; Roy, C.; Peach, R.; Turnbull, M.; Thiele, S.; Bock, C. *Chem. Rev.* **2022**, *122* (13), 11830–11895, DOI: 10.1021/acs.chemrev.1c00854.
- (7) Chung, D. Y.; Lopes, P. P.; Farinazzo Bergamo Dias Martins, Pedro; He, H.; Kawaguchi, T.; Zapol, P.; You, H.; Tripkovic, D.; Strmcnik, D.; Zhu, Y.; *et al.* *Nat. Energy* **2020**, *5* (3), 222–230, DOI: 10.1038/s41560-020-0576-y.
- (8) Kim, J. S.; Kim, B.; Kim, H.; Kang, K. *Adv. Energy Mater.* **2018**, *8* (11), DOI: 10.1002/aenm.201702774.
- (9) Tesch, M. F.; Neugebauer, S.; Narangoda, P. V.; Schlögl, R.; Mechler, A. K. *Energy Adv.* **2023**, *2* (11), 1823–1830, DOI: 10.1039/D3YA00340J.
- (10) Trotochaud, L.; Young, S. L.; Ranney, J. K.; Boettcher, S. W. *J. Am. Chem. Soc.* **2014**, *136* (18), 6744–6753, DOI: 10.1021/ja502379c.
- (11) Gohlke, C.; Gallenberger, J.; Niederprüm, N.; Ingendae, H.; Kautz, J.; Hofmann, J. P.; Mechler, A. K. *ChemElectroChem* **2024**, *11* (18), e202400318, DOI: 10.1002/celec.202400318.
- (12) Wang, S.; Lu, A.; Zhong, C.-J. *Nano convergence* **2021**, *8* (1), 4, DOI: 10.1186/s40580-021-00254-x.

- (13) Urbano, E.; Pahon, E.; Yousfi-Steiner, N.; Guillou, M. *J. Power Sources* **2024**, *623*, 235451, DOI: 10.1016/j.jpowsour.2024.235451.
- (14) Lange, H.; Klose, A.; Lippmann, W.; Urbas, L. *Int. J. Hydrogen Energy* **2023**, *48* (42), 15771–15783, DOI: 10.1016/j.ijhydene.2023.01.044.
- (15) Wolf, S. E.; Winterhalder, F. E.; Vibhu, V.; Haart, L. G. J. de; Guillon, O.; Eichel, R.-A.; Menzler, N. H. *J. Mater. Chem. A* **2023**, *11* (34), 17977–18028, DOI: 10.1039/D3TA02161K.
- (16) Sebbahi, S.; Assila, A.; Alaoui Belghiti, A.; Laasri, S.; Kaya, S.; Hlil, E. K.; Rachidi, S.; Hajjaji, A. *Int. J. Hydrogen Energy* **2024**, *82*, 583–599, DOI: 10.1016/j.ijhydene.2024.07.428.
- (17) Groot, M. T. de; Kraakman, J.; Garcia Barros, R. L. *Int. J. Hydrogen Energy* **2022**, *47* (82), 34773–34783, DOI: 10.1016/j.ijhydene.2022.08.075.
- (18) Ursúa, A.; San Martín, I.; Barrios, E. L.; Sanchis, P. *Int. J. Hydrogen Energy* **2013**, *38* (35), 14952–14967, DOI: 10.1016/j.ijhydene.2013.09.085.
- (19) *Highly efficient fuel cell and electrolysis stack technology: elcoCell, elcoStack and elcoModule*; Elcogen, Ed. [elcogen.com/products/solid-oxide-stack-modules/](http://elcogen.com/products/solid-oxide-stack-modules/) (accessed 03.09.25).
- (20) *Sunfire-HyLink SOEC*; Sunfire SE, Ed. [sunfire.de/en/products/sunfire-hylink-soec/](http://sunfire.de/en/products/sunfire-hylink-soec/) (accessed 03.09.25).
- (21) *PEM Electrolyser – PSM Series*; Nel, Ed. [nelhydrogen.com/product/psm-series-electrolyser/](http://nelhydrogen.com/product/psm-series-electrolyser/) (accessed 03.09.25).
- (22) *Hybrion PEM Electrolysis Stacks*; Bosch, Ed. [www.bosch-hydrogen-energy.com/pem-electrolysis/pem-electrolysis-stacks/](http://www.bosch-hydrogen-energy.com/pem-electrolysis/pem-electrolysis-stacks/) (accessed 03.09.25).
- (23) *Atmospheric Alkaline Electrolyser*; Nel, Ed. [nelhydrogen.com/product/atmospheric-alkaline-electrolyser-a-series/](http://nelhydrogen.com/product/atmospheric-alkaline-electrolyser-a-series/) (accessed 28.06.25).
- (24) *Green Hydrogen Solutions*; thyssenkrupp nucera, Ed. [www.thyssenkrupp-nucera.com/green-hydrogen-solutions/](http://www.thyssenkrupp-nucera.com/green-hydrogen-solutions/) (accessed 03.09.25).
- (25) Hauch, A.; Brodersen, K.; Chen, M.; Mogensen, M. B. *Solid State Ion.* **2016**, *293*, 27–36, DOI: 10.1016/j.ssi.2016.06.003.

- 
- (26) Adamski, M.; Skalski, T. J. G.; Britton, B.; Peckham, T. J.; Metzler, L.; Holdcroft, S. *Angew. Chem. Int. Ed.* **2017**, *56* (31), 9058–9061, DOI: 10.1002/anie.201703916.
- (27) Hartig-Weiss, A.; Miller, M.; Beyer, H.; Schmitt, A.; Siebel, A.; Freiberg, A. T. S.; Gasteiger, H. A.; El-Sayed, H. A. *ACS Appl. Nano Mater.* **2020**, *3* (3), 2185–2196, DOI: 10.1021/acsanm.9b02230.
- (28) Gollasch, M.; Schmeling, J.; Harms, C.; Wark, M. *Adv. Mater. Interfaces* **2023**, *10* (15), DOI: 10.1002/admi.202300036.
- (29) Oakton, E.; Lebedev, D.; Povia, M.; Abbott, D. F.; Fabbri, E.; Fedorov, A.; Nachtegaal, M.; Copéret, C.; Schmidt, T. J. *ACS Catal.* **2017**, *7* (4), 2346–2352, DOI: 10.1021/acscatal.6b03246.
- (30) Krivina, R. A.; Lindquist, G. A.; Yang, M. C.; Cook, A. K.; Hendon, C. H.; Motz, A. R.; Capuano, C.; Ayers, K. E.; Hutchison, J. E.; Boettcher, S. W. *ACS Appl. Mater. Interfaces* **2022**, *14* (16), 18261–18274, DOI: 10.1021/acсами.1c22472.
- (31) Lindquist, G. A.; Gaitor, J. C.; Thompson, W. L.; Brogden, V.; Noonan, K. J. T.; Boettcher, S. W. *Energy Environ. Sci.* **2023**, *16* (10), 4373–4387, DOI: 10.1039/D3EE01293J.
- (32) Klingenhof, M.; Trzesniowski, H.; Koch, S.; Zhu, J.; Zeng, Z.; Metzler, L.; Klinger, A.; Elshamy, M.; Lehmann, F.; Buchheister, P. W.; *et al.* *Nat. Catal.* **2024**, *7* (11), 1213–1222, DOI: 10.1038/s41929-024-01238-w.
- (33) Santoro, C.; Lavacchi, A.; Mustarelli, P.; Di Noto, V.; Elbaz, L.; Dekel, D. R.; Jaouen, F. *ChemSusChem* **2022**, *15* (8), e202200027, DOI: 10.1002/cssc.202200027.
- (34) Gladik, A.; Riedel, M.; Eichel, R.-A. *J. Power Sources* **2025**, *628*, 235878, DOI: 10.1016/j.jpowsour.2024.235878.
- (35) Drevon, D.; Görlin, M.; Chernev, P.; Xi, L.; Dau, H.; Lange, K. M. *Scientific reports* **2019**, *9* (1), 1532, DOI: 10.1038/s41598-018-37307-x.
- (36) Wygant, B. R.; Kawashima, K.; Mullins, C. B. *ACS Energy Lett.* **2018**, *3* (12), 2956–2966, DOI: 10.1021/acsenergylett.8b01774.

- (37) Grimaud, A.; Hong, W. T.; Shao-Horn, Y.; Tarascon, J.-M. *Nat. Mater.* **2016**, *15* (2), 121–126, DOI: 10.1038/nmat4551.
- (38) Hong, W. T.; Risch, M.; Stoerzinger, K. A.; Grimaud, A.; Suntivich, J.; Shao-Horn, Y. *Energy Environ. Sci.* **2015**, *8* (5), 1404–1427, DOI: 10.1039/c4ee03869j.
- (39) He, B.; Bai, F.; Jain, P.; Li, T. *Small* **2025**, e2411479, DOI: 10.1002/sml.202411479.
- (40) Hickling, A.; Hill, S. *Discuss. Faraday Soc.* **1947**, *1*, 236, DOI: 10.1039/DF9470100236.
- (41) Hu, J.; Zhu, K.; Chen, L.; Yang, H.; Li, Z.; Suchopar, A.; Richards, R. *Adv. Mater.* **2008**, *20* (2), 267–271, DOI: 10.1002/adma.200701389.
- (42) Taffa, D. H.; Brim, E.; Rücker, K. K.; Hayes, D.; Lorenz, J.; Bisen, O.; Risch, M.; Harms, C.; Richards, R. M.; Wark, M. *ACS Appl. Mater. Interfaces* **2024**, *16* (45), 62142–62154, DOI: 10.1021/acsami.4c14277.
- (43) Susman, M. D.; Pham, H. N.; Zhao, X.; West, D. H.; Chinta, S.; Bollini, P.; Datye, A. K.; Rimer, J. D. *Angew. Chem. Int. Ed.* **2020**, *59* (35), 15119–15123, DOI: 10.1002/anie.202003390.
- (44) Bucci, A.; García-Tecedor, M.; Corby, S.; Rao, R. R.; Martin-Diaconescu, V.; Oropeza, F. E.; La Peña O'Shea, V. A. de; Durrant, J. R.; Giménez, S.; Lloret-Fillol, J. *J. Mater. Chem. A* **2021**, *9* (21), 12700–12710, DOI: 10.1039/D1TA00072A.
- (45) Momma, K.; Izumi, F. *J. Appl. Crystallogr.* **2011**, *44* (6), 1272–1276, DOI: 10.1107/S0021889811038970.
- (46) Gražulis, S.; Daškevič, A.; Merkys, A.; Chateigner, D.; Lutterotti, L.; Quirós, M.; Serebryanaya, N. R.; Moeck, P.; Downs, R. T.; Le Bail, A. *Nucleic Acids Res.* **2012**, *40* (Database issue), D420-7, DOI: 10.1093/nar/gkr900.
- (47) Burke, L. D.; O'Sullivan, E. J. *J. Electroanal. Chem. Interfacial Electrochem.* **1981**, *117* (1), 155–160, DOI: 10.1016/S0022-0728(81)80459-7.
- (48) Bode, H.; Dehmelt, K.; Witte, J. *Electrochim. Acta* **1966**, *11* (8), 1079–1087, DOI: 10.1016/0013-4686(66)80045-2.

- 
- (49) Hall, D. S.; Lockwood, D. J.; Poirier, S.; Bock, C.; MacDougall, B. R. *J. Phys. Chem. A* **2012**, *116* (25), 6771–6784, DOI: 10.1021/jp303546r.
- (50) Hall, D. S.; Lockwood, D. J.; Bock, C.; MacDougall, B. R. *Proc. Math. Phys. Eng. Sci.* **2015**, *471* (2174), 20140792, DOI: 10.1098/rspa.2014.0792.
- (51) Hall, D. S.; Lockwood, D. J.; Poirier, S.; Bock, C.; MacDougall, B. R. *ACS Appl. Mater. Interfaces* **2014**, *6* (5), 3141–3149, DOI: 10.1021/am405419k.
- (52) Bergmann, A.; Martinez-Moreno, E.; Teschner, D.; Chernev, P.; Glied, M.; Araújo, J. F. de; Reier, T.; Dau, H.; Strasser, P. *Nat. Commun.* **2015**, *6*, 8625, DOI: 10.1038/ncomms9625.
- (53) Jung, S.; McCrory, C. C. L.; Ferrer, I. M.; Peters, J. C.; Jaramillo, T. F. *J. Mater. Chem. A* **2016**, *4* (8), 3068–3076, DOI: 10.1039/C5TA07586F.
- (54) Yu, M.; Budiayanto, E.; Tüysüz, H. *Angew. Chem. Int. Ed.* **2022**, *61* (1), e202103824, DOI: 10.1002/anie.202103824.
- (55) Suntivich, J.; May, K. J.; Gasteiger, H. A.; Goodenough, J. B.; Shao-Horn, Y. *Science (New York, N.Y.)* **2011**, *334* (6061), 1383–1385, DOI: 10.1126/science.1212858.
- (56) Fabbri, E.; Nachttegaal, M.; Binniger, T.; Cheng, X.; Kim, B.-J.; Durst, J.; Bozza, F.; Graule, T.; Schäublin, R.; Wiles, L.; *et al.* *Nat. Mater.* **2017**, *16* (9), 925–931, DOI: 10.1038/nmat4938.
- (57) Anantharaj, S.; Noda, S. *Small* **2020**, *16* (2), e1905779, DOI: 10.1002/sml.201905779.
- (58) Marquez, R. A.; Kalokowski, E.; Espinosa, M.; Bender, J. T.; Son, Y. J.; Kawashima, K.; Chukwunke, C. E.; Smith, L. A.; Celio, H.; Dolocan, A.; *et al.* *Energy Environ. Sci.* **2024**, *17* (5), 2028–2045, DOI: 10.1039/D3EE03617K.
- (59) Anantharaj, S.; Noda, S. *Energy Adv.* **2022**, *1* (8), 511–523, DOI: 10.1039/D2YA00076H.
- (60) Desilvestro, J.; Corrigan, D. A.; Weaver, M. J. *J. Electrochem. Soc.* **1988**, *135* (4), 885–892, DOI: 10.1149/1.2095818.

- (61) Gallenberger, J.; Moreno Fernández, H.; Alkemper, A.; Li, M.; Tian, C.; Kaiser, B.; Hofmann, J. P. *Catal. Sci. Technol.* **2023**, *13* (16), 4693–4700, DOI: 10.1039/D3CY00674C.
- (62) Friebel, D.; Louie, M. W.; Bajdich, M.; Sanwald, K. E.; Cai, Y.; Wise, A. M.; Cheng, M.-J.; Sokaras, D.; Weng, T.-C.; Alonso-Mori, R.; *et al.* *J. Am. Chem. Soc.* **2015**, *137* (3), 1305–1313, DOI: 10.1021/ja511559d.
- (63) Radinger, H.; Connor, P.; Tengeler, S.; Stark, R. W.; Jaegermann, W.; Kaiser, B. *Chem. Mater.* **2021**, *33* (21), 8259–8266, DOI: 10.1021/acs.chemmater.1c02406.
- (64) Görlin, M.; Chernev, P.; Ferreira de Araújo, J.; Reier, T.; Dresch, S.; Paul, B.; Krähnert, R.; Dau, H.; Strasser, P. *J. Am. Chem. Soc.* **2016**, *138* (17), 5603–5614, DOI: 10.1021/jacs.6b00332.
- (65) Mattinen, M.; Schröder, J.; D’Acunto, G.; Ritala, M.; Jaramillo, T. F.; Stevens, M. B.; Bent, S. F. *Cell Rep. Phys. Sci.* **2024**, *5* (11), 102284, DOI: 10.1016/j.xcrp.2024.102284.
- (66) Hausmann, J. N.; Mebs, S.; Dau, H.; Driess, M.; Menezes, P. W. *Adv. Mater.* **2022**, *34* (50), e2207494, DOI: 10.1002/adma.202207494.
- (67) Trzesniowski, H.; Deka, N.; van der Heijden, O.; Golnak, R.; Xiao, J.; Koper, M. T. M.; Seidel, R.; Mom, R. V. *J. Phys. Chem. Lett.* **2023**, *14* (2), 545–551, DOI: 10.1021/acs.jpcclett.2c03336.
- (68) Görlin, M.; Halldin Stenlid, J.; Koroidov, S.; Wang, H.-Y.; Börner, M.; Shipilin, M.; Kalinko, A.; Murzin, V.; Safonova, O. V.; Nachtegaal, M.; *et al.* *Nat. Commun.* **2020**, *11* (1), 6181, DOI: 10.1038/s41467-020-19729-2.
- (69) Wei, C.; Rao, R. R.; Peng, J.; Huang, B.; Stephens, I. E. L.; Risch, M.; Xu, Z. J.; Shao-Horn, Y. *Adv. Mater.* **2019**, *31* (31), e1806296, DOI: 10.1002/adma.201806296.
- (70) Seh, Z. W.; Kibsgaard, J.; Dickens, C. F.; Chorkendorff, I.; Nørskov, J. K.; Jaramillo, T. F. *Science (New York, N.Y.)* **2017**, *355* (6321), eaad4998, DOI: 10.1126/science.aad4998.
- (71) Füngrlings, A.; Wohlgemuth, M.; Antipin, D.; van der Minne, E.; Kiens, E. M.; Villalobos, J.; Risch, M.; Gunkel, F.; Pentcheva, R.; Baeumer, C. *Nat. Commun.* **2023**, *14* (1), 8284, DOI: 10.1038/s41467-023-43901-z.

- 
- (72) Poulain, R.; Klein, A.; Proost, J. *J. Phys. Chem. C* **2018**, *122* (39), 22252–22263, DOI: 10.1021/acs.jpcc.8b05790.
- (73) Sun, T.; Wang, D.; Mirkin, M. V.; Cheng, H.; Zheng, J.-C.; Richards, R. M.; Lin, F.; Xin, H. L. *Proc. Natl. Acad. Sci. U.S.A* **2019**, *116* (24), 11618–11623, DOI: 10.1073/pnas.1821091116.
- (74) Cadigan, C. A.; Corpuz, A. R.; Lin, F.; Caskey, C. M.; Finch, K. B. H.; Wang, X.; Richards, R. M. *Catal. Sci. Technol.* **2013**, *3* (4), 900–911, DOI: 10.1039/C2CY20373A.
- (75) Leonov, I.; Biermann, S. *Phys. Rev. B* **2021**, *103* (16), DOI: 10.1103/PhysRevB.103.165108.
- (76) Li, L.; Kanai, Y. *Phys. Rev. B* **2015**, *91* (23), DOI: 10.1103/PhysRevB.91.235304.
- (77) Kim, S. J.; Jo, S. G.; Lee, E. B.; Lee, J. W. *ACS Appl. Energy Mater.* **2023**, *6* (16), 8360–8367, DOI: 10.1021/acsaem.3c01046.
- (78) Hayes, D. W.; Brim, E.; Rücker, K.; Taffa, D. H.; Bisen, O.; Risch, M.; Alia, S. M.; Lorenz, J.; Harms, C.; Wark, M.; *et al.* *RSC Appl. Interfaces* **2025**, DOI: 10.1039/D5LF00072F.
- (79) Trotochaud, L.; Ranney, J. K.; Williams, K. N.; Boettcher, S. W. *J. Am. Chem. Soc.* **2012**, *134* (41), 17253–17261, DOI: 10.1021/ja307507a.
- (80) Fominykh, K.; Tok, G. C.; Zeller, P.; Hajiyani, H.; Miller, T.; Döblinger, M.; Pentcheva, R.; Bein, T.; Fattakhova-Rohlfing, D. *Adv. Funct. Mater.* **2017**, *27* (8), 1605121, DOI: 10.1002/adfm.201605121.
- (81) Fominykh, K.; Chernev, P.; Zaharieva, I.; Sicklinger, J.; Stefanic, G.; Döblinger, M.; Müller, A.; Pokharel, A.; Böcklein, S.; Scheu, C.; *et al.* *ACS nano* **2015**, *9* (5), 5180–5188, DOI: 10.1021/acsnano.5b00520.
- (82) Zhai, T.; Wang, H.; Beaudoin, S. R.; Zhang, R.; Kwak, M.; Hou, S.; Guo, Z.; Boettcher, S. W. *J. Am. Chem. Soc.* **2025**, *147* (18), 15448–15458, DOI: 10.1021/jacs.5c01621.

- (83) Xu, D.; Stevens, M. B.; Cosby, M. R.; Oener, S. Z.; Smith, A. M.; Enman, L. J.; Ayers, K. E.; Capuano, C. B.; Renner, J. N.; Danilovic, N.; *et al.* *ACS Catal.* **2019**, *9* (1), 7–15, DOI: 10.1021/acscatal.8b04001.
- (84) Corrigan, D. A. *J. Electrochem. Soc.* **1987**, *134* (2), 377–384, DOI: 10.1149/1.2100463.
- (85) Ou, Y.; Twight, L. P.; Samanta, B.; Liu, L.; Biswas, S.; Fehrs, J. L.; Sagui, N. A.; Villalobos, J.; Morales-Santelices, J.; Antipin, D.; *et al.* *Nat. Commun.* **2023**, *14* (1), 7688, DOI: 10.1038/s41467-023-43305-z.
- (86) Twight, L.; Tonsberg, A.; Samira, S.; Velinkar, K.; Dumpert, K.; Ou, Y.; Le Wang; Nikolla, E.; Boettcher, S. W. *J. Catal.* **2024**, *432*, 115443, DOI: 10.1016/j.jcat.2024.115443.
- (87) Son, Y. J.; Kim, S.; Leung, V.; Kawashima, K.; Noh, J.; Kim, K.; Marquez, R. A.; Carrasco-Jaim, O. A.; Smith, L. A.; Celio, H.; *et al.* *ACS Catal.* **2022**, *12* (16), 10384–10399, DOI: 10.1021/acscatal.2c01001.
- (88) Halldin Stenlid, J.; Görlin, M.; Diaz-Morales, O.; Davies, B.; Grigorev, V.; Degerman, D.; Kalinko, A.; Börner, M.; Shipilin, M.; Bauer, M.; *et al.* *J. Am. Chem. Soc.* **2025**, *147* (5), 4120–4134, DOI: 10.1021/jacs.4c13417.
- (89) Wittstock, G. *Lehrbuch der Elektrochemie: Grundlagen, Methoden, Materialien, Anwendungen*, 1st ed.; Wiley-VCH, **2023**, pp 85-115, pp 651-697.
- (90) Frumkin, A.; Nekrasov, L.; Levich, B.; Ivanov, J. *J. Electroanal. Chem. Interfacial Electrochem.* **1959**, *1* (1), 84–90, DOI: 10.1016/0022-0728(59)80012-7.
- (91) Dalton, F. *Electrochem. Soc. Interface* **2016**, *25* (3), 50–59, DOI: 10.1149/2.F03163if.
- (92) Anderson, G. C.; Pivovar, B. S.; Alia, S. M. *J. Electrochem. Soc.* **2020**, *167* (4), 44503, DOI: 10.1149/1945-7111/ab7090.
- (93) Bisen, O. Y.; Baumung, M.; Tatzel, M.; Volkert, C. A.; Risch, M. *Energy Adv.* **2024**, *3* (2), 504–514, DOI: 10.1039/D3YA00434A.
- (94) Hartig-Weiss, A.; Tovini, M. F.; Gasteiger, H. A.; El-Sayed, H. A. *ACS Appl. Energy Mater.* **2020**, *3* (11), 10323–10327, DOI: 10.1021/acsaem.0c01944.

- 
- (95) El-Sayed, H. A.; Weiß, A.; Olbrich, L. F.; Putro, G. P.; Gasteiger, H. A. *J. Electrochem. Soc.* **2019**, *166* (8), F458-F464, DOI: 10.1149/2.0301908jes.
- (96) Bornet, A.; Moreno-García, P.; Dutta, A.; Kong, Y.; Liechti, M.; Vesztergom, S.; Arenz, M.; Broekmann, P. *ACS Catal.* **2024**, *14* (23), 17331–17346, DOI: 10.1021/acscatal.4c05447.
- (97) Lazanas, A. C.; Prodromidis, M. I. *ACS Meas. Sci. Au* **2023**, *3* (3), 162–193, DOI: 10.1021/acsmesuresciau.2c00070.
- (98) Watzele, S.; Bandarenka, A. S. *Electroanalysis* **2016**, *28* (10), 2394–2399, DOI: 10.1002/elan.201600178.
- (99) Farhoosh, S.; Liu, S.; Beyer, P.; Mebs, S.; Haumann, M.; Dau, H. *Adv. Energy Mater.* **2025**, *15* (14), DOI: 10.1002/aenm.202403818.
- (100) Kim, J.-S.; Pyun, S.-I. *J. Solid State Electrochem.* **2011**, *15* (11-12), 2447–2452, DOI: 10.1007/s10008-011-1393-9.
- (101) Elgrishi, N.; Rountree, K. J.; McCarthy, B. D.; Rountree, E. S.; Eisenhart, T. T.; Dempsey, J. L. *J. Chem. Educ.* **2018**, *95* (2), 197–206, DOI: 10.1021/acs.jchemed.7b00361.
- (102) Lyons, M. E. G.; Doyle, R. L.; Godwin, I.; O'Brien, M.; Russell, L. J. *Electrochem. Soc.* **2012**, *159* (12), H932-H944, DOI: 10.1149/2.078212jes.
- (103) Wei, C.; Sun, S.; Mandler, D.; Wang, X.; Qiao, S. Z.; Xu, Z. J. *Chem. Soc. Rev.* **2019**, *48* (9), 2518–2534, DOI: 10.1039/c8cs00848e.
- (104) McCrory, C. C. L.; Jung, S.; Peters, J. C.; Jaramillo, T. F. *J. Am. Chem. Soc.* **2013**, *135* (45), 16977–16987, DOI: 10.1021/ja407115p.
- (105) Morales, D. M.; Risch, M. *J. Phys. Ener.* **2021**, *3* (3), 34013, DOI: 10.1088/2515-7655/abee33.
- (106) Chen, Y.; Zheng, D. J.; Xu, Z. J.; Shao-Horn, Y. *Nat. Sustain.* **2024**, *7* (4), 371–374, DOI: 10.1038/s41893-024-01285-y.
- (107) Risch, M. *Commun. Chem.* **2023**, *6* (1), 221, DOI: 10.1038/s42004-023-01024-y.
- (108) Gravelle, J.; Hihn, J.-Y.; Pollet, B. G. *Int. J. Hydrogen Energy* **2025**, *100*, 428–441, DOI: 10.1016/j.ijhydene.2024.12.243.

- (109) Ehelebe, K.; Schmitt, N.; Sievers, G.; Jensen, A. W.; Hrnjić, A.; Collantes Jiménez, P.; Kaiser, P.; Geuß, M.; Ku, Y.-P.; Jovanović, P.; *et al.* *ACS Energy Lett.* **2022**, *7* (2), 816–826, DOI: 10.1021/acseenergylett.1c02659.
- (110) Geuß, M.; Milosevic, M.; Bierling, M.; Löttert, L.; Abbas, D.; Escalera-López, D.; Lloret, V.; Ehelebe, K.; Mayrhofer, K. J. J.; Thiele, S.; *et al.* *J. Electrochem. Soc.* **2023**, *170* (11), 114510, DOI: 10.1149/1945-7111/ad07ac.
- (111) Berner, E.; Wiberg, G. K. H.; Arenz, M. *Adv. Energy Sustainability Res.* **2024**, DOI: 10.1002/aesr.202400050.
- (112) Günther, T. E.; Loukrakpam, R.; Gomes, B. F.; Soisson, A.; Moos, M.; Nguyen, B. D. L.; Shah, S.; Roth, C. *Electrochim. Acta* **2025**, *512*, 145474, DOI: 10.1016/j.electacta.2024.145474.
- (113) Calvin, S. *XAFS for everyone*, 1st ed.; CRC Press, **2013**, pp 3-29.
- (114) Risch, M.; Morales, D. M.; Villalobos, J.; Antipin, D. *Angew. Chem. Int. Ed.* **2022**, *61* (50), e202211949, DOI: 10.1002/anie.202211949.
- (115) Henke, B. L.; Gullikson, E. M.; Davis, J. C. *Atomic Data and Nuc. Data Tables* **1993**, *54* (2), 181–342, DOI: 10.1006/adnd.1993.1013.
- (116) Mefford, J. T.; Akbashev, A. R.; Kang, M.; Bentley, C. L.; Gent, W. E.; Deng, H. D.; Alsem, D. H.; Yu, Y.-S.; Salmon, N. J.; Shapiro, D. A.; *et al.* *Nature* **2021**, *593* (7857), 67–73, DOI: 10.1038/s41586-021-03454-x.
- (117) Hess, C. *Chem. Soc. Rev.* **2021**, *50* (5), 3519–3564, DOI: 10.1039/d0cs01059f.
- (118) Schlücker, S. *Angew. Chem. Int. Ed.* **2014**, *53* (19), 4756–4795, DOI: 10.1002/anie.201205748.
- (119) Steimecke, M.; Seiffarth, G.; Schneemann, C.; Oehler, F.; Förster, S.; Bron, M. *ACS Catal.* **2020**, *10* (6), 3595–3603, DOI: 10.1021/acscatal.9b04788.
- (120) Steimecke, M.; Seiffarth, G.; Bron, M. *Anal. Chem.* **2017**, *89* (20), 10679–10686, DOI: 10.1021/acs.analchem.7b01060.
- (121) Hofmann, S. *Auger- and X-ray photoelectron spectroscopy in materials science: A user-oriented guide*; Springer series in surface sciences, Vol. 49; Springer, **2013**, pp 43-58.

- 
- (122) Krishna, D. N. G.; Philip, J. *Appl. Surf. Sci. Adv.* **2022**, *12*, 100332, DOI: 10.1016/j.apsadv.2022.100332.
- (123) Biesinger, M. C. *Appl. Surf. Sci.* **2022**, *597*, 153681, DOI: 10.1016/j.apsusc.2022.153681.
- (124) Payne, B. P.; Biesinger, M. C.; McIntyre, N. S. *J. Electron Spectrosc. Relat. Phenom.* **2009**, *175* (1-3), 55–65, DOI: 10.1016/j.elspec.2009.07.006.
- (125) Biesinger, M. C.; Payne, B. P.; Grosvenor, A. P.; Lau, L. W.; Gerson, A. R.; Smart, R. S. *Appl. Surf. Sci.* **2011**, *257* (7), 2717–2730, DOI: 10.1016/j.apsusc.2010.10.051.
- (126) Dau, H.; Liebisch, P.; Haumann, M. *Anal. Bioanal. Chem.* **2003**, *376* (5), 562–583, DOI: 10.1007/s00216-003-1982-2.
- (127) Dittmer, J.; Iuzzolino, L.; Dörner, W.; Nolting, H.-F.; Meyer-Klaucke, W.; Dau, H., *A New Method for Determination of the Edge Position of X-ray Absorption Spectra*. In *Photosynthesis: Mechanisms and Effects: Volume I–V: Proceedings of the XIth International Congress on Photosynthesis, Budapest, Hungary, August 17–22, 1998*; Garab, G., Ed.; Springer, **1998**; pp 1339–1342, DOI: 10.1007/978-94-011-3953-3\_316.
- (128) Biesinger, M. C.; Payne, B. P.; Lau, L. W. M.; Gerson, A.; St. Smart, R. C. *Surf. Interface Anal.* **2009**, *41* (4), 324–332, DOI: 10.1002/sia.3026.
- (129) Márquez, R. A.; Kawashima, K.; Son, Y. J.; Castelino, G.; Miller, N.; Smith, L. A.; Chukwunke, C. E.; Mullins, C. B. *ACS Energy Lett.* **2023**, *8* (2), 1141–1146, DOI: 10.1021/acseenergylett.2c02847.
- (130) Nikhil Kadimi, *Comprehensive Performance Analysis of Novel Catalysts on Porous Transport Layers in Half-Cell Electrochemical System*, master thesis, Otto von Guericke Universität, Magdeburg, **2025**,
- (131) Fingerle, M.; Tengeler, S.; Calvet, W.; Jaegermann, W.; Mayer, T. *J. Electrochem. Soc.* **2020**, *167* (13), 136514, DOI: 10.1149/1945-7111/abbcdf.
- (132) Lu, L.; Yan, X.; Wang, J.; Zheng, H.; Hu, X.; Tang, Y.; Jia, Z. *J. Phys. Chem. C* **2012**, *116* (27), 14638–14643, DOI: 10.1021/jp301684m.

- (133) Meher, S. K.; Justin, P.; Rao, G. R. *ACS Appl. Mater. Interfaces* **2011**, *3* (6), 2063–2073, DOI: 10.1021/am200294k.
- (134) Scherrer, P. *Bestimmung der inneren Struktur und der Größe von Kolloidteilchen mittels Röntgenstrahlen*, 26th ed.; Springer, **1918**, pp 387–409.
- (135) Mironova-Ulmane, N.; Kuzmin, A.; Steins, I.; Grabis, J.; Sildos, I.; Pärs, M. *J. Phys.: Conf. Ser.* **2007**, *93*, 12039, DOI: 10.1088/1742-6596/93/1/012039.
- (136) Richardson, J. T.; Yiagas, D. I.; Turk, B.; Forster, K.; Twigg, M. V. *J. Appl. Phys.* **1991**, *70* (11), 6977–6982, DOI: 10.1063/1.349826.
- (137) Xing, W.; Zhang, Y.; Zhu, J.; Yu, R. *Appl. Surf. Sci.* **2020**, *532*, 147427, DOI: 10.1016/j.apsusc.2020.147427.
- (138) Dubey, P.; Kaurav, N.; Devan, R. S.; Okram, G. S.; Kuo, Y. K. *RSC Adv.* **2018**, *8* (11), 5882–5890, DOI: 10.1039/c8ra00157j.
- (139) Villalobos, J.; González-Flores, D.; Urcuyo, R.; Montero, M. L.; Schuck, G.; Beyer, P.; Risch, M. *Adv. Energy Mater.* **2021**, *11* (36), DOI: 10.1002/aenm.202101737.
- (140) Rücker, K. K.; Taffa, D. H.; Bisen, O.; Risch, M.; Hayes, D.; Brim, E.; Richards, R. M.; Harms, C.; Wark, M.; Lorenz, J. *J. Phys. Chem. C* **2025**, *129* (20), 9341–9355, DOI: 10.1021/acs.jpcc.5c00493.
- (141) Priamushko, T.; Guillet-Nicolas, R.; Yu, M.; Doyle, M.; Weidenthaler, C.; Tüysüz, H.; Kleitz, F. *ACS Appl. Energy Mater.* **2020**, *3* (6), 5597–5609, DOI: 10.1021/acsaem.0c00544.
- (142) Sivakumar, P.; Subramanian, P.; Maiyalagan, T.; Gedanken, A.; Schechter, A. *Mater. Chem. Phys.* **2019**, *229*, 190–196, DOI: 10.1016/j.matchemphys.2019.03.017.
- (143) Rabe, M.; Toparli, C.; Chen, Y.-H.; Kasian, O.; Mayrhofer, K. J. J.; Erbe, A. *Phys. Chem. Chem. Phys.* **2019**, *21* (20), 10457–10469, DOI: 10.1039/c9cp00911f.
- (144) Burke, M. S.; Zou, S.; Enman, L. J.; Kellon, J. E.; Gabor, C. A.; Pledger, E.; Boettcher, S. W. *J. Phys. Chem. Lett.* **2015**, *6* (18), 3737–3742, DOI: 10.1021/acs.jpcclett.5b01650.

- 
- (145) Stevens, M. B.; Enman, L. J.; Korkus, E. H.; Zaffran, J.; Trang, C. D. M.; Asbury, J.; Kast, M. G.; Toroker, M. C.; Boettcher, S. W. *Nano Res.* **2019**, *12* (9), 2288–2295, DOI: 10.1007/s12274-019-2391-y.
- (146) Bhandari, S.; Narangoda, P. V.; Mogensen, S. O.; Tesch, M. F.; Mechler, A. K. *ChemElectroChem* **2022**, *9* (17), DOI: 10.1002/celec.202200479.
- (147) Dionigi, F.; Zhu, J.; Zeng, Z.; Merzdorf, T.; Sarodnik, H.; Gliech, M.; Pan, L.; Li, W.-X.; Greeley, J.; Strasser, P. *Angew. Chem. Int. Ed.* **2021**, *60* (26), 14446–14457, DOI: 10.1002/anie.202100631.
- (148) Tian, T.; Gao, H.; Zhou, X.; Zheng, L.; Wu, J.; Li, K.; Ding, Y. *ACS Energy Lett.* **2018**, *3* (9), 2150–2158, DOI: 10.1021/acseenergylett.8b01206.
- (149) Moni, P.; Mooste, M.; Tammeveski, K.; Rezwan, K.; Wilhelm, M. *RSC Adv.* **2021**, *11* (63), 39707–39717, DOI: 10.1039/d1ra05688c.
- (150) Menezes, P. W.; Indra, A.; Levy, O.; Kailasam, K.; Gutkin, V.; Pfrommer, J.; Driess, M. *Chem. Commun.* **2015**, *51* (24), 5005–5008, DOI: 10.1039/c4cc09671a.
- (151) Simon, P.; Gogotsi, Y. *Nat. Mater.* **2008**, *7* (11), 845–854, DOI: 10.1038/nmat2297.
- (152) Baumung, M.; Kollenbach, L.; Xi, L.; Risch, M. *ChemPhysChem* **2019**, *20* (22), 2981–2988, DOI: 10.1002/cphc.201900601.
- (153) Calle-Vallejo, F.; Inoglu, N. G.; Su, H.-Y.; Martínez, J. I.; Man, I. C.; Koper, M. T. M.; Kitchin, J. R.; Rossmeisl, J. *Chem. Sci.* **2013**, *4* (3), 1245, DOI: 10.1039/c2sc21601a.
- (154) Suntivich, J.; May, K. J.; Gasteiger, H. A.; Goodenough, J. B.; Shao-Horn, Y. *Science (New York, N.Y.)* **2011**, *334* (6061), 1383–1385, DOI: 10.1126/science.1212858.
- (155) Du, J.; Morales-Santelices, J.; Bisen, O. Y.; Antipin, D.; Morales, D. M.; Risch, M. *Electrochim. Acta* **2025**, *512*, 145489, DOI: 10.1016/j.electacta.2024.145489.
- (156) Grosvenor, A. P.; Biesinger, M. C.; Smart, R. S.; McIntyre, N. S. *Surf. Sci.* **2006**, *600* (9), 1771–1779, DOI: 10.1016/j.susc.2006.01.041.

- (157) Zywitzki, D.; Taffa, D. H.; Lamkowski, L.; Winter, M.; Rogalla, D.; Wark, M.; Devi, A. *Inorg. Chem.* **2020**, *59* (14), 10059–10070, DOI: 10.1021/acs.inorgchem.0c01204.
- (158) Weidler, N.; Schuch, J.; Knaus, F.; Stenner, P.; Hoch, S.; Maljusch, A.; Schäfer, R.; Kaiser, B.; Jaegermann, W. *J. Phys. Chem. C* **2017**, *121* (12), 6455–6463, DOI: 10.1021/acs.jpcc.6b12652.
- (159) Junta, J. L.; Hochella, M. F. *Geochim. Cosmochim. Acta* **1994**, *58* (22), 4985–4999, DOI: 10.1016/0016-7037(94)90226-7.
- (160) Paul, D. K.; Giorgi, J. B.; Karan, K. *J. Electrochem. Soc.* **2013**, *160* (4), F464–F469, DOI: 10.1149/2.024306jes.
- (161) Friedman, A. K.; Shi, W.; Losovyj, Y.; Siedle, A. R.; Baker, L. A. *J. Electrochem. Soc.* **2018**, *165* (11), H733–H741, DOI: 10.1149/2.0771811jes.
- (162) Brown, P. L.; Ekberg, C. *Hydrolysis of metal ions*; Wiley-VCH, **2016**, pp 573–618, pp 632–650.
- (163) Guda, A. A.; Guda, S. A.; Martini, A.; Kravtsova, A. N.; Algasov, A.; Bugaev, A.; Kubrin, S. P.; Guda, L. V.; Šot, P.; van Bokhoven, J. A.; *et al.* *npj Comput. Mater.* **2021**, *7* (1), DOI: 10.1038/s41524-021-00664-9.
- (164) Bantignies, J. L.; Deabate, S.; Righi, A.; Rols, S.; Hermet, P.; Sauvajol, J. L.; Henn, F. *J. Phys. Chem. C* **2008**, *112* (6), 2193–2201, DOI: 10.1021/jp075819e.
- (165) Taylor, T. J.; Dollimore, D.; Gamlen, G. A.; Barnes, A. J.; Stuckey, M. A. *Thermochim. Acta* **1986**, *101*, 291–304, DOI: 10.1016/0040-6031(86)80060-0.
- (166) Redkov, A.; Melehin, V.; Zhurikhina, V. *J. Phys.: Conf. Ser.* **2019**, *1236* (1), 12001, DOI: 10.1088/1742-6596/1236/1/012001.
- (167) Sunny, A.; Balasubramanian, K. *J. Phys. Chem. C* **2020**, *124* (23), 12636–12644, DOI: 10.1021/acs.jpcc.0c02638.
- (168) Nobile, C.; Cozzoli, P. D. *Nanomaterials (Basel, Switzerland)* **2022**, *12* (10), DOI: 10.3390/nano12101729.
- (169) *NIST Standard Reference Database 20: The NIST X-Ray Photoelectron Spectroscopy (XPS) Database*; National Institute of Standards and Technology,

- 
- Ed. nvlpubs.nist.gov/nistpubs/Legacy/TN/nbstechnicalnote1289.pdf (accessed 14.06.25).
- (170) Krivina, R. A.; Ou, Y.; Xu, Q.; Twight, L. P.; Stovall, T. N.; Boettcher, S. W. *Acc. Mater. Res.* **2021**, *2* (7), 548–558, DOI: 10.1021/accountsmr.1c00087.
- (171) Stevens, M. B.; Trang, C. D. M.; Enman, L. J.; Deng, J.; Boettcher, S. W. *J. Am. Chem. Soc.* **2017**, *139* (33), 11361–11364, DOI: 10.1021/jacs.7b07117.
- (172) Jeon, S. S.; Kang, P. W.; Klingenhof, M.; Lee, H.; Dionigi, F.; Strasser, P. *ACS Catal.* **2023**, *13* (2), 1186–1196, DOI: 10.1021/acscatal.2c04452.
- (173) He, Z.-D.; Tesch, R.; Eslamibidgoli, M. J.; Eikerling, M. H.; Kowalski, P. M. *Nat. Commun.* **2023**, *14* (1), 3498, DOI: 10.1038/s41467-023-38978-5.
- (174) Klaus, S.; Cai, Y.; Louie, M. W.; Trotochaud, L.; Bell, A. T. *J. Phys. Chem. C* **2015**, *119* (13), 7243–7254, DOI: 10.1021/acs.jpcc.5b00105.
- (175) Dionigi, F.; Zeng, Z.; Sinev, I.; Merzdorf, T.; Deshpande, S.; Lopez, M. B.; Kunze, S.; Zegkinoglou, I.; Sarodnik, H.; Fan, D.; *et al.* *Nat. Commun.* **2020**, *11* (1), 2522, DOI: 10.1038/s41467-020-16237-1.
- (176) Song, F.; Hu, X. *Nat. Commun.* **2014**, *5*, 4477, DOI: 10.1038/ncomms5477.
- (177) Candelaria, S. L.; Bedford, N. M.; Woehl, T. J.; Rentz, N. S.; Showalter, A. R.; Pylypenko, S.; Bunker, B. A.; Lee, S.; Reinhart, B.; Ren, Y.; *et al.* *ACS Catal.* **2017**, *7* (1), 365–379, DOI: 10.1021/acscatal.6b02552.
- (178) Wu, J.-B.; Lin, M.-L.; Cong, X.; Liu, H.-N.; Tan, P.-H. *Chem. Soc. Rev.* **2018**, *47* (5), 1822–1873, DOI: 10.1039/c6cs00915h.
- (179) Schechterle, A., *Einfluss der Befeuchtung auf die Katalysatorausnutzung im Gasdiffusionselektroden-Halbzellen-Aufbau für die Protonenaustauschmembran-Brennstoffzelle*, master thesis, Carl von Ossietzky Universität Oldenburg, Oldenburg, **2023**,
- (180) Morales, D. M.; Villalobos, J.; Kazakova, M. A.; Xiao, J.; Risch, M. *ChemElectroChem* **2021**, *8* (15), 2979–2983, DOI: 10.1002/celec.202100744.
- (181) van der Heijden, O.; Park, S.; Vos, R. E.; Eggebeen, J. J. J.; Koper, M. T. M. *ACS Energy Lett.* **2024**, *9* (4), 1871–1879, DOI: 10.1021/acsenerylett.4c00266.

- (182) Caracciolo, L.; Madec, L.; Martinez, H. *ACS Appl. Energy Mater.* **2021**, *4* (10), 11693–11699, DOI: 10.1021/acsaem.1c02400.
- (183) Pinna, N.; Niederberger, M. *Angew. Chem. Int. Ed.* **2008**, *47* (29), 5292–5304, DOI: 10.1002/anie.200704541.
- (184) Kwak, M.; Ojha, K.; Shen, M.; Boettcher, S. W. *ACS Energy Lett.* **2024**, *9* (3), 1025–1034, DOI: 10.1021/acseenergylett.3c02620.

---

## Publications and contributions of the author

### Publications in peer-reviewed journals

- (1) Baues, S.; Vocke, H.; Harms, L.; Rücker, K. K.; Wark, M.; Wittstock, G.; Combinatorial Screening of Cu–W Oxide-Based Photoanodes for Photoelectrochemical Water Splitting *ACS Applied Materials & Interfaces* **2022**, 14 (5), 6590–6603, DOI: 10.1021/acsami.1c20837.
- (2) Krueger, B.; Rücker, K. K.; Wittstock, G.; Redox Mediators for Faster Lithium Peroxide Oxidation in a Lithium–Oxygen Cell: A Scanning Electrochemical Microscopy Study *ACS Appl. Energy Mater.* **2022**, 5 (3), 3724–3733, DOI: 10.1021/acsaem.2c00172.
- (3) Taffa, D. H.; Brim, E.; Rücker, K. K.; Hayes, D.; Lorenz, J.; Bisen, O.; Risch, M.; Harms, C.; Richards, R. M.; Wark, M.; Influence of Annealing Temperature on the OER Activity of NiO(111) Nanosheets Prepared via Microwave and Solvothermal Synthesis Approaches *ACS Appl. Mater. Interfaces* **2024**, 16 (45), 62142–62154, DOI: 10.1021/acsami.4c14277.
- (4) Rücker, K. K.; Taffa, D. H.; Bisen, O.; Risch, M.; Hayes, D.; Brim, E.; Richards, R. M.; Harms, C.; Wark, M.; Lorenz, J.; Influence of Co and Mn Doping on the Surface Reconstruction of Faceted NiO(111) Nanosheets after the Oxygen Evolution Reaction *J. Phys. Chem. C* **2025**, 129 (20), 9341–9355, DOI: 10.1021/acs.jpcc.5c00493.
- (5) Brim, E.; Hayes, D.; Rücker, K. K.; Taffa, D. H.; Bisen, O.; Risch, M.; Alia, S.; Lorenz, J.; Harms, C.; Wark, M.; Richards, R. M.; Supercritical preparation of doped (111) faceted nickel oxide for the oxygen evolution reaction *RSC Appl. Interfaces* **2025**, 2, 1407, DOI: 10.1039/d5lf00174a.
- (6) Hayes, D.; Brim, E.; Rücker, K. K.; Taffa, D. H.; Bisen, O.; Risch, M.; Alia, S.; Lorenz, J.; Harms, C.; Wark, M.; Richards, R. M.; Molten salt synthesis of increased (100)-facet and polycrystalline nickel oxide nanoparticles for the oxygen evolution reaction: impact of facet and crystallinity on electrocatalysis *RSC Appl. Interfaces* **2025**, 2, 1448. DOI: 10.1039/D5LF00072F.

---

## Oral and poster presentations

- (1) Rücker, K. K.; Lorenz, J.; Harms, C; Wittstock, G.; Imaging of Fuel Cell Components by Atomic Force Microscopy *JCF Frühjahrssymposium*, poster presentation, Hannover, Germany, **2022**.
- (2) Rücker, K. K.; Taffa, D. H.; Lorenz, J.; Harms, C; Wark, M.; Understanding the influence of ionomers on electrocatalyst materials for the oxygen evolution and reduction reactions in alkaline media *GDCh Electrochemistry*, oral presentation, Berlin, Germany, **2022**.
- (3) Rücker, K. K.; Taffa, D. H.; Brim, E.; Hayes, D.; Bisen, O.; Lorenz, J.; Alia, S.; Risch, M.; Richards, R. M.; Harms, C.; Wark, M.; Transition metal doped NiOx faceted nanosheets for electrocatalytic *74<sup>th</sup> Annual ISE Meeting*, poster presentation, Lyon, France, **2023**.
- (4) Rücker, K. K.; Lorenz, J.; Harms, C; Study of the Ionomer Distribution in Catalyst Layers by Atomic Force Microscopy *Operando SPM Workshop*, poster presentation, Berlin, Germany, **2023**.
- (5) Rücker, K. K.; Taffa, D. H.; Brim, E.; Hayes, D.; Bisen, O.; Risch, M.; E.; Harms, C.; Richards, R. M.; Wark, M.; Lorenz, J.; In situ metal incorporation vs. compounded doping of nickel (hydr)oxides: Effect on the oxygen evolution reaction *75<sup>th</sup> Annual ISE Meeting*, oral presentation, Montreal, Canada, **2024**.
- (6) Rücker, K. K.; Taffa, D. H.; Brim, E.; Hayes, D.; Bisen, O.; Risch, M.; E.; Harms, C.; Richards, R. M.; Wark, M.; Lorenz, J.; In situ metal incorporation vs. compounded doping of nickel (hydr)oxides: Effect on the oxygen evolution reaction, *GDCh Electrochemistry*, poster presentation, Braunschweig, Germany, **2022**.
- (7) Rücker, K. K.; Taffa, D. H.; Kadimi, N.; Bisen, O.; Risch, M.; van Lieshout, F.; Morales, D.; Hayes, D.; Brim, E.; Alia, S.; E.; Richards, R. M.; Harms, C.; Wark, M.; Lorenz, J.; *In situ* Fe<sup>3+</sup> Incorporation vs. Compounded Fe Doping of NiO and Ni(OH)<sub>2</sub> Catalysts for the Alkaline Oxygen Evolution Reaction *5<sup>th</sup> International Conference on Electrolysis*, Freiburg, Germany, **2025**.

## Appendix

### Supplementary material

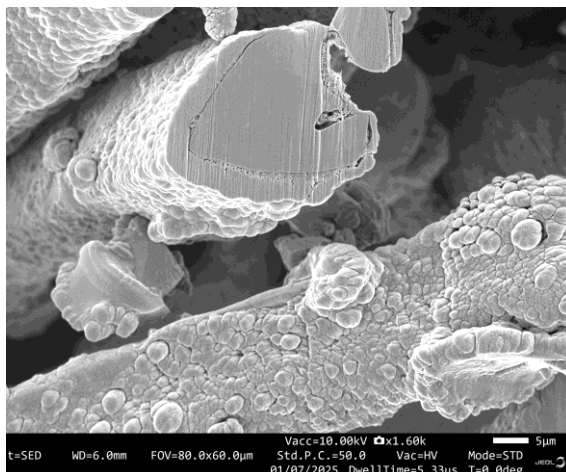


Figure A1: Scanning electron microscopy image of an ion beam milled Ni-felt coated with NiFeMo alloy for application as a porous transport electrode.

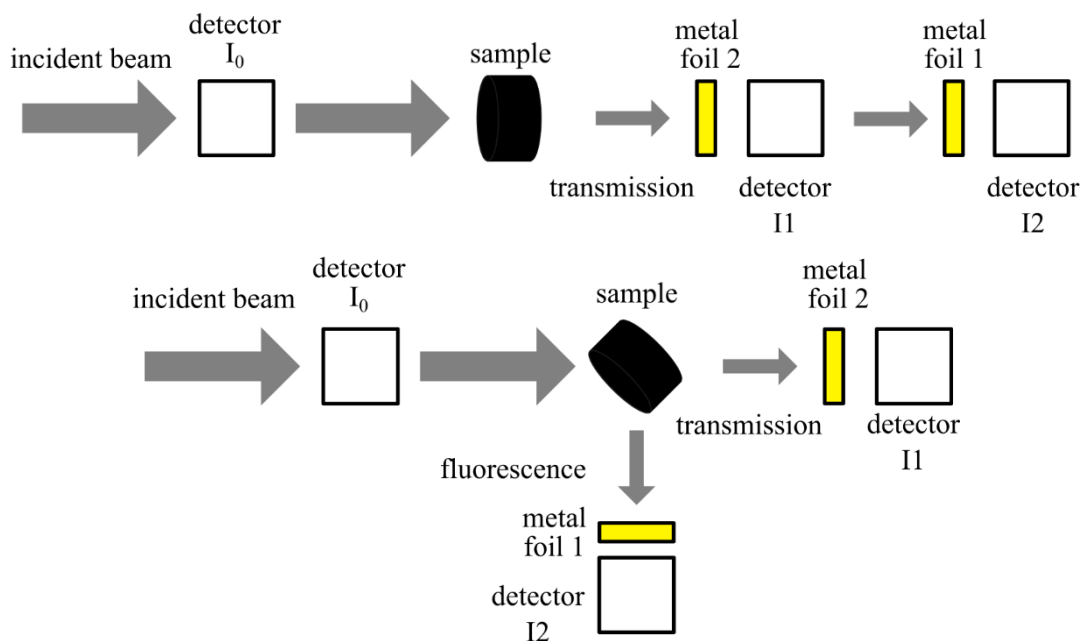


Figure A2: Schematic of the X-ray absorption spectroscopy experiments at KMC-2. The detector  $I_0$  measures the incident intensity. Above In transmission mode, the sample is placed straight in the beam path and between the detector  $I_1$  and the sample, metal foil 1 of the edge with the next lower energy (e.g. Cr foil for Mn edge, Fe foil for Co edge and Co foil for Ni edge) was placed as a filter. The corresponding metal for referencing the energy edge is placed in front of detector  $I_2$  as metal foil 2. Below In the case of the fluorescence mode, the sample is placed within a  $45^\circ$  angle between the beam path and the detector  $I_2$  with metal foil 1 as a filter.

## Synthesis and physical characterisation of NiO(111) nanosheets

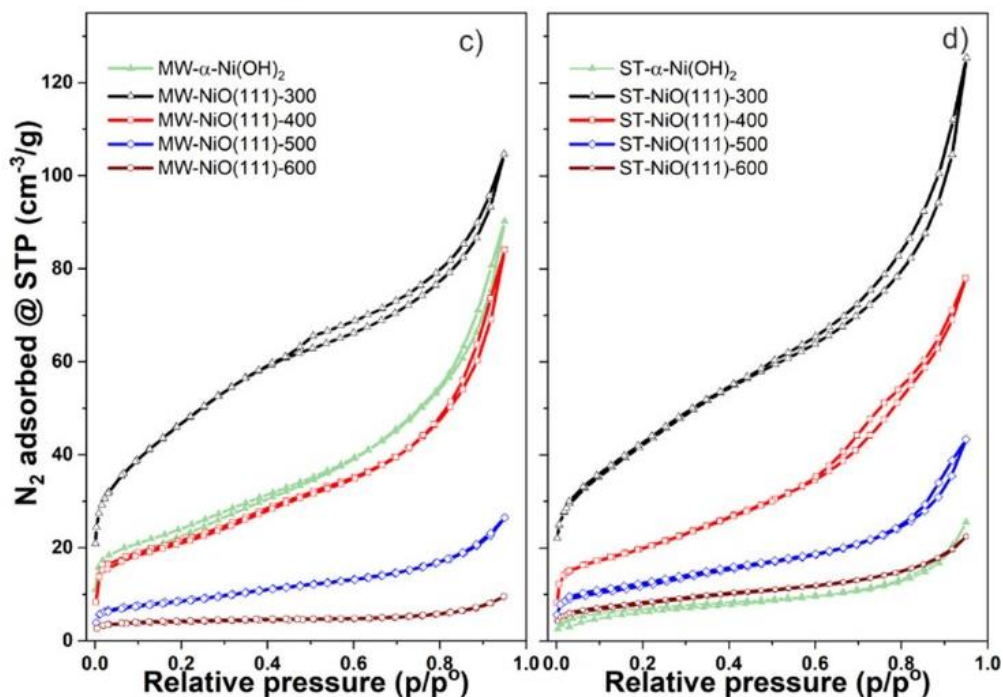


Figure A3: N<sub>2</sub> gas adsorption isotherms: (c) MW and (d) ST prepared NiO(111) nanosheets. Reproduced from Taffa et al.<sup>42</sup>

Table A1: Summary of the Results Obtained from PXRD and BET Analysis for the MW and ST samples. Adapted from Taffa et al.<sup>42</sup>

Annealing $T$ (°C)	BET area (m <sup>2</sup> /g)		Crystallite size (nm)		BJH pore size (nm)	
	MW	ST	MW	ST	MW	ST
-	67.2 ± 0.2	25.3 ± 0.3	-	-	3.0	-
300	165 ± 1.4	149.6 ± 1.0	4.4	6.0	2.9	3.0
400	75.9 ± 0.1	70.5 ± 0.2	11.0	10.2	3.5 (6.8)	3.4 (8.5)
500	30.2 ± 0.1	41.6 ± 0.1	26.3	17.9	3.4	3.4
600	15.4 ± 0.2	28.2 ± 0.1	49.2	25.3	-	3.0

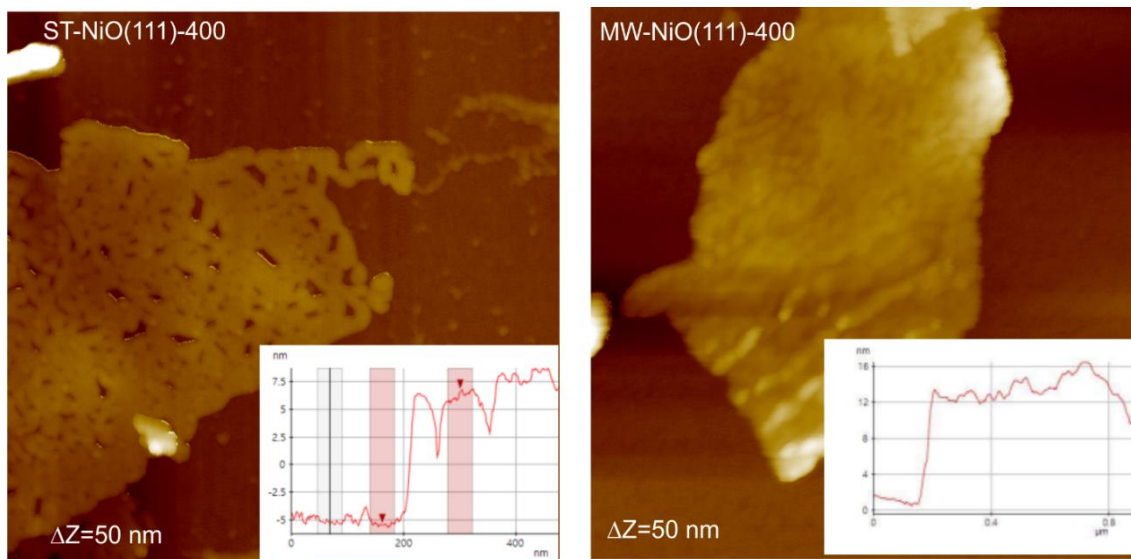


Figure A4: Non-contact mode atomic force microscopy images of a) ST sample ( $1 \times 1 \mu\text{m}^2$ ) and b) MW sample ( $1.5 \times 1.5 \mu\text{m}^2$ ) both annealed at  $400^\circ\text{C}$  showing the measured thickness. Reproduced from Taffa et al.<sup>42</sup>

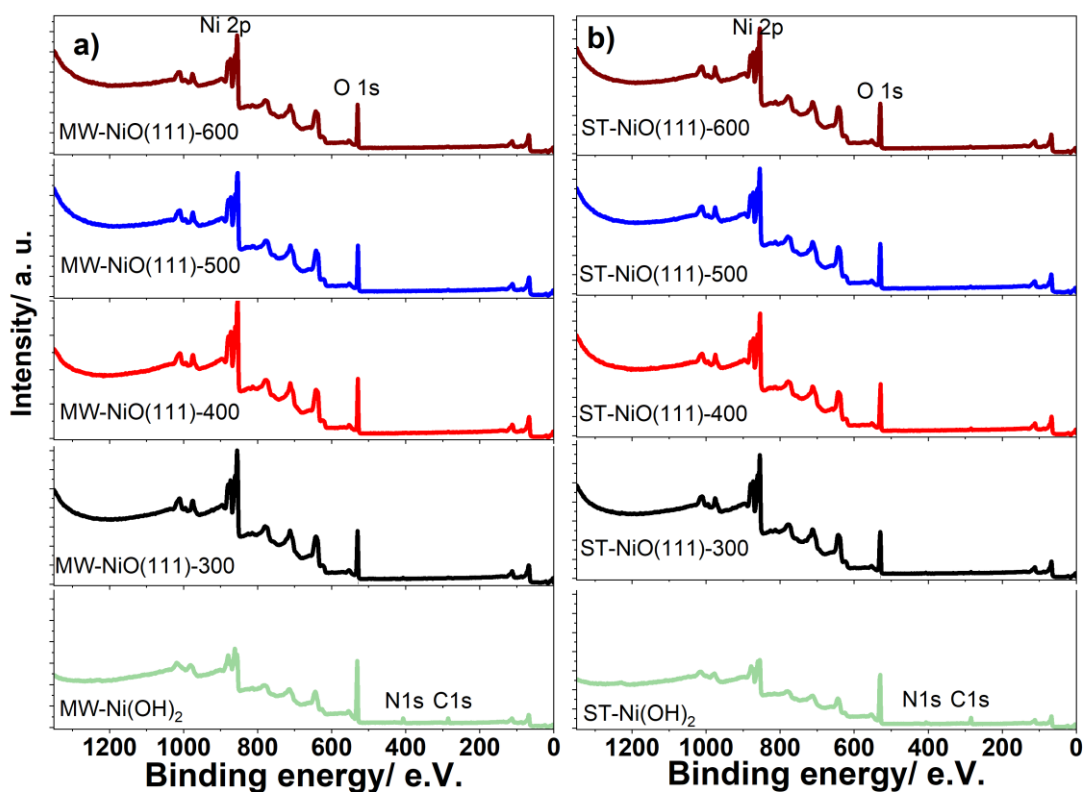


Figure A5: XPS survey spectra of a) the MW samples and b) the ST samples treated at different temperatures. Inserts highlight Ni, O, N and C signals. Reproduced from Taffa et al.<sup>42</sup>

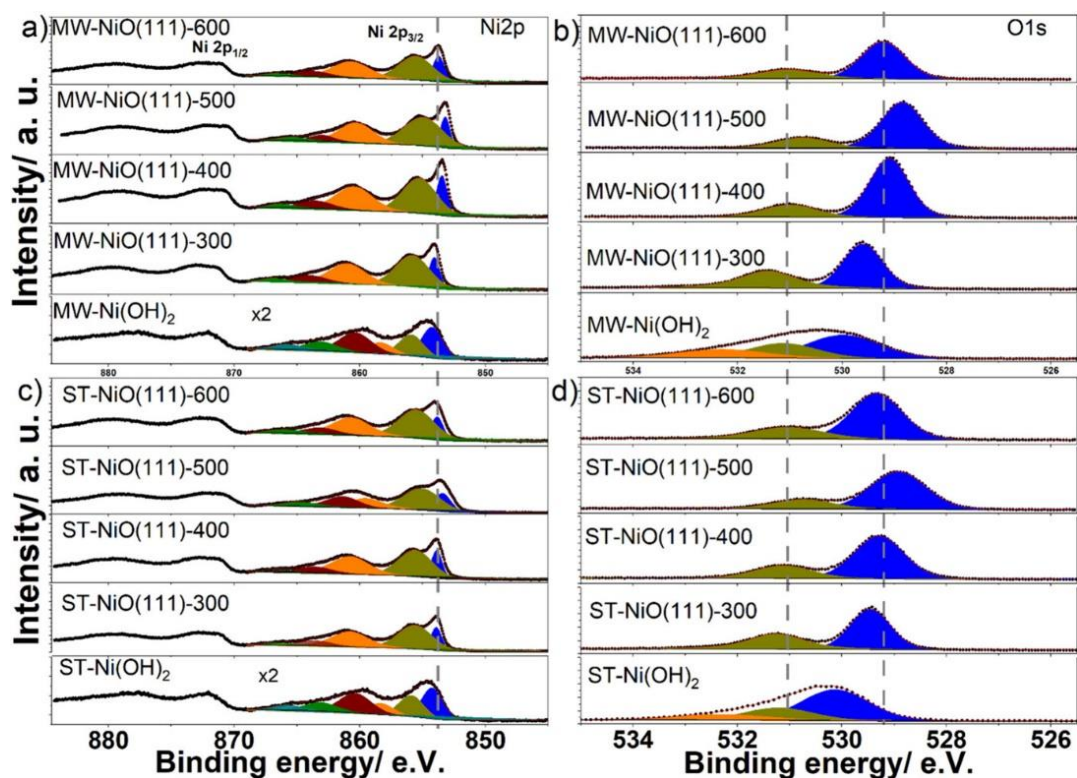


Figure A6: XPS Ni 2p (a, c) and O 1s (b, d) spectra for MW and ST NiO(111) nanosheets annealed at different temperatures. Reproduced from Taffa et al.<sup>42</sup>

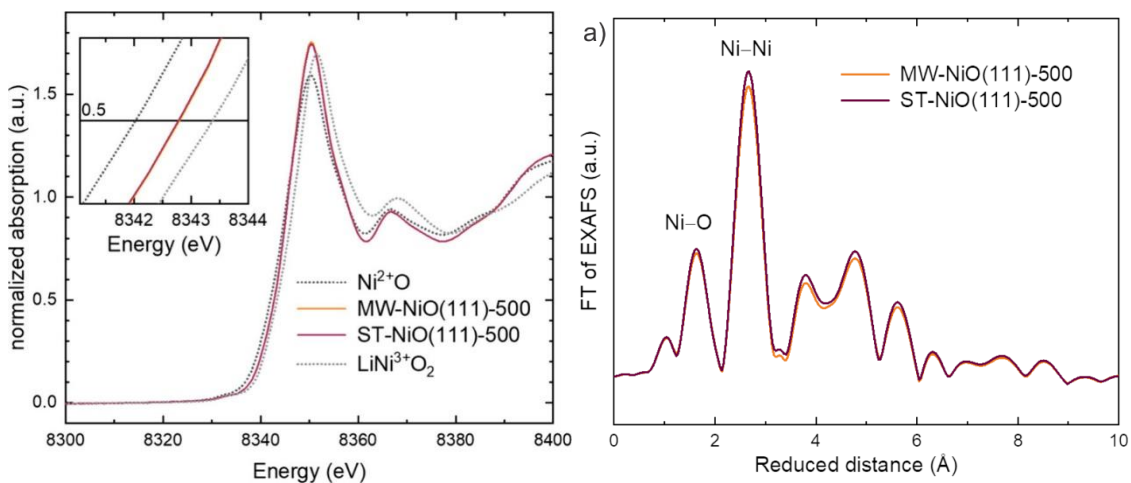


Figure A7: a) XANES spectra at the Ni K-edge showing the edge energy of the MW-NiO(111)-500 and ST-NiO(111)-500 samples with commercially available standards NiO and LiNi<sub>2</sub>O<sub>2</sub>. b) the Fourier transform (FT) of the EXAFS of MW-NiO(111)-500 and ST-NiO(111)-500. Reproduced from Taffa et al.<sup>42</sup>

Table A2: Sequence of the electrochemical characterization for the pure NiO(111) materials from ST and MW synthesis.

Step	Conditions
<b>1. Ar purge at OCP</b>	The electrolyte is purged while the coated electrode is rested at OCP in the electrolyte for 30 min.
<b>2. LSV for CDL</b>	Hold for 20 s at 0.915 V vs. RHE Potential window: 0.915 - 1.115 V vs. RHE Scan rates: 5, 10, 25, 50, 100, 250, 500 mV s <sup>-1</sup> Hold for 20 s at 1.115 V vs. RHE Repeat for backward scan 1.115 – 0.915 V vs. RHE Rotation: static iR post-compensation.
<b>3. Oxygen purge at OCP</b>	The electrolyte is purged while the coated electrode is rested at OCP in the electrolyte for 10 min
<b>4. CV for OER initial</b>	Hold for 120 s at start potential 1.14 V vs. RHE Potential window: 1.14 – 1.94 V vs. RHE Scan rates: 10 mV s <sup>-1</sup> Scans: 3 Rotation: 2400 rpm iR post-compensation.
<b>5. CV for EC conditioning</b>	Hold for 20 s at start potential 1 V vs. RHE Potential window: 1.04 – 1.64 V vs. RHE Scan rates: 100 mV s <sup>-1</sup> Scans: 50 Rotation: 1600 rpm iR post-compensation..
<b>6. CV for OER cycled</b>	Hold for 120 s at start potential 1.1 V vs. RHE Potential window: 1.0 – 2.0 V vs. RHE Scan rates: 10 mV s <sup>-1</sup> Scans: 3 Rotation: 2400 rpm iR post-compensation.
<b>7. EIS in Oxygen after conditioning</b>	Frequency: 100 kHz-1 Hz Points/decade: 10 10 mV amplitude at 1.0 V vs. RHE

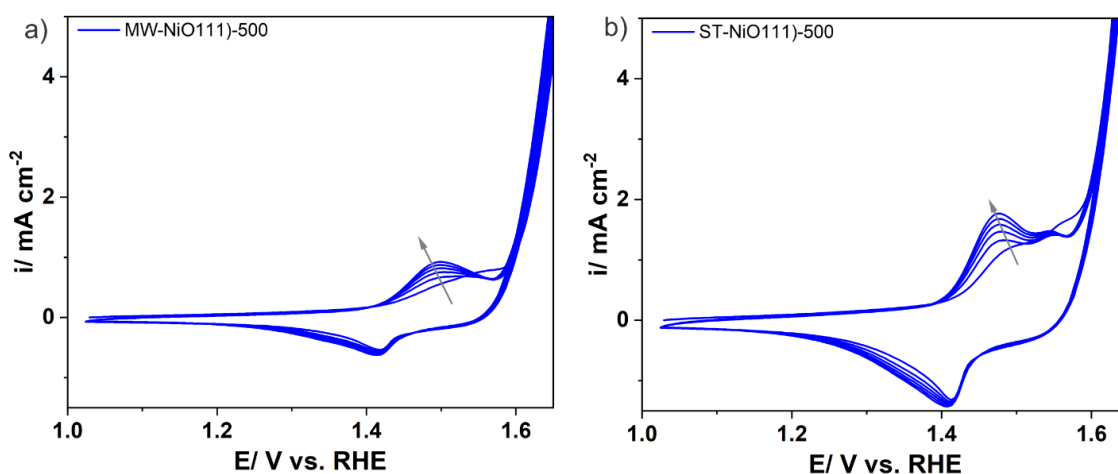


Figure A8: Electrochemical activation step of the NiO (111) nanosheets in 0.1 M KOH. a) CV measurement of MW-NiO (111) nanosheets and b) ST-NiO (111) nanosheets showing every 10<sup>th</sup> scan, the scan rate is 100 mV/s. The 1<sup>st</sup> scan of Ni<sup>II</sup>/Ni<sup>III</sup> redox transition peak shifted positively compared to the subsequent scans. Reproduced from Taffa et al.<sup>42</sup>

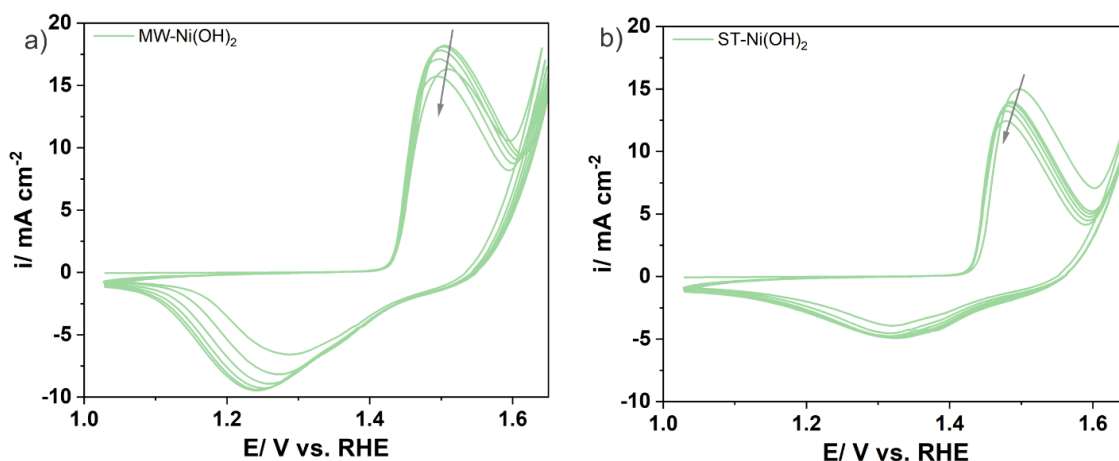


Figure A9: a) Electrochemical activation step of the MW-Ni(OH)<sub>2</sub> and b) ST-Ni(OH)<sub>2</sub> nanosheets in 0.1 M KOH. CV measurement showing every 10<sup>th</sup> scan, the scan rate is 100 mV/s. The 1<sup>st</sup> scan of Ni<sup>II</sup>/Ni<sup>III</sup> redox transition peak shifted positively compared to the subsequent scans. Reproduced from Taffa et al.<sup>42</sup>

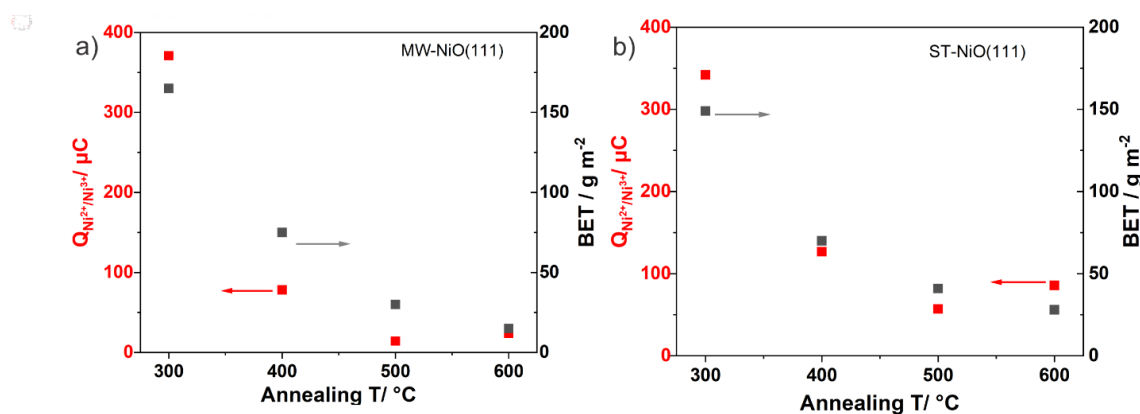


Figure A10: Plot of the integrated anodic charge under the Ni<sup>II</sup>/Ni<sup>III</sup> redox peak and the BET surface area against the annealing temperature of the a) MW and b) ST samples. Reproduced from Taffa et al.<sup>42</sup>

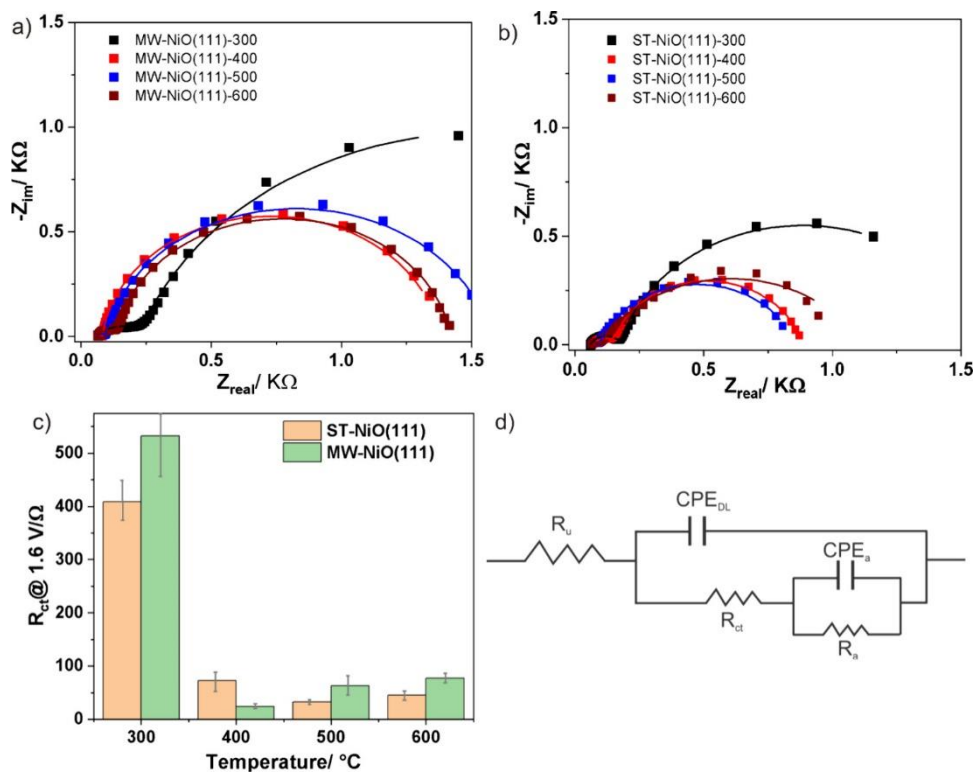


Figure A11: Representative Nyquist plots of NiO(111)-coated GC electrodes in 0.1 M KOH at 1.6 V vs. RHE. a) MW-NiO(111), b) ST-NiO(111), and c)  $R_{ct}$  values extracted from Nyquist plots a and b, and d) the equivalent circuit model. Reproduced from Taffa et al.<sup>42</sup>

## Synthesis and characterization of Co and Mn doped catalysts

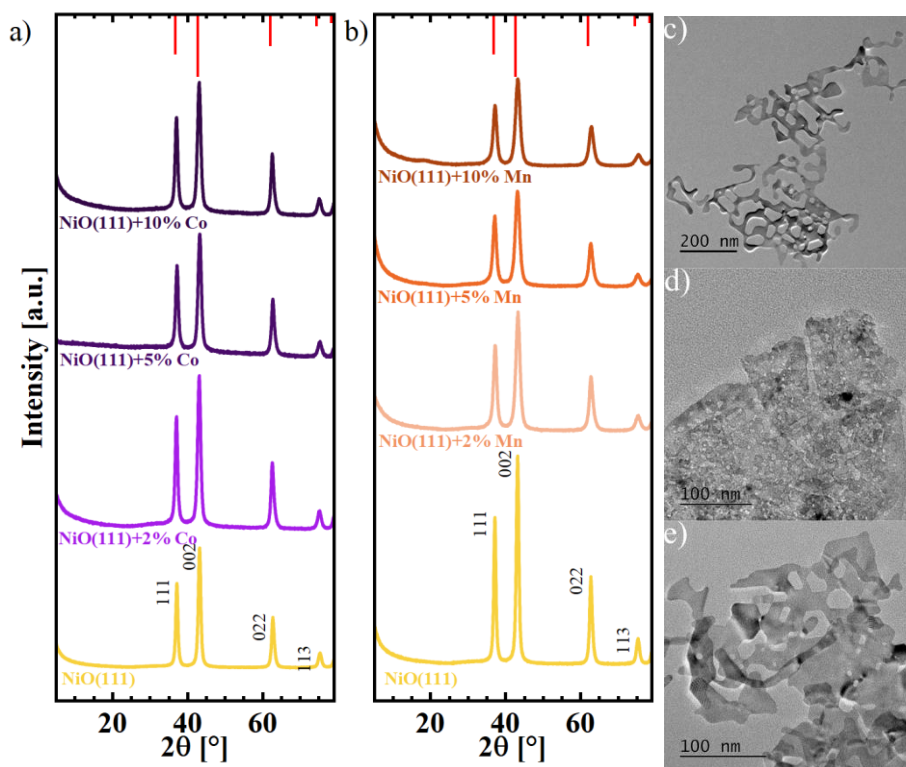


Figure A12: Structural Characterization of the Co and Mn doped NiO(111) materials including PXRD for the Co a) and Mn b) doped materials. Minor peak shifts were observed which are in the range of experimental error. HR-TEM images of the c) NiO(111), d) NiO + 5% Co and e) NiO + 5% Mn were taken to study the effect of the dopants onto the morphology of the catalysts. Adapted from R ucker et al.<sup>140</sup>

Table A3: ICP-MS results of the metal oxide after dissolution in concentrated nitric acid given as molar ratio of the metal content. Adapted from R ucker et al.<sup>140</sup>

Sample	$x_{\text{Co}} / \text{mol } \%$	$x_{\text{Mn}} / \text{mol } \%$	$x_{\text{Ni}} / \text{mol } \%$
NiO(111)	0.1	0.0	100.1
NiO(111)+2%Co	2.3	-	97.8
NiO(111)+5%Co	5.1	-	95.2
NiO(111)+10%Co	10.2	-	90.0
NiO(111)+2%Mn	-	2.3	97.0
NiO(111)+5%Mn	-	5.0	95.1
NiO(111)+10%Mn	-	10.1	90.1

Table A4: Steps of the electrochemical characterization of Co- and Mn-doped oxides with emphasis on an extensive conditioning (conditioning for 350 scans).

<b>Step</b>	<b>Conditions</b>
<b>1. Nitrogen purge at OCP</b>	The electrolyte is purged while the coated electrode is rested at OCP in the electrolyte for 30 min.
<b>2. EIS in Nitrogen</b>	Frequency: 30 kHz-1 Hz Points/decade: 10 10 mV amplitude at 1.0 V vs. RHE
<b>3. LSV for CDL</b>	Hold for 20 s at 0.9 V vs. RHE Potential window: 0.9 - 1.1 V vs. RHE Scan rates: 5, 10, 25, 50, 100, 250, 500 mV s <sup>-1</sup> Hold for 20 s at 1.1 V vs. RHE Repeat for backward scan 1.1 – 0.9 V vs. RHE Rotation: static No dynamic iR compensation.
<b>4. Oxygen purge at OCP</b>	15 min
<b>5. EIS in Oxygen before conditioning</b>	Frequency: 30 kHz-1 Hz Points/decade: 10 10 mV amplitude at 1.0 V vs. RHE
<b>6. CV for OER initial</b>	Hold for 120 s at start potential 1.1 V vs. RHE Potential window: 1.0 – 2.0 V vs. RHE Scan rates: 10 mV s <sup>-1</sup> Scans: 3 Rotation: 2400 rpm No dynamic iR compensation.
<b>7. CV for conditioning</b>	Hold for 20 s at start potential 1 V vs. RHE Potential window: 1.0 – 1.7 V vs. RHE Scan rates: 100 mV s <sup>-1</sup> Scans: 350 Rotation: 1600 rpm No dynamic iR compensation.
<b>8. CV for OER cycled</b>	Hold for 120 s at start potential 1.1 V vs. RHE Potential window: 1.0 – 2.0 V vs. RHE Scan rates: 10 mV s <sup>-1</sup> Scans: 3 Rotation: 2400 rpm No dynamic iR compensation.
<b>9. EIS in Oxygen after cycling</b>	Frequency: 30 kHz-1 Hz Points/decade: 10 10 mV amplitude at 1.0 V vs. RHE

Table A5: Crystallite sizes from the Scherrer Equation calculated for the (002) PXRD signal. Furthermore, the specific surface area of NiO nanosheets with different doping levels from BET analysis of nitrogen physisorption experiments is depicted. Adapted from R ucker et al.<sup>140</sup>

Material	Crystallite size [nm] (002)	BET surface area [m <sup>2</sup> g <sup>-1</sup> ]
NiO <sub>USnano</sub>	33	28
NiO(111)	11	71
NiO(111)+2% Co	9.7	85
NiO(111)+5% Co	8.9	86
NiO(111)+10% Co	9.1	62
NiO(111)+20% Co	8.0	52
NiO(111)+2% Mn	6.8	107
NiO(111)+5% Mn	6.4	107
NiO(111)+10% Mn	6.1	115

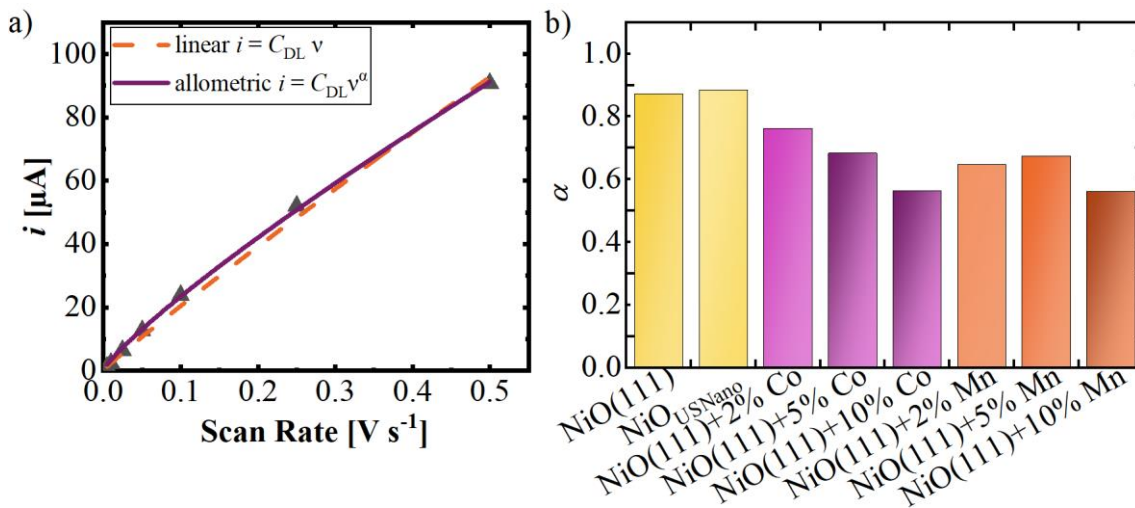


Figure A13: a) Regression of a representative NiO(111) sample with the linear and allometric models. b)  $\alpha$  from the allometric regression of the currents as a function of the scan rates from negative going linear sweeps different materials.  $\alpha$ -values different than 1 describe a deviation from an ideal capacitor. Adapted from R ucker et al.<sup>140</sup>

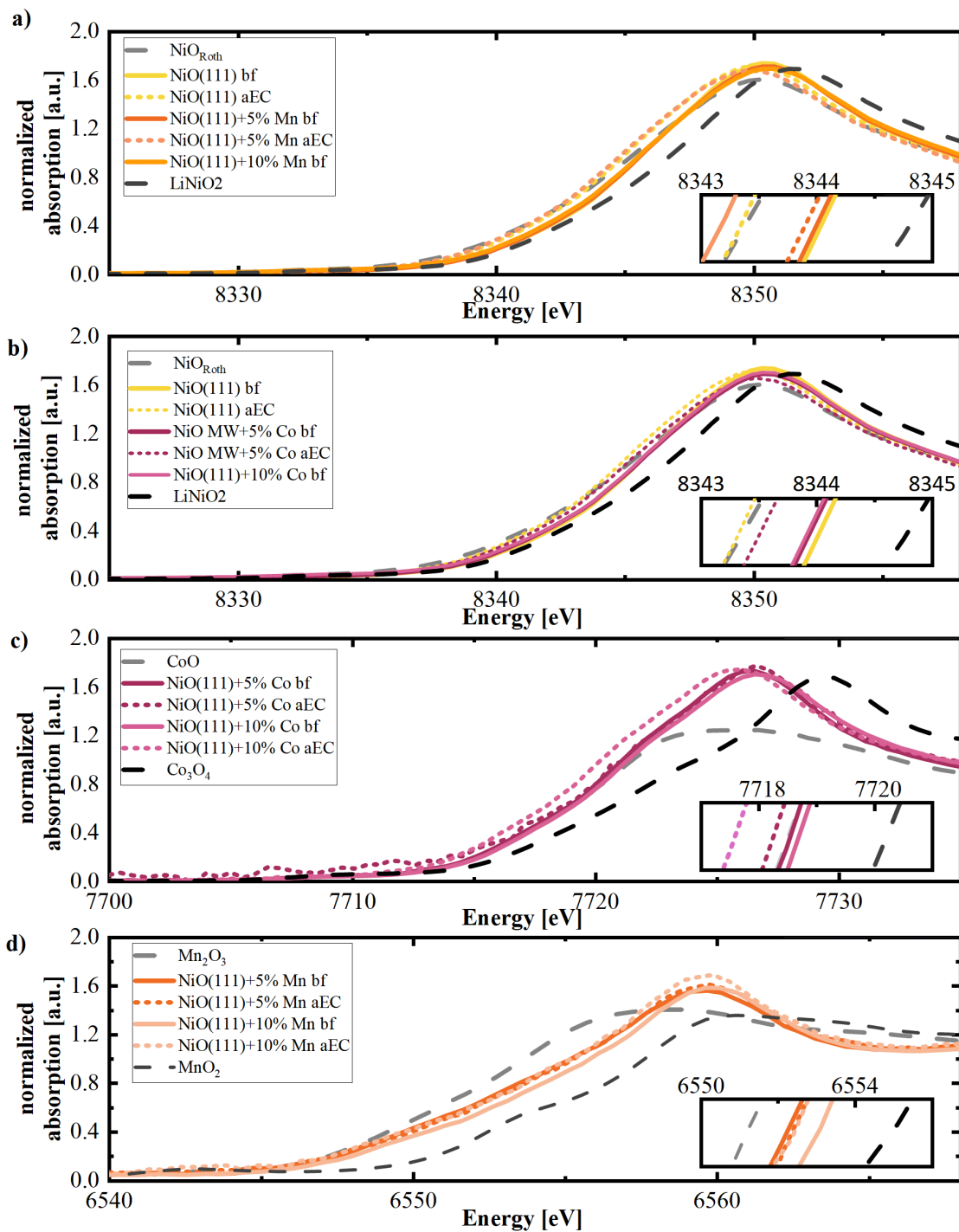


Figure A14: XANES data of the samples for a) the Ni k edge, b) the Mn k edge and c) the Co k edge as pristine sample and after electrochemical treatment aEC. Adapted from R ucker et al.<sup>140</sup>

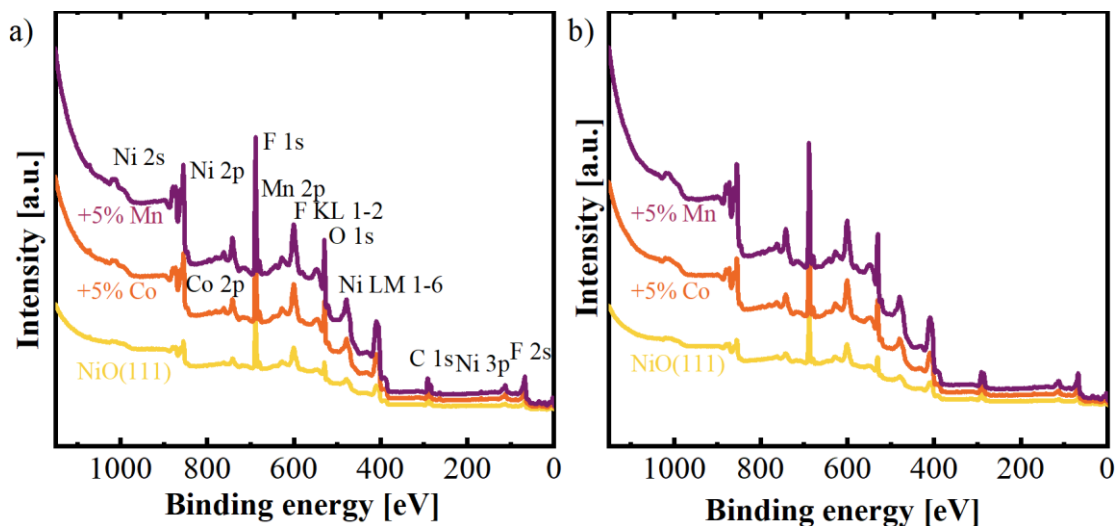


Figure A15: XPS survey spectra of NiO(111) together with +5% Co and +5% Mn doped samples. a) before and b) after Electrochemical treatment. The characteristic peaks are labeled, however the dopant metal signals are weak. Adapted from R ucker et al.<sup>140</sup>

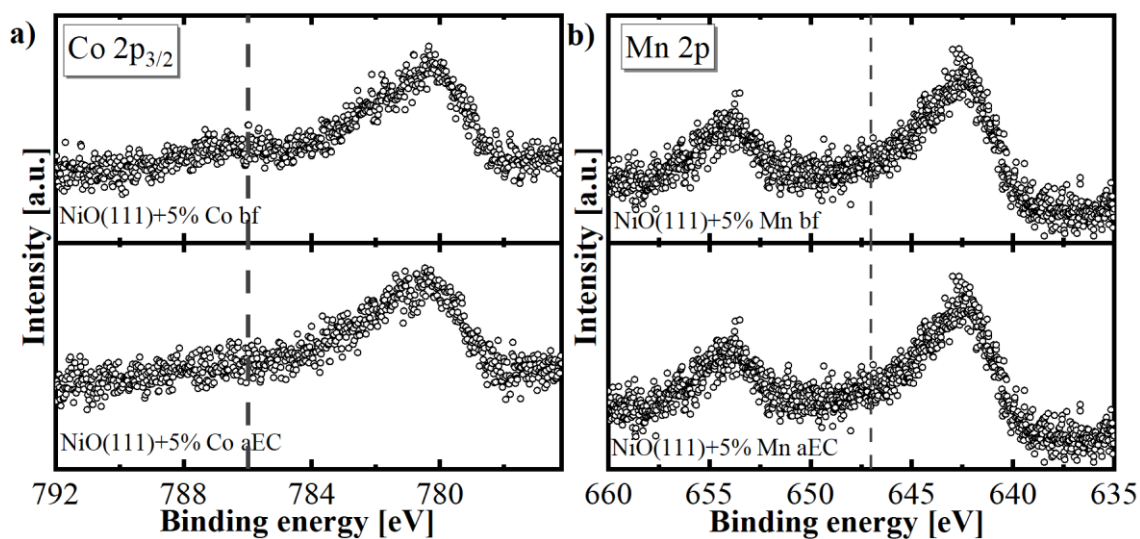


Figure A16: a) Co  $2p_{3/2}$  spectra of NiO(111)+ 5% Co with a mark for the prominent satellite at 786 eV as well as b) Mn 2p spectra of the 5% Mn sample with a mark for the prominent satellite at 647 eV, both before (bf) and after electrochemical treatment (aEC). Adapted from R ucker et al.<sup>140</sup>

## Supplementary data of the characterisation of Fe doped hydroxides and oxides

Table A6: ICP-MS results of the Fe doped samples from the MW synthesis approach.

Sample	Intended $x\text{Fe}$ [mol %]	$x\text{Fe}$ [mol %]	$x\text{Ni}$ [mol %]
$\text{Ni}(\text{OH})_2 + 1\% \text{ Fe}$	0.5	1.1	98.8
$\text{Ni}(\text{OH})_2 + 5\% \text{ Fe}$	2	5.3	94.7
$\text{Ni}(\text{OH})_2 + 13\% \text{ Fe}$	5	12.7	87.3
$\text{Ni}(\text{OH})_2 + 24\% \text{ Fe}$	10	24.4	75.5
$\text{Ni}(\text{OH})_2 + 31\% \text{ Fe}$	15	30.7	69.3

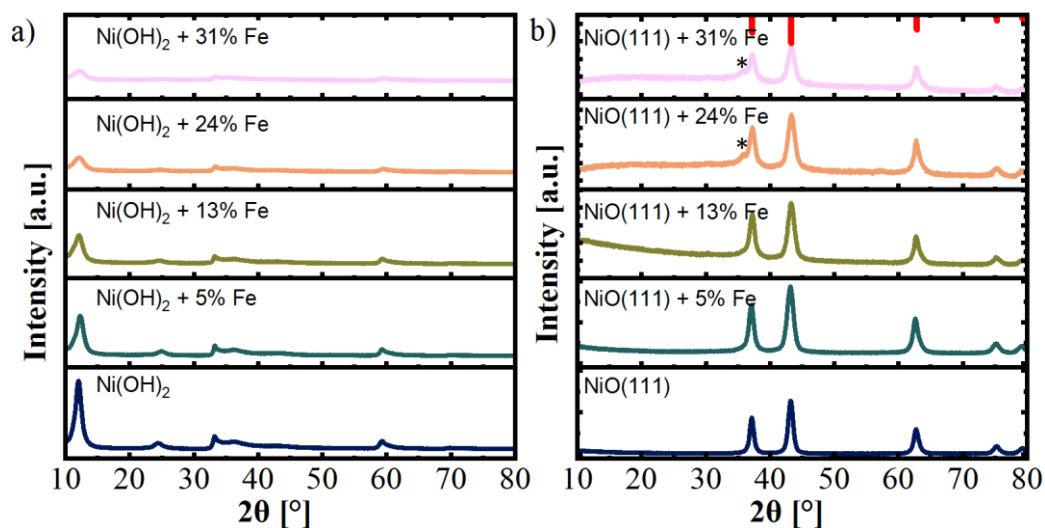


Figure A17: PXRD of the Fe doped samples of a) the hydroxides from the MW synthesis and b) of the oxide after thermal annealing at 400°C. Impurities of  $\text{Fe}_2\text{O}_3$  are highlighted as \*. Adapted from Rucker et al.<sup>140</sup>

Table A7: Crystallite sizes and physisorption results of the Fe-doped Scherrer Equation calculated for the (002) PXRD signal. Adapted from R cker et al.<sup>140</sup>

Fe doping (mol%)	Crystallite size [nm]		BET area [m <sup>2</sup> g <sup>-1</sup> ]	
	(unit cell parameter a �)			
	$\alpha$ -Ni(OH) <sub>2</sub>	NiO(111)	$\alpha$ -Ni(OH) <sub>2</sub>	NiO(111)
<b>0</b>	6.9	11.9 (4.19)	55.4	74.8
<b>1</b>	8.7	11.8 (4.18)	41.3	80.8
<b>5</b>	5.9	9.0 (4.20)	48.5	100.3
<b>13</b>	6.1	9.2 (4.20)	75.1	109.2
<b>24</b>	4.7	8.0 (4.20)	135.1	125.3
<b>31</b>	4.7	7.3 (4,19562)	160.7	136.9

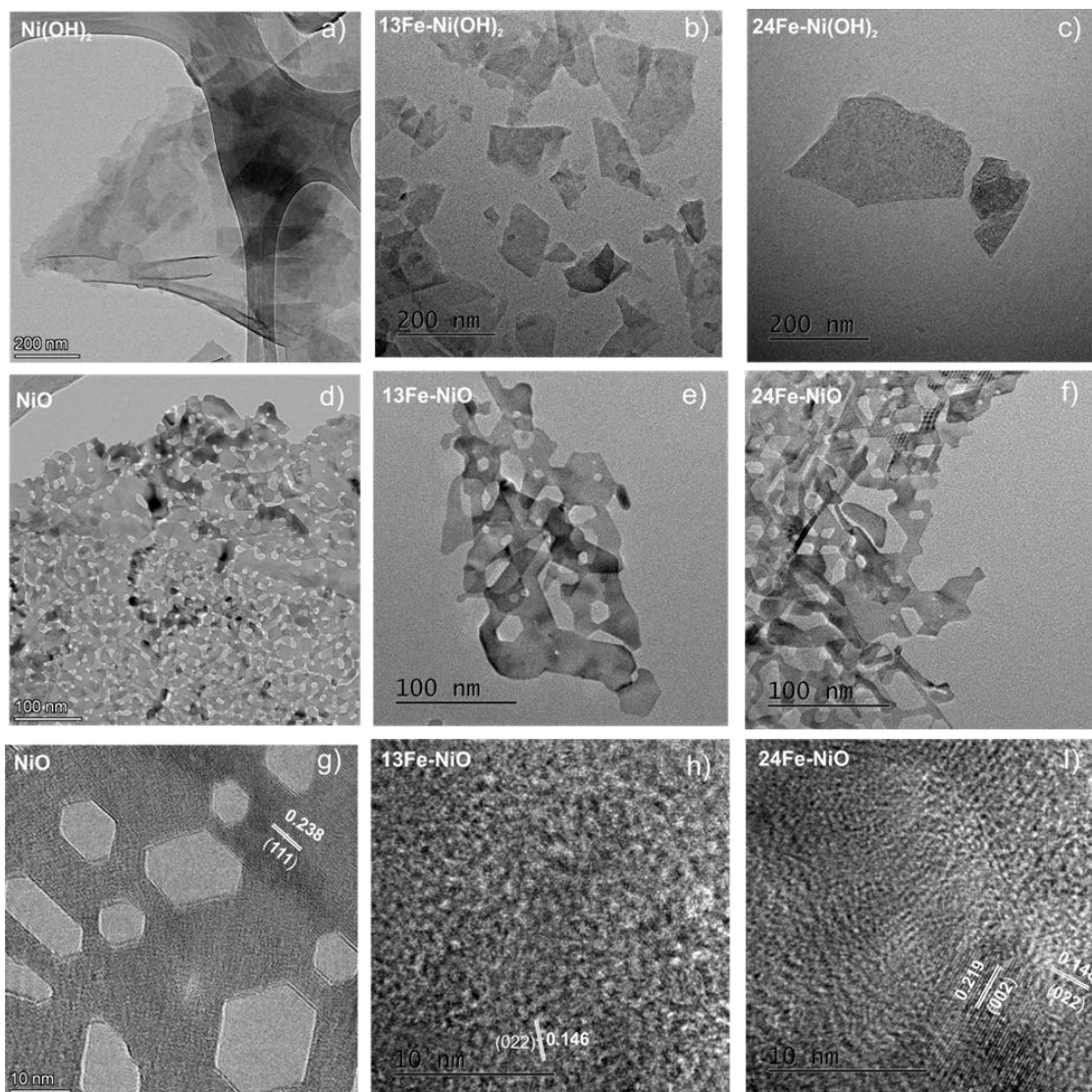


Figure A18: TEM images of the  $\text{Ni(OH)}_2$  samples a)-c), and the NiO samples with and without Fe doping d)-f). g)-i) exhibit HR-TEM images of the oxide samples.

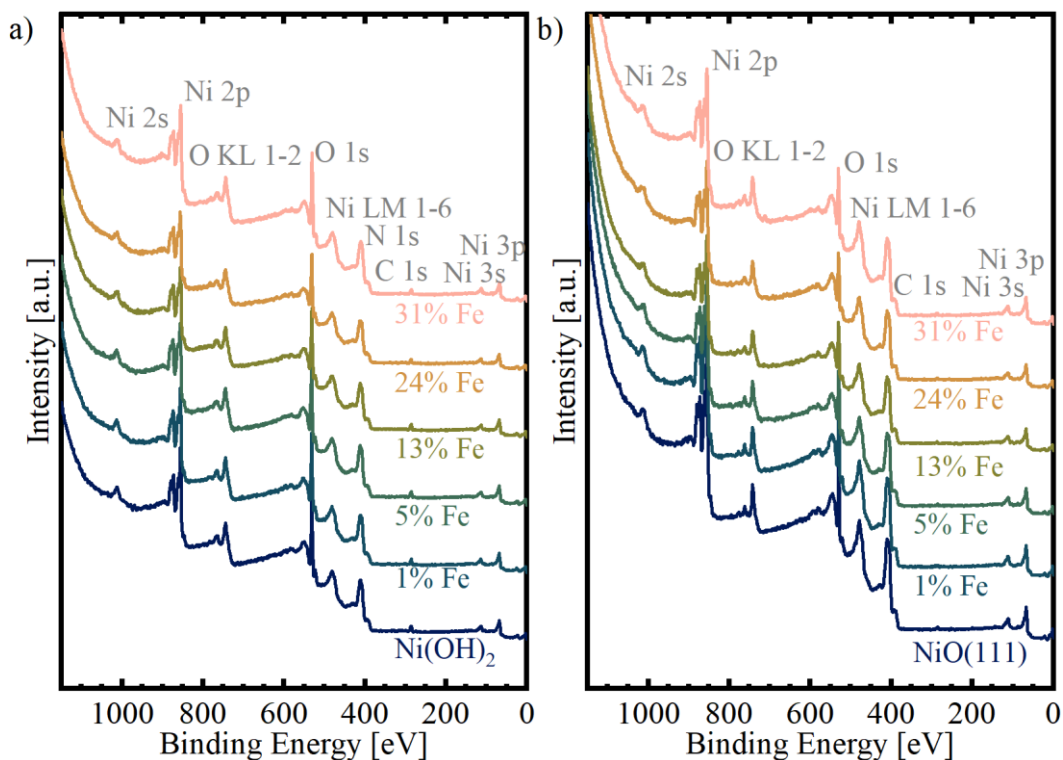


Figure A19: XPS survey spectra of the a) Ni(OH)<sub>2</sub> samples together with the b) oxide samples. The characteristic signals are labeled.

Table A8: Sequence of the electrochemical characterization of the Fe-containing materials.

Step	Conditions
<b>1. Argon purge at OCP</b>	The electrolyte is purged while the coated electrode is rested at OCP in the electrolyte for 30 min.
<b>2. EIS at OCP</b>	Frequency: 30 kHz-1 Hz Points/decade: 10 10 mV amplitude at OCP
<b>3. CV for OER initial</b>	Hold for 120 s at start potential 1.1 V vs. RHE Potential window: 1.0 – 2.2 V vs. RHE Scan rates: 10 mV s <sup>-1</sup> Scans: 2 Rotation: 2400 rpm No dynamic iR compensation. Stop current at 14 mA cm <sup>-2</sup> (avoiding bubble formation issues)
<b>4. CV for EC conditioning</b>	Hold for 20 s at start potential 1 V vs. RHE Potential window: 1.0 – 1.7 V vs. RHE Scan rates: 100 mV s <sup>-1</sup> Scans: 50 Rotation: 1600 rpm No dynamic iR compensation.
<b>5. EIS at OER conditions</b>	LSV 1 – 1.59 V vs. RHE  Frequency: 30 kHz-1 Hz Points/decade: 10 10 mV amplitude at 1.59 V vs. RHE (Bubble formation hindered data acquisition for active samples)
<b>6. CV for OER cycled</b>	Hold for 120 s at start potential 1.1 V vs. RHE Potential window: 1.0 – 2.2 V vs. RHE Scan rates: 10 mV s <sup>-1</sup> Scans: 2 Rotation: 2400 rpm No dynamic iR compensation. Stop current at 14 mA cm <sup>-2</sup> (avoiding bubble formation issues)

<b>7. Galvanostatic hold</b>	Hold for 3600 s at 10 mA cm <sup>-2</sup> Rotation: 2400 rpm Stop potential 2.2 V vs. RHE (avoiding carbon corrosion)
<b>8. EIS at OER conditions</b>	LSV 1 – 1.59 V vs. RHE  Frequency: 30 kHz-1 Hz Points/decade: 10 10 mV amplitude at 1.59 V vs. RHE (Bubble formation hindered data acquisition for active samples)
<b>9. CV for OER cycled</b>	Hold for 120 s at start potential 1.1 V vs. RHE Potential window: 1.0 – 2.2 V vs. RHE Scan rates: 10 mV s <sup>-1</sup> Scans: 2 Rotation: 2400 rpm No dynamic iR compensation. Stop current at 14 mA cm <sup>-2</sup> (avoiding bubble formation issues)

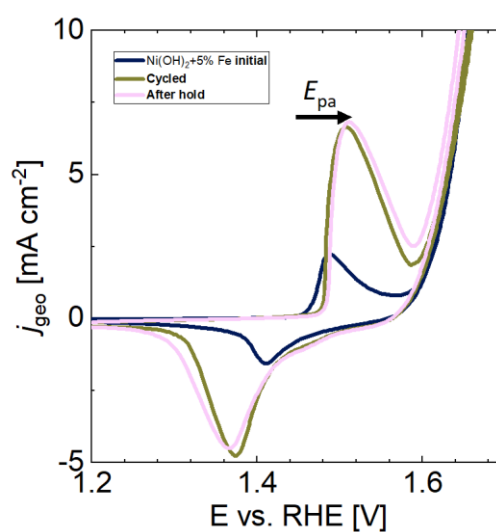


Figure A20: Representation of the minor shift of the Ni<sup>II</sup>/Ni<sup>III</sup> oxidation peak position ( $E_{\text{pa}}$ ) at the initial CV (step 3), the CV after conditioning (step 6) and the CV after the galvanostatic hold (step 9).

Table A9: Peak Position, Peak Area and Peak Ratios of the deconvolution from *in-situ* Raman experiments of the peak deconvolution in Figure 43.

Sample	Peak Position A	Peak Area A	Peak Position B	Peak Area B	Peak Position C	Peak Area C	Peak Ratio A/B	Peak Ratio B/C
Ni(OH) <sub>2</sub>	477	8.7	558	3.4	-	-	2.6	--
Ni(OH) <sub>2</sub> +1% Fe	476	5.0	554	1.8	-	-	2.8	--
NiO(111)	407	0.6	484	6.5	555	4.5	0.08	1.4
NiO(111)+1% Fe	404	1.6	478	8.7	549	6.0	0.18	1.4

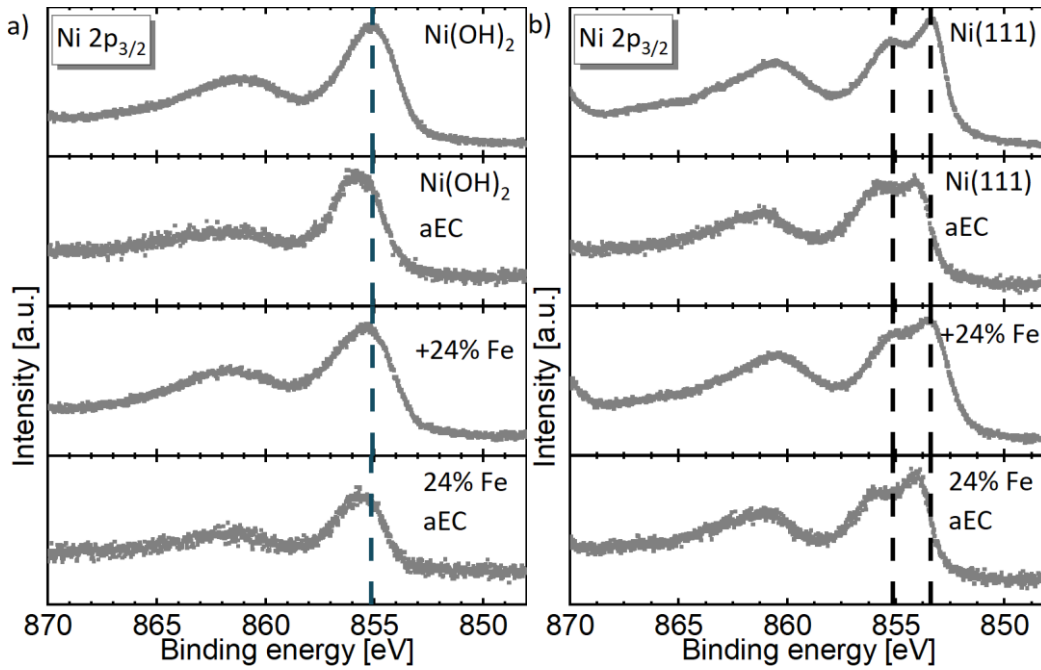


Figure A21: Comparison of XPS spectra of the Ni 2p<sub>3/2</sub> signal of pristine samples to samples after electrochemical treatment (aEC) of a) Ni(OH)<sub>2</sub> and b) NiO(111) samples. For both samples representative 24% Fe containing sample were measured.

## Supplementary data for the *in-situ* Fe incorporation

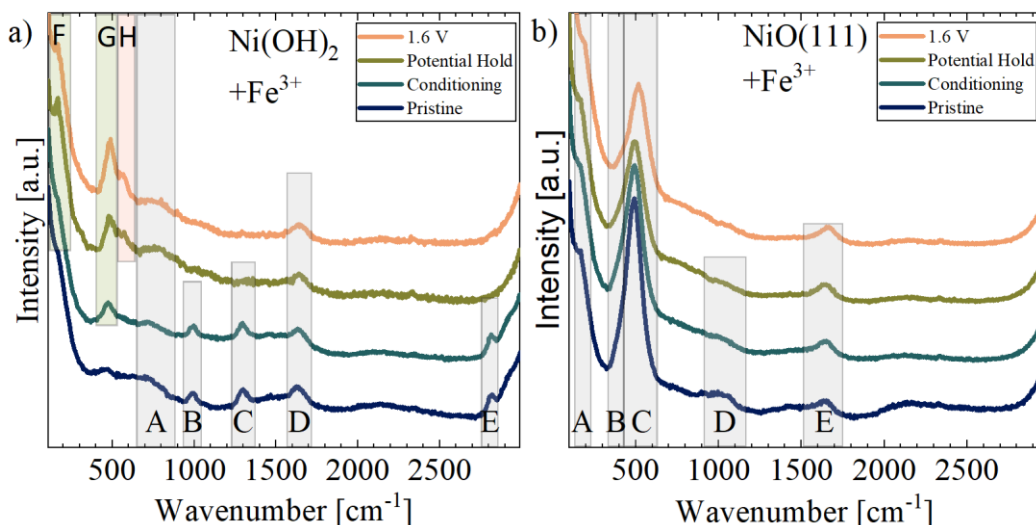


Figure A22: *In-situ* Raman experiments of representative samples for the study of the *in-situ* Fe<sup>3+</sup> containing Ni(OH)<sub>2</sub> and NiO(111) samples after background correction.

## Supplementary data of the implementation of the PTE setup

Table A10: Sequence of the electrochemical characterization of the Fe-containing materials with the PTE half-cell

Step	Conditions
<b>1. Argon purge at OCP</b>	The electrolyte is purged while the PTE is rested at OCP in the electrolyte for 30 min.
<b>2. EIS at OCP</b>	OCP determination (5 min) Frequency: 100 kHz-1 Hz Points/decade: 10 10 mV amplitude at OCP
<b>3. CV for EC activation</b>	Hold for 20 s at start potential 1 V vs. RHE Potential window: 1.0 – 1.6 V vs. RHE Scan rates: 100 mV s <sup>-1</sup> Scans: 50 95% iR compensation and 5% post correction of $R_u$
<b>5. EIS at OER conditions</b>	LSV 1 – 1.59 V vs. RHE  Frequency: 100 kHz-1 Hz Points/decade: 10 10 mV amplitude at 1.59 V vs. RHE (Bubble formation disrupted data acquisition for active samples)
<b>6. CV for OER activity</b>	Hold for 120 s at start potential 1.1 V vs. RHE Potential window: 1.0 – 1.7 V vs. RHE Scan rates: 10 mV s <sup>-1</sup> Scans: 2 95% iR compensation and 5% post correction of $R_u$
<b>7. Galvanostatic hold</b>	Hold for 3600 s at 50 mA cm <sup>-2</sup>  Subsequent GEIS for post correction of $R_u$ Frequency: 100 kHz-1 Hz Points/decade: 10 10 mV amplitude at 50 mA cm <sup>-2</sup>
<b>5. EIS at OER conditions</b>	LSV 1 – 1.59 V vs. RHE  Frequency: 30 kHz-1 Hz Points/decade: 10 10 mV amplitude at 1.59 V vs. RHE

<b>6. CV for OER activity</b>	Hold for 120 s at start potential 1.1 V vs. RHE Potential window: 1.0 – 1.7 V vs. RHE Scan rates: 10 mV s <sup>-1</sup> Scans: 2 95% iR compensation and 5% post correction of $R_u$
<b>7. Polarisation curve</b>	Current steps at 1, 5, 10 mA cm <sup>-2</sup> for 60 s Current steps at 25, 50, 100, 250 mA cm <sup>-2</sup> for 30 s Current steps at 500, 750, 1000 mA cm <sup>-2</sup> for 5 s Subsequent GEIS for post correction of $R_u$ Frequency: 100 kHz-1 Hz Points/decade: 10 20% current amplitude at each step
<b>8. EIS at OER conditions</b>	LSV 1 – 1.59 V vs. RHE  Frequency: 100 kHz-1 Hz Points/decade: 10 10 mV amplitude at 1.59 V vs. RHE (Bubble formation disrupted data acquisition for active samples)
<b>9. CV for OER activity</b>	Hold for 120 s at start potential 1.1 V vs. RHE Potential window: 1.0 – 1.7 V vs. RHE Scan rates: 10 mV s <sup>-1</sup> Scans: 2 95% iR compensation and 5% post correction of $R_u$

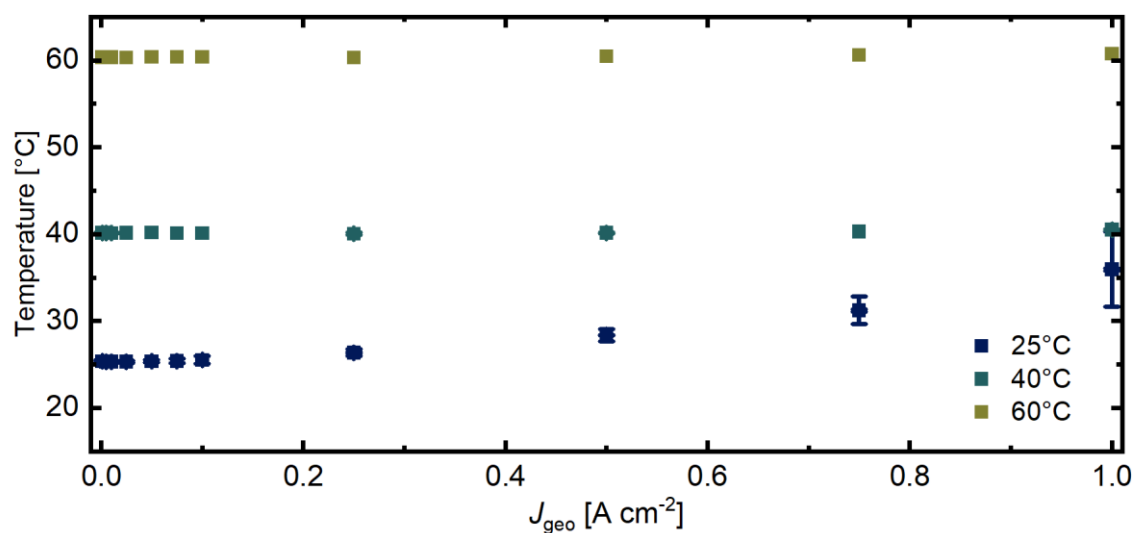


Figure A23: Temperature vs. the current density of the half-cell polarization curves at different temperatures. The experiments were conducted in 1 M KOH, at a flow rate of 60 mL min<sup>-1</sup>, with a working electrode area of 0.78 cm<sup>2</sup> ( $\varnothing$  1 cm). Adapted from Kadimi.<sup>130</sup>

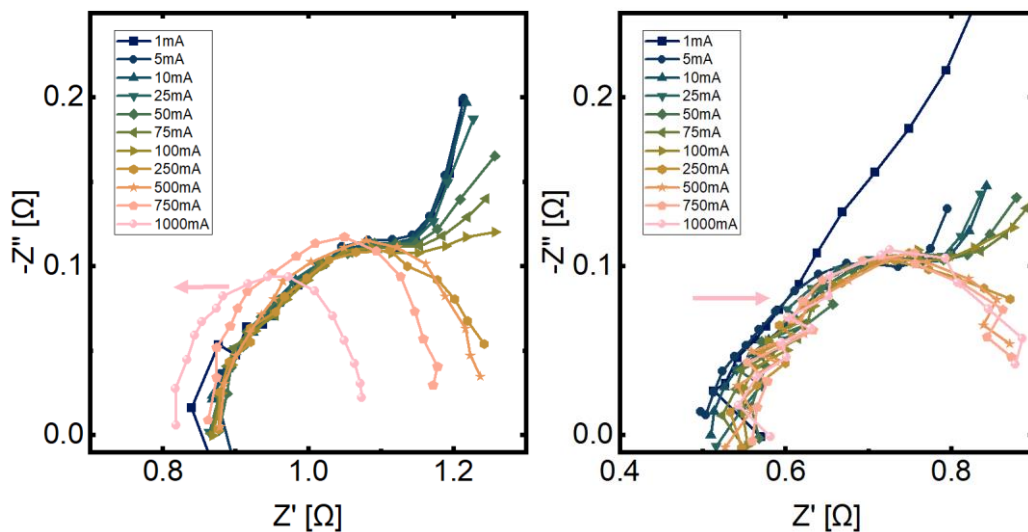


Figure A24: Representative GEIS results of the half-cell set up at left 25°C and right 80°C, respectively. The experiments were conducted in 1 M KOH, at a flow rate of 60 mL min<sup>-1</sup>, with a working electrode area of 0.78 cm<sup>2</sup> (∅ 1 cm). Adapted from Kadimi.<sup>130</sup>

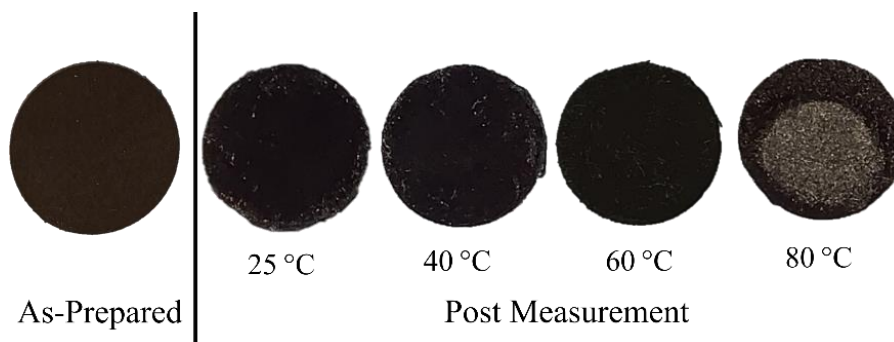


Figure A25: Representative photographs of NiFe<sub>2</sub>O<sub>4</sub> coated PTEs before and after electrochemical experiments at different temperatures in 1 M KOH, at a flow rate of 60 mL min<sup>-1</sup>, with a working electrode area of 0.78 cm<sup>2</sup> (∅ 1 cm). Adapted from Kadimi.<sup>130</sup>

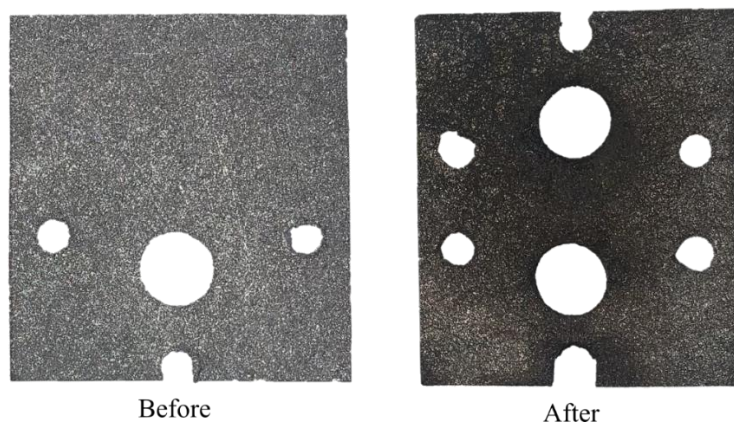


Figure A26: Titanium current collector made of a Titanium mesh, before and after multiple electrochemical experiments with the PTE setup. Adapted from Kadimi.<sup>130</sup>

---

## List of abbreviations

aEC	after electrochemical treatment
AEM	Anion exchange membranes
AEMWE	anion exchange membrane water electrolysis
AWE	alkaline water electrolysis
BET	Brunauer-Emmett-Teller
bf	before electrochemical treatment
CV	cyclic voltammetry
ECSA	electrochemically active surface area
EIS	Electrochemical impedance spectroscopy
EXAFS	extended X-ray absorption fine structure
GC	glassy carbon
GEIS	galvanostatic electrochemical impedance spectroscopy
HER	hydrogen evolution reaction
ICP-MS	inductively coupled plasma mass spectrometry
LDH	layered double hydroxide
LSV	linear sweep voltammetry
MW	microwave
NiO(111)	NiO with predominant (111) plane
OCP	open circuit potential
OER	oxygen evolution reaction
ORR	oxygen reduction reaction
PEMWE	proton exchange membrane water electrolysis
PTE	porous transport electrode
PXRD	Powder X-ray diffraction
RDE	rotating disc electrode
RHE	reversible hydrogen electrode
RRDE	rotating ring disc electrode
SOE	solid oxide electrolysis
ST	solvothermal
TEM	transmission electron microscopy
TRL	technology readiness level
WE	water electrolysis
XANES	X-ray absorption near-edge structure

---

XAS	X-ray absorption spectroscopy
XPS	X-ray photoelectron spectroscopy

---

## List of symbols

$E^0$	standard electrode potential
$U^0$	equilibrium voltage
$\eta$	overpotential
$E(j)$	applied electrode potential
$j$	Current density
$j_{\text{geo}}$	geometric current density
$Z'$	real component of the impedance
$Z''$	imaginary component of the impedance
$Z$	impedance
$R_u$	uncompensated resistance
$C_{\text{DL}}$	double layer resistance
$R_{\text{CT}}$	charge transfer resistance
$Z_{\text{W}}$	Warburg impedance
$C_{\text{Ads}}$	adsorption capacitance
$R_{\text{ads}}$	adsorption resistance
$i$	current
$R$	resistance
$\nu$	scan rate
$i_c$	capacitive charging current
$\alpha$	exponent describing ideal capacitive behavior
$E_{\text{B}}$	Binding energy in XPS
$h$	Plank's constant
$V$	photon wavelength
$E_{\text{K}}$	kinetic photon energy
$\varphi$	spectrometer constant

---

## **Erklärung des Bewerbers**

Hiermit versichere ich, Konstantin Kimon Rücker, geboren am 13.05.1998, dass ich die vorliegende Dissertation selbstständig und ohne unzulässige Hilfe verfasst habe. Alle von mir benutzten Hilfsmittel, Quellen und Hilfen sind vollständig angegeben. Ich erkläre, dass die Dissertation weder in ihrer Gesamtheit noch in Teilen einer anderen Hochschule zur Begutachtung in einem Promotionsverfahren vorliegt oder vorgelegen hat. Die Regelungen zur guten wissenschaftlichen Praxis der Carl von Ossietzky Universität Oldenburg wurden von mir befolgt. Teile der in der Dissertation enthaltenen Daten sind bereits veröffentlicht oder befinden sich in Vorbereitung zur Veröffentlichung. Diese sind entsprechend gekennzeichnet. Ferner erkläre ich, dass im Zusammenhang mit dem Promotionsvorhaben keine kommerziellen Vermittlungs- oder Beratungsdienste („Promotionsberatung“) in Anspruch genommen worden sind.

Oldenburg, den

Konstantin Kimon Rücker

---

## Curriculum vitae

### Personal data

Name: Konstantin Kimon Rücker  
Date of birth: 13.05.1998  
Place of birth: Wittmund, Germany

### Education

02/2022–10/2025 **PhD Candidate** at the Division Electrochemical Energy Technology of the DLR Institute of Engineering Thermodynamics and the Carl von Ossietzky University Oldenburg  
**Graduate School** “OLTECH”, PhD program “Molecular and Nanoscale Science”, Carl von Ossietzky University Oldenburg

10/2019–10/2021 **Master of Science in Chemistry**, Carl von Ossietzky University Oldenburg  
**Master Thesis:** “Structural investigation of the catalyst layer of proton exchange membrane fuel cells with atomic force microscopy” at the DLR Institute of Engineering Thermodynamics and the Carl von Ossietzky University Oldenburg

09.2019–01/2020 **Erasmus Program**,  
Uppsala University, Sweden, Chemistry for renewable energies

10/2016–09/2019 **Bachelor of Science in Chemistry** Carl von Ossietzky University Oldenburg

04/2019–08/2019 **Bachelor Thesis:** “Characterization of Redox Mediators for Lithium Peroxide Oxidation in a Lithium–Oxygen by Scanning Electrochemical Microscopy”

07/2008–06/2016 **Abitur**, Niedersächsisches Internatsgymnasium Esens

### Professional experience

Since 02/2022 **Research Scientist** at the Division Electrochemical Energy Technology of the DLR Institute of Engineering Thermodynamics and the Carl von Ossietzky University Oldenburg

04/2025 **Research Visit** at the University of Groningen, Netherlands

---

06/2023–07/2023 **Research Visit** at the Colorado School of Mines, Golden, CO, USA

03/2020–01/2022 **Student Assistant** at the Division Electrochemical Energy Technology of the DLR Institute of Engineering Thermodynamics and the Carl von Ossietzky University Oldenburg

**Instruction and guidance of theses**

2024 **MSc Thesis by Nikhil Kadimi** “Comprehensive Performance Analysis of Novel Catalysts on Porous Transport Layers in Half-Cell Electrochemical System” from the Otto-von-Guericke University Magdeburg

**Awards and scholarships**

2023 **Poster price** at the ISE 2023 74th Annual ISE Meeting, Lyon, France

2023 ReTraP (Research & Travel Program) Grant for the Research visit at the Colorado School of Mines

2018/2019 “Niedersachsenstipendium“ of the Carl von Ossietzky University Oldenburg